Nonlinear exciton-polaritons from infrared to ultraviolet in photonic microstructures based on transition metal dichalcogenides and GaN materials

The University Of Sheffield.

Ruggero Pietro Antonio EMMANUELE

Department of Physics and Astronomy
The University of Sheffield

This dissertation is submitted for the degree of
Doctor of Philosophy

February 2021

Acknowledgements

First of all, I would like to deeply thank the whole Low Dimensional Structures and Devices (LDSD) group in the Department of Physics and Astronomy at The University of Sheffield for the great opportunity to join it.
I am really grateful to my supervisor Prof. D. N. Krizhanovskii for his patient support and productive guidance throughout my PhD studies, without whose ideas and advice it would not have been possible to achieve what is shown in this thesis.
I wish to show profound appreciation to Prof. M. S. Skolnick, whose expert direction and deep involvement in research were crucial during our group meetings in order to progress in our studies.
I would like to express my gratitude to Dr. M. Sich, who not only helped me a lot with the daily lab work on TMDC-microcavities, but also taught me what are the characteristics of a good researcher.
I am thankful to Dr. P. M. Walker for letting me contribute constructively to a different project on GaN-waveguides, always guiding me with great punctuality and availability.
Moreover, I want to say thanks to Dr. F. Li and Dr. L. Giriunas, who first got me into the lab. If I enjoyed the work in the laboratory, it is also thanks to Dr. D. M. Di Paola, Dr. T. Kuriakose, Mr. T. Dowling and Dr. L. T. Rodriguez, to whom I wish the best in continuing the experiments. I want to show my thankfulness to Dr. C. E. Whittaker, Mr. F. A. Benimetskiy and Dr. J. Ciers as well, for the short but fruitful partnership.
I am obliged to all our collaborators, specially Dr. F. Withers and Dr. A. Catanzaro (also for his friendship), who furnished lots of $MoSe_2$ samples, and Dr. O. Kyriienko, who produced an amazing theoretical explanation to out experimental results.
I do not forget the guidance of Dr. M. Mears and Dr. M. Quinn during my teaching experience and my application as Associate Fellow of the Higher Education Academy (AFHEA), the edifying exchange of knowledge with other group members (Prof. A. I. Tartakovskii, Dr. S. Dufferwiel, Dr. T. Lyons, Dr. A. Genco, Dr. G. Buonaiuto and Dr. L. Sortino), as well as the essential technical help provided by the whole workshop, Mr. C. Vickers and Mr. P. Taylor.
Last but not least, I want to thank my parents and all my old and new friends around the world for their support during this long and wonderful journey.

Abstract

Being a superposition of photons and excitons in the strong coupling regime, exciton-polaritons inherit properties from both the constituents. We are interested in the interaction arising from their matter component, since the enhancement of the interaction strength compared to that in nonlinear optical materials in the weak coupling regime might lead to the development of new technological platforms, where light can be controlled by light thanks to Kerr-like nonlinearity.

In Chapter 1, we define exciton-polaritons and introduce the fundamental many-body phenomena in which they are involved, like Bose-Einstein condensation and solitons.

In Chapter 2, we describe the active media used in polaritonics, especially the two employed in this thesis, i.e. transition-metal dichalcogenide (TMDC) monolayers and GaN.

In Chapter 3, we outline the different geometries utilised to confine the light and make it interacts with excitons, specifically microcavities and waveguides.

In Chapter 4, we detail the experimental setups we used to study exciton-polaritons in TMDC-microcavities and GaN-waveguides.

In Chapter 5, we report on the preliminary results obtained on bare $MoSe_2$ monolayers and when we embedded them in our open-access microcavity.

In Chapter 6, we narrate about the interesting results achieved on TMDC-polaritons, focusing on the giant trion-polariton interaction strength, which lays the foundation for a new generation of nonlinear devices in the IR spectral range, foreshadowing highly efficient polariton blockade.

In Chapter 7, we observe for the first time nonlinear self-modulation of UV pulses operating up to room temperature, opening the way for potential technological platform for ultrafast nonlinear optics without cryogenics in the UV spectral range.

Finally, in Chapter 8, we summarise all the results obtained and trace possible future outcome in polaritonics, ranging from topological studies to superconductivity.

Appedices A and B are the theoretical models underneath the two experimental Chapters 6 and 7, respectively.

Table of contents

1 Background on polariton physics **3**

1.1 Introduction . . . 3

1.2 Exciton-polaritons . . . 5

1.2.1 Excitons . . . 5

1.2.2 Light-matter interaction . . . 7

1.2.3 Nonlinear optical effects . . . 10

1.2.3.1 Relaxation mechanism and bottleneck . . . 11

1.2.3.2 Bose-Einstein condensation . . . 13

1.2.3.3 Superfluidity, vortices and solitons . . . 15

1.2.3.4 Parametric oscillation and bistability . . . 19

2 Optical active media **21**

2.1 Introduction . . . 21

2.2 Transition-metal dichalcogenides . . . 22

2.2.1 Valley excitons . . . 24

2.2.2 Fabrication techniques . . . 27

2.2.2.1 Mechanical exfoliation . . . 28

2.2.2.2 Chemical vapour deposition . . . 28

2.3 III-nitride semiconductors . . . 28

2.3.1 Polarity . . . 30

2.3.2 GaN optical properties . . . 31

2.3.3 QW excitons . . . 32

2.3.4 Fabrication techniques . . . 33

3 Photonic microstructures **35**

3.1 Introduction . . . 35

3.2 Planar Fabry-Pérot microcavities . . . 36

3.2.1 Hemispherical tunable open-access microcavities . . . 39

3.2.2 Fabrication techniques . . . 41
3.3 Waveguides . . . 42
3.3.1 Grating couplers . . . 44
3.3.2 Fabrication techniques . . . 45
3.4 Waveguides vs microcavities . . . 46

4 Experimental setups 49
4.1 Introduction . . . 49
4.2 $MoSe_2$ experiments . . . 49
4.2.1 Microscope for flake search . . . 49
4.2.2 Excitation paths . . . 50
4.2.2.1 Excitation lasers . . . 50
4.2.3 Cryostats . . . 52
4.2.3.1 Continuous-flow cryostat . . . 53
4.2.3.2 Bath cryostat . . . 53
4.2.4 Detection path . . . 57
4.2.4.1 Spectrometer and streak camera . . . 57
4.3 GaN experiments . . . 59
4.3.1 Excitation path . . . 59
4.3.1.1 Excitation lasers . . . 60
4.3.1.2 Pulse shaper . . . 60
4.3.2 Detection path . . . 60

5 Characterisation of TMDC-polaritons in a tunable open-access microcavity 63
5.1 Introduction . . . 63
5.2 Characterisation of bare $MoSe_2$ monolayers . . . 64
5.2.1 Exfoliated vs CVD sample . . . 64
5.2.2 Power dependence studies . . . 66
5.2.2.1 CW laser . . . 66
5.2.2.2 Pulsed laser . . . 68
5.3 $MoSe_2$ monolayers in a hemispherical open cavity . . . 70
5.3.1 Characterisation of polariton states formation . . . 70
5.3.2 Pumping LG_{01} and detecting LG_{00} . . . 73
5.3.3 Resonantly pumping LG_{00} at different detunings . . . 75
5.4 Summary . . . 77

6 Nonlinear exciton- and trion-polaritons in TMDCs under resonant pulsed excitation 79
6.1 Introduction . . . 79
6.2 Sample characterisation . . . 80
6.3 Polariton nonlinearity . . . 82
6.4 Trion-polariton nonlinearity . . . 85
6.4.1 Nonlinear refractive index n_2 due to trion-polaritons . . . 92
6.4.1.1 Nonlinear refractive index n_2 of hybrid microcavity-$MoSe_2$ polariton system . . . 92
6.4.1.2 Effective nonlinear refractive index $n_2(MoSe_2)$ per single TMDC monolayer arising from trion-polariton nonlinearity 93
6.5 Exciton-polariton nonlinearity . . . 94
6.6 Summary . . . 99

7 Nonlinear UV pulse propagation in a GaN-waveguide up to room temperature 101
7.1 Introduction . . . 101
7.2 Dispersion measurement and fitting . . . 102
7.3 Resonant excitation and detection of propagating polariton pulses . . . 105
7.4 Self-phase modulation . . . 109
7.5 Estimate of nonlinear refractive index from first-principle calculations . . . 114
7.6 Comparison of nonlinear refractive index with literature values . . . 116
7.7 Summary . . . 117

8 Conclusions and future perspectives 119
8.1 Summary . . . 119
8.2 Discussion on experimental results . . . 120
8.2.1 $MoSe_2$-microcavity . . . 120
8.2.2 GaN-waveguide . . . 122
8.3 Outlook . . . 123

References 133

Appendix A Theory on TMDC-polaritons in microcavities 147
A.1 Introduction . . . 147
A.2 Nonlinear neutral exciton-polaritons . . . 148
A.2.1 Exciton-polariton Rabi splitting . . . 148

A.2.2 Nonlinear exciton energy shift 154
A.2.3 Exciton-polaritons at increasing density 157
A.3 Nonlinear trion-polaritons 158
A.3.1 Trion-polariton Rabi splitting 158
A.3.2 Trion binding energy and variation 162
A.3.3 Trion Rabi splitting quench 163
A.3.4 Deviation from fermionicity for the composite trion anti-commutator 165
A.3.5 Effects of medium saturation 166
A.3.6 Trion-polaritons at increasing density 169
A.4 Quantum trion-polaritons 171

Appendix B Theory on GaN-based polariton waveguides 175
B.1 Introduction 175
B.2 Coupling efficiency and losses 175
B.3 Numerical simulations 177

List of publications

- The work described in Chapter 6 and in Appendix A has resulted in:

  Highly nonlinear trion-polaritons in a monolayer semiconductor

  R. P. A. Emmanuele, M. Sich, O. Kyriienko, V. Shahnazaryan, F. Withers, A. Catanzaro, P. M. Walker, F. A. Benimetskiy, M. S. Skolnick, A. I. Tartakovskii, I. A. Shelykh and D. N. Krizhanovskii

  *Nature Communications, **11**, 3589 (2020)*

- The work described in Chapter 7 and in Appendix B has resulted in:

  Ultrafast-nonlinear ultraviolet pulse modulation in an AlInGaN polariton waveguide operating up to room temperature

  D. M. Di Paola, P. M. Walker, R. P. A. Emmanuele, A. V. Yulin, J. Ciers, Z. Zaidi, J.-F.Carlin, N. Grandjean, I. Shelykh, M. S. Skolnick, R. Butté and D. N. Krizhanovskii

  arXiv:2009.02059

Chapter 1

Background on polariton physics

1.1 Introduction

The current electronic devices, that we all use in everyday life, are intrinsically limited by their very nature. Because of the resistance experienced by electrons in wires, they are characterised by high heating and energy consumption, the information is carried over short distances and logic operations are slow. From this point of view, the use of all-optical elements would represent a milestone for future information processing in order to overcome all the above-mentioned restrictions [1]. Indeed, the information would be carried faster and over longer distances thanks to the lack of interaction with the surrounding environment, providing long coherence time and then making photons suitable candidates for quantum bits (i.e. qubits).

However, at the same time, the interaction between photonic signals is crucial for the realization and the development of novel technological devices for quantum optics applications [2]. Since there is no interaction between photons in free space, we can make them interact through nonlinear optical processes inside nonlinear optical materials. Because the nonlinearity in bulk materials is very weak, intense light beams are necessary to modify their refractive index, inducing Kerr-like nonlinearity. Nevertheless, it is vital to work at extremely low signal intensities (preferably at single photon level) for new quantum practical applications. Ideally one photon in one optical mode should vary the phase of another photon in another optical mode by π, i.e. they should interact strongly. Thus, in order to dramatically enhance photon interaction and then considerably increase this nonlinear response, coupling with matter systems is necessary.

It is then possible to couple photons to artificial atoms such as quantum dots (QDs) [3]. Their discrete energy level structure allows highly nonlinear optical response, since the absorption of a single photon significantly modifies the response to a second incident photon. Although these systems can reach a large phase shift up to $\sim \pi/10$ [4], they unfortunately manifest intrinsic problems of scalability, since they cannot be positioned deterministically and show large spread in energy. Moreover, their operation time is limited by the system "reset" time arising from the radiative recombination lifetime, which is in the *ns* range. However, this latter limitation can be partially overcome using cross-phase modulation (XPM) due to Kerr-like nonlinearity, speeding up the operation in the *ps* timescale [5] (this phenomenon will be deepened in Section 8.3).

Providentially, this impediment for practical applications can be overcome by employing micrometric exciton-polariton systems: as a matter of fact, micrometric structures are less sensitive to energy fluctuations and allow deterministic positioning, making them scalable. Furthermore, thanks to the limited polariton lifetime (~ 10 *ps*), they still guarantee the short operation time needed for technological implementation [6]. In the light of the above, and as we are going to demonstrate throughout this thesis, exciton-polaritons can certainly play a major role in the realisation of tomorrow's technology, favouring the transition from electronic to optical devices thanks to their unique characteristics.

Theoretically predicted in 3D bulk more than sixty years ago [7, 8] and experimentally observed for the first time in 2D quantum-well (QW) about thirty years later [9], exciton-polaritons are part-light part-matter quasi-particles originating from the strong coupling between photons and excitons. They inherit interesting properties from both the constituents, such as very low effective mass (4-5 orders of magnitude smaller than the electron mass m_e) and light speed propagation ($1-10\%$ of the speed of light c) from photons, and strong interaction from excitons. The latter produces nonlinear effects at relatively small absorption, then lowering the power thresholds and diminishing the length-scales, leading to smaller energy consumption and device size.

Specifically, it was already shown that the polariton-polariton interaction is $10^3 - 10^4$ times larger than the photon-photon interaction in nonlinear optical materials weakly coupled to light [10], thanks to its excitonic nature. This aspect is fundamental in the development of more compact (micrometric) and efficient all-optical devices such as switches and modulators, since the power needed decreases by 3-4 orders of magnitude.

This enhanced interaction might lead to the development of new technological platforms, for example ultrafast quantum source of light [11, 12] and photonic signal processing cir-

cuitry [13, 14], where light can be controlled by light thanks to Kerr-like nonlinearity, on fast timescales and low powers.

It is also possible to confine polaritons in all three dimensions implementing appropriate photonic resonators, as opposed to the more classic 2D geometry. This leads to discretisation of the polariton modes, further increasing the interaction strength to the point of being sensitive to the presence of few quanta, as happens for QDs, but overcoming the above-mentioned limitation of scalability and operation speed.

Moreover, exciton-polaritons have already revealed their importance in studying basic physics concepts, exploring fundamental many-body phenomena, for instance Bose-Einstein condensation [15], superfluidity [16], optical parametric oscillation [17] and solitons [18], just to name a few that we are going to deepen in Section 1.2.3.

1.2 Exciton-polaritons

1.2.1 Excitons

An atom is composed of a nucleus and electrons, that occupy the innermost discrete atomic orbitals around the nucleus. When two atoms are moved to a close proximity, these electronic orbitals overlap and split, as derived by the properties of two coupled classical oscillators. Considering the huge number of atoms forming a crystal ($\sim 10^{23}\ atoms/cm^3$), this energy splitting creates a band structure, where a moving electron is described by the Bloch wavefunction $\psi(r) = e^{ik\cdot r}u(r)$, representing a plane wave (where k is the crystal wavevector) multiplied by a periodic function $u(r)$ with the same periodicity of the crystal [19].
The highest filled band is called the valence band (VB) and the lowest unfilled band is called the conduction band (CB). Depending on the value of the energy gap (bandgap E_g) between them, we classify: metals ($E_g = 0\ eV$), semiconductors ($E_g < 6\ eV$) and insulators ($E_g > 6\ eV$). We also distinguish between direct and indirect bandgap materials: in the former, VB maximum and CB minimum have the same k (we refer to the energy minimum as a valley) and an electron can jump from one to the other when a photon with energy $E_{ph} > E_g$ is absorbed; in the latter, such as Si, the VB maximum and the CB minimum have different k, so the electron transition requires also a phonon to have conservation of both energy E and momentum $p = \hbar k$.

In both cases, the electron leaves a vacancy in the VB, called a hole, with opposite charge, spin and momentum, and the Coulomb interaction between them may form a new quasi-particle, called an exciton. This hydrogen-like bound state can be described by the Schrödinger equation

$$\left[-\frac{\hbar^2}{2m_X}\nabla^2 - \frac{e^2}{4\pi\varepsilon\varepsilon_0 r}\right]\psi_X(r) = E\psi_X(r) \tag{1.1}$$

where $m_X = \frac{m_e^* m_h^*}{m_e^* + m_h^*}$ is the reduced mass of the bound electron (effective mass m_e^*) and hole (effective mass m_h^*), and r is their separation. Then, the exciton wavefunction of the ground state is

$$\psi_{1s}(r) = \frac{1}{\sqrt{\pi a_B^3}} e^{-\frac{r}{a_B}} \tag{1.2}$$

where

$$a_B(3D) = \frac{4\pi\hbar^2\varepsilon\varepsilon_0}{m_X e^2} \tag{1.3}$$

is the Bohr radius, while the binding energy of the ground state is

$$E_B(3D) = \frac{\hbar^2}{2m_X a_B^2} \tag{1.4}$$

So, the bigger the Bohr radius, the smaller the binding energy. More generally, the energy for each exciton state (ground state given by $n = 1$ and excited states given by $n > 1$) is

$$E_X^n(3D) = -\frac{R_X}{n^2}, \quad n = 1,\ 2,\ ... \tag{1.5}$$

where the reduced Rydberg energy R_X reads [20]

$$R_X = \frac{m_X e^4}{32\pi^2\varepsilon_0^2\varepsilon^2\hbar^2} \tag{1.6}$$

The size of the Bohr radius allows us to distinguish between Wannier-Mott and Frenkel excitons, whether they are larger or smaller than the crystal unit cell respectively, while the binding energy gives a measure of their stability: excitons can be observed when their binding energy is bigger than the thermal energy $k_B T$, which is 25 meV at room temperature (RT).

Another important quantity, since we are interested in exciton-photon coupling, is the excitonic oscillator strength, which measures the probability of the optical transition:

$$f_X(3D) = f_{cv}\frac{V}{\pi a_B^3} \tag{1.7}$$

where

$$f_{cv} = \frac{2m_X\omega_{cv}|r_{cv}|^2}{\hbar} \tag{1.8}$$

is the interband oscillator strength, multiplied by the factor $\frac{V}{\pi a_B^3}$, which takes into account the enhanced electron-hole interaction within an exciton compared to a free electron-hole pair. In Equation 1.8, ω_{cv} is the interband transition frequency and $r_{cv} = \langle u_v|r\cdot e|u_c\rangle$ is the matrix element representing the interaction of the exciton dipole (electron and hole with Bloch wavefunction $|u_c\rangle$ and $|u_v\rangle$, respectively) with an electromagnetic field [21].

1.2.2 Light-matter interaction

To further enhance exciton-photon coupling, excitons can be spatially confined (for example in QWs) and photons can be trapped in small volumes using different geometries, like microcavities and waveguides. The spatial confinement increases the oscillator strength and the binding energy of excitons, while the trapped photons can interact repeatedly with the active medium. These two concepts are going to be addressed in Chapter 2 and Chapter 3, respectively.

Studying the light-matter interaction with a classical approach, an exciton and a photon can be considered as two oscillators coupled through a spring, with damping rate γ_X and γ_{ph}, respectively. When the coupling constant $g_0 << \gamma_X, \gamma_{ph}$, we enter in the so-called weak coupling regime, characterised by irreversible energy transfer between the two oscillators. On the contrary, when $g_0 >> \gamma_X, \gamma_{ph}$, the energy transfer is reversible and we get into the strong coupling regime [22].

Using a quantum approach, we can define the Hamiltonian of the system

$$\hat{H} = (E_X - i\gamma_X)\,\hat{a}^+\hat{a} + \left(E_{ph} - i\gamma_{ph}\right)\hat{b}^+\hat{b} + g_0\left[\hat{a}^+\hat{b} + \hat{b}^+\hat{a}\right] \tag{1.9}$$

where

$$g_0 \propto \sqrt{\frac{f_X \cdot N_{QW}}{V_{eff}}} \tag{1.10}$$

is the coupling constant (with number of QWs N_{QW} and effective volume V_{eff}), $\hat{a}^+, \hat{b}^+$ are the creation operators and $\hat{a}, \hat{b}$ are the annihilation operators for exciton and photon, respectively. We can represent this Hamiltonian as a matrix

$$\hat{H} = \begin{bmatrix} E_X - i\gamma_X & g_0 \\ g_0 & E_{ph} - i\gamma_{ph} \end{bmatrix} \tag{1.11}$$

and thus obtain its two eigenvalues for the Upper and Lower Polariton Branches (UPB and LPB, respectively)

$$E_{UPB,LPB} = \frac{E_{ph} + E_X - i\left(\gamma_{ph} + \gamma_X\right)}{2} \pm \frac{1}{2}\sqrt{4g_0^2 + \left[E_{ph} - E_X - i\left(\gamma_{ph} - \gamma_X\right)\right]^2} \tag{1.12}$$

We can then define two important quantities, the detuning

$$\Delta = E_{ph} - E_X \tag{1.13}$$

and, when $\Delta = 0$, the Rabi splitting

$$\hbar\Omega_X = \sqrt{4g_0^2 - \left(\gamma_{ph} - \gamma_X\right)^2} \tag{1.14}$$

We can now easily distinguish between the weak and the strong coupling regime: when

$$g_0 < \frac{|\gamma_{ph} - \gamma_X|}{2} \tag{1.15}$$

the Rabi splitting $\hbar\Omega_X$ becomes imaginary and we enter in the weak coupling regime, while when

$$g_0 > \frac{|\gamma_{ph} - \gamma_X|}{2} \tag{1.16}$$

the Rabi splitting $\hbar\Omega_X$ becomes real and we get into the strong coupling regime [23], with the characteristic anticrossing between the two polariton branches (Figure 1.1, top panel).

We can also calculate the eigenvectors of Equation 1.11, whose squares give the Hopfield coefficients ($\gamma_{ph} = \gamma_X = 0$ for simplicity)

$$|C_X|^2 = \frac{1}{2}\left[1 + \frac{\Delta}{\sqrt{4g_0^2 + \Delta^2}}\right] \tag{1.17}$$

$$|C_{ph}|^2 = \frac{1}{2}\left[1 - \frac{\Delta}{\sqrt{4g_0^2 + \Delta^2}}\right] \tag{1.18}$$

which represent the excitonic and the photonic fraction of the polariton mode respectively, where $|C_X|^2 + |C_{ph}|^2 = 1$. Being a superposition of photons and excitons, polariton mass and linewidth depend on those of its constituents [24]:

$$\frac{1}{m_{UPB}} = \frac{|C_{ph}|^2}{m_X} + \frac{|C_X|^2}{m_{ph}}, \quad \frac{1}{m_{LPB}} = \frac{|C_X|^2}{m_X} + \frac{|C_{ph}|^2}{m_{ph}} \tag{1.19}$$

and

$$\gamma_{UPB} = |C_{ph}|^2\gamma_X + |C_X|^2\gamma_{ph}, \quad \gamma_{LPB} = |C_X|^2\gamma_X + |C_{ph}|^2\gamma_{ph} \tag{1.20}$$

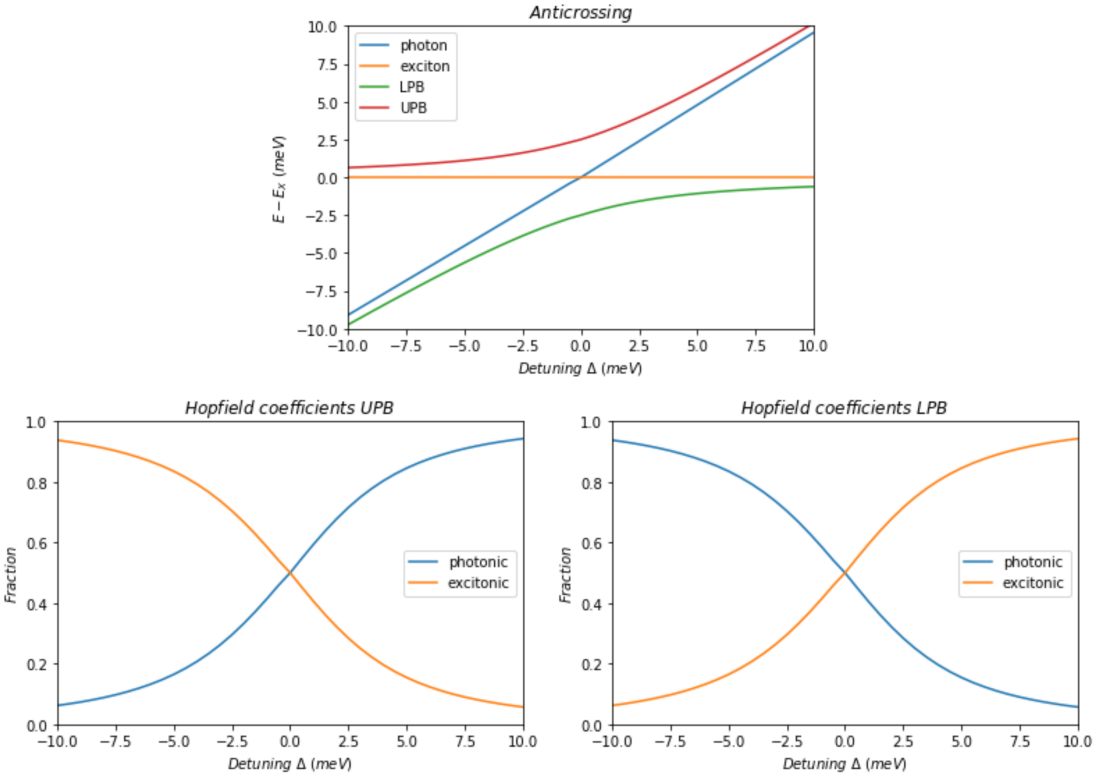

Fig. 1.1 **Top panel**: anticrossing of upper and lower polariton branches (UPB and LPB, red and green respectively) as function of the detuning Δ, tuning the photon energy E_{ph} (blue) across the exciton resonance E_X (orange). **Bottom panels**: Hopfield coefficients of photonic (blue) and excitonic (orange) fraction in upper (left) and lower (right) polariton branches.

In Section 2.2.1, we will briefly introduce the concept of charged excitons (or trions) in transition metal dichalcogenides (TMDCs). This will be useful later on since we will also experimentally observe strong coupling between photons and trions (leading to formation of the so-called trion-polaritons) when placing a $MoSe_2$ monolayer (ML) within our open-access microcavity (see Section 3.2.1). Only in this case, we will adopt the three-coupled oscillator model, that expands the theory just described (see Section 5.3.1).

1.2.3 Nonlinear optical effects

As already mentioned in Section 1.1, a material under an optical field can respond nonlinearly:

$$P(t) = \varepsilon_0 \left[\chi^{(1)} E(t) + \chi^{(2)} E^2(t) + \chi^{(3)} E^3(t) + ... \right] \tag{1.21}$$

where $\chi^{(2)}$ is the second-order nonlinear optical susceptibility and $\chi^{(3)}$ is the third-order nonlinear optical susceptibility. To observe this nonlinear response, the optical field should be strong enough to be comparable with the field of the nucleus acting on its electrons [25].

For exciton-polaritons, as declared in Section 1.1, the optical nonlinearity is due to their excitonic component $|C_X|^2$. Polaritons with opposite spins interact attractively, while those with identical spins repel each other, but the latter interaction is approximately 10 times stronger [26]. So, the polariton-polariton interaction, related to $\chi^{(3)}$ [27], causes the renormalisation of the polariton energy state. In particular, this blueshift of the polariton energy state is a consequence of two different phenomena related both to excitons.
The first one is the blueshift of the exciton resonance due to the Coulomb interaction between excitons, represented by [28]

$$g_X^{eff} = \frac{dE_X}{dn_X} = g_{pol} \frac{N_{QW}}{|C_X|^4} \tag{1.22}$$

where n_X is the exciton density and g_{pol} is the polariton-polariton interaction. Theoretically, the exciton-exciton interaction strength is given by $g_X \sim 3\ E_B\ a_B^2$, which results in $g_X \sim 3\ \mu eV \cdot \mu m^2$ in GaAs QW, the most studied optically active material in polaritonics [29]. Higher values were experimentally obtained [30], but the build-up of the incoherent exciton reservoir (see Section 1.2.3.1) was not taken into account, underestimating the particle density.
The second one is the phase-space filling effect, represented by [28]

$$\beta_X^{eff} = \frac{d(\hbar\Omega_X)}{dn_X} = g_{pol} \frac{N_{QW}}{|C_{ph}|\ |C_X|^3} \tag{1.23}$$

Increasing the pump power, more carriers are injected in the system, offering less states for exciton formation (as a result of the Pauli exclusion principle) and so causing a reduction of the collective exciton oscillator strength, consequently diminishing the Rabi splitting.

Further increasing the pump power (i.e. increasing the exciton density), the distance between excitons decreases, approaching the exciton Bohr radius. The resulting screening of the Coulomb interaction leads to dissociation of excitons themselves, creating an electron-hole plasma with the consequent loss of bosonic behaviour. The critical density for this transition is the so-called Mott density [20]

$$n_{Mott}(3D) = \frac{1}{\frac{4}{3}\pi a_B^3} \tag{1.24}$$

As previously stated in Section 1.1, the nonlinear response of a medium under an intense optical excitation can be characterised by the optical Kerr effect, showing a change in the refractive index that is proportional to the intensity of the excitation field

$$n = n_0 + n_2 I \tag{1.25}$$

where $n_2 \propto \frac{\chi^{(3)}}{n_0^2}$ is the nonlinear refractive index. When $n_2 > 0$, a self-focusing behaviour is noticed because the refractive index grows at the centre of the beam, working as a lens. As already outlined in Section 1.1, the nonlinear refractive index measured in a GaAs-waveguide in the strong coupling regime is $n_2 = -1.6 \times 10^{-14}\ m^2/W$ [10], three orders of magnitude larger than that obtained in a AlGaAs-waveguide in the weak coupling regime ($n_2 = 1.8 \times 10^{-17}\ m^2/W$) [31] and four orders of magnitude larger than that achieved in Si- [32] and InGaP-based [33] photonic crystal geometries ($n_2 \sim 6 \times 10^{-18}\ m^2/W$).
In case of optical excitation through a pulsed laser, this variation of the refractive index provokes a time dependent phase shift, phenomenon known as self-phase modulation (SPM), which induces spectral broadening [34]. SPM is going to be deepened in Chapter 7, once waveguides are fully introduced in Chapter 3.

1.2.3.1 Relaxation mechanism and bottleneck

Let us consider a polariton system under non-resonant excitation, one of the most common configurations used to investigate the physics behind it. The whole process that we are going to describe is depicted in Figure 1.2. The laser creates electron-hole pairs, which relax to lower energies via optical phonon emission. As an outcome of this process, the laser coherence is lost and an exciton reservoir at high momentum is formed. Now, further relaxation can be possible only by scattering with acoustic phonons, because at this point

excitons have to lose momentum above all. Once excitons reach the light cone $\left(k_X < \frac{\omega}{c}\right)$, they can couple with light and form polaritons.
Looking at GaAs QWs in microcavities, the most studied polariton system so far, polariton-phonon interaction lasts 10 *ps* and causes an energy loss of about 1 *meV*. However, polariton lifetime is usually around 5 *ps* and also they have to dissipate approximately 10 *meV* in order to reach the ground state [35]. Ergo, polaritons accumulate at high-k states [36]. In spite of that, this bottleneck effect can be overcome via polariton-electron and elastic polariton-polariton interaction at high density. The former process plays an important role in relaxing the polariton gas in the lowest part of the dispersion, where the electron gas reservoir mimics the previously described behaviour of acoustic phonons in the relaxation process, showing however a greater efficiency [23, 37, 38].

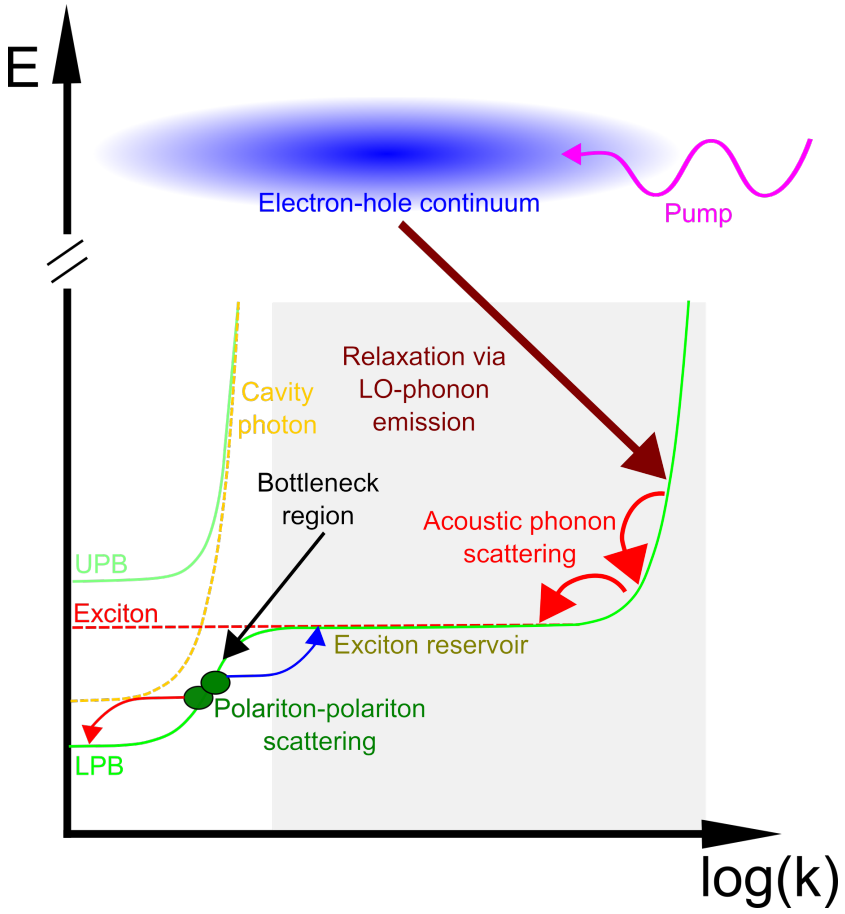

Fig. 1.2 Schematic of the relaxation mechanism. A non-resonant excitation (purple) creates an electron-hole continuum (blue), which relaxes through optical and then acoustic phonons (dark and light red respectively). Polariton-polariton scattering (dark green) overcomes the bottleneck region. The grey area shows the optical inactive region outside the light cone.

1.2.3.2 Bose-Einstein condensation

Given the dual nature of the particles, they can be related to a wave linked to their momentum p

$$\lambda_{dB} = \frac{h}{p} = \sqrt{\frac{2\pi\hbar^2}{mk_BT}} \tag{1.26}$$

whose (de Broglie) wavelength is inversely proportional to both mass m and temperature T. When the de Broglie wavelength becomes comparable to the interparticle distance, the particles wavefunctions overlap and a macroscopic occupation of the lowest energy state described by a single wavefunction is possible [39]. To observe this condensation, the particles taken into consideration must be bosons, which are indistinguishable and obey the Bose-Einstein distribution (hence the name Bose-Einstein condensation - BEC)

$$f(k,T,\mu) = \frac{1}{e^{\frac{E(k)-\mu}{k_BT}} - 1} \tag{1.27}$$

where μ is the chemical potential.
Since polaritons arise from two particles with integer spins, they are bosonic quasi-particles and so they fulfil this basic requirement. Moreover, their low effective mass (10^{-5} m_e) enlarges the de Broglie wavelength, making them an ideal candidate to study BEC. The other two necessary conditions in order to observe BEC are low temperature and high particle density, whose critical values for condensation to occur are linked by the following equation

$$T_c = \frac{2\pi\hbar^2}{m}\left(\frac{n_c}{2.612}\right)^{\frac{2}{3}} \tag{1.28}$$

where the critical density is given by

$$n_c = \lim_{\mu\to 0} \frac{1}{(2\pi)^d} \int_0^\infty f(k,T,\mu)\, dk \tag{1.29}$$

It is possible to show that this integral converges for systems with more than two dimensions ($d > 2$) and diverges for systems with less than three-dimensions ($d \leq 2$).

Polaritons in microcavities (which are going to be completely described in Chapter 3) have two-dimensional characteristics because their motion is confined in the orthogonal direction, so they cannot condense in the strict sense. Indeed, in pure 2D geometries, BEC characterised by long range spatial coherence cannot be observed. However, formation of a condensate with a finite spatial coherence extending over a finite distance is possible. Talking about waveguides, they do not present any ground state, so they cannot show BEC at all.
Furthermore, BEC is defined in conservative systems of ideal boson gases in thermodynamic

equilibrium, while polaritons interact with each other and have to continuously be replaced in the system because of their finite lifetime, which is usually shorter than the thermalisation time.
However, it is worth to note that recently BEC of polaritons in thermal equilibrium was observed [40]. To obtain that, a very long polariton lifetime was needed to achieve full thermalisation (thermalisation time is at least 40 *ps* for exciton-like polaritons and longer for photon-like polaritons, which are less interacting), so a GaAs high-Q microcavity was grown with a quality factor of about 3×10^5 and a polariton lifetime of 270 *ps* (for the definition of the quality factor Q, see Section 3.2).

In spite of those lacks, polaritons certainly manifest many fundamental characteristics of BEC [15], first of all the macroscopic occupation of the lowest energy state through a threshold behaviour, as shown in Figure 1.3.
Below threshold: the population enlarges linearly with the pump power; a broad distribution is detected looking at the energy-momentum emission; since the laser phase is lost in the non-resonant excitation configuration (as stated in Section 1.2.3.1), a short-range correlation is observed, with a size comparable to that of the de Broglie wavelength; emission from the polariton is completely depolarised.
Above threshold: the population enlarges nonlinearly with the pump power; a narrow distribution is detected looking at the energy-momentum emission, and this spectral narrowing leads to temporal coherence; a long-range spatial coherence is observed, with a finite size comparable to that of the entire condensate; emission from the polariton is linearly polarised, regardless of laser polarisation [41].
Given the macroscopic phase coherence, the macroscopic wavefunction for the polariton ground state reads

$$\psi_{pol}(r,t) = \sqrt{n_{pol}(r,t)}\, e^{i\phi(r,t)} \tag{1.30}$$

and the polariton dynamics are described with a nonlinear Schrödinger equation, known as Gross-Pitaevskii equation

$$i\hbar\frac{\partial \psi_{pol}(r,t)}{\partial t} = \left\{ -\frac{\hbar^2\nabla^2}{2m_{pol}} + V_{ext}(r,t) + \frac{i\hbar}{2}\left[R\left(n_R(r,t)\right) - \gamma_{pol}\right] + \right.$$
$$\left. + g_{pol}|\psi_{pol}(r,t)|^2 + g_R n_R(r,t) \right\} \psi_{pol}(r,t) \tag{1.31}$$

where $V_{ext}(r,t)$ is an external potential due to disorder, $R\left(n_R(r,t)\right)$ represents the creation of polaritons through scattering from the exciton reservoir with density $n_R(r,t)$, γ_{pol} is the

polariton linewidth, g_R is the strength of the interaction between polaritons and excitons in the reservoir. The rate equation for the exciton reservoir is given by

$$\frac{\partial n_R(r,t)}{\partial t} = P_R(r,t) - \gamma_R\left(n_R(r,t)\right) - R\left(n_R(r,t)\right)\left|\psi_{pol}(r,t)\right|^2 \tag{1.32}$$

where P_R represents the external pump rate to feed the polariton system and γ_R is the reservoir lifetime [39].

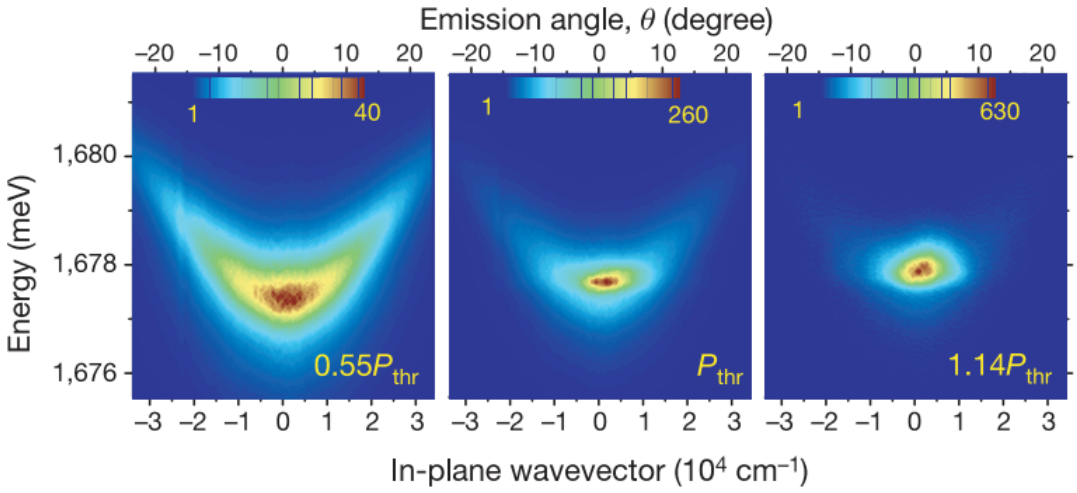

Fig. 1.3 Far-field emission for increasing pump powers (from left to right). Below threshold (**left panel**), the emission is broad in energy and momentum, while above threshold (**right panel**), the emission shrinks to the lowest energy state. It is also possible to see blueshift for increasing pump power, sign of polariton behaviour. Source: [15]

1.2.3.3 Superfluidity, vortices and solitons

It is extremely informative to investigate the behaviour of the polariton fluid through the interaction with some obstacle, from which several many-body phenomena closely related to BEC have been studied [42].

Let us first consider a defect smaller than the polariton-polariton interaction length, known as the healing length

$$\xi = \frac{h}{m_{pol}\, v_{sound}} \tag{1.33}$$

where

$$v_{sound} = \sqrt{\frac{\hbar g_{pol} |\psi_{pol}|^2}{m_{pol}}} \tag{1.34}$$

is the sound velocity.
At low power (i.e. low polariton density), the interaction between polaritons is negligible and we are in the linear regime, where the polariton dispersion is parabolic and so the elastic scattering is still possible (Figure 1.4, top-left panel). Looking at the real-space image, parabolic waves are detected (Figure 1.5, left panel). Increasing the pump power (i.e. higher polariton density), the interaction between polaritons is no longer negligible and we move into the nonlinear regime, where the dispersion curve modifies as shown in the right panels of Figure 1.4: it blueshifts to the pump level (yellow dot in Figure 1.4) and becomes linear (red curves in Figure 1.4, right panels) due to polariton-polariton interaction.
Now, we need to distinguish two different regimes, whether the group velocity

$$v_{pol} = \frac{\hbar k_{pol}}{m_{pol}} \tag{1.35}$$

is smaller or bigger than the speed of sound, where the fluid velocity depends on the excitation angle θ through

$$k_{pol} = \frac{\omega_{pol}}{c} \sin\theta \tag{1.36}$$

As shown in Figure 1.4 (top-right panel), when $v_{pol} < v_{sound}$, there are no states available for polaritons to elastically scatter into, the fluid does not see the defect anymore and parabolic waves are no longer detected (Figure 1.5, middle panel). Thus, we get into the **superfluidity** regime, that is the fluid flows with zero viscosity [43], when the Landau criterion for the critical velocity

$$v_c = \min_k \frac{\omega(k)}{k} \tag{1.37}$$

is fulfilled.
When $v_{pol} > v_{sound}$, we enter in the **supersonic** regime and we observe the characteristic linear density wavefronts of the Čerenkov waves (Figure 1.5, right panel), where the angle ϑ of the fringes

$$\vartheta = \arcsin \frac{v_{sound}}{v_{pol}} \tag{1.38}$$

may be used to extract the speed of sound.

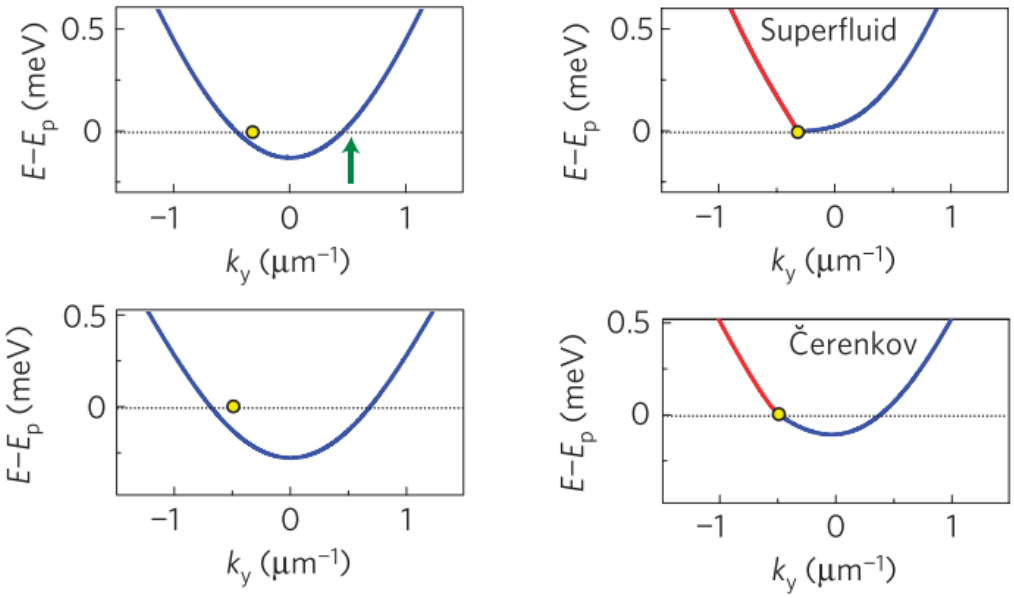

Fig. 1.4 Dispersion of LPB, where the yellow dot shows the pump wavevector (E_p is the pump energy). **Top-left panel**: at low density, polaritons elastically scatter to the states specified by the green arrow, at the same energy. **Top-right panel**: at high density the LPB blueshifts and, for $v_{pol} < v_{sound}$, the Landau criterion represented by Equation 1.37 is fulfilled, thus polaritons do no longer have states available for elastic scattering. **Bottom-left panel**: the pump wavevector is larger than before in order to increase the fluid velocity v_{pol}, as shown by Equation 1.36. **Bottom-right panel**: at high density and for $v_{pol} > v_{sound}$, polaritons enter into the supersonic (Čerenkov) regime. Source: [16]

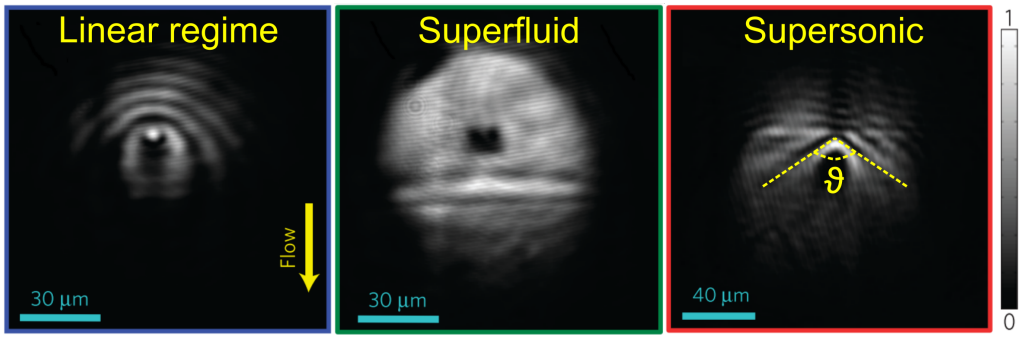

Fig. 1.5 Near-field imaging of a polariton fluid impinging on a small obstacle. **Left panel**: at low density, polaritons elastically scatter when hitting the defect, creating parabolic fringes. **Middle panel**: at high density and for $v_{pol} < v_{sound}$, superfluidity regime is attained, where scattering with the obstacle is no longer present. **Right panel**: at high density and for $v_{pol} > v_{sound}$, polaritons enter into the supersonic regime, with its characteristic linear Čerenkov waves. Source: [16]

Let now consider an obstacle (Figure 1.6, panel (a), red circle) larger than the healing length ξ (which is around 5 μm in GaAs) and vary the ratio between group velocity and speed of sound, changing the excitation angle or the polariton density.
For $v_{pol} << v_{sound}$, we are in the superfluid regime, as revealed in Figure 1.6 (panel (b)). At higher v_{pol} (or lower $|\psi_{pol}|^2$), the Landau criterion is locally violated because of the acceleration of the fluid in the vicinity of the obstacle [44]. These currents can give rise to turbulences, such as quantised vortices and vortex-antivortex pairs (Figure 1.6, panel (c), red and blue circles). **Vortices** represent a fluid that rotates around a core of minimum density, whose dimension is indicated by the healing length ξ. Their circulation is quantised because the phase of the condensate wavefunction changes as a multiple of 2π [45]. A vortex and an antivortex (a vortex with opposite circulation) move in pairs since they attract each other, while vortices with the same spin repel, as a Coulomb-like interaction, and they can annihilate. The presence of free vortices or vortex-antivortex pairs depends on the temperature of the system, whether it is higher or lower than the Berezinskii-Kosterlitz-Thouless (BKT) temperature

$$k_B T_{BKT} = \frac{\pi \hbar^2 n_{s.f.}}{2 m_{pol}} \tag{1.39}$$

where $n_{s.f.}$ is the superfluid density. When $T > T_{BKT}$ a disordered phase is observed, while for $T < T_{BKT}$ the phase fluctuations are cancelled out thanks to pairs formation and both long-range order of BEC and superfluidity are restored [46].

At even greater v_{pol} (or smaller $|\psi_{pol}|^2$), vortices start to overlap, creating another topological excitation called oblique dark solitons (Figure 1.6 (panels (d), (e) and (f)), which are represented by a π shift in phase [47]. More generally, **solitons** are defined as non-spreading non-decaying wave, localised in space (spatial solitons) or time (temporal solitons). They do not spread as a result of some sort of nonlinear effect, such as the repulsive polariton-polariton interaction or optical Kerr effect, that introduces a nonlinear refractive index and SPM (Section 1.2.3). They can be further distinguished as dark or bright solitons, whether they are a localised minimum or maximum in intensity compared to a homogeneous background, respectively. In the specific case of repulsive polariton-polariton interaction, dark solitons manifest when the polariton effective mass m_{pol} is positive, while bright solitons need a negative polariton effective mass [18]. They can be also differentiated between conservative and dissipative solitons, whether they are created in low or high losses systems, that is the number of particles remains constant or an external pump is needed to compensate the decreasing of particle number.

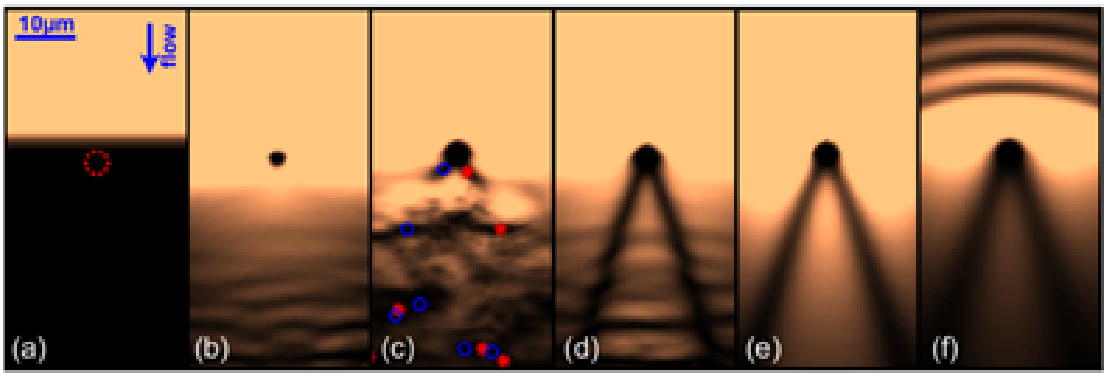

Fig. 1.6 **Panel (a)**: obstacle (red circle) larger than the healing length ξ. **Panel (b)**: for $v_{pol} << v_{sound}$, we are in the superfluid regime. **Panel (c)**: at higher v_{pol} (or lower $|\psi_{pol}|^2$), nucleation of turbulences such as quantised vortices and vortex-antivortex pairs is observed. **Panels (d), (e), (f)**: at even greater v_{pol} (or smaller $|\psi_{pol}|^2$), vortices start to overlap, creating another topological excitation called oblique dark solitons. Source: [48]

1.2.3.4 Parametric oscillation and bistability

The polariton-polariton scattering introduced in Section 1.2.3.1 is a four-wave mixing (FWM) process [24]: two particles scatter to two distinct states, conserving both energy and momentum. Specifically, when polaritons are injected approximately at the inflection point of the LPB (k_p is the pump laser wavevector), they undergo through optical parametric oscillation (OPO) and scatter to signal ($k_{signal} = 0$) and idler ($k_{idler} = 2k_p$) states (see Figure 1.7, left panel) [17]. When a probe is used to populate the ground state in order to stimulate the polariton scattering with a rate given by $(N+1)$, where N is the number of polaritons already in the state, we refer to optical parametric amplification (OPA) [49].

Polariton-polariton interaction also leads to bistability [50, 51], which consists in the hysteresis cycle shown in Figure 1.7 (right panel), when the condition

$$\omega_p - \omega_{LPB}(k_p) > \sqrt{3}\gamma_p \tag{1.40}$$

is satisfied. Here, ω_p is the pump frequency, $\omega_{LPB}(k_p)$ is the frequency of the LPB corresponding to the wavevector of the pump k_p and γ_p is the pump linewidth. The laser is blue-detuned compared to the LPB, so increasing the pump power, the LPB blueshifts because of the renormalisation of the dispersion via FWM [52]. When it reaches the pump energy, the signal intensity suddenly increases (see Figure 1.7, right panel, curve 1 in blue). Now, the decreasing of the pump power causes a redshift of the LPB, but the transmission

moves back to the previous value at a lower power than before (see Figure 1.7, right panel, curve 2 in red). The interplay between the two phenomena analysed in this section was demonstrated in [53].

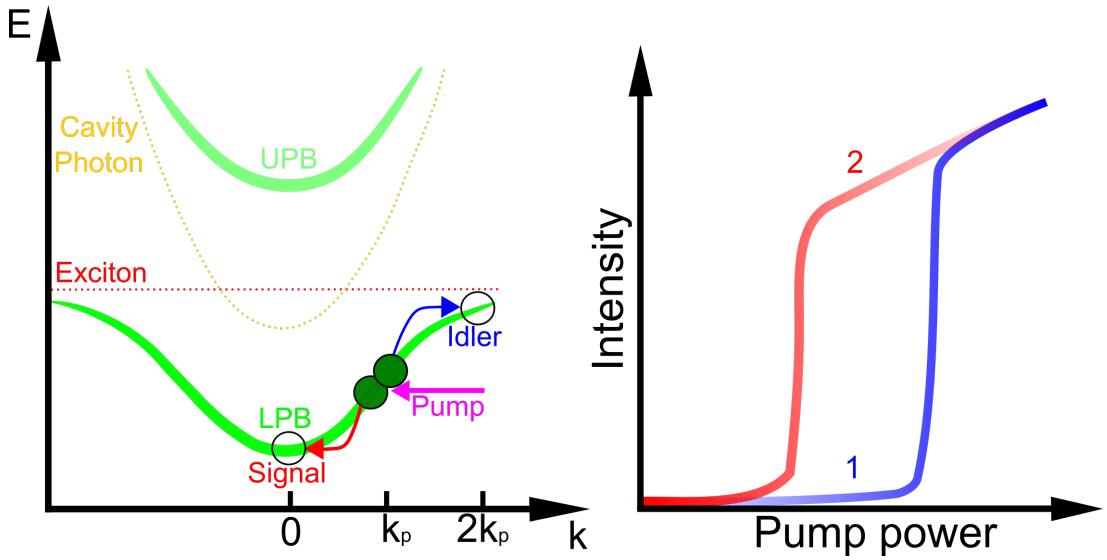

Fig. 1.7 **Left panel**: schematic of the OPO process. The pump (purple) injects two polaritons (dark green) in the LPB at k_p. The two polaritons scatter to the signal (red at $k = 0$) and idler (blue at $k = 2k_p$) states. **Right panel**: schematic of the bistability process. The blue (red) curve shows the transition from low (high) to high (low) signal intensity increasing (decreasing) the pump power, in a two step operation (labelled as 1 and 2).

Chapter 2

Optical active media

2.1 Introduction

Many materials have been used throughout the years as active media in polaritonics, but without a shadow of doubt GaAs-based systems have been the most investigated thanks to its mature fabrication techniques [6]. The large dielectric constant characterising this III-V material (as well as CdTe, a II-VI material) leads to small exciton binding energy ($5-25$ meV) and then small Rabi splitting ($3-25$ meV), making necessary to work at cryogenic temperature [54]. Because of the interest for technological applications, alternative platforms operating at RT need to be found. Still looking at inorganic semiconductors, GaN [55, 56], ZnO [57, 58] and two-dimensional transition-metal dichalcogenides (2D TMDCs) [59, 60] show excitons with binding energies large enough ($30-500$ meV) to be stable at RT, with consequent large Rabi splitting ($30-150$ meV). Hybrid inorganic-organic perovskites can be part of this category of platforms suitable for practical implementation, as they showed polariton existence at high temperature [61]. Considering organic materials [62, 63], it is true that the exciton binding energy and so the Rabi splitting are even higher ($0.5-1$ eV and $0.1-1$ eV, respectively), however the very small Bohr radius of their Frenkel excitons implies an increased sensitivity to sample inhomogeneity, causing linewidth broadening of the exciton resonance ($25-200$ meV in organic materials compared to $0.1-10$ meV in inorganic materials) and polariton localization in potential minima, frustrating their interaction [64]. Indeed, organic compounds have manifested much smaller nonlinearities (10^{-3} $\mu eV \cdot \mu m^2$) than inorganic materials ($1-10$ $\mu eV \cdot \mu m^2$) so far [6].

Table 2.1 Excitonic properties of the different active media used in polaritonics, from [65].

	GaAs QW	GaN QW	organic (Lumogen)	TMDC ML ($MoSe_2$)	2D Perovskites
Exciton resonance (eV)	1.5	3.5	2	1.6	2.4
Binding energy (meV)	~ 10	40	830	480	370
Bohr radius (nm)	12.5	3.5	1	1	4.5
Oscillator strength (μm^{-2})	$\sim 10^4$	$\sim 10^5$	$\sim 10^{7}$ *	$\sim 10^6$	$\sim 10^5$
Linewidth (meV)	~ 0.01	~ 0.1	~ 10	~ 1	~ 10
Interaction ($\mu eV \cdot \mu m^2$)	~ 1	~ 0.1	~ 0.01	~ 0.01	~ 1

* Oscillator strength of organic (Lumogen) is in μm^{-3}.

2.2 Transition-metal dichalcogenides

Despite all the most fundamental physical and optical properties of 2D TMDCs were already known in the early 1970s on a theoretical level [66], they were experimentally revived after the fabrication of graphene (single layer of carbon atoms) in 2004 by mechanical exfoliation [67], that was awarded the Nobel Prize in 2010. Dozens of MX_2 compounds, where M stands for transition-metal atom sandwiched between two chalcogen atoms X, fall into the category of TMDCs, ranging from insulators, semiconductors and metals, according to the way electrons fill the bands [68].

Since we are interested in the coupling between light and matter for device applications, we are going to focus on the semiconductor materials, in particular those where M = Mo, W and X = S, Se, which present a trigonal prismatic geometry (Figure 2.1(a)). Because of the weak van der Waals (vdW) inter-layer bonds and the strong covalent bonds within a layer, it is possible to isolate a monolayer (ML) with a thickness of $0.6 - 0.7$ nm using simple techniques as bare mechanical exfoliation, as previously done for graphene (Figure 2.1(a)) [69].

These materials undergo a transition from indirect to direct bandgap in the ML limit, as shown in Figure 2.2(a), where it is possible to notice that the K valley is almost unaffected by the decrease in size, while the indirect transition increases. This behaviour, like many others, mostly depends on the d-orbitals of the metal atom. This strong confinement in a plane reduces the dielectric screening (see Figure 2.2(b)), leading to attractive optical properties linked to exciton resonance, such as high binding energy and large oscillator strength, which is a hundred times stronger than that of the band-to-band transition [70]. The transition from

indirect to direct bandgap is certified by the massive increase in the photo-luminescence (PL) emission from the ML, which is two (four) orders of magnitude higher than that in bilayers (bulk) [71].

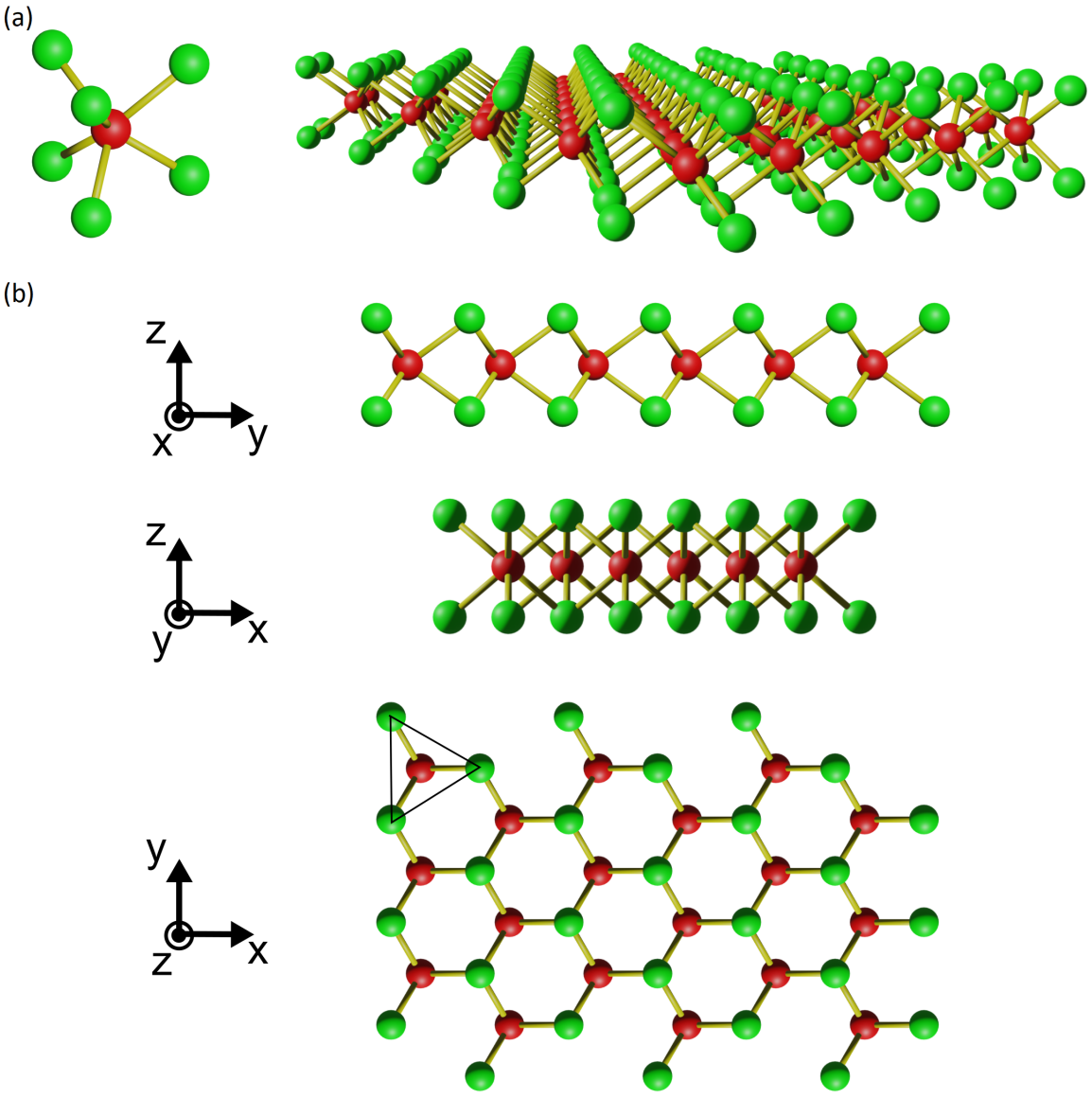

Fig. 2.1 **(a)**: on the left hand side, a view of the trigonal prismatic geometry of a MX_2 compound, where M = Mo, W is depicted in red and X = S, Se is represented in green. The intralayer covalent bonds are shown in yellow, and a single layer is represented on the right hand side. **(b)**: views of the different planes are presented, in particular the *xy* plane manifests a hexagonal lattice structure.

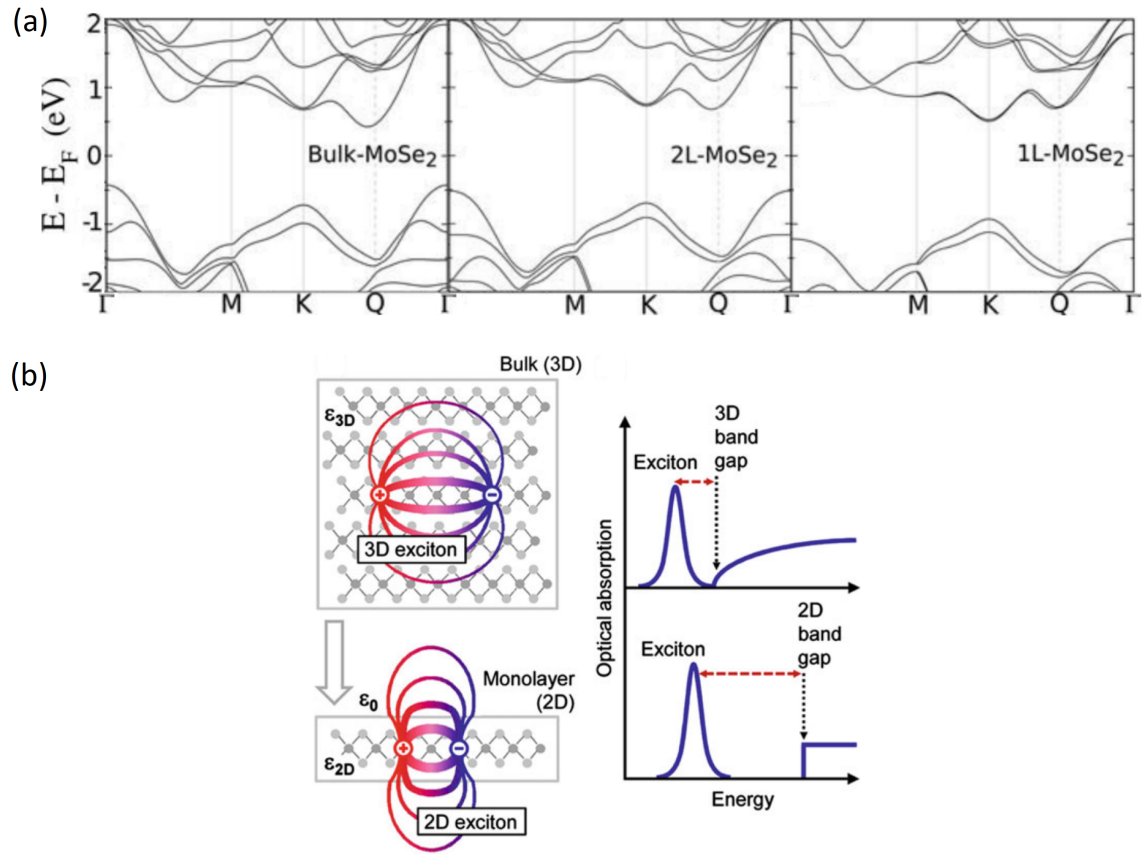

Fig. 2.2 **(a)**: energy-momentum dispersion for bulk, bilayer and monolayer $MoSe_2$. While the VB at the Γ point and the CB at the Q point change with decreasing the dimensionality, the K valley is almost unaffected, provoking the transition from indirect to direct bandgap. Source: [72]. **(b)**: in the left column, a representation of an exciton in bulk and ML displaying the different dielectric environment and the Bohr radius reduction. In the right column, the increase of both bandgap and exciton binding energy with reducing dimensionality. Source: [73].

2.2.1 Valley excitons

It is also interesting to notice that, in spite of the small Bohr radius (1 *nm*) and large binding energy (up to 0.5 *eV*), which would suggest the presence of Frenkel excitons, the exciton wavefuction is still that of Wannier-Mott excitons [74]. Moreover, the spatial dependence of the dielectric constant due to the quantum confinement causes a significant deviation from the hydrogen model usually used to describe excitons [73].

As displayed in Figure 2.1(b), MoS_2, $MoSe_2$, WS_2 and WSe_2 also have a hexagonal lattice structure in the xy plane. Consequently, the Brillouin zone in the momentum space

is hexagonal as well, as shown in Figure 2.3(a), where the two valleys K^+ and K^- show different characteristics.
Because of the broken inversion symmetry in MLs (restored in a bilayer), the exciton transitions at the K^+ and K^- points are degenerate, but the spin-orbit coupling (SOC) splits the spin degeneracy at each valley. The spin splitting for different valleys is opposite, as a result of the time-reversal symmetry. In this way, spin and valley degrees of freedom are linked and thus it is possible to select an individual valley using circularly polarised light: σ^+ and σ^- for K^+ and K^-, respectively (see Figure 2.3(b)) [75, 76].

As depicted in Figure 2.3(b), the degeneracy splitting is different between the CB ($15-30$ *meV*) and the VB ($0.2-0.5$ *eV*) and the sign of the CB splitting depends on the metal atom, producing an optically bright (same spin for VB and CB) ground state for MoX_2 and an optically dark (opposite spin for VB and CB) ground state for WX_2.

Since the two valleys are well separated in momentum space, the valley depolarisation arising from inter-valley carrier interactions is strongly suppressed: to move from one valley to the other, the carriers need large momentum and energy, or a spin-flip, leading to high polarisation retention once the two valleys are initialised by the corresponding circularly polarised light.

This robust polarisation retention has been experimentally detected in MoS_2, WS_2 and WSe_2, but not in $MoSe_2$. This different behaviour of $MoSe_2$ could be attributed to the darkish nature of the lowest energy state of the other three TMDC compounds (SOC splitting for MoS_2 is negative, but extremely small, as shown in Table 2.2) [77].

We can also observed two different kind of excitons, labelled in Figure 2.3(b) as X_A and X_B, depending on the transition energy. While the radiative lifetime of X_A is of the order of 1 *ps* (linewidth of about 1 *meV*), the X_B lifetime is shorter due to its relaxation to lower energy states through non-radiative channels [78], including exciton-exciton annihilation via Auger recombination, carrier-phonon scattering into dark states outside the light cone (creating an exciton reservoir with a lifetime of the order of 1 *ns*) and exciton complexes formation [74].
Indeed, thanks to the strong overlap of electron and hole wavefunctions, it is also possible to observe trions T (i.e. charged excitons, so also labelled as X^*) [79], biexcitons XX and charged biexcitons XT (or equivalently XX^*) [80]. Since unintentional doping in TMDCs is usually n-type, we refer to negative trions X^-. In Table 2.2 is presented a summary of the most important electronic and optical properties of the four TMDC semiconductors considered so far.

Exciton and trion states were unambiguously observed using a $MoSe_2$-based field effect transistor (FET) [81]. Performing gate-dependent measurements, the neutral and charged (both positive and negative) exciton resonances were electrostatically tune. Specifically, studying their PL peak intensities as function of the gate voltage, it is remarkable to notice that the maximum intensity of X resonance is equal to that of X^* when the X peak disappears, indicating the conservation of the total number of neutral excitons, since the PL intensity represents the amount of that particular species. So, the existing excitons simply bind to the excess electrons (holes) to form trions. Then, looking at the absorption area, which is proportional to the oscillator strength [59], for increasing gate voltages the exciton resonance disappears while the trion resonance gradually increases its weight [79]: as the electron density (i.e. Fermi energy) is increased, the oscillator strength is transferred from X to T [82].
Another interesting result obtained from this kind of structure is related to the redshift of the PL peak for increasing doping level (i.e. Fermi energy) compared to the absorption peak, called Stokes shift (for further details on this phenomenon, see Section 5.3.1).
Moreover, since the CB and VB curvatures are roughly the same, we aspect that the electron and hole effective masses are approximately the same. This is further confirm by the measured charging energies of both positively (X^+) and negatively (X^-) charged excitons in this kind of gated sample, which are almost identical. This similar value is approximately 10 times bigger than that in QWs (a quasi-2D system) thanks to the reduced dielectric screening guaranteed by the 2D nature of MLs, with consequent enlarged Coulomb interaction, and the heavy effective masses of excitonic components [79].

Another difference between these four TMDCs is given by the PL spectrum: $MoSe_2$, the TMDC we investigated in our tunable open-access microcavity, shows only two peaks arising from excitons and trions, while WX_2 compounds manifest many peaks at lower energy than X^-, usually attributed to localised excitons [77].

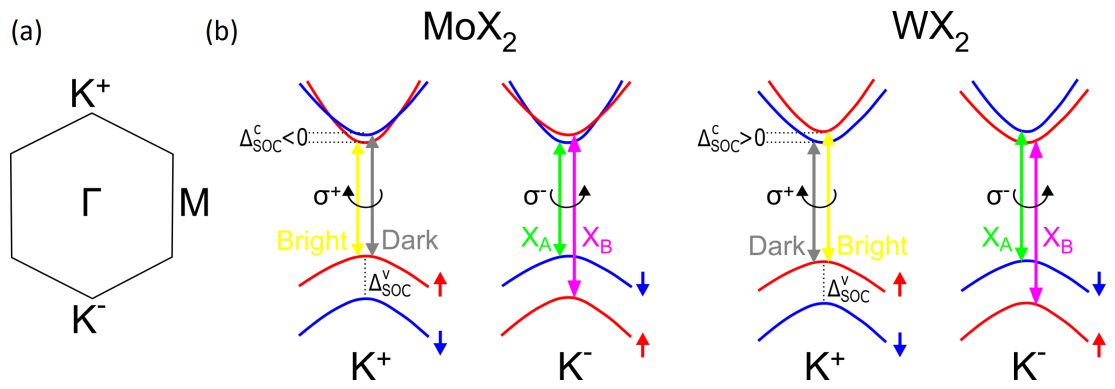

Fig. 2.3 **(a)**: hexagonal first Brillouin zone of TMDCs, with Γ, M and K valleys, as shown in Figure 2.2(a). **(b)**: schematic in a single-particle picture of the difference between MoX_2 and WX_2 valleys, which arises from the opposite value of the CB splitting due to spin-orbit coupling (SOC). This leads to opposite optical characteristic of their ground state, bright for MoX_2 and dark for WX_2, yellow and grey respectively. It is also emphasised the non-identical splitting between the K^+ and K^- valleys in both compounds, causing the divergent polarisation behaviour (σ^+ for K^+ and σ^- for K^-). Moreover, two exciton resonances X_A and X_B are indicated in green and purple for increasing energy, respectively.

Table 2.2 Electronic and optical properties of monolayer TMDC compounds, from [70, 83].

	MoS_2	$MoSe_2$	WS_2	WSe_2
Bandgap E_g (eV)	2	1.7	2.1	1.8
SOC for CB (meV)	-3	-20	30	35
SOC for VB (meV)	150	180	430	470
X binding energy (meV)	~ 530	~ 480	~ 520	~ 470
X^- binding energy (meV)	32	28	33	29
XX binding energy (meV)	23	19	24	21
XX^- binding energy (meV)	17	16	15	15

2.2.2 Fabrication techniques

Many approaches can be employed to fabricate TMDC-MLs, but here we are going to quickly deepen the two used to make the sample studied in this thesis.

2.2.2.1 Mechanical exfoliation

Historically, the very first fabrication techniques utilised for TMDCs is mechanical exfoliation, a top-down method where a scotch tape is used to cleave the bulk crystal [84]. Once the procedure is applied a few times, the exfoliated materials is placed onto a SiO_2 substrate to find MLs. The flake-search can be performed using different equipment, for example an optical microscope, as done in our case (it is going to be described in Section 4.2.1). Once the MLs are found, they are picked up using poly-dimethylsiloxane (PDMS), a visco-elastic polymer whose vdW forces with the flakes are stronger than those between MLs and the SiO_2 substrate. The polymer is then pressed onto the desired substrate (distributed Bragg reflector, described in Chapter 3) and peeled off [85]. Since the small thickness of MLs, they are really sensitive to the local environment and so the roughness of the substrate surface becomes a fundamental parameter. In order to improve flatness, and also to prevent contamination from the surrounding environment, a ML can be encapsulated between two hexagonal boron nitride (hBN) layers, a wide-bandgap semiconductor ($E_g \sim 6\ eV$). In this configuration, flakes reveal a better linewidth [86].

2.2.2.2 Chemical vapour deposition

Chemical vapour deposition (CVD) is a bottom-up method which is starting to play an important role in TMDC fabrication. The whole procedure is carried out inside a quartz tube, where Ar and H_2 can be used as carrier gasses. However, it was noticed that Ar produces few-layer flakes, while H_2 gives rise to MLs. In the case of $MoSe_2$, Se and MoO_3 powder precursors are heated to 300 $^\circ C$ and 750 $^\circ C$, respectively [87]. Then, they decompose, diffuse and are adsorbed onto the heated substrate. Two fundamental parameters influencing the flake size and the substrate coverage are the H_2 flow rate and the substrate temperature, which favour the diffusion of the precursors onto the substrate but may also cause their desorption [88].

2.3 III-nitride semiconductors

Another group of materials that is acquiring a fundamental role in the development of advanced technologies is represented by III-nitride wide-bandgap semiconductors, as demonstrated by the Nobel Prize won in 2014 [89]. This family consists of InN, GaN and AlN. Given the energy bandgaps of these three materials (shown in Table 2.4) and taking into account their ternary alloys, it is also possible to continuously tune the bandgap and explore

a wide range of wavelengths, from the IR to the UV [90]. Indeed, considering the lattice parameters a_A and a_B of two different binary compounds A and B, we can derive the alloy lattice parameter from Vegard's law [90]

$$a_{A_xB_{1-x}} = x \cdot a_A + (1-x) \cdot a_B \tag{2.1}$$

where x represents the content of that particular element, and then we can extract the bandgap variation for the alloy

$$E_{g_{AB}} = x \cdot E_{g_A} + (1-x) \cdot E_{g_B} + b \cdot x(1-x) \tag{2.2}$$

where the bowing parameter b gives a correction factor compared to the bare linear interpolation (see Table 2.3).

Table 2.3 Bowing parameter for the ternary compounds from [90].

Bowing parameter	AlGaN	InGaN	AlInN
b (eV)	-0.7	-1.7	-5.4

Since we performed temperature dependence studies, it is also important to consider the bandgap variation as a function of the temperature through the Varshni's law [91]

$$E_g(T) = E_g(T = 0\ K) - \frac{\alpha T^2}{T + \beta} \tag{2.3}$$

where the values for the parameters α and β are listed in Table 2.4. The bandgap of GaN changes from $\sim 3.4\ eV$ at 300 K to $\sim 3.5\ eV$ at 4 K, due to the reduction of the lattice parameter decreasing the temperature.
An even better model is given by [92]

$$E_X(T) = E_X(T = 0\ K) - \frac{2\alpha_B}{e^{\frac{\Theta_B}{T}} - 1} \tag{2.4}$$

where $E_X(T = 0\ K)$ is the exciton energy at 0 K and the second term is the Bose-Einstein distribution for phonons, where $\alpha_B \sim 70\ meV$ and $\Theta_B \sim 322\ K$ represent the electron-phonon interaction constant and the phonon temperature, respectively [93].

2.3.1 Polarity

Table 2.4 Parameters of III-nitride binary compounds at RT. E_g, α and β from [94]; a, c and u from [95, 96].

Parameters (T = 300 K)	AlN	GaN	InN
E_g (eV)	6.2	3.4	0.7
a $(\dot{A})$	3.112	3.189	3.545
c $(\dot{A})$	4.982	5.185	5.703
u $(\dot{A})$	1.903	1.950	2.150
α (meV/K)	1.799	0.909	0.245
β (K)	1462	830	624

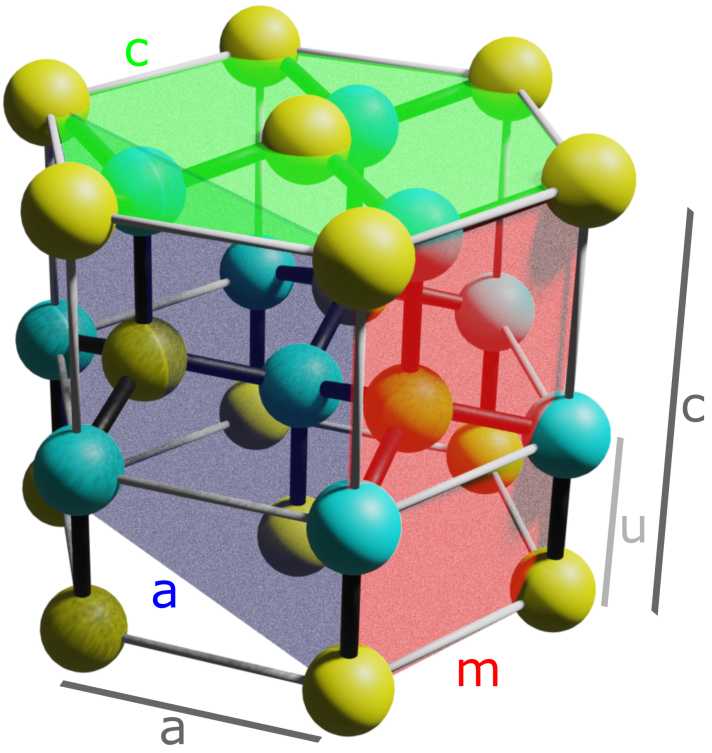

Fig. 2.4 Schematic representation of the wurtzite crystal structure of a III-nitride semiconductor, where the N atom is in light blue and the group-III atom is in yellow. The ionic-covalent bonds between the anion (N) and the cation (group-III) are shown in black. The two lattice constants a and c are labelled in dark grey, while the distance u between N and the group-III atom along c is labelled in light grey. The principal planes c, a and m are shown in green, blue and red, respectively.

The stable phase of these wide-bandgap semiconductors is represented by the wurtzite crystal structure, consisting of a hexagonal unit cell, as depicted in Figure 2.4. In this structure we have two lattice constants: the basal length a and the prism height c, while the distance between the anion (N) and the cation (group-III) along c is labelled as u (Figure 2.4). The values of these three parameters are shown in Table 2.4.
The wurtzite crystal shows a lack of inversion symmetry which, together with the big difference in electronegativity between anions and cations and the consequent ionicity of the covalent bond between them, leads to different centres of gravity for N and group-III atom charges. This situation causes the built-up of an intrinsic polarisation, called pyroelectricity [97], which can be further increased by lattice strain (the latter is called piezoelectric polarisation). Because of the different polarisation in the different III-nitride materials, electric charge accumulates at the interface between them (when creating a heterostructure), as happens in a capacitor. The c-plane (green in Figure 2.4) is a polar plane, while the a-plane and the m-plane (blue and red in Figure 2.4, respectively) are non-polar planes.

2.3.2 GaN optical properties

Specifically looking at the band structure of GaN, which is the active medium in our waveguides, the CB minimum and the VB maximum both lie at the centre of the Brillouin zone, at the Γ-point, where the properties are governed by the s-orbital and the p-orbital, respectively. The spin-orbit interaction and the crystal field split the VB into three, labelled as A for heavy holes, B for light holes and C is the split-off band, from lower to higher energies of the holes [98]. The three different exciton resonances arising from the Coulomb interaction between CB electrons and the different kind of VB holes, however, show the same binding energy of approximately 25 meV (in bulk) and high oscillator strength [99]. It is also important to note that only an electric field orthogonal to the c-plane allows formation of A-excitons, while B- and C-excitons do not have this restriction.
As it happens for TMDCs, we further distinguish between bright and dark excitons depending on their spin. Considering that the electron spin is $\pm\frac{1}{2}$, while heavy and light holes have spins $\pm\frac{3}{2}$ and $\pm\frac{1}{2}$ respectively, the exciton spin can be $0, \pm 1, \pm 2$. Since photons have a ± 1 spin, exclusively excitons with identical spin can couple with them, while the others are optically inactive, as well as excitons with a wavevector outside the light cone.

Observing a PL spectrum of GaN, it is also possible to note an emission peak at lower energy than A-exciton, attributed to excitons bound to donors. In particular, a substitutional Si atom in a Ga site creates an exciton with a binding energy of 6.2 meV, while a substitutional

O atom in a N site creates an exciton with a binding energy of 7.0 *meV* [100].

2.3.3 QW excitons

As stated in Section 1.2.2, to further improve the light-matter interaction, we can confine excitons in 2D QW systems. These are nanoscale heterostructure, where a smaller bandgap material is sandwiched between two layers of a bigger bandgap material in order to spatially trap the exciton in the first one.

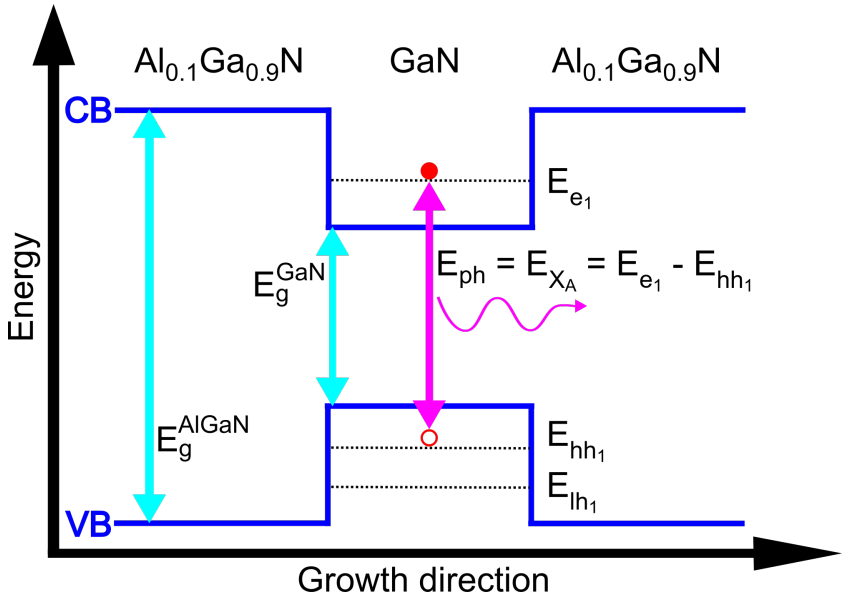

Fig. 2.5 Schematic representation of a GaN/$Al_xGa_{1-x}N$ QW, where $x = 0.1$ in our samples. The $Al_{0.1}Ga_{0.9}N$ bandgap is $E_g^{AlGaN} \approx 3.7\ eV$, while the GaN bandgap is $E_g^{GaN} \approx 3.5\ eV$ at 4K. Electrons (full red dot) and holes (empty red dot) are then confined in GaN. The discrete energy levels in both bands arise from the nanoscale thickness of the heterostructure (1.5 *nm* for GaN layer and 3.5 *nm* for $Al_{0.1}Ga_{0.9}N$ layer). Electrons (e) and heavy holes (hh) occupy their respective ground states (labelled as 1) and, interacting attractively, give rise to *A*-excitons, with binding energy $E_B^{X_A} \approx 50\ meV$.

In the waveguides studied in this thesis, we used GaN/$Al_xGa_{1-x}N$ QWs (where $x = 0.1$) as the active medium (Figure 2.5). Excitons are confined in a 1.5nm-thick GaN layer encompassed in the growth direction by two 3.5nm-thick $Al_{0.1}Ga_{0.9}N$ layers [101] thanks to their different bandgap ($\sim 3.5\ eV$ and $\sim 3.7\ eV$, respectively).
This kind of design is also convenient because the lattice mismatch of just 2.5% between

AlN and GaN prevents dislocation formation (at least in nanoscale structures) thanks to the small lattice strain [102].

Thanks to this quantum confinement of the carriers, their radiative recombination rate is enhanced. Moreover, the exciton binding energy in 2D now reads

$$E_X^n(2D) = -\frac{R_X}{(n-0.5)^2}, \quad n = 1,\ 2,\ \ldots \tag{2.5}$$

which is four times larger than that in 3D bulk (only in a fully, ideal 2D system). Correspondingly, the Bohr radius is two times smaller in a QW than in bulk and so the oscillator strength increases even further

$$f_X(2D) = f_{cv}\frac{A}{\pi a_B^2} \tag{2.6}$$

while the Mott density, because of the reduced dimensionality, reads

$$n_{Mott}(2D) = \frac{1}{\pi a_B^2} \tag{2.7}$$

2.3.4 Fabrication techniques

In order to fabricate the GaN/$Al_{0.1}Ga_{0.9}N$ heterostructures used as active medium in our waveguides, metal-organic chemical vapour deposition (MOCVD) was employed [103]. In this case, trimethyl- Ga (TMGa), In (TMIn), Al (TMIn) and ammonia (NH_3) were used as precursors, while H_2 and N_2 were the carrier gases. Because of the strong bonding between group-III and N atoms, higher temperatures are needed ($\sim 900\ ^\circ C$). Moreover, the growth of III-nitride heterostructure is of course affected by the lattice mismatch with the substrate, eventually creating dislocation. In order to prevent defect creation, and ensure best sample quality, a freestanding GaN substrate was utilised. Besides, a homogeneous $Al_{0.1}Ga_{0.9}N$ composition is necessary, as well as smooth hetero-interfaces, to reduce alloy disorder and decrease inhomogeneous broadening [104].

Since a waveguide works thanks to total internal reflection (see Chapter 3), the active medium needs to be enclosed between two smaller refractive index materials. In light of the above, $Al_{0.83}In_{0.17}N$ was employed as a cladding to optically isolate QWs from the GaN substrate [105], while the top cladding is guaranteed by SiO_2. In addition, $Al_{0.83}In_{0.17}N$ is characterised by a higher bandgap than GaN [106], which also favours the active medium isolation, and same lattice constant, avoiding dislocation formation.

Chapter 3

Photonic microstructures

3.1 Introduction

As stated in Section 1.2.2, a number of design can be employed to increase the interaction between light and matter [107]. Certainly, the most used geometry adopted for this purpose has been the monolithic planar microcavity (discussed in Section 3.2), since the birth of experimental polaritonics [9]. In this configuration, the electric field is trapped between two mirrors on a scale of the emitter wavelength only in the orthogonal direction. To completely enclose the light in the other two dimensions, spherical mirrors (detailed in Section 3.2.1) or etched micropillars can be utilised, leading to the discrete optical modes whose energy separation depends on the confinement length [23]. In the latter configuration, the lateral confinement is achieved by total internal reflection (TIR) thanks to the difference in the refractive indices between the optical resonator and the surrounding vacuum. This method is also applied in waveguides (described in Section 3.3) and whispering-gallery resonators [108], where the light is guided around the structure. The disadvantage of this geometry is represented by the impossibility to create small structures because diffraction comes into play [23]. Another possible solution to imprison the electric field is given by photonic crystals, periodic structures where a small asymmetry is produced through the creation of a nanoscale defect [65]. In this way, the light propagation is influenced by multiple scattering arising from the difference in the refractive indices. The overall design simulates the behaviour of an electron moving in the periodic potential of a crystal, mimicking a solid state configuration [109]. Because of the difficulties in the fabrication process of such a structure, array of micropillars can be implemented instead [110].

3.2 Planar Fabry-Pérot microcavities

As stated in Section 3.1, a planar microcavity is formed by two high reflectivity mirrors with an active medium between them. Specifically, the mirrors are two distributed Bragg reflectors (DBRs), characterised by two alternating $\frac{\lambda}{4n}$ layers of high and low refractive indices n_1 and n_2 respectively, where λ is the emitter wavelength. The reflectivity of a mirror is given by

$$R = \left[\frac{1 - \left(\frac{n_2}{n_1}\right)^{2N}}{1 + \left(\frac{n_2}{n_1}\right)^{2N}} \right]^2 \tag{3.1}$$

which shows that the bigger the refractive index difference and the higher the number N of layer pairs, the higher the reflectivity. When the two DBRs are brought together, with a separation of just few wavelengths, an optical resonator is formed. The π phase shift of the reflected light between layer interfaces leads to constructive interference, creating a region of high reflectivity which extends over a large range of wavelengths, called the stopband

$$\Delta\lambda \approx \frac{2\,\bar{\lambda}\,(n_1 - n_2)}{\pi\, n_{eff}} \tag{3.2}$$

where $\bar{\lambda}$ is the central wavelength of the stopband and $n_{eff} = 2\,(\frac{1}{n_1} + \frac{1}{n_2})^{-1}$ is the effective refractive index.

Because of the light confinement, the photon dispersion is modified compared to the free space case, where it is linear: $E = \hbar\omega = \hbar ck$. The microcavity geometry causes a quantisation of the light wavevector in the DBR growth direction (perpendicular to the mirror), while k in the parallel direction is still unaffected:

$$E = \frac{\hbar ck}{n_{cav}} = \frac{\hbar c}{n_{cav}} \sqrt{k_\perp^2 + k_{\shortparallel}^2} \tag{3.3}$$

where

$$k_\perp = \frac{q\pi}{L_{cav}} \tag{3.4}$$

The quantity q is called the order of the cavity mode and represents the integer number of half wavelengths of the light confined between the two mirrors so that a stationary wave survives within the cavity. Depending on the order q of the longitudinal mode, we refer to different $\frac{q\lambda}{2}$ cavities. Substituting Equation 3.4 in Equation 3.3, we get the dispersion relation for a microcavity (see Figure 3.1):

$$E(k_{\shortparallel}) = \frac{\hbar c}{n_{cav}} \frac{q\pi}{L_{cav}} \sqrt{1 + \left(\frac{L_{cav}\, k_{\shortparallel}}{q\pi}\right)^2} \approx$$

$$\approx \frac{\hbar c}{n_{cav}} \frac{q\pi}{L_{cav}} \left[1 + \frac{1}{2}\left(\frac{L_{cav}\, k_{\shortparallel}}{q\pi}\right)^2\right] = E_0 + \frac{\hbar^2\, k_{\shortparallel}^2}{2m_{ph}} \tag{3.5}$$

where

$$E_0 = \frac{q\pi\hbar c}{n_{cav}\, L_{cav}} \tag{3.6}$$

and

$$m_{ph} = \frac{q\pi\hbar n_{cav}}{cL_{cav}} \tag{3.7}$$

is the cavity photon effective mass of about $10^{-4} - 10^{-5}\ m_e$, arising from the parabolic dispersion in a Fabry-Pérot cavity [21].
A fundamental parameter used to describe a microcavity is the quality factor Q, denoted as the fraction between the energy stored and the energy dissipated within a round trip of a photon between the two mirrors

$$Q = \frac{E_{ph}}{\gamma_{ph}} = \omega_{ph} \cdot \tau_{ph} \tag{3.8}$$

So, the quality factor depends on the lifetime of photons within the cavity, which leak out through the mirrors. Detecting these photons, it is possible to measure polariton characteristics, retained by them [111].

Linked to the Q-factor, there is another important parameter used to specify the spectral resolution of the cavity, the finesse [23]

$$F = \frac{\Delta\omega_{cav}}{\gamma_{ph}} \tag{3.9}$$

where $\Delta\omega_{cav}$ is the longitudinal mode separation, which depends on the cavity length L_C through

$$\Delta\omega_{cav} = \frac{2\pi c}{L_{cav}} \tag{3.10}$$

Because of the electric field penetration inside the DBRs, as shown by transfer-matrix method simulations in Figure 3.2 of our tunable open-access microcavity (consisting of 13 pairs of SiO_2/Ta_2O_5 quarter-wave layers), the real cavity length is actually given by

$$L_{eff} = L_{cav} + L_{DBR_1} + L_{DBR_2} \tag{3.11}$$

where the penetration length of the electric field in a single DBR can be quantify by [112]

$$L_{DBR} = \frac{n_1\, n_2\, \bar{\lambda}}{2(n_1 - n_2)} \tag{3.12}$$

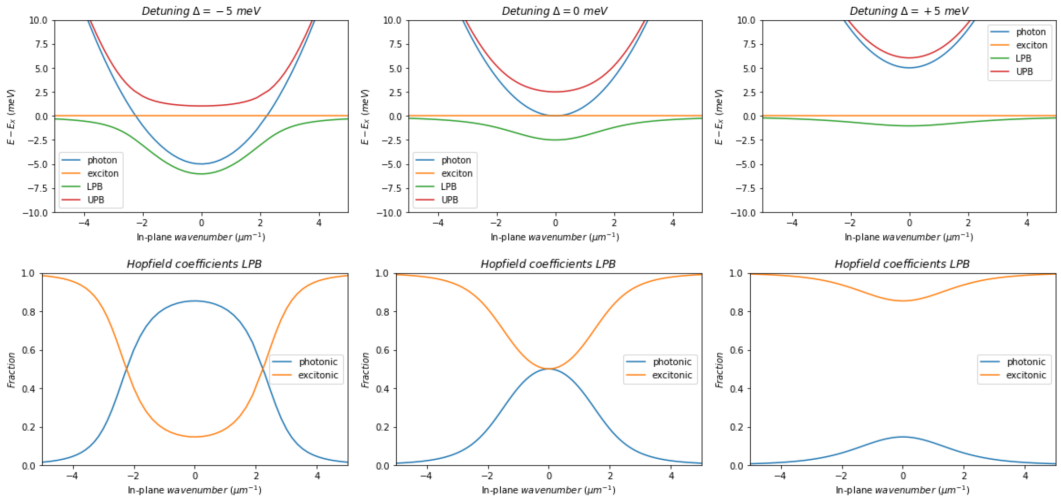

Fig. 3.1 Negatively (**left panel**), zero (**middle panel**) and positively (**right panel**) detuned GaAs-microcavity dispersion with Hopfield coefficients for the LPB.

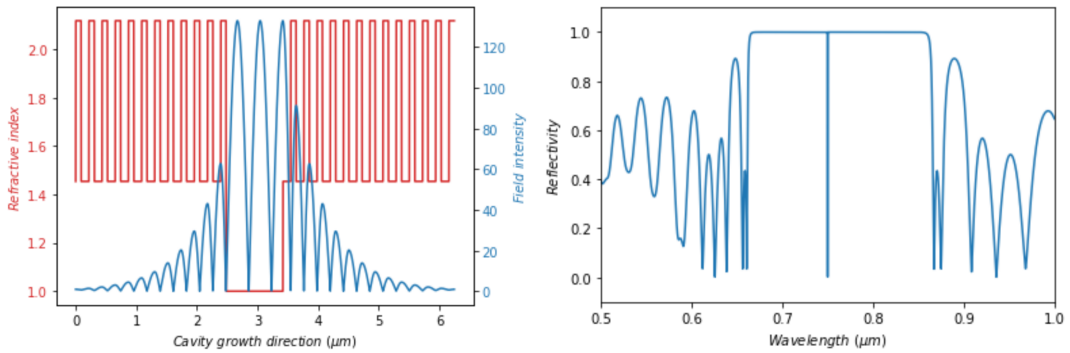

Fig. 3.2 Transfer-matrix method simulations of our tunable open-access microcavity consisting of 13 pairs of SiO_2/Ta_2O_5 quarter-wave layers, with refractive indices $n_{SiO_2} = 1.46$ and $n_{Ta_2O_5} = 2.13$, respectively. **Left panel**: The electric field is calculated in the case of a $\frac{5\lambda}{2}$ cavity configuration, with $n_{air} = 1$. **Right panel**: Reflectivity of the system showing a cavity resonance at $\sim 750\ nm$, corresponding to A-exciton energy in $MoSe_2$ ML.

3.2.1 Hemispherical tunable open-access microcavities

Looking in slightly more detail at the microcavity used to study polaritons with TMDCs, the two DBRs were mounted separately to vary the distance between them and therefore tune the photon energy to select a specific exciton-photon detuning. Moreover, the hemispherical geometry guaranteed by the concave shape of one of the two mirrors (the other one with the active medium on top is planar) provides 3-dimensional confinement of the photonic mode, leading to 0-dimensional polaritons. This lateral confinement should also yield a high Q-factor and small mode volume, depending on the radius of curvature (RoC) of the concave mirror [113]. In particular, the smaller the RoC, the smaller the mode volume and so the stronger the polariton-polariton interaction, but at the same it has a detrimental effect on the Q-factor [114], which is also reduced by not perfect mirror alignment and coupling with leaky modes [23].

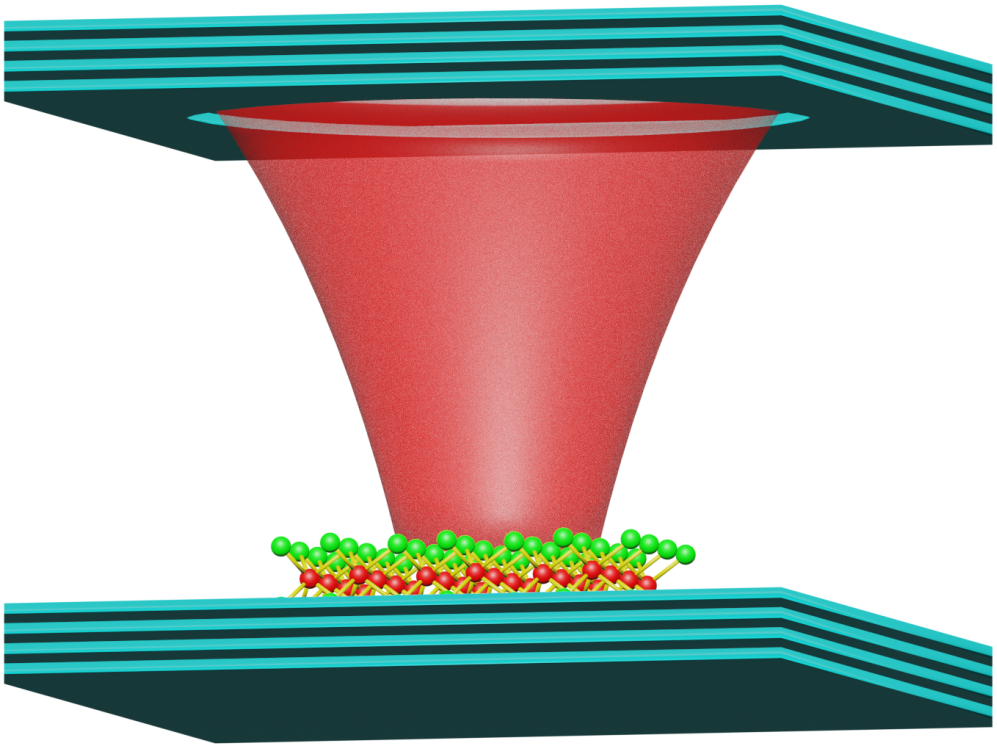

Fig. 3.3 Schematic of our hemispherical tunable open-access microcavity, with a bottom planar DBR with deposited $MoSe_2$, an air gap and a top concave DBR, under infrared laser excitation.

To further illustrate the behaviour of the electric field inside our hemispherical tunable open-access microcavity [115], let us consider the electric field in a vacuum, represented by the wave equation

$$\nabla^2 E(r,t) - \frac{1}{c^2}\frac{\partial^2}{\partial t^2} E(r,t) = 0 \tag{3.13}$$

Applying the separation of variables to this partial differential equation (PDE), we get that a trivial solution is represented by the monochromatic wave

$$E(r,t) = E(r)\, e^{-i\omega t} \tag{3.14}$$

and so we obtain the time-independent wave equation, called the Helmholtz equation

$$\nabla^2 E(r) + k^2 E(r) = 0 \tag{3.15}$$

A trial solution is now the plane wave

$$E(r) = E_0\, e^{-ik\cdot r} \tag{3.16}$$

In the paraxial (small-angle) approximation, where z is the wave propagation direction, it is possible to show that the complete solution of the PDE is given by the Gaussian beam (a rigorous derivation is provided in [115])

$$E(r) = E_0\, \frac{w_0}{w(z_R)}\, e^{-\frac{(x^2+y^2)}{w(z)}}\, e^{-ikz}\, e^{ik\frac{(x^2+y^2)}{2R(z)}}\, e^{i\Phi(z)} \tag{3.17}$$

where:

- w_0 is the beam waist at the beam focus;
- $w(z_R) = \sqrt{2}\, w_0$ is the real spot size at the Rayleigh length $z_R \equiv \dfrac{\pi\, w_0^2}{\lambda}$;
- $R(z)$ is the radius of curvature of the beam wavefront;
- $\Phi(z) = \arctan\dfrac{z}{z_R}$ is the Gouy phase shift.

In particular, $\Phi(z) = -\pi$ through the waist for the lowest-order mode TEM_{00}, so that the apparent change of wavelength does not affect the longitudinal mode but might become relevant for higher-order transverse modes. Specifically, the latter can be described by (see Figure 3.4):

- **Hermite-Gaussian HG$_{m,n}$ modes** in Cartesian coordinates, where (m,n) refer to x and y directions respectively, and modes with the same $|m+n|$ are degenerate in energy,
- **Laguerre-Gaussian LG$_{l,p}$ modes** in cylindrical coordinates, where (l,p) refer to azimuthal and radial direction respectively, and modes with the same $|2l+p|$ are degenerate in energy.

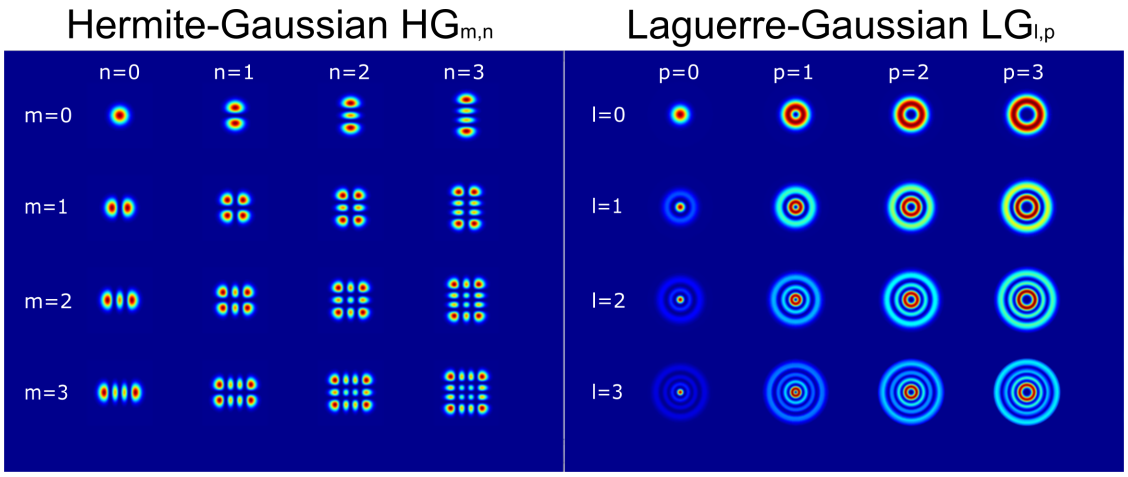

Fig. 3.4 The electric field profiles of the first 16 Hermite-Gaussian HG$_{(m,n)}$ (**left panel**) and Laguerre-Gaussian LG$_{(l,p)}$ (**right panel**) modes.

Since our hemispherical cavity is circularly symmetric, it should ideally show LG modes, but the defects in the cavity create asymmetry, actually leading to the observation of HG modes.

Previous simulations performed in our research group show that [114]:

- the beam waist of the planar DBR is $w_1 \sim 1\ \mu m$ for $L_{cav} < RoC$;
- the beam waist of the concave DBR w_2 diverges for $L_{cav} > RoC$;
- $w_1 \sim w_2$ for $L_{cav} \sim 1\ \mu m$;
- the beam waist is $w \sim 1\ \mu m$ for $RoC \sim 20\ \mu m$, as used in our work.

3.2.2 Fabrication techniques

The $\frac{\lambda}{4n}$ layers that make up the DBRs are fabricated using Molecular Beam Epitaxy (MBE). The deposition of these thin layers onto a heated sapphire substrate is performed inside

a high vacuum chamber, where the constituent materials are stored in separate Knudsen effusion cells in the solid phase. After being heated, they sublime and then condense onto the substrate. The layer thickness depends on the deposition rate, which represents one of the most important parameters to obtain DBRs with high reflectivity.

The hemispherical surface of the concave mirror is attained using focused ion beam (FIB) milling, where a Ga beam is focussed down to 5 *nm* onto the DBR surface, achieving a roughness of about 1 *nm*. Employing this technique, many concave mirrors with different RoCs can be fabricated onto the plinth, whose values are checked using atomic force microscopy (AFM), where the variation in height of an atomic-sized tip that scans the surface of the sample is probed by a laser reflected from the tip itself [116].

3.3 Waveguides

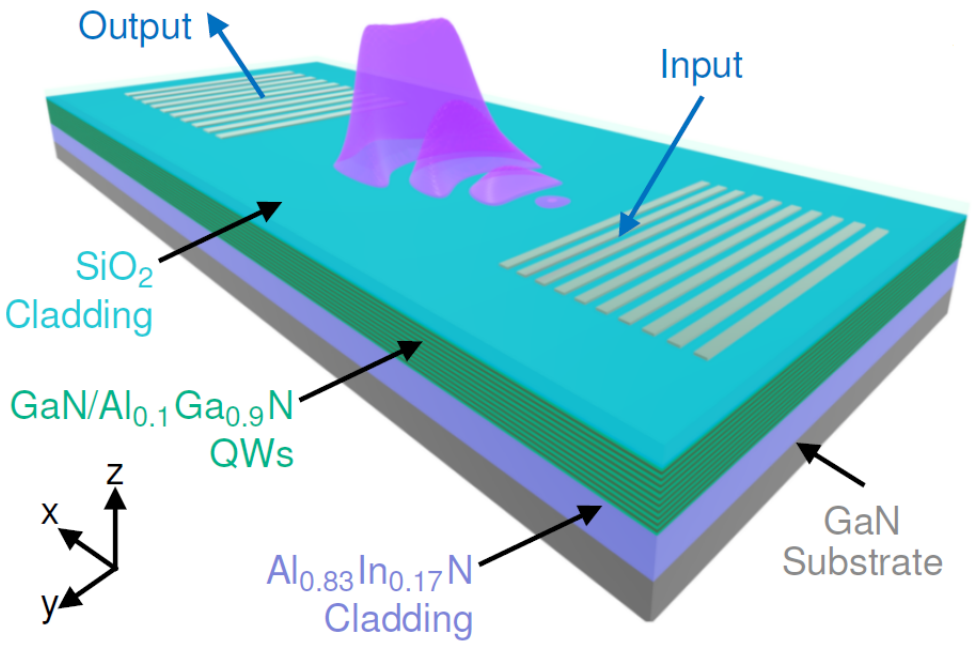

Fig. 3.5 Schematic of our GaN polariton waveguide under an UV laser, whose parts were fabricated as indicated in Section 7.1. The strips depict the grating couplers (described in Section 3.3.1) on top of the 100nm-thick SiO_2 cladding. Underneath the active medium, formed by 22 QWs of $GaN/Al_{0.1}Ga_{0.9}N$ and sketched with alternating grey (1.5 *nm*) and green (3.5 *nm*) layers respectively, the purple zone represents the 400nm-thick $Al_{0.83}In_{0.17}N$ cladding. Finally, the grey section reproduces the GaN substrate. Source: [117]

As mentioned in Section 3.1, waveguides work through TIR (see Figure 3.6). In general, this phenomenon manifests when the incident angle of light to the planar interface between a high refractive index (n_1) material and a low refractive index (n_2) material exceeds the critical angle

$$\theta_c = \arcsin \frac{n_2}{n_1} \tag{3.18}$$

as derived by the Snell's law

$$n_1 \sin\theta_1 = n_2 \sin\theta_2 \tag{3.19}$$

when $\theta_2 = \frac{\pi}{2}$.
Therefore, to build up an optical waveguide, we enclose a core of high refractive index material of thickness d_{core} between two low refractive index cladding layers. Alternatively, since $k_1 = \frac{2\pi}{\lambda} n_1 = \frac{\omega}{c} n_1$ and $k_2 = \frac{2\pi}{\lambda} n_2 = \frac{\omega}{c} n_2$ are the wavevectors in the two media, Equation 3.19 can be written as

$$k_1 \sin\theta_1 = k_2 \sin\theta_2 \tag{3.20}$$

In order to have TIR and enter in the waveguide regime, the in-plane wavevector k_x, defined as

$$k_x \equiv k_1 \sin\theta_1 = \frac{\omega}{c} n_1 \sin\theta_1 = \frac{\omega}{c} n_{eff} \tag{3.21}$$

where $n_{eff} \equiv n_1 \sin\theta_1$, must satisfy the following condition

$$k_x > k_2 = \frac{\omega}{c} n_2 \tag{3.22}$$

otherwise we get into the Fabry-Pérot regime (already described in Section 3.2). Satisfaction of the condition represented by Equation 3.18 follows directly from Equations 3.21 and 3.22. The in-plane wavevector k_x is usually called the propagation constant and labelled as β (see Figure 3.6) [104].

The wave inside the waveguide must constructively interfere with itself after two reflections in order to survive within the system and form a standing wave. Taking into account that the path length of a round trip is $2d_{core}\ \frac{\omega}{c} n_1 \cos\theta_m$ and the π phase shift due to each reflection, we get the condition

$$2d_{core}\ \frac{\omega}{c} n_1 \cos\theta_m = 2\pi m, \quad m = 1,\ 2,\ \ldots \tag{3.23}$$

where m is the mode order surviving within the waveguide, i.e. the number of the standing wave nodes. It is usually possible to discriminate between transverse-electric (TE) and transverse-magnetic (TM) modes along the propagation direction x, but in our specific case we only consider the TE_{00} mode, since it is the only one to strongly couple to QW A-excitons (see Section 2.3.2).

Despite the fact that waveguides are theoretically lossless, the dissipation experimentally observed may arise from different causes, such as absorption, scattering and radiative losses. Absorption is mainly due to intra- and inter-band transitions, while scattering is a consequence of defects in the structure itself (that can be reduced using the MBE fabrication technique), and finally radiative losses into the cladding ascribable to evanescence waves can be neglected for well confined modes into the core. In any case, losses are described through the loss coefficient α $(dB \cdot cm^{-1})$ from [118]

$$I_{out} = I_{in} \cdot e^{-\alpha x} \tag{3.24}$$

3.3.1 Grating couplers

Since the waveguide modes are outside the air light cone and it is very challenging to collect the light from the end of the sample in a flow cryostat, grating couplers with a periodicity Λ etched onto the waveguide surface are necessary to couple the incoming light inside the system. As usual, the contribution from the different grooves of the grating must interfere constructively, with a total phase difference equal to a multiple integer of 2π. Looking at Figure 3.6, the purple path gives a phase shift of $\beta\Lambda$, while the green path results in a phase shift of $k_{out}\Lambda\ \cos(90^\circ - \Theta) = k_{out}\Lambda\ \sin(\Theta) = k_{x,out}\Lambda$. Combining the two together, we then obtain

$$\beta\Lambda - k_{x,out}\Lambda = 2\pi q, \quad q = \pm 1,\ \pm 2,\ ... \tag{3.25}$$

where q is the diffraction order. Rearranging Equation 3.25, we finally derive

$$k_{x,out} \equiv \frac{\omega}{c}\sin\Theta = \beta - \frac{2\pi}{\Lambda}q \tag{3.26}$$

which allows us to calculate β from the emission angle Θ. First-order gratings are used to maximise the output light and their period Λ is chosen to have modes within the light cone [104].

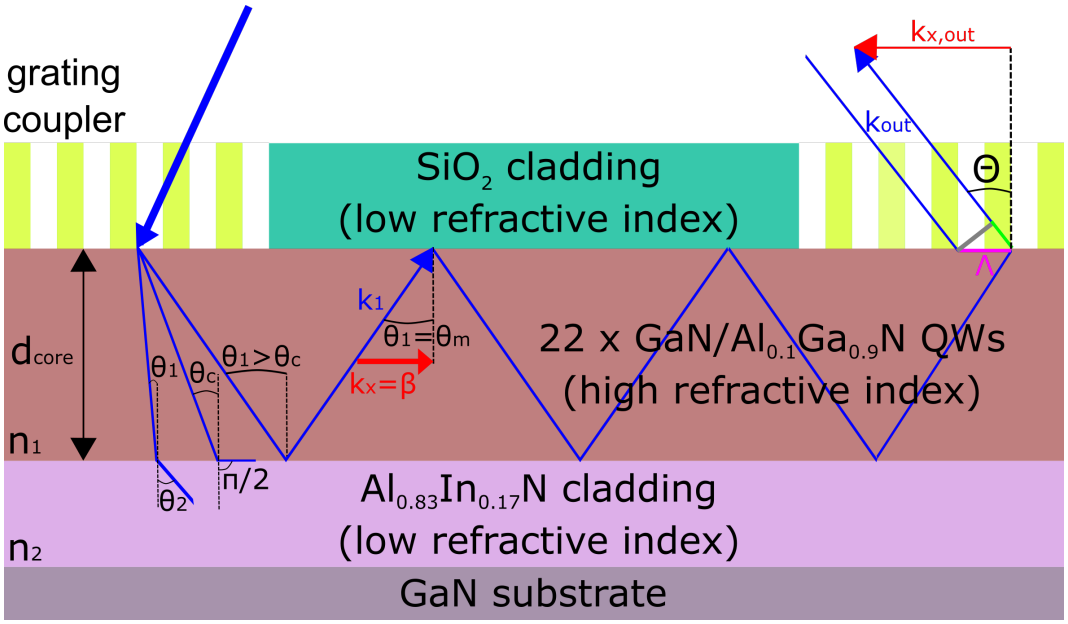

Fig. 3.6 Schematic of our GaN polariton waveguide under an ultraviolet laser to show how TIR and grating couplers work. The light that is shined onto the system is coupled to the waveguide thanks to the gratings etched in the SiO_2 cladding. To have propagation of light inside the waveguide, TIR must occur. As depicted on the left hand side of the 22 $GaN/Al_{0.1}Ga_{0.9}N$ QWs core of thickness $d_{core} = 130\ nm$ and high refractive index n_1, when the incident angle θ_1 on the interface with the low refractive index n_2 cladding is smaller than the critical angle θ_c, the light propagates into the cladding itself. When $\theta_1 = \theta_c$, then $\theta_2 = \frac{\pi}{2}$ and the light does not propagate in the $Al_{0.83}In_{0.17}N$ layer anymore. Finally, when $\theta_1 > \theta_c$, we enter in the TIR regime. The in-plane wavevector $k_x \equiv k_1 \sin\theta_1$ is usually called propagation constant and labelled as β. Once the light reaches the output grating coupler, it can be collected and β can be calculated from the emission angle Θ through Equation 3.26. The purple path gives a phase shift of $\beta\Lambda$, while the green path results in a phase shift of $k_{out}\Lambda \sin(\Theta) = k_{x,out}\Lambda$ which give the constructive interference of the contributions from the different grooves (with a total phase difference equal to a multiple integer of 2π), necessary for the light to come out of the waveguide, as shown in Equation 3.25.

3.3.2 Fabrication techniques

The grating couplers for light input and output are realized after the deposition of SiO_2 top cladding onto the active medium, consisting of 22 QWs of $GaN/Al_{0.1}Ga_{0.9}N$. A thin resist layer ($\sim 120\ nm$) is spun onto the sample and the grating pattern is then exposed to electron-beam lithography (EBL) and developed, where the electron beam changes the solubility of the resist deposited on the desired area. Before the residual resist is removed by a solvent, a 20nm-thick nickel metallisation deposition is performed. Finally, a 175nm-thick

SiO_2 passivation as anti-reflection (AR) and protective coating is carried out.
Specifically, the grating couplers have the following characteristics:

- their size is 100 $\mu m \times 100$ μm;
- their linewidth is 65 nm;
- their periodicity is 130 nm;
- their separation is 50, 100 or 200 μm.

3.4 Waveguides vs microcavities

In this last section, we have a look at the differences between the two optical confinement structures used in this thesis.

The large penetration depth of the electric field into the microcavity DBRs provokes large L_{eff}, while the small penetration depth of the electric field into the waveguide cladding layer thanks to TIR leads to small L_{eff} and so to better spatial confinement [101] and stronger coupling, i.e. higher Rabi splitting $\hbar\Omega_X$ (see Figure 3.7).

The photon lifetime is longer in waveguides, which should be theoretically lossless (unless there is absorption, as mentioned in Section 3.3), compared to a microcavity, where the DBRs reflectivity is around 99% in the best scenario.

The photon dispersion in waveguides is given by [118]

$$E_{ph} = E_0 + \hbar v_g^c \beta \tag{3.27}$$

where E_0 is the energy at $\beta = 0$, and v_g^c is the group velocity inside the waveguide. Since it is linear, the waveguide LPB does not show a ground state, preventing the observation of BEC, in contrast to what happens in microcavities, where the dispersion is parabolic (see Section 3.2 and Figures 3.1, 3.7).

Whereas anticrossing occurs at $k \approx 0$ in microcavities and at higher values in waveguides, the latter exhibits a 10 times higher group velocity, leading to higher polariton speed [119, 120] and longer propagation distances (see Figure 3.7). The group velocity of light can be calculated through its definition

$$v_k \equiv \frac{\partial \omega}{\partial k} = \frac{1}{\hbar}\frac{\partial E_{ph}}{\partial k} \tag{3.28}$$

where k is the in-plane wavevector and E_{ph} is the photon energy given by Equation 3.5 and 3.27 for microcavities and waveguides, respectively. The polariton group velocity is then obtained weighting Equation 3.28 with the photonic fraction $|C_{ph}|^2$.

Finally, in terms of practical applications, the waveguide geometry manifests ease of fabrication. For example, while the resonance of the photonic mode with excitons is not affected by this structure, it is dramatically influenced by cavity length and DBR thickness in microcavities.

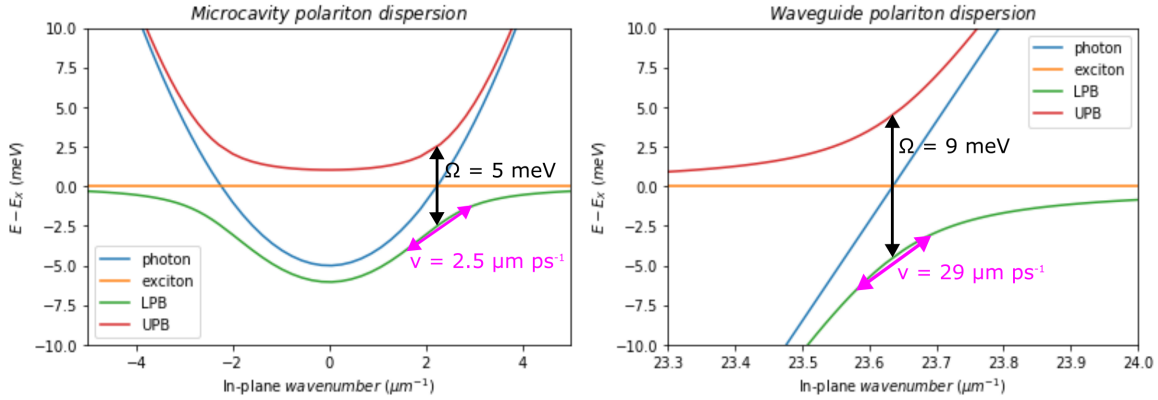

Fig. 3.7 **Left panel**: a negatively detuned GaAs-microcavity dispersion with Rabi splitting and polariton group velocity. **Right panel**: a GaAs-waveguide dispersion with higher Rabi splitting and higher polariton group velocity compared to a GaAs-microcavity. Numerical values taken from [119, 120].

Chapter 4

Experimental setups

4.1 Introduction

In this chapter, we are going to describe the experimental setups used to study both $MoSe_2$ MLs (in Chapters 5 and 6, on their own inside a flow cryostat or within a tunable open-access microcavity inside a bath cryostat) and GaN-waveguides (in Chapter 7, inside a flow cryostat), under non-resonant or resonant excitation.

4.2 $MoSe_2$ experiments

4.2.1 Microscope for flake search

First of all, once the $MoSe_2$ MLs are fabricated as described in Section 2.2.2, they have to be located on the DBR in order to easily find their position once put inside a cryostat. To do that, the LV150N bright-field microscope (produced by Nikon) shown in Figure 4.1 was used [121].
It consists of a white light source, whose IR emission is cut out by the 550 *nm* short-pass filter (550 SPF) in the excitation path. A beam-splitter (labelled as BS) is implemented to work in reflection. Then, to detect only the PL signal emitted by the MLs and exclude the source reflection, a 600 *nm* long-pass filter (600 LPF) is placed before the detector, a charge-coupled device (CCD).

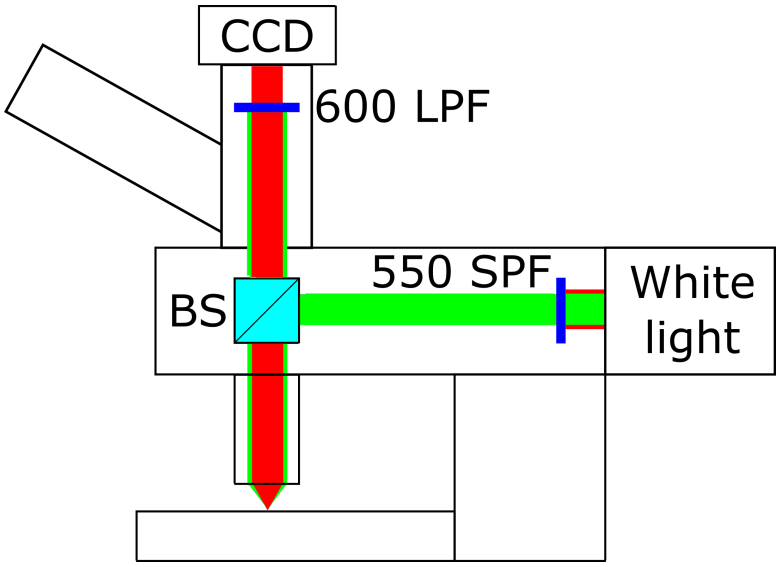

Fig. 4.1 Schematic of our LV150N bright-field microscope, produced by Nikon. A white light source, whose IR spectrum is cut out by the 550 *nm* short-pass filter (550 SPF), excites the MLs. The PL emission is collected by a charge-coupled device (CCD). To block the WL reflection, a 600 *nm* long-pass filter (600 LPF) is positioned in the collection path.

4.2.2 Excitation paths

Once the MLs were located, the samples were placed inside a cryostat (flow or bath, described in Section 4.2.3) and excited with different lasers, depending on the experiment we wanted to perform. To conduct power dependence studies, a gradient ND filter was employed.

4.2.2.1 Excitation lasers

For off-resonant measurements, we utilised a red Helium-Neon (He-Ne) laser, a gas laser that uses the transition between electronic states of the atoms. The He atoms are pumped to long-lived excited states and transfer their energy to specific Ne states, whose relaxation gives the emission at 632.8 *nm*. A 700 *nm* short-pass filter is placed in front of this laser to cut out its tale when measuring the PL emission from the sample.

For resonant measurements, several lasers were used for different experiments and purposes. Because of the photoinduced lattice heating and material damage verified despite the implementation of a chopper under continuous-wave (CW) excitation (as we are going to show in Chapter 5), we needed to operate with pulsed lasers.

Consequently, we employed two different kind of pulsed lasers: the first one with $2-ps$ pulse duration and 80 MHz repetition rate; the second one with $100-fs$ pulse duration and 1 kHz repetition rate. The first one was used to investigate both the bare $MoSe_2$ MLs and the polariton states quasi-resonantly (see Chapter 5), while the second one was used only in the microcavity configuration (see Chapter 6): its lower repetition rate prevents photoinduced lattice heating and material damage (at least at low powers) and its broader energy spectrum (due to shorter pulse duration) allows resonant excitation of the polariton state (for more details, see Sections 5.3.2 and 5.3.3).
The first laser is a tunable mode-locked titanium:sapphire (Ti:sapphire) laser, produced by Spectra-Physics and pumped by a green Ar laser. Its emission ranges from ~ 700 *nm* to ~ 1100 *nm*, but manifests absorption from oxygen and water vapour at ~ 750 *nm*, namely the $MoSe_2$ exciton wavelength. Instead of circulating with a random phase and so having a constant output intensity, as happens in CW lasers, here the cavity modes oscillate with a defined phase, constructively interfering [122]. In order to obtain a single pulse, an acousto-optic modulator (AOM) is implemented: a standing wave is created inside the material thanks to a piezoelectric transducer, with a frequency equal to half of the laser repetition rate $\Delta\nu = \frac{c}{2L}$, namely the distance between two consecutive cavity modes (where L is the cavity length). For fine adjustments of the pulse when the wavelength is changed, a Gires-Tournois interferometer (GTI) comes into play in order to compensate the pulse spreading, arising from SPM (described in Section 7.4) and group velocity dispersion (GVD, see again Section 7.4): different frequencies of the pulse experience a different refractive index of the gain medium, leading to pulse stretching. The pulse duration is then checked with an autocorrelator, similar to a Michelson interferometer, where the overlap of the two beams provides information on the pulse width.
The second laser (depicted in Figure 4.2) is obtained from the frequency-doubled output of an optical parametric amplifier (Light-Conversion TOPAS), used to acquire wavelength extension. It is pumped by 800 *nm* pulses from a Ti:sapphire regenerative amplifier system (Spectra-Physics Spitfire), which is seeded by Spectra-Physics Mai-Tai Ti:sapphire Oscillator to provide the original pulses at 800 *nm* with a repetition rate of 80 MHz and pumped by Spectra-Physics Empower, a Nd:YLF green laser (527 *nm*) with a repetition rate of 1 kHz. The initial pulse generated by the Mai:Tai enters into the Spitfire, which amplifies the short laser pulse by virtue of the chirped pulse amplification (CPA) technique, developed 35 years ago [123], whose inventors won the Nobel Prize in 2018. The pulse is spectrally stretched using a pair of gratings in order to prevent gain medium damaging due to self-focusing, since the peak intensity is now reduced. In this way, the gain medium (a Ti:sapphire crystal pumped by Spectra-Physics Empower to get population inversion) can safely amplify the pulse, which

is then recompressed by another pair of gratings [124]. After exiting the Spitfire, the beam reaches the TOPAS to be converted into the desired wavelength, varying the phase-matching conditions.

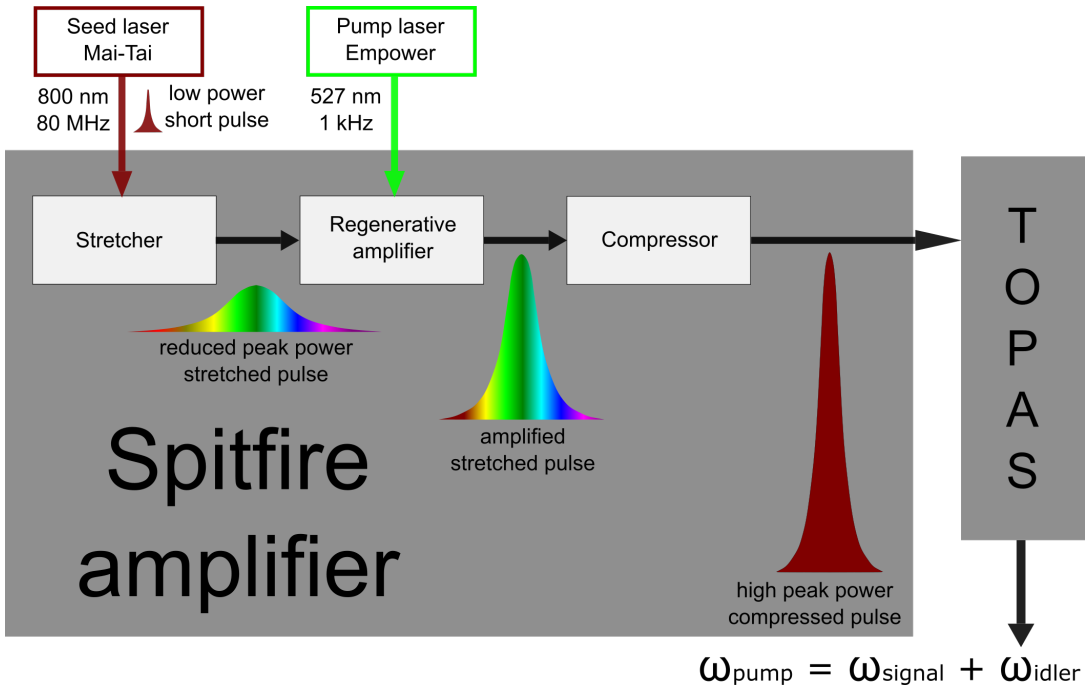

Fig. 4.2 Schematic of the optical parametric amplifier (TOPAS) pumped by the Spitfire amplifier system, that works thanks to chirped pulse amplification (CPA), once seeded by Mai-Tai to provide the original pulse at 800 *nm* with a repetition rate of 80 MHz and pumped by Empower, a green laser (527 *nm*) with a repetition rate of 1 kHz.

4.2.3 Cryostats

As mentioned in Section 4.2.2, the $MoSe_2$ samples were placed inside a cryostat in order to vary their temperature. All our experiments on TMDCs (on their own or within the open-access microcavity), were performed at RT or at liquid-He temperature ($\sim$ 4 K). Specifically, when we analysed the behaviour of bare flakes, we decided to benefit from the ease of use of the continuous-flow cryostat, while to study TMDC-polaritons in our tunable microcavity, a bath cryostat was necessary.

4.2.3.1 Continuous-flow cryostat

This kind of cryostat is connected to a storage dewar that continuously replenishes the boiled-off liquid-He by means of a vacuum pump. The evaporated helium is then collected in the recovery line of the building and transferred to a compressor in order to get liquid-He back. The sample is placed onto a cold finger to reach the desired temperature and, since we work at ~ 4 K, another pump is needed to keep a good vacuum level inside the cryostat.

4.2.3.2 Bath cryostat

Unlike the previous cryostat, in this one the boiled-off helium is replenished periodically (approximately everyday in our custom-built bath cryostat). Since our goal was to resonantly pump the polariton states, our design allows transmission measurements, so avoiding the reflection of the resonant laser, which is orders of magnitude stronger than the signal we wanted to detect (see Figure 4.3).
The main part of the cryostat is the sample chamber, which is in contact with a 10-litres helium vessel through a copper plate. The three piezo stacks, employed to move the two lenses and one of the two mirrors forming the microcavity, are placed on another copper plate and the whole sample chamber is filled with a small amount of He gas utilised as an exchange gas. The sample room cap is attached to the main body of the cryostat by an indium seal. It is thermally isolated from the surrounding environment thanks to an external radiation shield, formed by alternating layers of aluminium foils and a net of a super insulator material, which is further covered by another shield, where a high vacuum is created.

To move the piezoelectric nanopositioners inside the sample chamber, have a readout of their position and control the temperature, 50 thin wires connected to external controllers by a 50 pin SUB-D are implemented. These wires are twisted to avoid cross-talk between them when a voltage is applied through the controllers. Each of the 11 nanopositioners needs 5 connections, 2 for the control and 3 for the readout, so the feedback of some of them was disabled. It is possible to check the chamber temperature using the piezos capacitance (1.3 μF at RT and 0.2 μF at 4 K), but this method is definitely less accurate than using a proper controller.

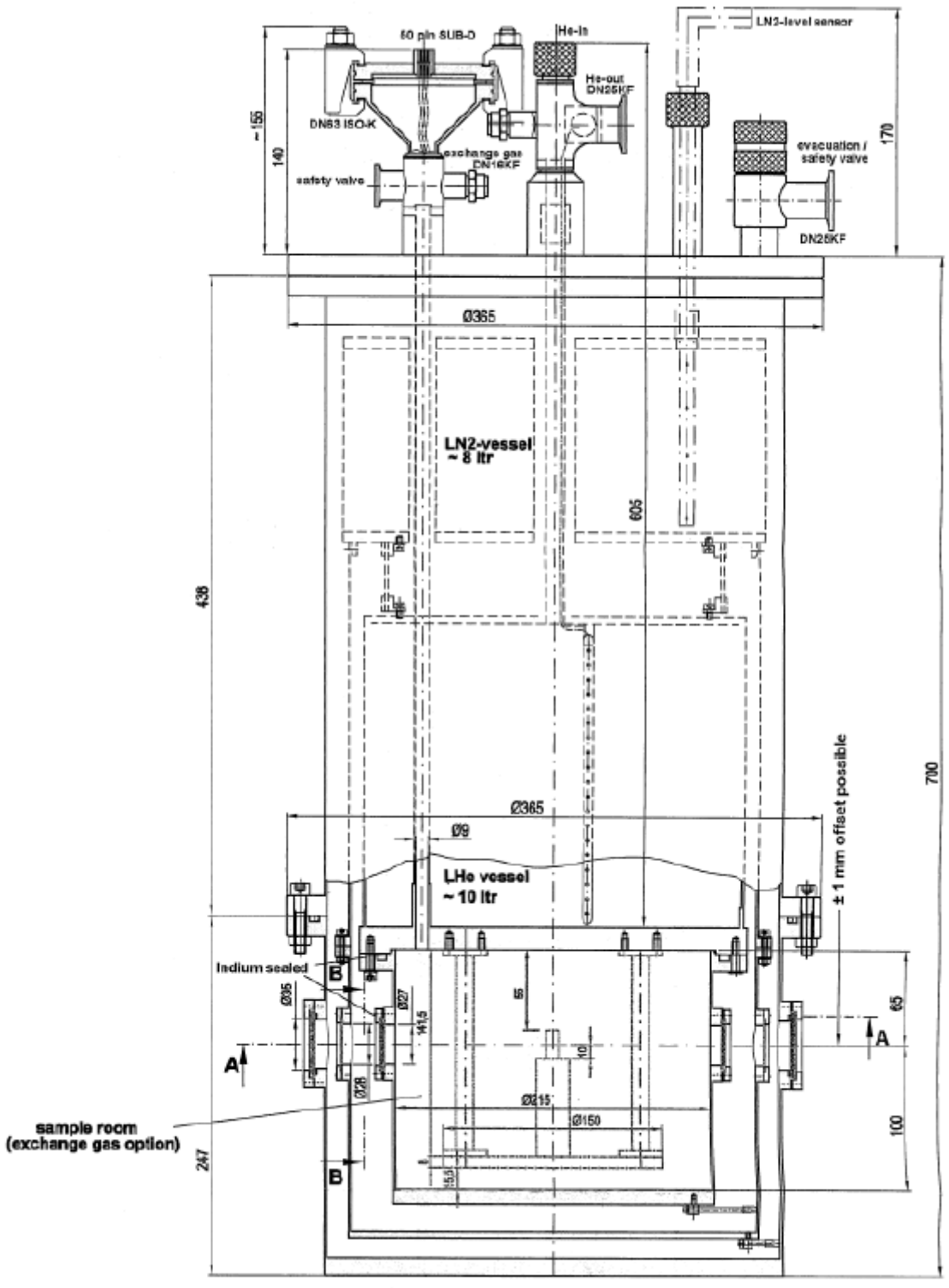

Fig. 4.3 Schematic of the cross-section in the vertical axis of our custom-built helium bath cryostat for transmission measurements. On top, the 50 pin SUB-D to connect all the nanopositioners (produced by Attocube) with their controllers, the two valves to create vacuum in the outer and inner chambers, inputs and outputs for both the 8-litres LN_2-vessel and 10-litres LHe-vessel. At the bottom, the indium sealed sample space filled with exchange gas inside the high vacuum outer jacket.

Tunable open-access microcavity setup

The two DBRs forming the microcavity are mounted vertically on individual holders. One of them is fixed on top of a five Attocube closed-loop nanopositioner stack to control their relative position (see Figure 4.4). Indicating with z the beam axis, ANPx101 are used for x- and z-positioning and ANPz101 for y-positioning (with a travel range of 5 *mm*), while the angles between the mirrors can be controlled by a goniometer stage (ANGp101, with a travel range of 5.4°) as tilt and a rotator stage (ANR101, with a travel range of 360°), labelled as *P* and *ROT* in Figure 4.4. The two lenses of 7.5 *mm* focal length are both manoeuvred by ANPx51 for x- and z-positioning and ANPz51 for y-positioning (with a travel range of 3 *mm*) and are located at each side of the cavity for excitation and collection. The fine position of the piezoelectric nanopositioners can be manipulated applying a DC voltage ($0-70\ V$), whose value is known thanks to their resistive readout. They are made from titanium, as well as the sample holders, to reduce the thermal contraction when the system is cooled down to very low temperature.

To form the cavity, the concave mirrors are moved close to the flat DBR using the z-nanopositioner. Shining white light, fringes appear when the mirrors are close enough because of the angle between them. Looking at these fringes, we are able to adjust and minimise the relative angle employing the rotation and the tilt stages. After that, the mirrors can be moved closer in order to observe the cavity modes. This happens when their distance is smaller than the RoC of the concave mirror (20 μm). Now, the cavity length can be modified allowing the tunability of the photonic modes through the exciton and trion resonances, leading to polariton formation.

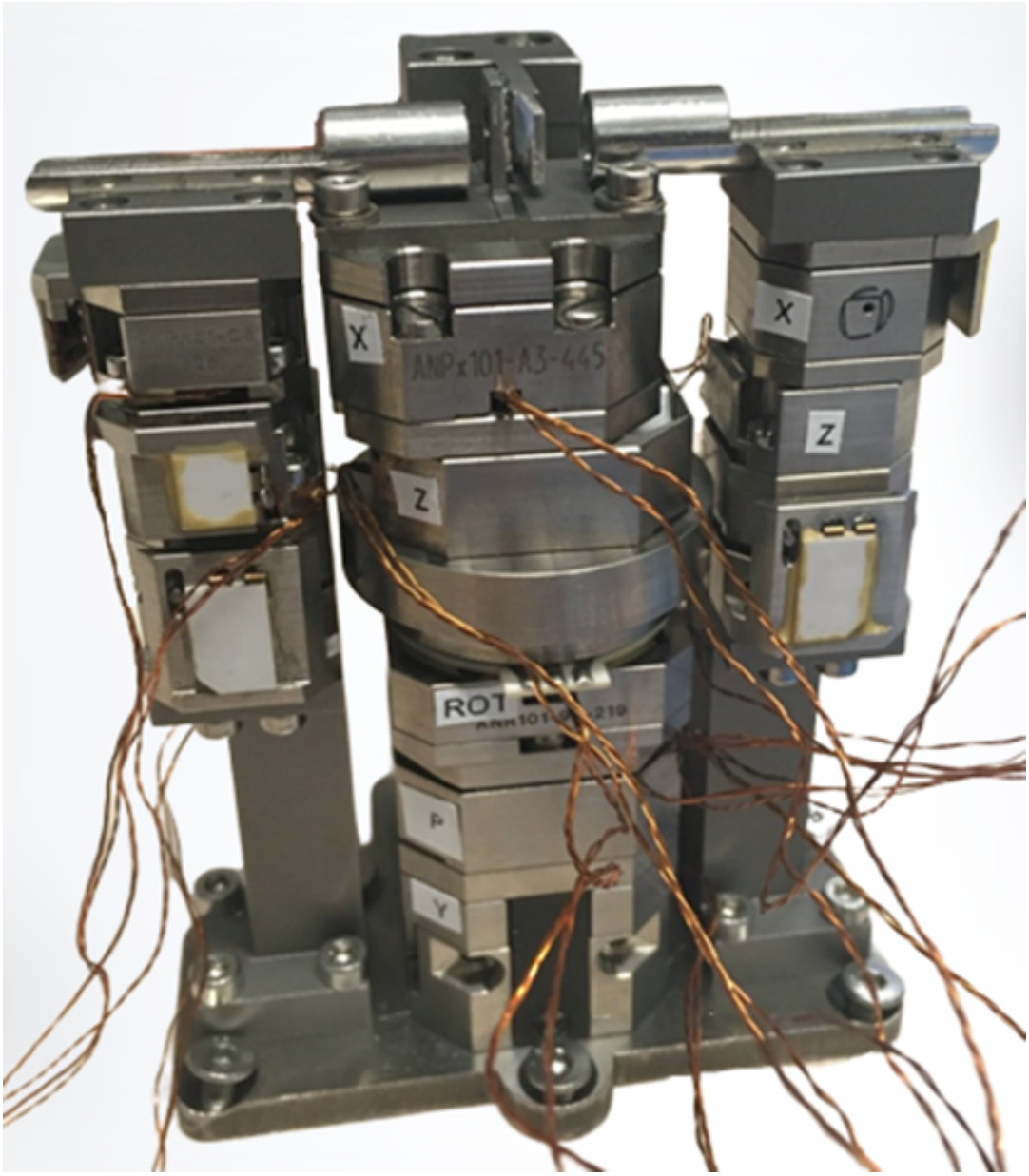

Fig. 4.4 Picture of the three Attocube piezoelectric nanopositioner stacks employed in our TMDC-polariton studies. From left to right: the detection lens (focal length of 7.5 *mm*) with ANPx51 for x- and z-positioning and ANPz51 for y-positioning; the central stack to move the concave mirrors with ANPx101 for x- and z-positioning, ANPz101 for y-positioning, ANGp101 for tilt angle and ANR101 for rotation angle, labelled as *P* and *ROT*; the fixed flat DBR with $MoSe_2$ MLs on top; the excitation lens, with the same characteristics of the detection lens. z refers to the beam axis.

4.2.4 Detection path

Since the geometry of the concave-planar microcavity setup, we only performed real space (near-field) imaging measurements. A 700 *nm* long-pass filter was always implemented in front of the detector to cut out the He-Ne emission.

Specifically, we employed a 4 *cm* focal length objective for all the measurements effectuated on bare MLs in the flow cryostat to characterise the active medium. Thanks to the ~ 7.5 *cm* diameter of this collection lens, we could work in reflection, exciting the sample at a big angle and then cutting out the reflected laser, collecting only the PL emission, as depicted in Figure 4.5 (top panel). To further exclude the reflected laser, we also implemented a combination of linear polariser and half-waveplate ($\lambda/2$) in both excitation and detection path in order to perform measurements in cross-polarisation configuration. The aforementioned 7.5 *mm* focal length lens was utilised for the microcavity measurements inside the bath cryostat. In the reflection setup we made use of a 100 *cm* focal length imaging lens to focus into the spectrometer slit, while in the transmission setup we operated with a 50 *cm* focal length imaging lens, obtaining a magnification $M = \frac{f_{imaging}}{f_{collection}} = 25 \ / \sim 67$, respectively (see Figure 4.6).

4.2.4.1 Spectrometer and streak camera

To detect emission from our samples, an Acton SpectraPro SP-2500 spectrometer (produced by Princeton Instruments), equipped with an interchangeable triple grating turret ($600, 1200, 1800$ $grooves/mm$), was used. A Pixis:256 CCD (produced by Princeton Instruments), characterised by a 1026×256 pixel array, with 26 μm pixel size, was employed as a camera.

We also carried out time resolved measurements on polaritons using a streak camera, produced by Hamamatsu, with a resolution of 2 *ps* (see Figure 4.7). The light passing through the side exit slit of the Acton SpectraPro SP-2500 spectrometer is focused on a photocathode, that converts impinging photons into electrons, whose number is proportional to the light intensity. They are then accelerated by the accelerating mesh and proceed through a sweep electrode, whose applied voltage change is triggered by a signal synchronised with the employed laser. In this way, electrons arriving at different times are deflected at different angles. After being further multiplicated by a micro-channel plate (MCP), they are converted back to photons when hitting a phosphor screen and finally detected.

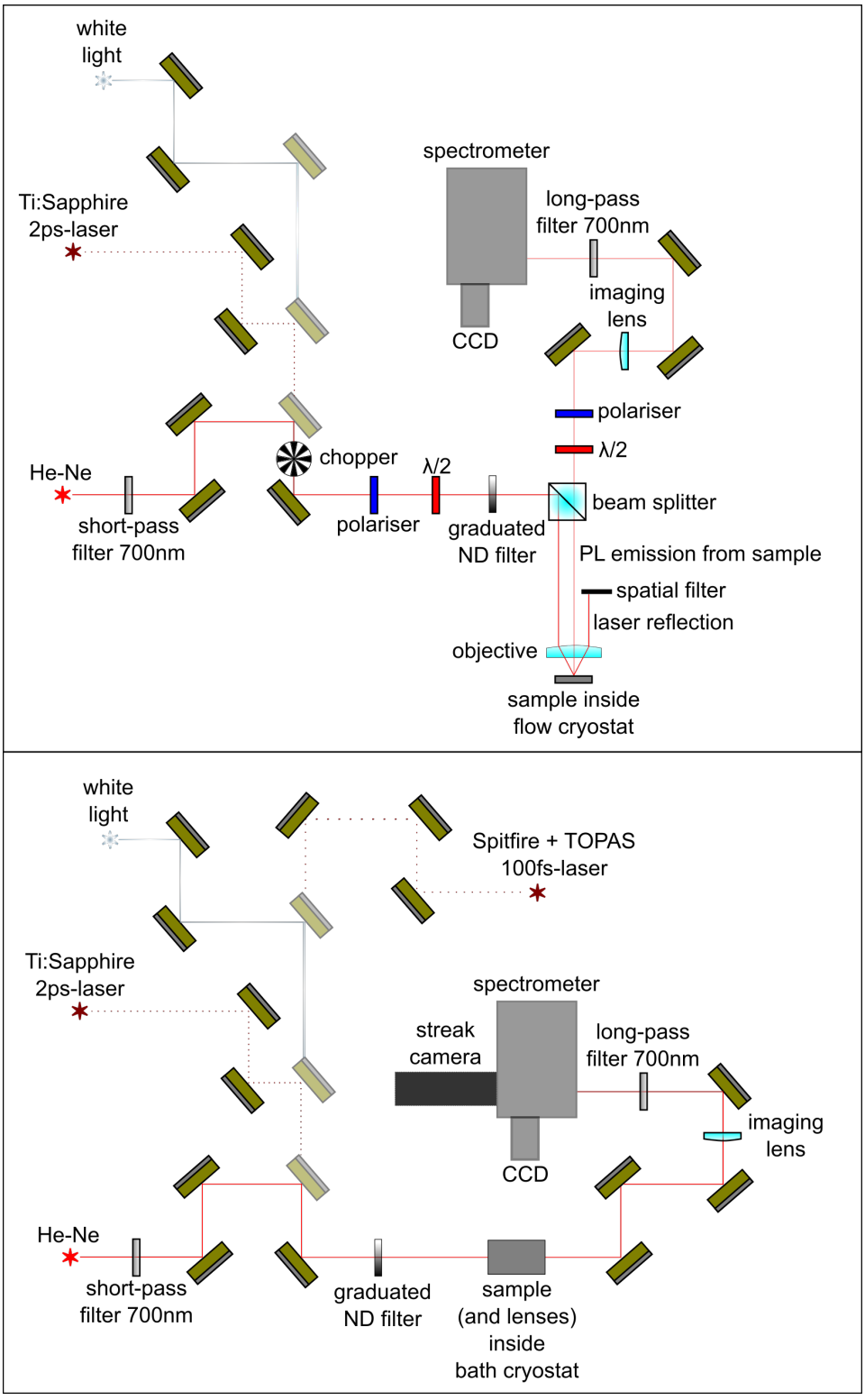

Fig. 4.5 **Top panel**: schematic of the reflection setup. **Bottom panel**: schematic of the transmission setup. Note the use of gold mirrors, which are characterised by high reflectivity in the near-IR range. Semi-transparent mirrors are placed onto flip mounts.

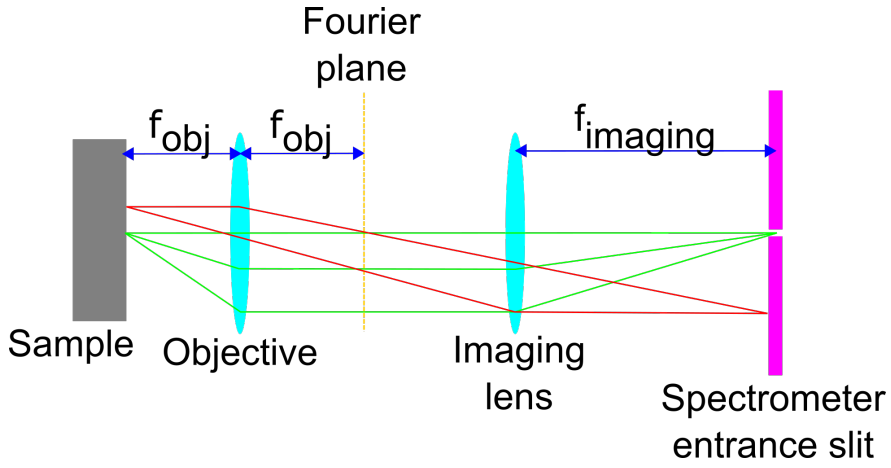

Fig. 4.6 Schematic of the real space (near-field) detection path implemented for TMDC measurements.

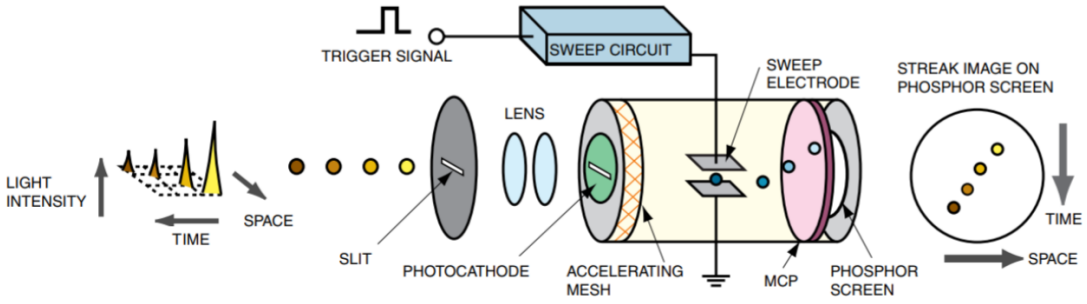

Fig. 4.7 Schematic of the operation principles of the streak camera. Source: Hamamatsu Guide to Streak Cameras

4.3 GaN experiments

4.3.1 Excitation path

A half-waveplate ($\lambda/2$) allows to maximise the laser power passing through the vertically polarised Glan-Thomson polariser, that couples the light to the grating and the waveguide. The last mirror before the cryostat was placed onto a translation stage to change the excitation angle (i.e. polariton wavevector, according to Equation 1.36) when performing power dependences in resonant experiment. Alternatively, by moving into the beam path a 30 *cm* lens placed on a flip mount, the translation stage enabled to change the position of the laser spot on the waveguide. A LMU-20X-UVB (produced by Thorlabs), with 1 *cm* focal length and

numerical aperture $NA = 0.40$, was used as an objective (the setup is illustrated in Figure 4.8).

4.3.1.1 Excitation lasers

As an off-resonant CW excitation, we used a Helium-Cadmium (He-Cd) laser produced by Kimmon, whose emission is in the UV range (325 *nm*) and principles of operation are those illustrated for He-Ne laser (in this case the excited He atoms collide with Cd atoms, transferring energy to the emitting state).
As a pulsed excitation, we utilised the Spitfire-TOPAS output described in Section 4.2.2.1, tuned in the UV range.

4.3.1.2 Pulse shaper

To change the pulse width (i.e. duration), we added in the excitation path a pulse shaper, consisting of two diffraction gratings, two lenses and one spatial filter (represented by a pair of adjustable slits), as outlined in Figure 4.8. The first grating diffracts the input laser in different wavelength components depending on the diffraction angle. After being collimated with the first lens, the diffracted laser is spectrally filtered by passing through mechanical slits placed on the Fourier plane. The uncut beam is then focused onto the second grating by the second lens [125]. So, varying the slits size, we were able to get an output pulse different in both energy width and duration.

4.3.2 Detection path

A dove-prism allows image rotation in order to have the grating edge along the spectrometer slits and properly measure the spectral broadening, described in Section 7.3.
The light coming out from the sample went through a half-waveplate and a vertically aligned linear polariser (the reflection efficiency of vertically polarised light is higher than for horizontally polarised light because grooves on the spectrometer diffraction gratings are vertical).
Since in this experiment it is possible to study the propagating polaritons into the waveguide, we performed both real space (near-field) and momentum space (far-field) imaging measurements.
In the near-field imaging detection, the magnification was $M = \frac{f_{imaging}}{f_{real}} \frac{f_{Fourier}}{f_{collection}} = \frac{15\ cm}{50\ cm} \frac{30\ cm}{1\ cm} = 9$. A spatial filter (represented by a pinhole and placed on a flip mount on the real space plane) allowed the detection of the incoming light from a specific spot of the grating coupler,

when necessary in resonant measurements (see Figure 4.9).
In the far-field imaging detection, the real space lens is flipped out of the path in order to focus the Fourier plane of the collection lens onto the spectrometer slit. In this way, rays emitted from the sample at the same angle represent a single point in the image (see Figure 4.10), permitting angle resolved measurements, where changing the angle is equivalent to changing the polariton momentum. We then got dispersion curves, representing intensity as a function of energy and momentum.
We used the same spectrometer described in Section 4.2.4.1, but for GaN experiments we moved to a Newton 940 CCD - Andor (produced by Oxford Instruments) with 26 μm pixel size and 1024×255 pixel array.

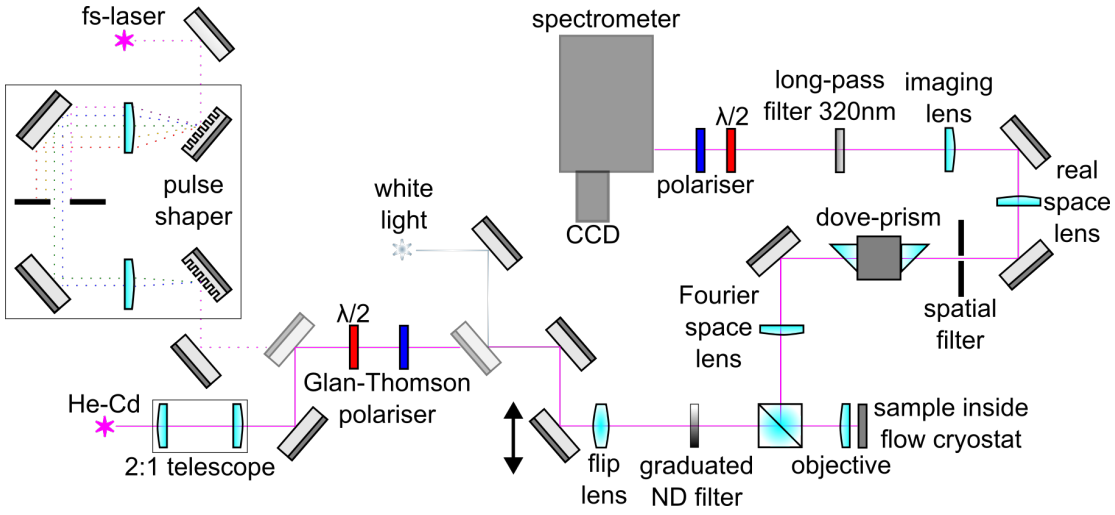

Fig. 4.8 Schematic of the reflection setup, with the detail of the pulse shaper. Note the use of silver mirrors, which are characterised by high reflectivity in the UV range. Semi-transparent mirrors are placed onto flip mounts.

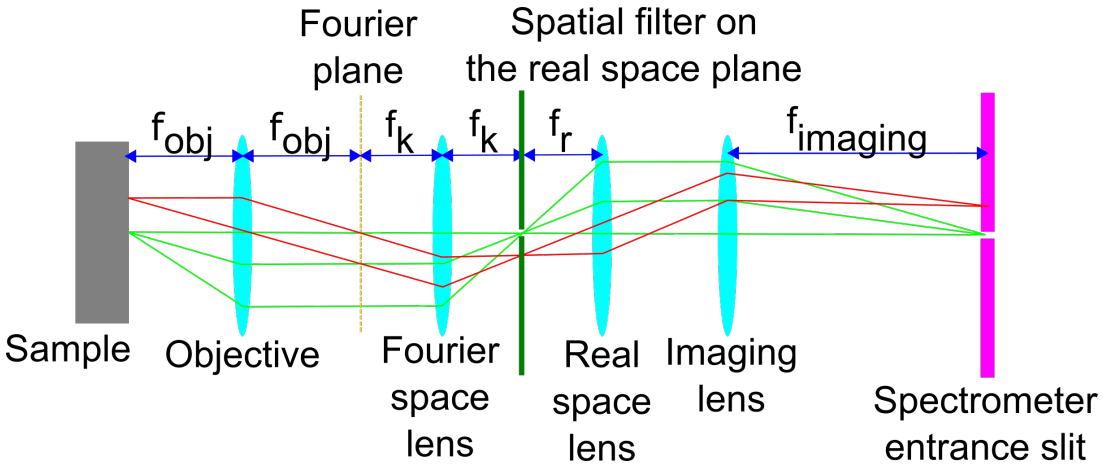

Fig. 4.9 Schematic of the real space (near-field) detection path.

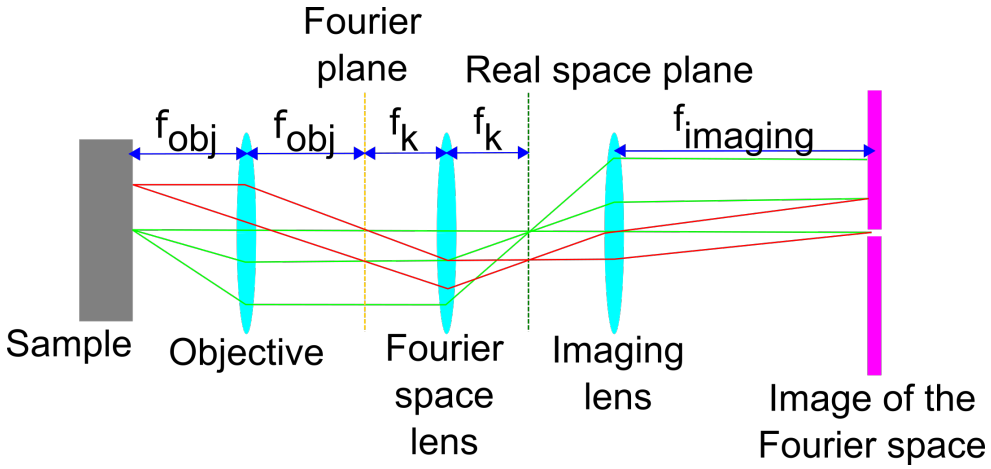

Fig. 4.10 Schematic of the momentum space (far-field) detection path.

Chapter 5

Characterisation of TMDC-polaritons in a tunable open-access microcavity

5.1 Introduction

Excitons in bare TMDCs have already shown their interesting nonlinear properties [126], making these new materials suitable for optoelectronic applications. After being integrated into a monolithic microcavity and observed in the strong coupling regime [127], great effort has been put to investigate this regime. Though small nonlinearity of exciton-polaritons in TMDCs was already discovered [128], they have not been studied in detail. Thanks to our more versatile experimental setup that allows transmission measurements (i.e. resonant excitation) and tuning of the light-matter polariton content, we aim to further and fully examine nonlinearity of TMDC-polaritons, in particular by focusing on the emerging and unexplored trion-polaritons [129].

In this chapter, we first investigate the nonlinear behaviour of the exciton resonance of a $MoSe_2$ ML under non-resonant CW and pulsed excitation. We detect a redshift using a CW laser for increasing pump powers, symptom of sample heating, accompanied by irreversible degradation after few power cycles. Conversely, a blueshift of the exciton resonance due to exciton-exciton interaction was noted under pulsed excitation, before permanent deterioration occurred. The different energy shift arises from the duty cycle guaranteed by the pulsed laser. Once the bare single layer is optically characterised, we place it in our tunable open-access microcavity to observe TMDC-polaritons. Thanks to the peculiar large oscillator strength of exciton complexes in TMDC, we are able to observe trion-polariton resonance, which manifests stronger nonlinearities than exciton-polaritons at low pump powers. After the qual-

itative study of the nonlinear behaviour of these two quasi-particles in this chapter, in the next one we will quantify the interaction strength of both, also extrapolating the corresponding nonlinear refractive index n_2.

First of all, the optical properties of the bare active medium were experimentally studied, using the experimental setup depicted in the top panel of Figure 4.5. Specifically, we compared the PL emission of exfoliated and CVD samples of $MoSe_2$ at both RT and ~ 4 K, to understand what kind of sample was more suitable to our final purpose, namely studying TMDC-polariton nonlinearity. The former samples were provided by Dr. A. Catanzaro, using the technique described in Section 2.2.2.1, while the latter were furnished by Prof. A. I. Tartakovskii. Moreover, power dependence studies were performed to deepen the nonlinear behaviour and resistance of TMDC to photoinduced damage. The latter measurements were carried out on CVD speciments, since this technique guarantees a large-scale coverage of the substrate with a huge amount of deposited MLs.

Once the naked $MoSe_2$ flakes were characterised, they were put into the cavity setup illustrated in Figure 4.4 inside the bath cryostat described in Section 4.2.3.2 and examined using the transmission setup sketched in the bottom panel of Figure 4.5. Various measurements under different configurations were then performed in order to characterise TMDC-polariton formation (non-resonant CW excitation) and outline their nonlinear behaviour (quasi-resonant pulsed excitation), as we are going to gradually specify throughout this chapter.

5.2 Characterisation of bare $MoSe_2$ monolayers

5.2.1 Exfoliated vs CVD sample

As mentioned above, we first deepened the optical quality of the available $MoSe_2$ samples, as shown in Figure 5.1, employing the setup sketched in the top panel of Figure 4.5.

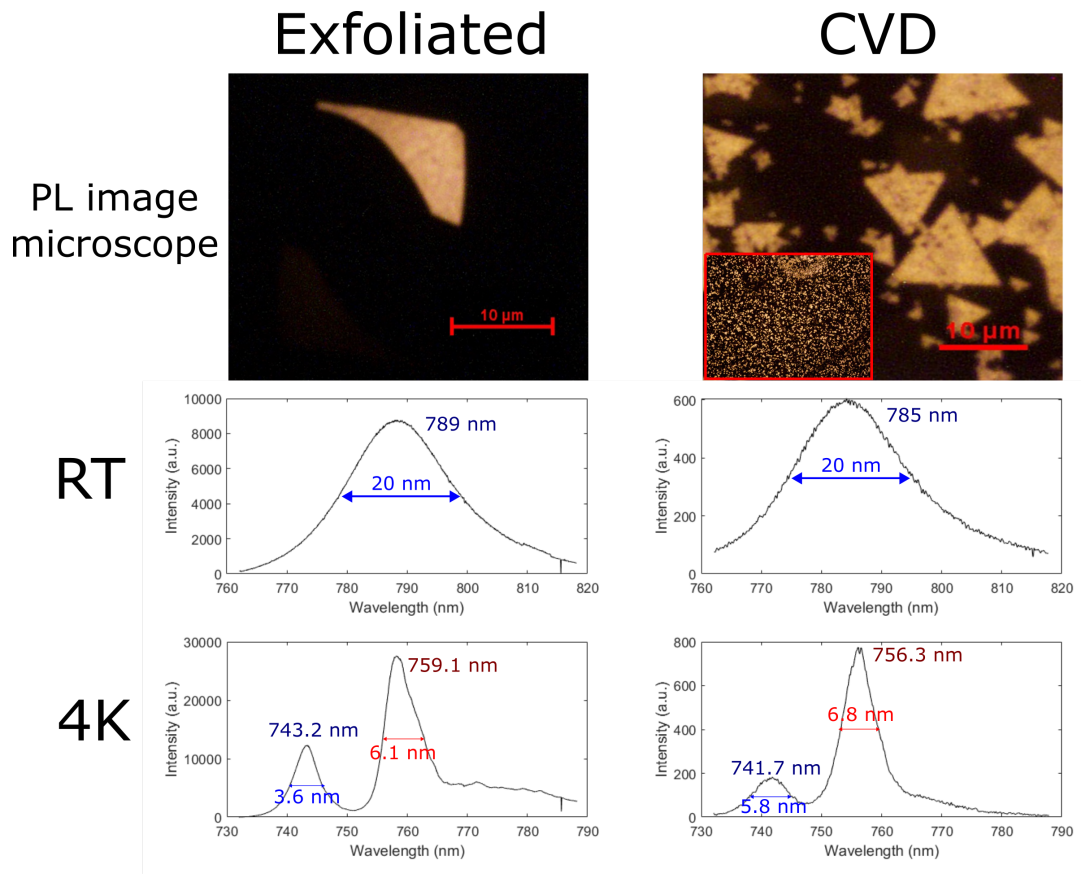

Fig. 5.1 **Left column**: PL image and spectra of an exfoliated flake. **Right column**: PL image and spectra of a CVD flake. **Top row**: PL images acquired with the optical microscope described in Section 4.2.1 for both samples. **Middle row**: PL emission spectrum at room temperature (RT) from both samples, excited with He-Ne laser. **Bottom row**: PL emission spectrum at 4 K (liquid-He temperature) from both samples, excited with He-Ne laser. In dark and light blue the peak position and the full width at half maximum (FWHM) of excitons, respectively. In dark and light red the peak position and the FWHM of trions, respectively. These values are obtained through Gaussian fitting, since the inhomogeneous broadening of the two resonances in both samples. **Inset of top-right panel**: low magnification PL image to show the homogeneous coverage of CVD MLs on the DBR surface.

The PL images obtained with the LV150N Nikon microscope (schematic in Figure 4.1) show the irregular shape of exfoliated samples, while the CVD ones appear to be triangular with different sizes. This peculiar shape depends on thermodynamic and unit cell symmetry reasons [130].

Referring to the PL spectra of Figure 5.1, the variation in the peak position of excitonic resonances in different MLs and within the same flake arises from thermodynamically inevitable point defects and distinct strain conditions during the growth process [131], which strongly

affect the TMDC band structure [132, 133].
Looking at RT spectra, the exciton resonance linewidth is quite broad mainly due to interaction with phonons [134], preventing observation of strong coupling regime at high temperature. As suggested in [135], in order to overcome this limitation, stacks of multiple MLs separated by hBN layers could be implemented, since the coupling strength g_0 is given by Equation 1.10.
Reducing the temperature down to ~ 4 K, we observe a blueshift of the exciton peak as predicted by the Varshni's law (Equation 2.4) and the appearance of a second peak at higher wavelengths due to trion emission. As emerges from temperature-dependence studies in [81], the charged exciton feature actually emerges at $\sim 150\ K$. The long tail at higher wavelength characterising the trion arises from electron recoil effect [136]. The reduction of the exciton linewidth due to the freezing of the phonon bath favours the formation of polariton states.
In this perspective, exfoliated MLs are still superior in quality than CVD flakes despite the effort of recent years to improve the fabrication technique. Their smaller exciton linewidth (2 *meV* in [137]) and their higher intensity guarantee a larger Rabi splitting, since the higher the number of available bright excitons the higher the collective oscillator strength (see Equation 1.14), leading to stronger nonlinear effects (see Equation 1.23). It is also interesting to note that the trion peak is two to four times higher than the exciton peak, indicating that both samples were already slightly doped, as we are going to investigate further in the next section.

5.2.2 Power dependence studies

Once the best type of sample was identified, keeping in mind the ultimate purpose of studying the nonlinear behaviour of exciton resonances at different excitation density, we performed power dependence studies. Doing that, we were also able to estimate the damage threshold under CW and pulsed excitation.

5.2.2.1 CW laser

First of all, we studied exciton PL emission under off-resonant CW excitation. We carried out these experiments employing the He-Ne laser mentioned above, whose emission is at $\sim 635\ nm$, well above the $MoSe_2$ exciton resonance.

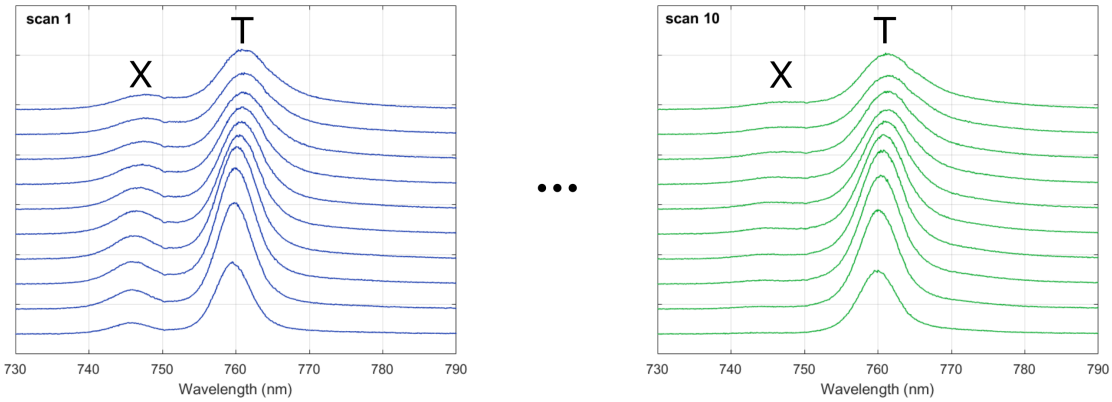

Fig. 5.2 PL spectra at 4 K obtained through multiple power scans under off-resonant CW excitation (for brevity, only the 1st and the 10th are shown). The bottom curve of the waterfall represents the lowest pump power $P = 0.83\ mW$, that corresponds to a photon flux $n = 1.85 \times 10^{20}\ cm^{-2}\ s^{-1}$. The top curve of the waterfall represents the highest pump power $P = 416\ mW$, that corresponds to a photon flux $n = 9.27 \times 10^{22}\ cm^{-2}\ s^{-1}$. The 1st scan is blue, while the 10th scan is green, referring to Figure 5.3. X and T indicate exciton and trion peak, respectively.

As shown in Figure 5.2, this set of measurements consisted of many consecutive power scans, each of them lasting around three minutes. The bottom curve of the waterfall represents the lowest pump power ($P = 0.83\ mW$), while the top one represents the highest pump power ($P = 416\ mW$). According to our calibration, which takes into account the actual power at the region of interest (detected with the spectrometer grating at '0-order mode') and ~ 90 % of cryostat window transmission, we get that 1 mW of nominal power corresponds to a power density of $\sim 70\ W \cdot cm^{-2}$. Considering that the energy of the impinging photon is 1.953 eV, we finally obtain a photon flux of $2.23 \times 10^{20}\ cm^{-2} \cdot s^{-1}$. The peak intensity, peak position and linewidth for both exciton and trion resonance are then plotted as a function of the photon flux in Figure 5.3, where blue illustrates the first scan, while green illustrates the last scan.

As it is demonstrated in Figures 5.2 and 5.3, the CW excitation degrades the ML optical properties, even though we already implemented a chopper in the reflection setup (see Figure 4.5, top panel) to prevent photoinduced substrate heating. This heating effect can be noted in the redshift of both exciton and trion peak position. This irreversible deterioration under high-power excitation, as revealed by the subsequent scans, appeared at a critical photon flux of $\sim 3 \times 10^{22}\ cm^{-2} \cdot s^{-1}$, or equivalently at a power density of $\sim 10\ kW \cdot cm^{-2}$. This deterioration affects the trion to a lesser extent, as shown by the same behaviour of all the scans.

The massive oscillations in the peak position and linewidth for the last scans (especially at low pump powers) related to excitons is a clear manifestation of this degradation to a greater extent. Finally, we can attribute the linewidth broadening mechanism to the lattice heating, for increasing pump powers [126].

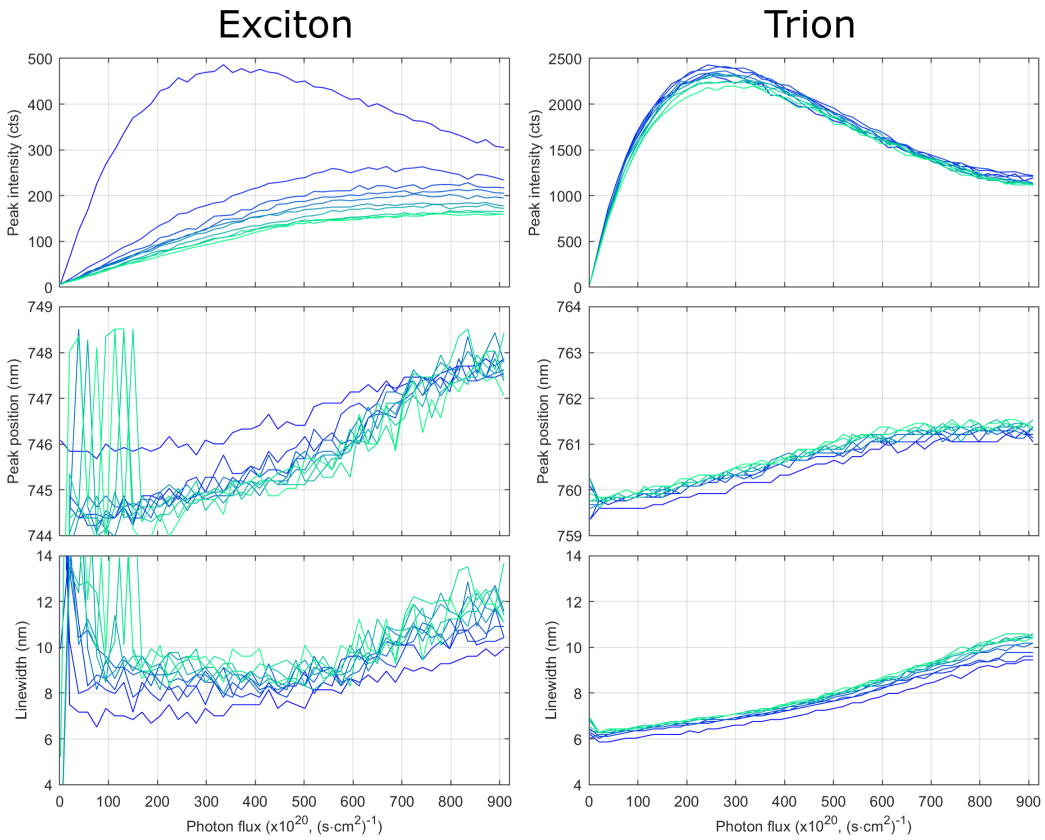

Fig. 5.3 Same set of measurements shown in Figure 5.2. **Left column**: data corresponding to the exciton resonance. **Right column**: data corresponding to the trion resonance. **Top row**: peak intensity for increasing photon flux, i.e. pump power. **Middle row**: peak position for increasing photon flux. **Bottom row**: linewidth for increasing photon flux. The blue curve always illustrates the first scan, while the green curve always illustrates the last scan.

5.2.2.2 Pulsed laser

We then moved to the Ti:sapphire pulsed laser with a repetition rate of 80 MHz described in Section 4.2.2.1, with a pulse duration of $\sim$ 1.7 ps detected by the autocorrelator. Since the quasi-resonant excitation at 713.5 nm, for this specific measurement we implemented polarisers and half-waveplates in the excitation and detection path in order to measure in the cross-polarised configuration to cut out the scattered light of the excitation laser. With the

same procedure explained in Section 5.2.2.1, we get that 1 mW average power corresponded to $\sim 22.5\ kW \cdot cm^{-2}$ average power density. Dividing this value by the repetition rate, we obtain a fluence of 280 $\mu J \cdot cm^{-2}$ per pulse, and further dividing by the photon energy, we derive a photon density of $\sim 10^{15}\ cm^{-2}$ per pulse. This power scan is displayed in Figure 5.4.

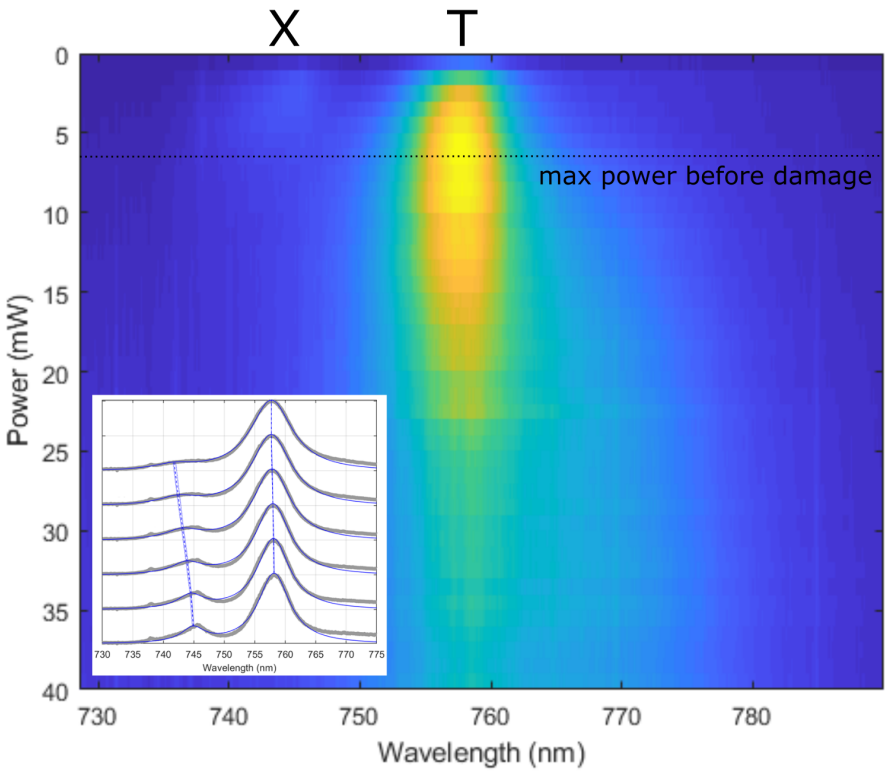

Fig. 5.4 Power scan under pulsed laser (713.5 nm excitation and 80 MHz repetition rate). On the y-axis the average power measured before the cryostat window, where 1 mW corresponds to 280 $\mu J \cdot cm^{-2}$ fluence and $\sim 10^{15}\ cm^{-2}$ photon density, per pulse. Exciton X emission disappears at around 6 mW, the maximum power before irreversible damage. **Inset**: peaks positions for the lowest pump powers (from 1 mW to 6 mW), showing the blueshift of the exciton resonance.

Excitons (X) blueshift by $\sim 2\ nm$ at low powers until they disappear around 6 mW, corresponding to $\sim 1.7\ mJ \cdot cm^{-2}$. At higher pump powers, the flake experience an irreversible photoinduced damage, manifested not only by the above mentioned bleaching of the excitonic resonance, but also by photoinduced doping [138] and consequent appearance of emission from localised defect states [139] above the trions (T). This means that nonlinear effects are expected at lower powers ($\sim 10 - 100\ \mu J \cdot cm^{-2}$), as reported in [140, 141]. In the case of

pulsed excitation, the nonlinear blueshift can be attributed to exciton-exciton interaction, as opposed to the redshift observed under CW excitation arising from lattice heating [126].

We then concluded that low pulsed excitation is needed to avoid irreversible sample damage during our exploration of nonlinear physics in TMDC-polariton systems under resonant excitation. However, low CW off-resonant excitation is still valid in performing very basic polariton states characterisation, namely their formation.

5.3 $MoSe_2$ monolayers in a hemispherical open cavity

5.3.1 Characterisation of polariton states formation

Once the optical quality and the damage threshold of the bare $MoSe_2$ MLs had been characterised, we started our studies on TMDC-polaritons. We then moved to the transmission setup (illustrated in Figure 4.5, bottom panel), employing the bath cryostat and the tunable open-access microcavity, both described in Section 4.2.3.2.

The top mirror consisting of a 13-pair DBR deposited on a hemispherical surface (see Section 3.2.2) was moved onto the planar DBR. The two mirrors were then aligned and brought into a close proximity to each other (the distance between the mirrors was set to 1 μm) using the piezo nanopositioners described in Section 4.2.3.2, forming the open-cavity system with the resulting formation of discrete microcavity Laguerre-Gaussian (LG_{mn}) photonic modes, evoked in Section 3.2.1. The excitation beam was focused into the spot size of about $5-10$ μm on the flat mirror, so that only a fraction of the incident photons couples to the highly confined LG_{00} cavity mode.
To characterise the polaritons, the open-access microcavity was excited with the He-Ne laser at 1.95 eV and polariton emission was recorded as a function of the detuning between the excitons and photonic mode LG_{00} mode.

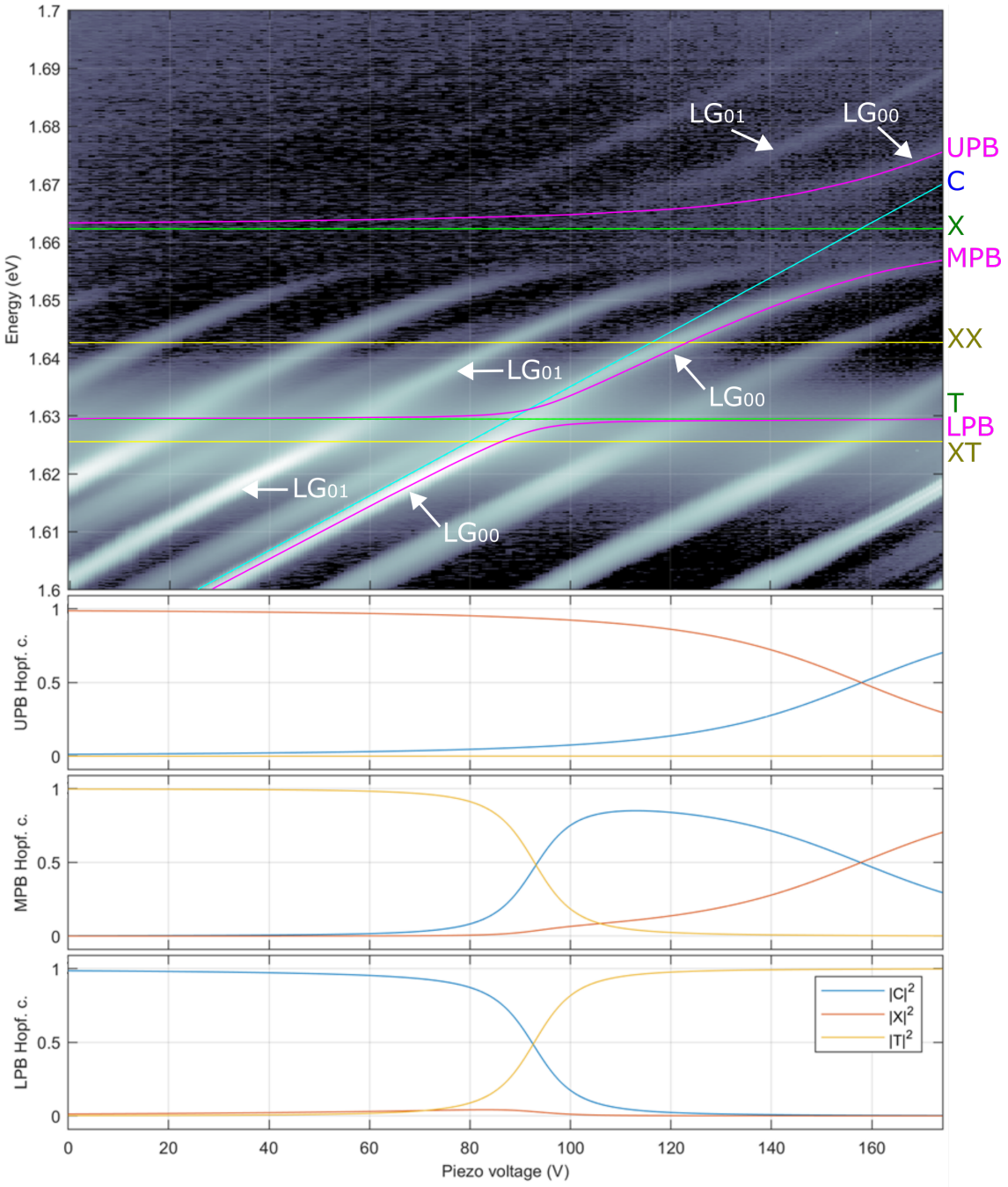

Fig. 5.5 **Top panel**: PL emission as function of piezo voltage (i.e. cavity length and so photon-exciton detuning) under off-resonant excitation shows anticrossing of the different cavity modes $LG_{l,p}$ with both excitons X and trions T, leading to formation of upper, middle and lower polariton branches (UPB, MPB and LPB, respectively). Biexcitons XX and charged biexcitons XT are also indicated, whose values are taken from [80]. **Bottom panels**: photonic $|C|^2$, excitonic $|X|^2$ and trionic $|T|^2$ fraction of upper, middle and lower polariton branches (from top to bottom).

To describe the polariton system where the photonic mode is strongly coupled to both excitons and trions we employ a model of three-coupled oscillators, which can be described in a compact way by the matrix equation

$$\begin{bmatrix} E_{\mathrm{C}}(L) & \frac{1}{2}\hbar\Omega_{\mathrm{X}} & \frac{1}{2}\hbar\Omega_{\mathrm{T}} \\ \frac{1}{2}\hbar\Omega_{\mathrm{X}} & E_{\mathrm{X}} & 0 \\ \frac{1}{2}\hbar\Omega_{\mathrm{T}} & 0 & E_{\mathrm{T}} \end{bmatrix} \psi = E\psi, \tag{5.1}$$

where $E_{\mathrm{C}}(L)$, E_{X}, E_{T} are the cavity photon, exciton, and trion energies; $\hbar\Omega_{\mathrm{X}}$ and $\hbar\Omega_{\mathrm{T}}$ are the cavity mode-exciton and the cavity mode-trion coupling strength. ψ is a three-component basis vector. Eigenvalues of the matrix in the left-hand side of Equation (5.1) give the polariton mode resonances of the upper, middle, and lower polariton branches (UPB, MPB, and LPB, respectively). Their eigenvectors provide the Hopfield coefficients.

It is interesting to note the different energy values for both exciton and trion resonances when measured first on bare flake and then inside the cavity, as summarised in Table 5.1.

Table 5.1 Exciton and trion resonances outside and inside the cavity.

	X (meV)	T (meV)
Bare flake	1659	1627
Inside cavity	1662	1630

This difference in the energy values is called Stokes shift and manifests itself as an offset between absorption (inside cavity) and emission (bare flake) spectra. It originates from the opposite nature of the two processes (excitons creation and recombination, respectively), where the luminescence peak is at lower energy because of the excitons interaction with other particles before their decay [142]. Specifically in TMDCs, this phenomenon was attributed to MLs doping [79], further confirmation of the photoinduced charge transfer into $MoSe_2$ flake. Its small value (~ 3 meV) indicates a low doping level [143] and consequently the high quality of the exfoliated sample under investigation [144].

It is also worth to mention at this stage one of the biggest issues found in the open-cavity geometry: mechanical vibrations. As shown in Figure 5.6, we observe a periodic oscillation (every ~ 30 minutes) of the cavity length, due to light contact between the two DBRs, indicating the poor mechanical stability of the system. This periodicity of the relative tremor of the two halves of the open cavity is due to the connection of the bath cryostat to the recovery

line and then to the He compressor, as mentioned in Section 4.2.3.1. In order to overcome this problem, we have been obliged to put the two DBRs in contact. In this way, we have dramatically reduced the vibrations, which cause broadening (i.e. decreasing in Q-factor) and energy shift of the cavity mode, having a detrimental effect especially in long exposure time experiments. As a drawback, the relative angle between the two halves of the open cavity implies a reduction of the coupling efficiency of the excitation laser to the cavity mode.

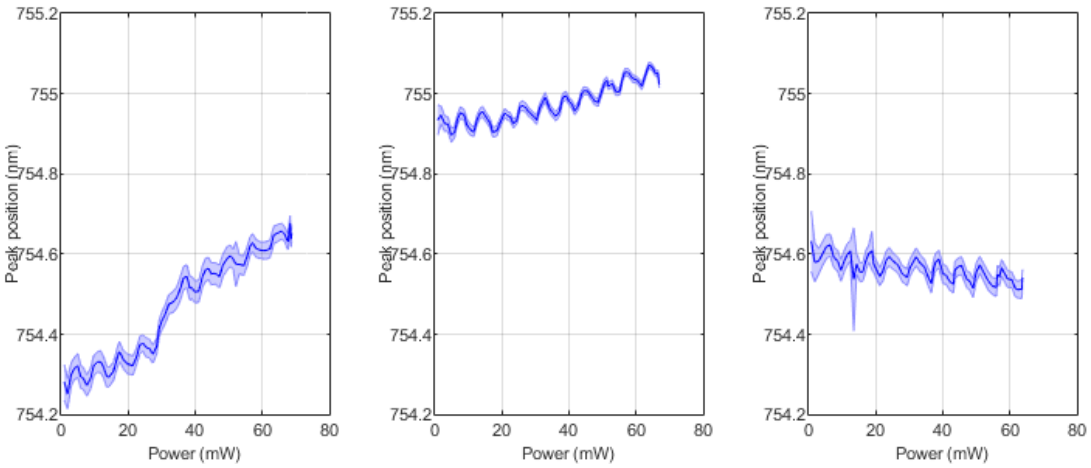

Fig. 5.6 Three examples of polariton mode oscillations due to poor mechanical stability of the open-cavity system, causing relative vibration of the two halves.

5.3.2 Pumping LG_{01} and detecting LG_{00}

We then performed another kind of experiment, where we pumped the first-excited polariton state with the $2-ps$ pulsed resonant laser at different detunings and detected the population of the ground polariton mode, as we previously did in [145]. In that case, the active medium was a GaAs QW, excited with a CW laser, not employed in this experiment since the lattice heating noticed in TMDCs (see Section 5.2.2.1). Since the $2-ps$ pump laser is narrower (FWHM $\sim 1\ meV$) than the polariton resonance itself (FWHM $\sim 4\ meV$), in resonant transmission we do not detect the mode but the envelope function of the mode with the pump laser, so any effect of broadening or energy shift is concealed and reduced in detection. Pumping LG_{01} and detecting LG_{00} as a "probe" implies that the energy shift and the linewidth changes are then real. Given the above mentioned limitation of the laser wavelength tuning (see Section 4.2.2.1), we explored two different configurations:

- LG_{01} and LG_{00} both in the MPB (see Figure 5.7, top panel);

- LG_{01} in the MPB while LG_{00} in the LPB (see Figure 5.7, bottom panel).

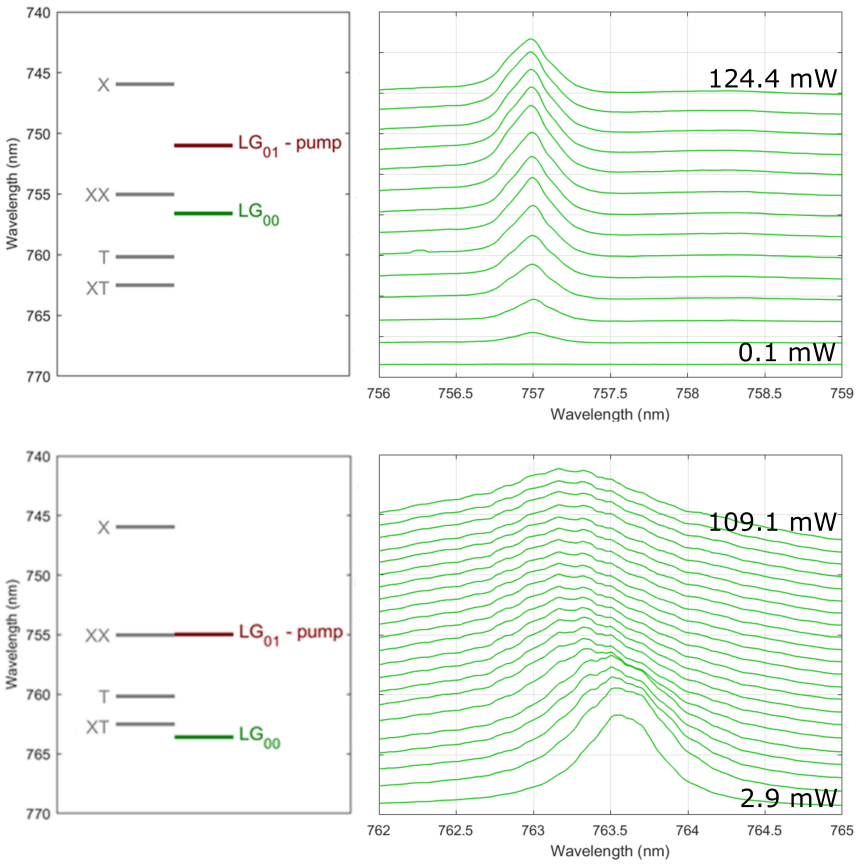

Fig. 5.7 **Top panel**: on the LHS, schematic of the energy level configuration, where the pumped mode LG_{01} and the detected mode LG_{00} are both in the MPB. On the RHS, power dependent spectra of the ground mode. **Bottom panel**: on the LHS, schematic of the energy level configuration, where the pumped mode LG_{01} is in the MPB and the detected mode LG_{00} is in the LPB. On the RHS, power dependent spectra of the ground mode. All the excitonic-like resonances values in the LHS are taken from [80].

For the two different configurations, both measured on the very same point of the flake, we detect a blueshift of ~ 0.1 *nm* and ~ 0.4 *nm*, respectively. This behaviour implies the importance of the trion component in the polariton interactions, as further confirmed by the subsequent measurements at two different points of the same ML (see Figure 5.8). These measurements were performed in the same energy level configuration that showed the biggest blueshift, where the pumped mode LG_{01} is in the MPB and the detected mode LG_{00} is in the LPB (see Figure 5.7, bottom panel).

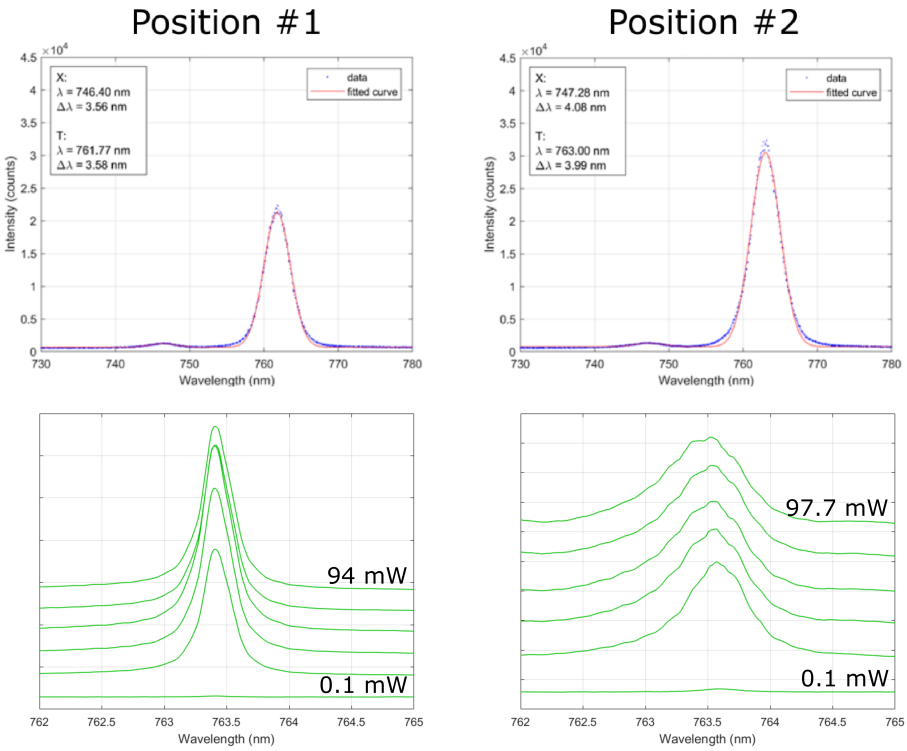

Fig. 5.8 **Top row**: PL emissions of the bare flake at two different points of the same ML. **Bottom row**: power dependent spectra of the ground mode in the same two different points of the same ML. **Left column**: PL emission of the bare flake and power dependent spectra of the ground state in the first point. **Right column**: PL emission of the bare flake and power dependent spectra of the ground state in the second point.

The top row of Figure 5.8 shows that the optical properties vary along the same ML, i.e. depend on the specific point of the flake under investigation. The trion peak is at $\sim 761.8\ nm$ and $\sim 763\ nm$ for position 1 and 2, with a linewidth of $\sim 3.6\ nm$ and $\sim 4\ nm$, respectively. Looking at the LG_{00}, nominally fixed at $\sim 763.5\ nm$ as detected under off-resonant excitation, we observe a blueshift of $\sim 0\ nm$ and $\sim 0.2\ nm$ for position 1 and 2, with a linewidth of $\sim 0.3\ nm$ and $\sim 0.6\ nm$, respectively. That means that polariton interaction increases when the ground mode is closer to the trion resonance, as happens in position 2.

5.3.3 Resonantly pumping LG_{00} at different detunings

Given the interesting role of trions just detected, we decided to further investigate these trion-polaritons. Because of the difficulty in quantifying the actual polariton number in the quasi-resonant configuration adopted so far, this time we employed the $100 - fs$ pulsed laser

described in Section 4.2.2. Thanks to its spectrum being much broader (FWHM $\sim 15\ meV$) than the polariton resonance (FWHM $\sim 4\ meV$), we could resonantly excite the ground mode, contrary to what we previously did (see Section 5.3.2) with the narrower $2-ps$ laser (FWHM $\sim 1\ meV$). Table 5.2 shows the energy shift of the resonantly pumped LG_{00} for different detunings, varying the excitation power over two orders of magnitude (from $0.04\ \mu W$ to $4\ \mu W$) and back, to verify that the process is reversible. Blueshift is observed for the more excitonic-like mode (exciton energy $E_X \sim 1658\ meV$), while a redshift is interesting detected for the more trionic-like mode in the MPB (trion energy $E_T \sim 1632\ meV$). Looking at the LPB, the more trionic-like detuning shows again a strong blueshift, that reduces moving to more photonic-like detunings, until it disappears because of the lack of polariton interactions.

Table 5.2 Resonantly pumped LG_{00} at different detunings.

Polariton branch	LG_{00} energy (meV)	Energy shift (meV)
MPB	1649	0.64 ± 0.05
	1642	0.13 ± 0.12
	1636	-0.59 ± 0.17
LPB	1627	1.12 ± 0.12
	1621	0.39 ± 0.08
	1610	0.03 ± 0.06

This last preliminary qualitative study, performed on simple exfoliated ML, paves the way to a quantitative investigation of this redshift-blueshift behaviour of the polariton mode in MPB and LPB, respectively, that foreshadows the quenching of the trion-photon strong coupling. As we are going to study in greater detail in the next chapter, using a higher quality sample encapsulated in hBN to improve the exciton complexes linewidths, the trion-polariton nonlinearity here prefigured is ~ 100 higher than that of exciton-polaritons, leading to a nonlinear refractive index n_2 three to five orders of magnitude greater than that measured in the weak coupling regime.

The last measurement before moving to the more detailed quantitative analysis, reported in next chapter, we executed a sanity check to quickly evaluate whether our claims and results are really related to trion- and exciton-polariton nonlinearities. We performed a power dependence (in the same range of Figure 6.10) without the active medium, i.e. for the bare cavity mode. LG_{00} was tuned at $\sim 1636\ meV$, energy belonging to the MPB, if we were in

the strong coupling regime. As shown in Figure 5.9, no energy shift is observed, confirming that the nonlinear behaviour we previously measured was due to polariton interactions.

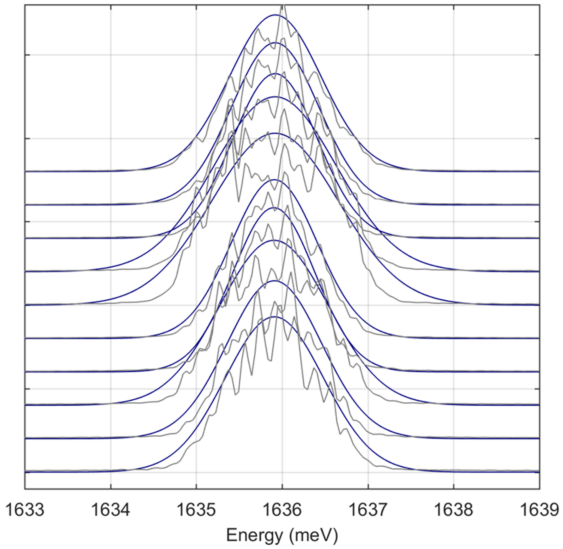

Fig. 5.9 Spectra of the bare cavity LG_{00} mode (in grey) for the pump powers from 1 to 10 μW (power increases from bottom to top) and respective Gaussian fit (in blue).

5.4 Summary

To sum up, in this chapter we first characterised bare $MoSe_2$ monolayers, performing power dependence studies under both CW and pulsed excitation (see Section 5.2.2). We observed redshift of the excitonic resonances in the first case, arising from sample heating and leading to irreversible degradation of the sample under investigation. In contrast, we detected blueshift for increasing pump powers under ps-pulsed excitation, signature of exciton-exciton interaction.

After these preliminary investigations of the naked optically active medium, we moved the sample into the open-cavity setup, where we investigated TMDC-polariton nonlinearities under pulsed laser in different configurations, varying pump scheme, exciton-photon detuning of the polariton resonance and pulsed laser. Overall, we recognised the relevant role played by charged excitons in polariton nonlinear behaviour compared to that of neutral excitons, which will be further deepened in the next chapter.

Chapter 6

Nonlinear exciton- and trion-polaritons in TMDCs under resonant pulsed excitation

6.1 Introduction

In light of what we observed about trion-polaritons in the previous chapter, we further explored the physics behind these interesting quasi-particles.

In this chapter, the main result we report is a very large Kerr-like nonlinearity by employing the strong optical transition of these charged excitons observed in semiconducting TMDCs. The large oscillator strength of trions enables formation of well-resolved trion-polariton resonances at relatively small electron density, which, as we show here, leads to a pronounced phase-space filling effect enabling nonlinearity of one to two orders of magnitude bigger (depending on exciton-photon detuning) than that of neutral exciton-polaritons in TMDC platforms.

By hybridising trions (in a brand new $MoSe_2$ ML fabricated by Dr. F. Whithers) at low electron densities with the ground open-access microcavity mode, trion-polaritons exhibit significant energy shifts at very small photon fluxes due to phase-space filling. We found that the ratio of trion- to neutral exciton-polariton interaction strength is in the range from 10 to 100 in TMDC materials and that the trion-polariton nonlinearity at least is comparable to that in other polariton systems (see Section 6.4).

Furthermore, the nonlinear refractive index (n_2) per single TMDC ML due to trion-polaritons is estimated to exceed by 3 to 5 orders of magnitude the Kerr-nonlinearity in bare

TMDCs, graphene and other widely used optical materials (e.g. Si, AlGaAs etc.) in weak light-matter coupling regimes (see Section 6.4.1).

We probe nonlinearities due to neutral exciton-polaritons, which are observed to decrease by more than an order of magnitude with power. Such a result is explained by three-exciton and possibly trion-mediated exciton-exciton scattering processes (see Section 6.5).

The results are in good agreement with a theory provided by Dr. O. Kyriienko, Dr. V. Shahnazaryan and Prof. I. A. Shelykh, which accounts for the composite nature of excitons and trions and deviation of their statistics from that of ideal bosons and fermions (see Appendix A).

The results shown in this chapter and in the respective Appendix A are published in Reference [146].

6.2 Sample characterisation

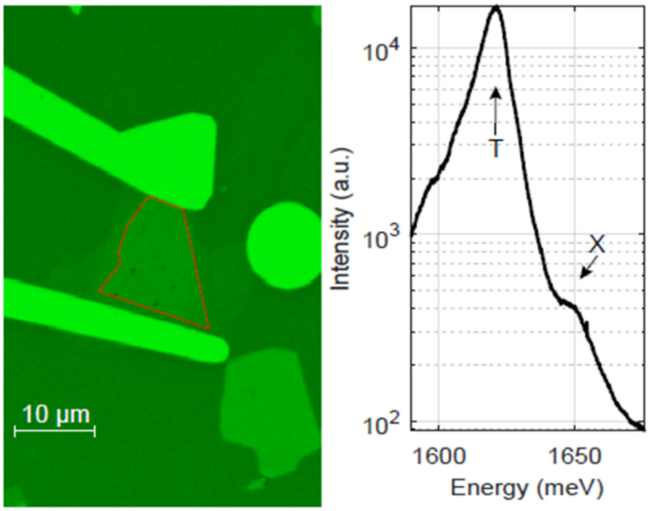

Fig. 6.1 **Left panel**: bright field image of the $MoSe_2$ flake, highlighted with a red border, encapsulated in hBN and clamped with two golden contacts on top of the planar mirror, using the green filter provided within the optical microscope shown in Figure 4.1. **Right panel**: PL emission of the flake under off-resonant He-Ne excitation with exciton (X) and trion (T) peaks highlighted, in the half-cavity configuration (no concave mirrors on top of the flat DBR). The observed order of magnitude difference for the intensity of the PL of the trion relative to the exciton arises from fast neutral exciton to trion states relaxation processes due to scattering with phonons and electrons.

In this experiment, as mentioned in Section 6.1, we employed a brand new ML of $MoSe_2$ covered with a single layer of hBN, to protect it from contamination (see Figure 6.1, left panel). The heterostructure of hBN/$MoSe_2$ was fabricated using the standard mechanical exfoliation technique described in Section 2.2.2.1 and dry transfer methods. To subsequently form the microcavity, the hBN/$MoSe_2$ structure was positioned on top of a planar DBR consisting of 13 pairs SiO_2/Ta_2O_5 quarter-wave layers. Figure 6.1 (right panel) shows the spectrum of PL emission from the ML. The strong peak at lower energy $\sim 1.62\ eV$ arises from the trion (T) emission due to the natural doping in the sample, while the weaker peak at $\sim 1.65\ eV$ corresponds to neutral (X) excitons.

Once the bare $MoSe_2$ ML was optically characterised, a cavity scan was performed in order to observe coupling of cavity photons with excitonic resonances under off-resonant excitation, specifically using the He-Ne laser, as already fully described in Section 5.3.1.

In Figure 6.2 (left panel), the lower, middle and upper polariton branches (labelled as LPB, MPB and UPB, respectively) are observed due to the strong coupling of the photon mode with T and X, respectively. The peak polariton positions (red dots in Figure 6.2, right panel) were fitted using the model of three-coupled oscillators described in Section 5.3.1. We started by fitting this model to the experimental data shown in Figure 6.2, and obtained the following values for the ground LG_{00} mode: $E_X = 1646.0 \pm 0.5\ meV$, $E_T = 1621.2 \pm 0.5\ meV$, $\hbar\Omega_X = 17.2 \pm 0.5\ meV$, and $\hbar\Omega_T = 5.8 \pm 0.5\ meV$. Using these parameters, we can plot polariton resonances and Hopfield coefficients for the different values of cavity resonance energies E_C expressed as a cavity-exciton detuning (δ_{C-X} in Figure 6.2). Note that this three-oscillator model is valid for the low-density case. In the high-density regime, as we are going to discuss in Section 6.5, the nonlinearity quenches photon-trion coupling, and the polariton system can be described by the two-oscillator model outlined in Section 1.2.2.

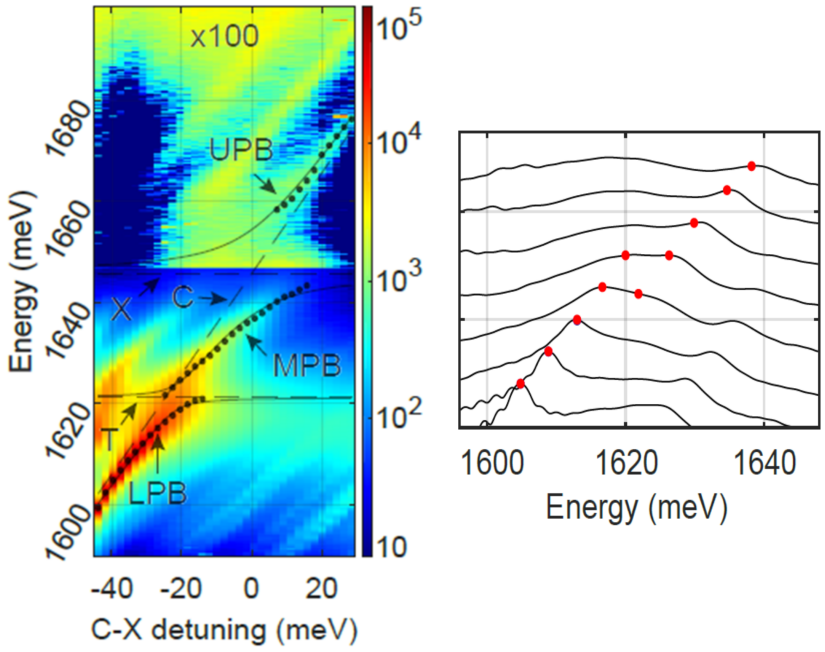

Fig. 6.2 **Left panel**: PL emission as a function of the detuning between the bare cavity LG_{00} mode (C) and exciton (X) plotted on a logarithmic colour scale; black points (dots) are experimental peak positions of the polariton resonances extracted from the fitting of experimental spectra at each detuning with a Gaussian; solid lines are theoretical polariton branches. Higher order transverse LG_{mn} modes are also observed on the left and right-hand side of the LG_{00} polariton states. **Right panel**: normalised PL spectra around trion resonance, showing anticrossing behaviour.

6.3 Polariton nonlinearity

In order to probe the polariton nonlinearity, the polaritons were excited resonantly using the laser with $100-fs$ pulse duration described in Section 4.2.2. The excited polaritons then decay via photon emission through the DBRs with a rate $\gamma_C \cdot |C|^2$ given by the cavity mode linewidth $\gamma_C \sim 0.4\ meV$ ($|C|^2$ is the photonic fraction) or are absorbed in the 2D material with a rate given by the polariton linewidth γ_{pol} ($\gamma_{pol} \sim 3-5\ meV >> \gamma_C \cdot |C|^2$) due to scattering with exciton disorder, resulting in creation of an exciton-trion reservoir (see Figure 6.3). Measurements of the intensity of transmitted light enable us to estimate the polariton density excited inside the microcavity and the density of the reservoir. Monitoring the energy shift of the polariton resonance with increasing pump power, we observe the influence of interaction between polaritons and the exciton-trion reservoir (see Figure 6.3), and can extract the strength of exciton- and trion-based nonlinearity.

The scattering of polaritons by the excitonic disorder potential (which we estimate in the order of $10-15$ *meV* from the inhomogeneous linewidths of exciton/trion emission) effectively populates the reservoir states [147, 148, 149, 150] with a scattering rate of the order of the polariton linewidth γ_{pol}. The polariton nonlinearity is driven by the total density of excitons and trions n_{tot} excited in the system with a single pulse, i.e excitons and trions due to polariton density and due to the reservoir. By measuring the total number of photons transmitted through the microcavity in a single pulse n_{phot}, we can deduce this density as

$$n_{tot} = n_{phot} \cdot \left(|X|^2 + |T|^2 + \frac{\gamma_{pol}}{\gamma_C \cdot |C|^2} \right) \tag{6.1}$$

Here $|X|^2$, $|T|^2$, $|C|^2$ are exciton, trion and photon fractions of polaritons. The bare cavity mode linewidth $\gamma_C \sim 0.4$ *meV* corresponds to the photon lifetime of $\tau_C \sim 3$ *ps*. The third term in Equation 6.1 is dominant. It describes the ratio of absorbed to radiatively escaped polaritons as follows from a simple rate equation model, assuming that the lifetime of the reservoir is much longer than the cavity photon lifetime and that there is no backscattering from the reservoir to polariton states. Indeed, suppose the density of polaritons excited with a short $100-fs$ pulse in the cavity is equal to N. This density may decay in the system by absorption due to scattering into the reservoir or by escape through the Bragg mirrors. The absorption rate into the reservoir is given by $dn_R/dt = N/\tau_R$, where the scattering rate $1/\tau_R = \gamma_{pol}/h$, since $\gamma_{pol} >> \gamma_C$ and n_R is the density of polaritons absorbed into the reservoir. The escape rate into free space through the Bragg mirrors is given by $dn_{phot}/dt = N/\tau_C$, where $1/\tau_C = |C|^2 \cdot \gamma_C/h$, and n_{phot} is the detected number of photons normalised to the cavity mode area A. Dividing the two equations above, we obtain $dn_R/dn_{phot} = \tau_C/\tau_R = \gamma_{pol}/(|C|^2 \cdot \gamma_C)$ or $dn_R = \gamma_{pol}/(\gamma_C \cdot |C|^2)\ dn_{phot}$. Integrating this equation over the duration of a single pulse, we obtain the population of the reservoir with respect to the total number of the emitted photons within a single pulse $n_R = \gamma_{pol}/(\gamma_C \cdot |C|^2)\ n_{phot}$, which corresponds to the third term in Equation 6.1.

There is a possibility that we may slightly overestimate the total excited exciton/trion density and hence underestimate polariton nonlinearity if there are backscattering processes from the reservoir to polariton mode. On the other hand, since the absorption rate of the resonantly excited polaritons cannot occur at a rate larger than that given by the measured polariton linewidth γ_{pol}, we exclude an experimental underestimation of n_{tot} and hence overestimation of polariton nonlinearity.

Finally, we note some uncertainty of $\sim 20\%$ in the deduction of the the total excited exciton/trion density may arise from the deduction of polariton linewidths of the transmission spectra. While the trion-polariton spectra in Figure 6.6 can be well fitted with a Gaussian

profile, the fitting of the neutral exciton-polariton spectra in Figure 6.10 (panels a and b) is not perfect, where the tails of the polariton spectra cannot be accounted for by a simple Gaussian form. This uncertainty in γ_{pol} could lead to the $\sim 20\%$ uncertainty of the absolute values of the polariton nonlinear coefficients.

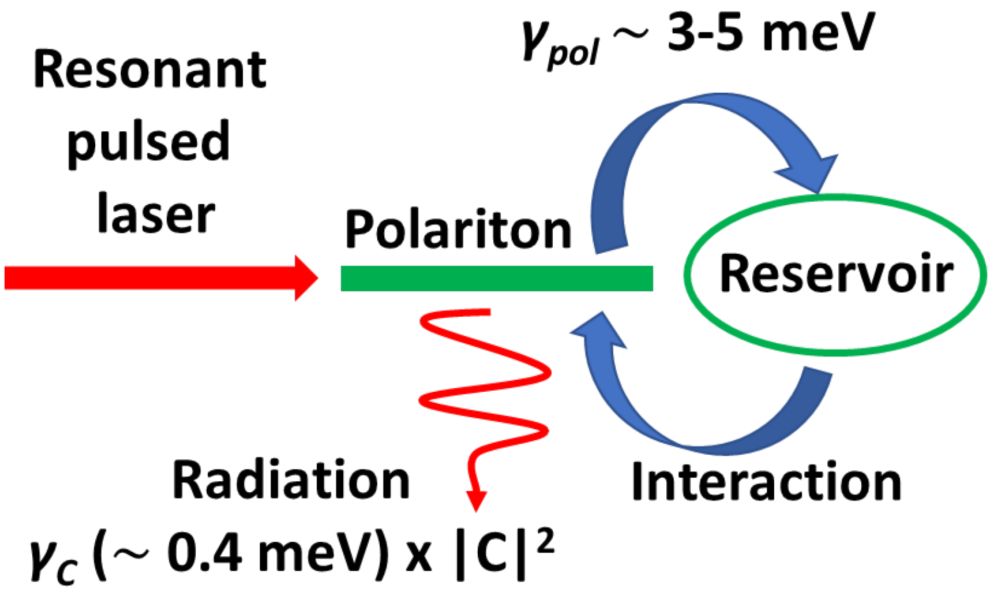

Fig. 6.3 Schematic showing emission and absorption of driven polariton resonance and interactions with the reservoir of trions and excitons.

To deduce n_{tot}, one has to measure the number of photons n_{phot} emitted by the cavity in a single pulse after the resonant excitation with the $100-fs$ pulsed laser. To do that, we shifted the position of the photon mode to the very negative detuning about 10 nm below the trion level and ramped up the power of the laser, so that the power of the light transmitted through the microcavity is about 50 nW. The corresponding photon counts of the transmitted light on the CCD were measured as a reference value. By relating the measured photon counts of light emitted by polariton microcavity to this reference value, it is possible to deduce the average power of the polariton emission in W, I_{pol}. The density of photons emitted by microcavity in a single pulse is then calculated as

$$n_{phot} = \frac{I_{pol}}{f \cdot \hbar\omega \cdot A} \tag{6.2}$$

where $\hbar\omega$ is the polariton energy, $f = 10^3\ Hz$ is the repetition rate of our pulsed laser and $A \approx 3\ \mu m^2$ is the mode area. Importantly, the very low repetition rate of our laser prevents

the effect of dark exciton/trion reservoir excited in previous pulses.

The bare cavity mode decay rate (γ_C) was deduced from the temporal decay of the emission intensity of the bare LG_{00} mode (without the flake in the cavity) excited resonantly with $100-fs$ pulse. The measurements were performed using the streak-camera described in Section 4.2.4, with the resolution time of 2 ps (see Figure 6.4). We obtained the experimental cavity lifetime of approximately 3 ps, which corresponds to the FWHM of the bare cavity mode $\sim 400\ \mu eV$, the value we measured on the spectrometer.

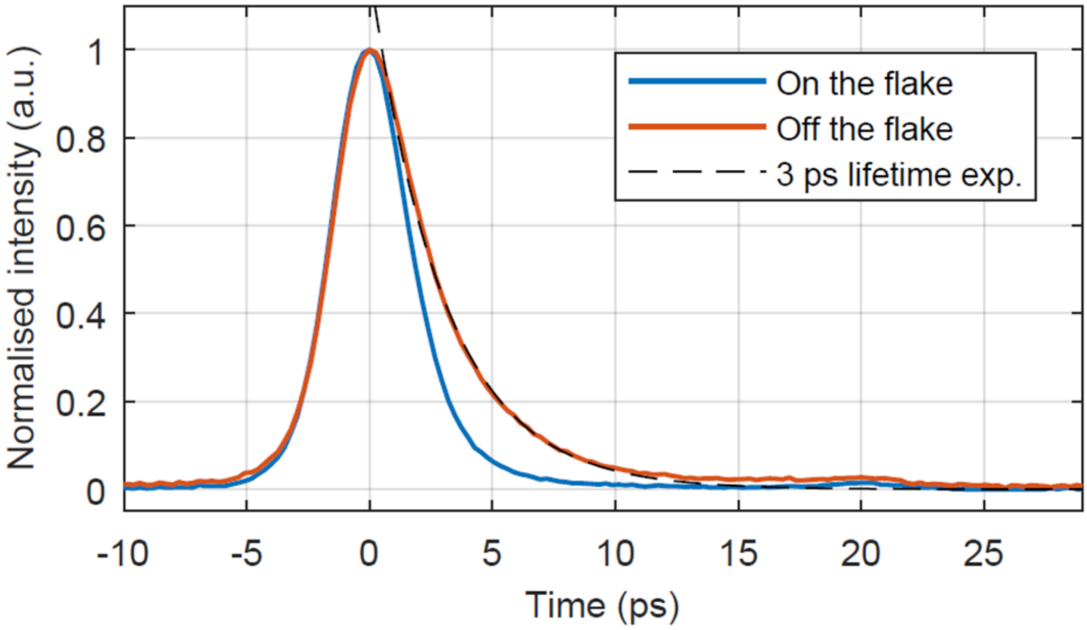

Fig. 6.4 Microcavity lifetime measured using the streak camera described in Section 4.2.4. Blue response measured with resonant transmission of a $100-fs$ pump pulse, when the cavity was on the flake. Orange curve corresponds to the bare cavity, off the flake, with no active region. Note that the detected signal profile is limited by the streak camera resolution of $1-2$ ps and possible laser pulse jitter.

6.4 Trion-polariton nonlinearity

We first present the results for interacting trion-polaritons. In this experiment, the laser energy was fixed at approximately the trion level, $E_p = 1.62\ eV$ and the transmission spectrum was recorded as the energy of the photon LG_{00} mode is scanned through the trion resonance.

Since the linewidth of the pulsed laser ($\sim 15\ meV$) is significantly larger than the observed photon-trion Rabi splitting of $\hbar\Omega_T \sim 5.8\ meV$, it was possible to inject a similar number of polaritons in the vicinity of the trion resonance for each cavity mode position. Excitation of the UPB is negligible, since it is located at energies more than $\sim 30\ meV$ above the trion-polariton states.

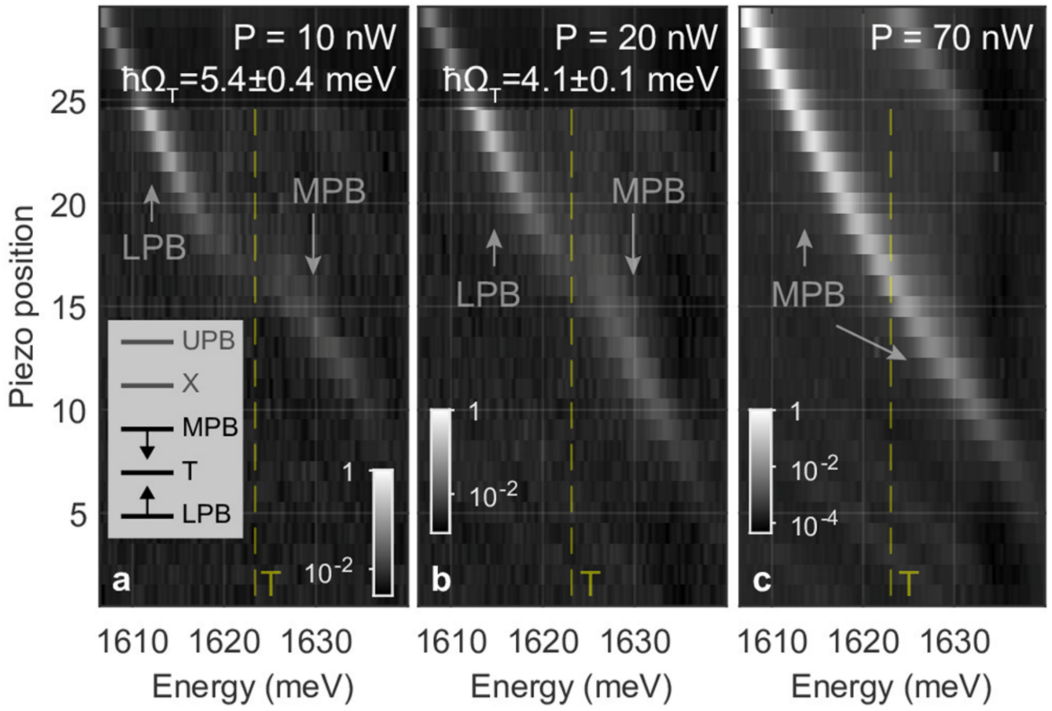

Fig. 6.5 Cavity scan of the LG_{00} mode across the trion resonance for different pump powers: (**a**) 10, (**b**) 20, and (**c**) 70 nW, respectively. The peak energy of the pump laser is fixed at $\sim 1.62\ eV$. Pseudo-colour scale is logarithmic. Estimates for the trion Rabi splittings are obtained by fitting extracted peak positions for each piezo step with a coupled oscillator model. **Inset**: schematic diagram showing how the energies MPB and LPB renormalise in the case of phase-space filling effect, leading to reduction of the Rabi splitting between the trion level and the bare photon mode.

Figure 6.5 shows the results of three cavity scans performed for different pump powers. At the lowest pulse power, $10\ nW$ (Figure 6.5, panel a), an anticrossing between the cavity mode and the trion level is clearly observed, as in the case under the non-resonant excitation. With an increase of the pump power, the photon-trion Rabi splitting is reduced (Figure 6.5, panel b), leading to the the blueshift and redshift of the LPB and MPB states in the vicinity of the trion resonance (Figure 6.5, inset in panel a), respectively. At $P = 70\ nW$, no anticrossing

is observed (Figure 6.5, panel c), with the MPB and the LPB merging together and forming a single polariton branch.

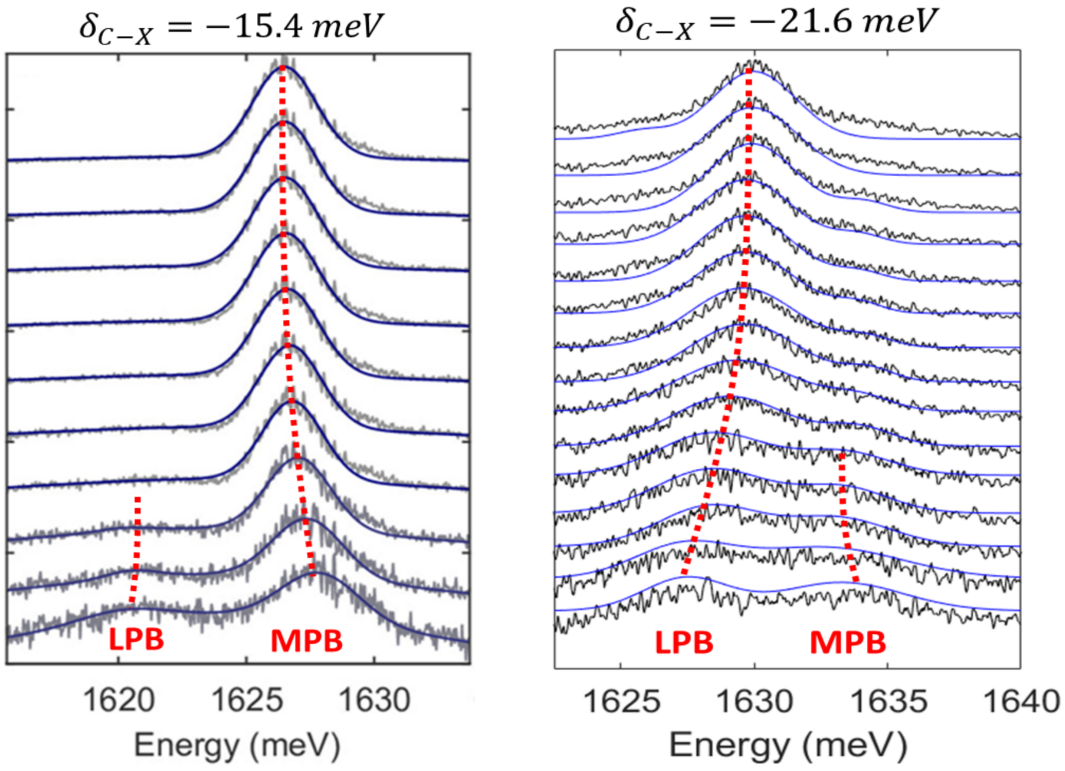

Fig. 6.6 Spectra of the MPB and LPB for the excitation power from 5 to 50 nW (power increases from bottom to top) for detuning $\delta_{C-X} = -15.4\ meV$ (**left panel**) and $\delta_{C-X} = -21.6\ meV$ (**right panel**). The MPB and LPB peaks are fitted with Gaussians. The fitting of the exciton-like LPB peak (lower energy peak) is performed for the first 4 and 5 powers respectively, since it becomes broad and weak at higher densities and the fitting procedure is not reliable.

To quantify the strength of the nonlinearity, we recorded the spectra of the transmitted light as a function of pump power at a fixed photon mode energy near the trion resonance (Figure 6.6), at a fixed photon-exciton detuning, $\delta_{C-X} = -15,4\ meV$ and $\delta_{C-X} = -21.6\ meV$, for left and right panel of Figure 6.6, respectively. Specifically, in the left panel of Figure 6.6, two peaks are observed at low power of 5 nW; the MPB peak has a higher intensity due to the higher photonic fraction. With increase of the pulse power, the MPB peak exhibits a fast redshift. The intensity of the trion-like LPB quickly reduces down to zero with power, due to reduction of its photon fraction as the strong trion-photon coupling collapses. Conversely, in

the right panel of Figure 6.6, for more negative detuning, we can clearly see the blueshift of the LPB for increasing pump powers.

The collapse of the strong coupling is driven by the population of both polaritons inside the cavity and reservoir, determining the total density of excited excitons and trions n_{tot} (see Equation 6.1). The reservoir may consist of localised or dark exciton/trion states as well as high-momenta trions degenerate with trion-polariton resonances [120, 145]. For the case of resonantly driven trion-polaritons, n_{tot} is dominated mostly by the trion density n_T ($n_{tot} \approx n_T$), since the peak of the exciton density of states is blue-detuned by $\sim 30\ meV$ from the trion.

The Hopfield coefficients used in Equation 6.1 for the total reservoir density also have to be determined for each pump power, since the change of cavity-trion (or cavity-exciton, in Section 6.5) Rabi splitting would change these values. To illustrate this, we fix the cavity-exciton Rabi splitting and plot theoretical peak positions of LPB and MPB modes as a function of cavity-trion Rabi splitting, which is shown in Figure 6.7 (top panel) for the cavity mode-exciton detuning used in Figure 6.6 (left panel). The theoretical dependence of the photonic fraction of the polariton branches on the cavity-trion Rabi splitting is shown in Figure 6.7 (middle panel). Combining these two sets of data, one can produce the "calibration" dependencies of the Hopfield coefficients. The photonic fractions $|C|^2$ vs MPB and LPB energies are shown in Figure 6.7 (bottom panel). This can be used to infer the values of the actual Hopfield coefficients of the MPB in Figure 6.8 for each pump power. This method is valid since in the experiment the cavity-trion Rabi splitting is completely quenched before any effect is seen on the cavity-exciton Rabi splitting. Thus, to deduce the total reservoir density, we first determined the peak position of the MPB mode by fitting each measured spectra, and then, using this value, we determined effective photon, exciton, and trion fractions of the MPB mode from the calibration curves. Finally, the total reservoir density for each pump power was calculated using Equation 6.1.

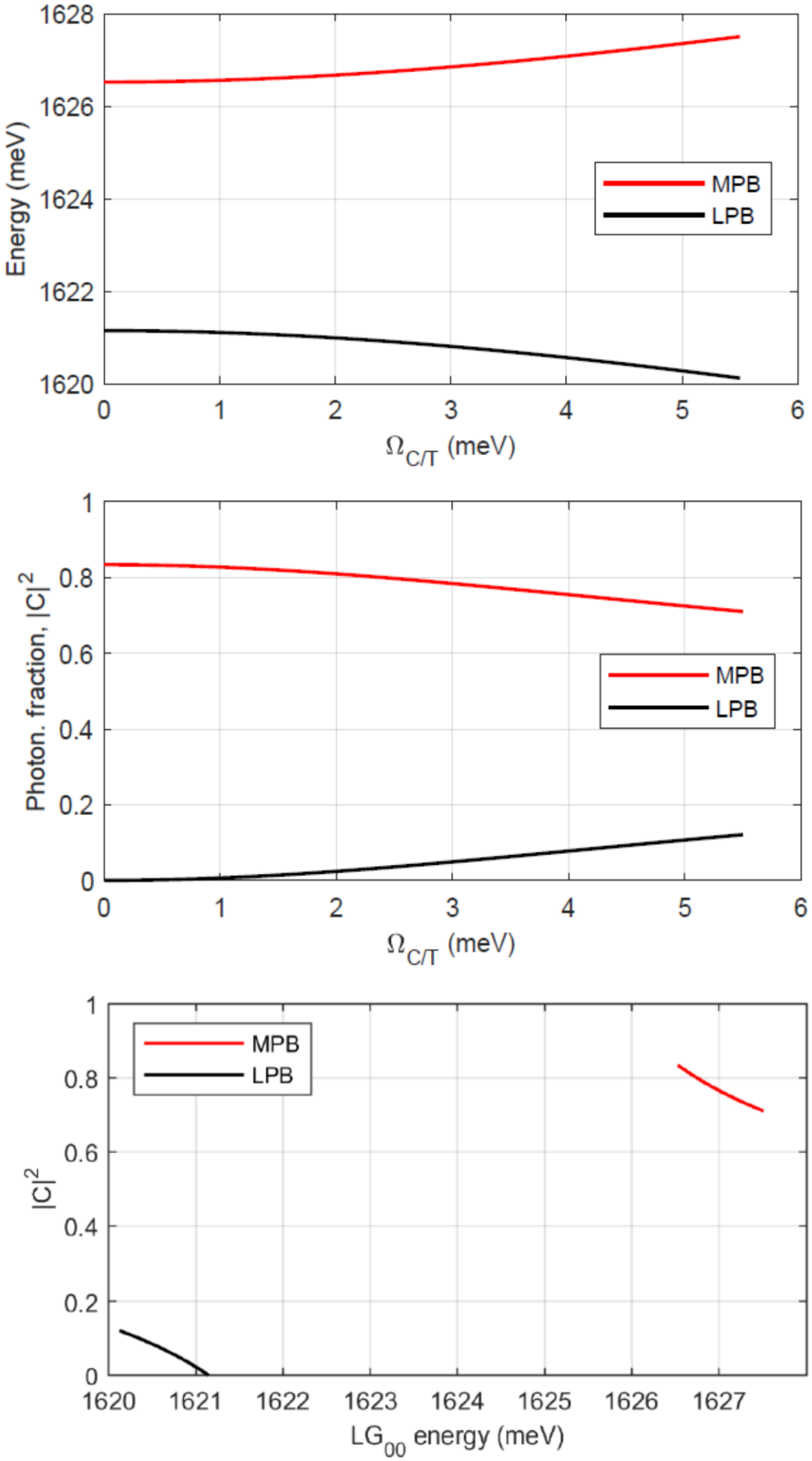

Fig. 6.7 **Top panel**: LG_{00} peak positions as function of $\hbar\Omega_{C/T}$ at a fixed cavity detuning, $\delta_{C-X} = -15.4\ meV$. **Middle panel**: photonic fraction, $|C|^2$, of the MPB and LPB as function of $\hbar\Omega_{C/T}$ at a fixed cavity detuning, $\delta_{C-X} = -15.4\ meV$. **Bottom panel**: Combined $E_{LG_{00}}$ vs $|C|^2$ calibration curves for MPB and LPB for a fixed cavity detuning, $\delta_{C-X} = -15.4\ meV$.

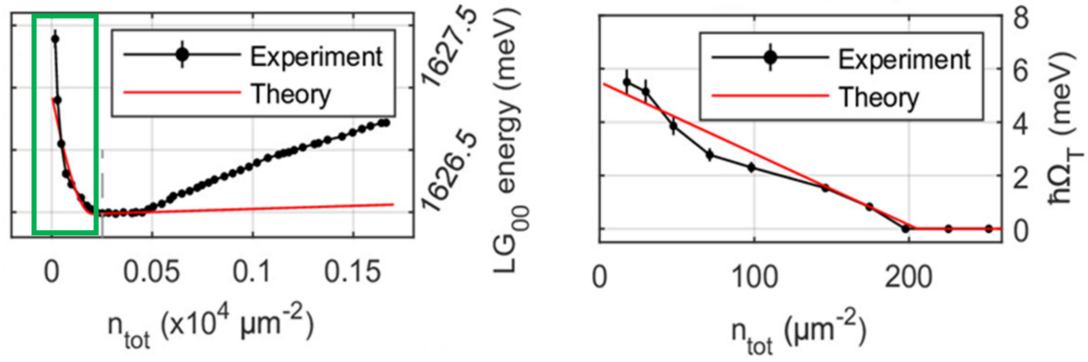

Fig. 6.8 **Left panel**: extracted peak positions of the MPB mode vs estimated total exciton-trion density, for $\delta_{C-X} = -15.4\ meV$. **Right panel**: trion-polariton Rabi splitting vs exciton-trion density (range highlighted by green box in left panel). Red solid curves in both panels correspond to the theoretical modelling results. The error bars (95% CI) are estimated taking into account the random error in determination of the peak positions in Figure 6.6 (left panel) as well as possible systematic error ($\Delta\Omega_T = 0.5\ meV$) due to the uncertainty of the fitting parameters in the coupled oscillators model.

Figure 6.8 (left panel) shows that the MPB energy shifts rapidly to the red wavelengths with n_{tot} at densities $n_{tot} < 2 \cdot 10^2\ \mu m^{-2}$ and then exhibits a plateau corresponding to the quenching of the trion-photon coupling, followed by a gradual increase. From the redshift of the MPB branch in Figure 6.8 (left panel, green box), we plot the value of the Rabi splitting $\hbar\Omega_T$ vs n_{tot} in Figure 6.8 (right panel). The collapse of trion-photon coupling occurs at a small density of $n_{tot} \sim 2 \cdot 10^2\ \mu m^{-2}$ very close to half the estimated density of free electrons $n_e/2 \approx 2 \cdot 10^2\ \mu m^{-2}$ (see Section A.3.2). Remembering that the effective strength of the trion-polariton nonlinearity β_T^{eff} responsible for the quenching of strong coupling (and large energy shifts) is defined by Equation 1.23 [28], in the first order approximation β_T^{eff} can alternatively be related directly to the redshift of the MPB branch in Figure 6.8 (left panel) as follows

$$\beta_T^{eff} = -\eta_T \frac{\delta E_{MPB}}{\delta n_{tot}} \tag{6.3}$$

where $\eta_T = \sqrt{\delta_{P-T}^2 + (\hbar\Omega_T)^2}/(\hbar\Omega_T/2)$ and $\delta_{P-T} = +5.3\ meV$ is the energy detuning between the trion energy level and the LPB arising from coupling between the photon and the neutral exciton only for $n_{tot} < 2 \cdot 10^2\ \mu m^{-2}$. In Equation 6.3, the minus sign explicitly accounts that Rabi frequency is decreasing function of density. From Figure 6.8, we deduce an average value of $\beta_T^{eff} \simeq 37 \pm 3\ \mu eV \cdot \mu m^2$ (further details from Figure 6.9). Note that the $3\ \mu eV \cdot \mu m^2$ error above is a random error arising from the uncertainty in $\hbar\Omega_T$ in Figure 6.8

(right panel) and does not include possible systematic error, as discussed in Section 6.3.

To explain the observed result, we account for phase-space filling effects, which become important at increasing excited trion density (see Section A.3). This leads to the quenching of the collective trion oscillator strength: as more and more trions are excited in the system, the extra injected photons have less electrons and trions to couple to and to form trion-polaritons. As a result the collapse of strong photon-trion coupling occurs at the density of excited trions equal to half the density of available free electrons, $n_T \approx n_e/2$. The results of the theoretical modelling (see Appendix A) are shown by the red solid curves in Figure 6.8, reproducing the experimental redshift of E_{MPB} and the corresponding reduction of $\hbar\Omega_T$. Overall, the trion Rabi splitting can be approximated as

$$\Omega_T(n_T) = \Omega_T(0)\left(1 - \frac{n_T}{n_e/2}\right) \tag{6.4}$$

and the value of theoretical nonlinearity is then given by

$$\beta_T^{eff} = \frac{\hbar\Omega_T(0)}{n_e/2} \approx 30\ \mu eV \cdot \mu m^2 \tag{6.5}$$

for $n_e \approx 400\ \mu m^{-2}$ and $\hbar\Omega_T(0) \approx 5.8\ meV$ (see Section A.3.5), in agreement with the experimental value of $37 \pm 3\ \mu eV \cdot \mu m^2$. It is the low electron density and high oscillator strength per single trion (large $\hbar\Omega_T(0)$), that lead to the high value of trion-polariton nonlinearity.

In the first order approximation, our theory predicts a constant value of β_T^{eff} with density, or, in other words, a linear reduction of the trion-polariton Rabi-splitting with density (see Section A.3). As it is seen in Figure 6.8 (right panel), there is a good qualitative agreement between the dependence of the trion Rabi splitting and the theoretical prediction as a function of trion density: the experimental average value of $\beta_T^{eff} = 37 \pm 3\ \mu eV \cdot \mu m^2$ is in quantitative agreement with the theoretical estimate of $30\ \mu eV \cdot \mu m^2$. Nevertheless, it is seen that the experimental points in Figure 6.8 (right panel) are not precisely positioned on the straight theoretical line. This is reflected by the fact that the experimental values of β_T^{eff} (deduced from the experimental data in Figure 6.8, right panel) vary from 120 to 20 $\mu eV \cdot \mu m^2$ over the density range n_{tot} from 0 to 200 μm^2, which is shown in Figure 6.9. We believe that this variation of β_T^{eff} with n_{tot} observed in the experiment may arise from the higher order effects due to composite nature of trions, not included in the theoretical treatment (see Section A.3).

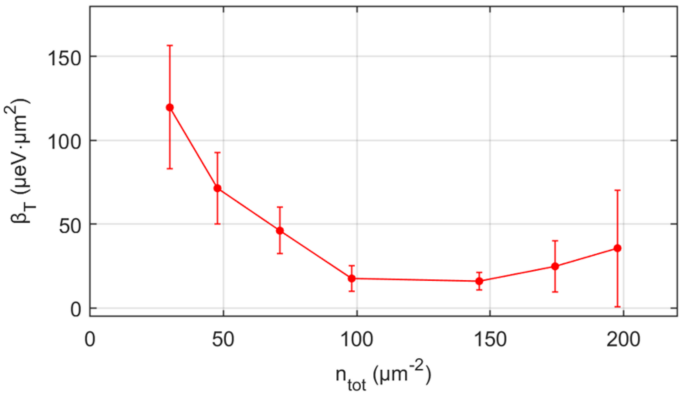

Fig. 6.9 β_T^{eff} as a function of n_{tot}. The error bars are 95% CI deduced taking into account the random error in the determination of the trion-polariton peak position at each power from the fitting procedure.

6.4.1 Nonlinear refractive index n_2 due to trion-polaritons

6.4.1.1 Nonlinear refractive index n_2 of hybrid microcavity-$MoSe_2$ polariton system

We note that applications of 2D materials imply that they would be integrated into photonic structures made of bulk semiconductors/dielectrics. Therefore, when characterising nonlinear optical properties of 2D materials, it is useful to consider the nonlinearity of the whole hybrid 2D materials-semiconductor/dielectric photonic system and compare it with that of bulk photonic materials.

In order to compare trion-polariton nonlinearity with Kerr-like optical nonlinearity observed in bulk materials, we can treat our open-access microcavity (MC) system with embedded $MoSe_2$ as a microcavity filled with a bulk of some nonlinear optical material, characterised by the effective nonlinear refractive coefficient $n_2(MC)$. The $n_2(MC)$ coefficient due to trion-polariton nonlinearity can be estimated taking into account the effective optical path covered by a photon during the round trip between the two mirrors of the microcavity, which must be equal to an integer number of polariton wavelengths

$$2\left(n_{eff}+n_2(MC)\,\frac{N_{pol}\,h\,c^2}{L_{cav}\,\lambda}\right)L_{cav}=m(\lambda+\delta\lambda) \tag{6.6}$$

Here n_{eff} is the effective refractive index of the microcavity, N_{pol} is the total number of polaritons excited inside the MC with a single pulse, L_{cav} is the effective cavity length, λ is the wavelength of the trion-polariton emission in free space, $\delta\lambda$ is the nonlinear shift of trion-polariton resonance, m is the order of the longitudinal cavity mode coupled with the

trion. $2\ n_2(MC)\ (N_{pol}\ h\ c^2)/(L_{cav}\ \lambda)\ L_{cav}$ is the nonlinear optical path acquired by photon during the round trip between the two mirrors. Given absorption is the dominant process in our system, $N_{pol} \approx n_{tot}$. Using Equations 6.3 and 6.6, we get the following expression

$$n_2(MC) = \frac{n_{eff}\ L_{cav}\ \beta_T^{eff}\ \lambda^2}{h^2\ c^3\ \eta_T} \tag{6.7}$$

Taking into account the effective cavity refractive index $n_{eff} \approx 1$ (since most of the cavity electromagnetic field is confined in the gap between the two mirrors), the wavelength of the trion-polariton resonance $\lambda \approx 760\ nm$, the effective cavity size $L_{cav} \approx 1\ \mu m$, $\beta_T^{eff} = 37\ \mu eV \cdot \mu m^2$ and $\eta_T = 2$ ($\delta_{P-T} = 0$), we estimate $n_2(MC) \sim 1.4 \cdot 10^{-13}\ m^2/W$. This $n_2(MC)$ is about four to five orders of magnitude larger than $1.82 \cdot 10^{-17}\ m^2/W$ in planar AlGaAs-waveguides in the weak coupling regime [31] and $6 \cdot 10^{-18}\ m^2/W$ in silicon [32] and InGaP [33], which have been used in a suspended membrane photonic crystal geometry. Kerr nonlinear effects (optical bistability) have been investigated in slab photonic crystal Si microcavities with an embedded graphene layer [151]. The effective n_2 of a hybrid graphene-Si microcavity system has been derived to be of the order $n_2 \simeq 7.7 \cdot 10^{-17}\ m^2/W$, which is $\sim 3-4$ orders of magnitude less than $n_2(MC)$ due to trion-polariton nonlinearity. Finally, we note that the value $n_2(MC) \sim 1.4 \cdot 10^{-13}\ m^2/W$ due to trion-polariton nonlinearity is an order of magnitude higher than $n_2 \sim 1 \cdot 10^{-14}\ m^2/W$ reported in a neutral exciton-polariton GaAs-based system [10].

6.4.1.2 Effective nonlinear refractive index $n_2(MoSe_2)$ per single TMDC monolayer arising from trion-polariton nonlinearity

To the best of our knowledge, no Kerr-like nonlinear optical effects were studied in microcavities with embedded TMDC materials in the weak light-matter coupling regime. However, there were several studies of the effects associated with Kerr-like optical nonlinearity of bare layers of TMDCs and graphene in the weak light-matter coupling regime on a picosecond timescale [152]. The values of n_2 coefficients for TMDCs layers were measured in the range $10^{-16} - 10^{-17} m^2/W$ depending on the excitation energy (above or below bandgap). The reference [153] reports the n_2 coefficient for WS_2 monolayer to be about $1.1 \cdot 10^{-15}\ m^2/W$ The value of the n_2 coefficient for pure graphene flakes was measured about $2 \cdot 10^{-15}\ m^2/W$ [152]. The reference [151], which studied a nonlinear hybrid Si-graphene microcavity, deduced an n_2 coefficient for a single graphene layer to be of the order $10^{-13} m^2/W$.

In our trion-polariton microcavity system, we can derive the effective nonlinear refractive index $n_2(MoSe_2)$ per single TMDC monolayer taking into account that in reality the

nonlinear optical phase is acquired by light only on the passage of the monolayer during the round trip between the mirrors. Therefore, $n_2(\mathrm{MoSe_2})$ can be simply obtained by normalising $n_2(MC)$ to d_{MoSe_2}/L_{cav}, where $d_{MoSe_2} \sim 1\ nm$ is the $\mathrm{MoSe_2}$ thickness, yielding $n_2(MoSe_2) \sim 1.4 \cdot 10^{-10}\ m^2/W$. This value is at least five (three) orders of magnitude larger than in TMDC 2D materials (graphene) studied in the weak light-matter coupling regime without formation of polaritons.

6.5 Exciton-polariton nonlinearity

Next, we studied the neutral exciton-polariton nonlinearity, which may arise from (see Section 1.2.3):

1. the reduction of exciton-photon Rabi splitting $\hbar\Omega_X$, and/or
2. the blueshift of the neutral exciton level E_X.

Mechanism (1) is characterized by the rate of reduction of the Rabi splitting $\hbar\Omega_X$ with exciton density, as already shown by Equations 1.23 and 6.3. Mechanism (2) is characterised by the rate of the blueshift of the exciton level with exciton density, as already shown by Equation 1.22. Similarly to what was done in Section 6.4, assuming that only mechanism (2) contributes to polariton blueshift, g_X^{eff} can be related to the polariton energy shift [28]:

$$g_X^{eff} = \xi_X \frac{\delta E_{MPB}}{\delta n_{tot}} \tag{6.8}$$

where $\xi_X = [1/2 + \delta_{C-X}/(2\sqrt{\delta_{C-X}^2 + (\hbar\Omega_X)^2})]^{-1}$ is the inverse of the excitonic fraction.

Both mechanisms should lead to blueshift of the MPB. The blueshift of the MPB peak associated with the neutral exciton-polariton nonlinearity is observed in Figure 6.8 (left panel) for $\delta_{C-X} = -15.4\ meV$ at $n_{tot} > 5 \cdot 10^2\ \mu m^2$, above the threshold of strong trion-photon coupling collapse. We further studied neutral exciton-polariton nonlinearity for several photon-exciton detunings in the range from $+8.8\ meV$ to $-2.4\ meV$, where the trion fraction is negligible ($\sim 3\%$ or less). The central laser frequency was shifted to be in resonance with the MPB in each case. Substantial blueshifts of the MPB mode of the order of $2\ meV$ are observed at much higher excitation power in the range from 1 to 9 μW (see Figure 6.10, panels a and c). The MPB energy depends sublinearly on the total exciton/trion density n_{tot}, as shown in Figure 6.10 (panels b and d). In this power range, the density of excited

neutral excitons n_X is much higher than that of trions and n_{tot} is dominated mostly by neutral excitons ($n_{tot} >> n_e$, $n_{tot} \simeq n_X$).

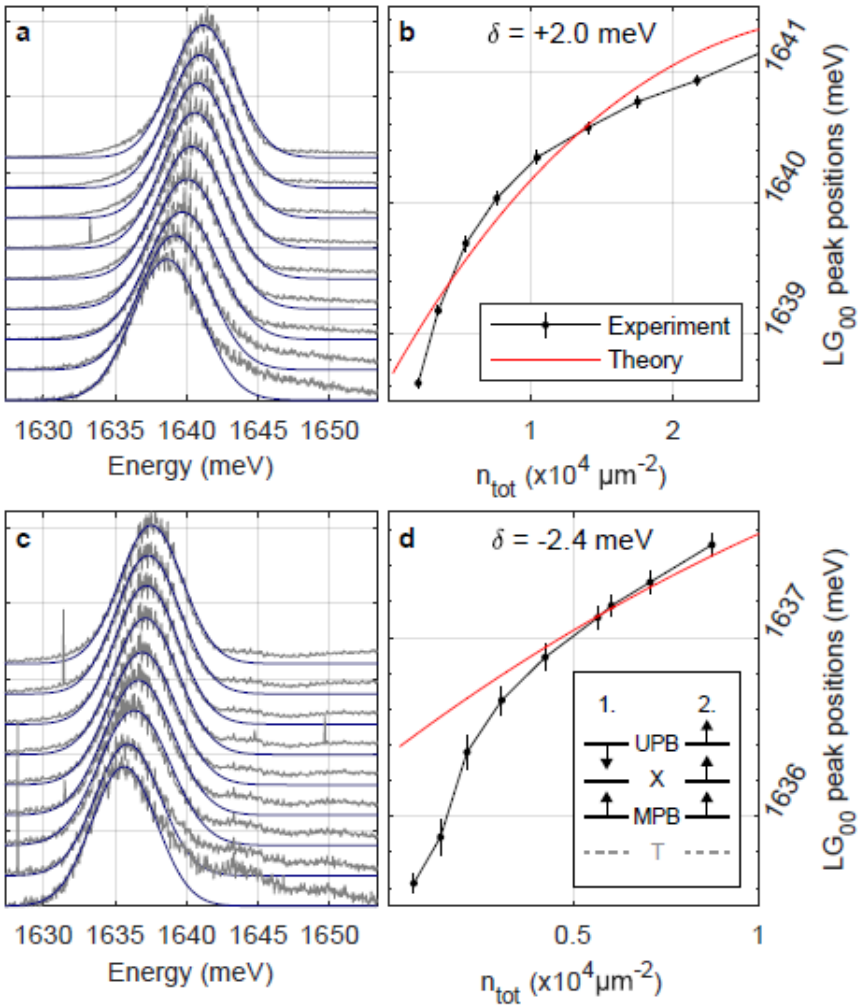

Fig. 6.10 **a, b**: $\delta_{C-X} = +2.0\ meV$. **a**: spectra of the MPB LG_{00} mode for the pump powers from 1 to 9 μW (power increases from bottom to top). **b**: extracted peak positions of the mode vs exciton density. **c, d**: $\delta_{C-X} = -2.4\ meV$. **c**: spectra of the MPB LG_{00} mode for the pump powers from 1 to 9 μW (power increases from bottom to top). **d**: extracted peak positions of the mode vs estimated exciton density. The error bars (95% CI) in b-d are deduced from the fitting procedure in a-c. Red solid curves correspond to the theoretical modelling results. **Inset**: schematic diagrams showing how the MPB and UPB shift in the case of phase-space filling [mechanism (1)], leading to reduction of Rabi splitting between the neutral exciton level and the bare photon mode, and the neutral exciton blueshift [mechanism (2)].

As mentioned above, since the neutral exciton-polariton nonlinearities are weak in comparison to trion-polaritons, they are studied at high pump (in the range from 1 to 9 μW), when the strong coupling between photons and trions is quenched. In this case, the polariton system can now be described by the simpler two-oscillator model presented in Section 1.2.2, which results in two polariton branches UPB and LPB. Separate MPB and LPB do not longer exist, since they recombine into a single MPB. This model is applicable for all polariton densities $> 200\ \mu m^2$, which is the case for all data shown in Figure 6.10 and portion (above $200\ \mu m^2$) in Figure 6.8 (left panel). Using the same approach as discussed in Section 6.4, one can obtain the calibration curves (E_{MPB} vs $|C|^2$) for different cavity mode-exciton detunings by using this two-oscillator model and varying cavity-exciton Rabi splitting. The data for the detunings used in the experiment are summarised in Figure 6.11. Finally, the total exciton density for each exciton-photon detuning is deduced using Equation 6.1 (there, we assume that the trion fraction $T = 0$, since at high excitation density the trion-photon strong coupling is quenched).

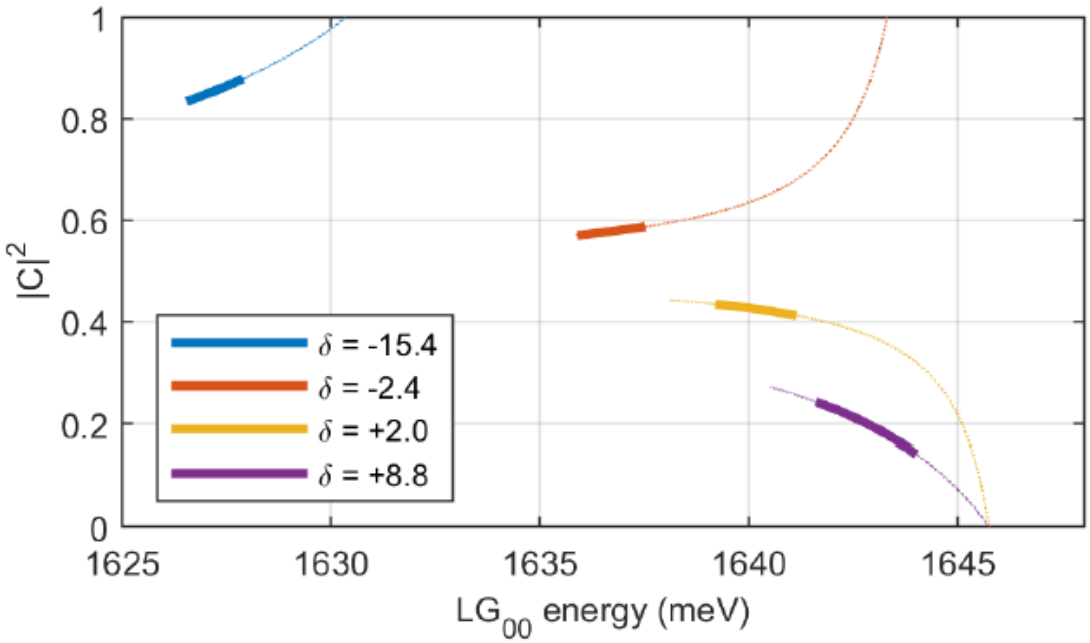

Fig. 6.11 Calibration curves $E_{LG_{00}}$ vs $|C|^2$ for the MPB with a two-coupled oscillator model, obtained by varying the cavity-exciton Rabi splitting from 0 to 19 *meV* for the four experimental cavity-exciton detunings. Bold solid sections of the curves correspond to the experimentally observed ranges of MPB peak positions for the corresponding detunings.

In the experiment, we can measure only the nonlinear behaviour (blueshift) of the MPB. The UPB cannot be measured due to tunability of our laser. Therefore, experimentally we cannot separate the contributions to the neutral exciton-polariton optical nonlinearity from mechanisms (1) and (2). However, assuming that either only mechanism (1) or (2) is responsible for the blueshift of MPB, we can deduce the dependencies of the upper limits of $\beta_X^{eff} = -d(\hbar\Omega_X)/dn_{tot}$ and $g_X^{eff} = dE_X/dn_{tot}$ factors on exciton density [28], respectively. In Figure 6.12 (top panel), we show that the theoretical g_X^{th} parameter is in semi-quantitative agreement with the experimental values of the upper limit of g_X^{eff} in the range of exciton densities $3 \cdot 10^3 < n_{tot} < 3 \cdot 10^4$ μm^{-2}. So, at intermediate densities, the optical nonlinearity arises mainly from the exciton blueshift (Mechanism 2) [28], which is characterised by the parameter $g_X^{eff} = dE_X/dn_{tot}$. The g_X^{eff} is expected to be constant in a system where only pair exciton-exciton interactions are important [28]. By contrast, Figure 6.12 (top panel) shows that the experimental g_X^{eff} decreases with n_{tot} from $\simeq 2-5$ $\mu eV \cdot \mu m^2$ at $n_{tot} \sim 10^3$ μm^{-2} to $\simeq 0.01$ $\mu eV \cdot \mu m^2$ at $n_{tot} \sim 10^5$ μm^{-2}, which suggests the importance of higher-order exciton-exciton interactions. Overall, in TMDC, the neutral exciton-polariton nonlinearity is one to three orders of magnitude lower than that of trion-polaritons. The lower values $\simeq 0.05$ $\mu eV \cdot \mu m^2$ are similar to the values reported in WS_2-waveguide structures, where only very high excitation powers were used [128].

To describe the observed neutral-exciton nonlinearity, we developed a model taking into account the two- and three-exciton exchange processes [29, 154] (see Section A.2). At $3 \cdot 10^3 < n_{tot} < 3 \cdot 10^4$ μm^{-2}, within an experimental error, there is agreement between theory and experiment (Figure 6.12, top panel). The values of g_X^{eff} in exciton density are also in agreement with the values of the exciton-exciton interaction parameter in monolayer WSe_2 characterising excitation induced exciton broadening in the same density range [134]. The theory also qualitatively reproduces the sublinear shifts in Figure 6.10 (panels b and d). At $n_{tot} > 3 \cdot 10^4$ μm^{-2}, our theory is not applicable anymore, since in this case higher-order nonlinearities should be taken into account. By contrast, at $n_{tot} < 3 \cdot 10^3$ μm^{-2}, the model accounting only for exciton-exciton interactions results in the very weak theoretical blueshift of E_{MPB}, much smaller than that observed in the experiment in Figure 6.8 (left panel). This is also reflected in Figure 6.12 (top panel), where at $n_{tot} < 3 \cdot 10^3$ μm^{-2} the theoretical $g_X^{th} \sim 0.3$ $\mu eV \cdot \mu m^2$ is observed to be below the corresponding experimental values $g_X^{eff} \sim 0.5-3$ $\mu eV \cdot \mu m^2$. Such a discrepancy indicates that at these exciton densities the trion-mediated exciton-exciton interactions, which are characterised by increased scattering cross-section and number of exchange processes, might play an important role in the

observed large polariton blueshift (see Appendix A).

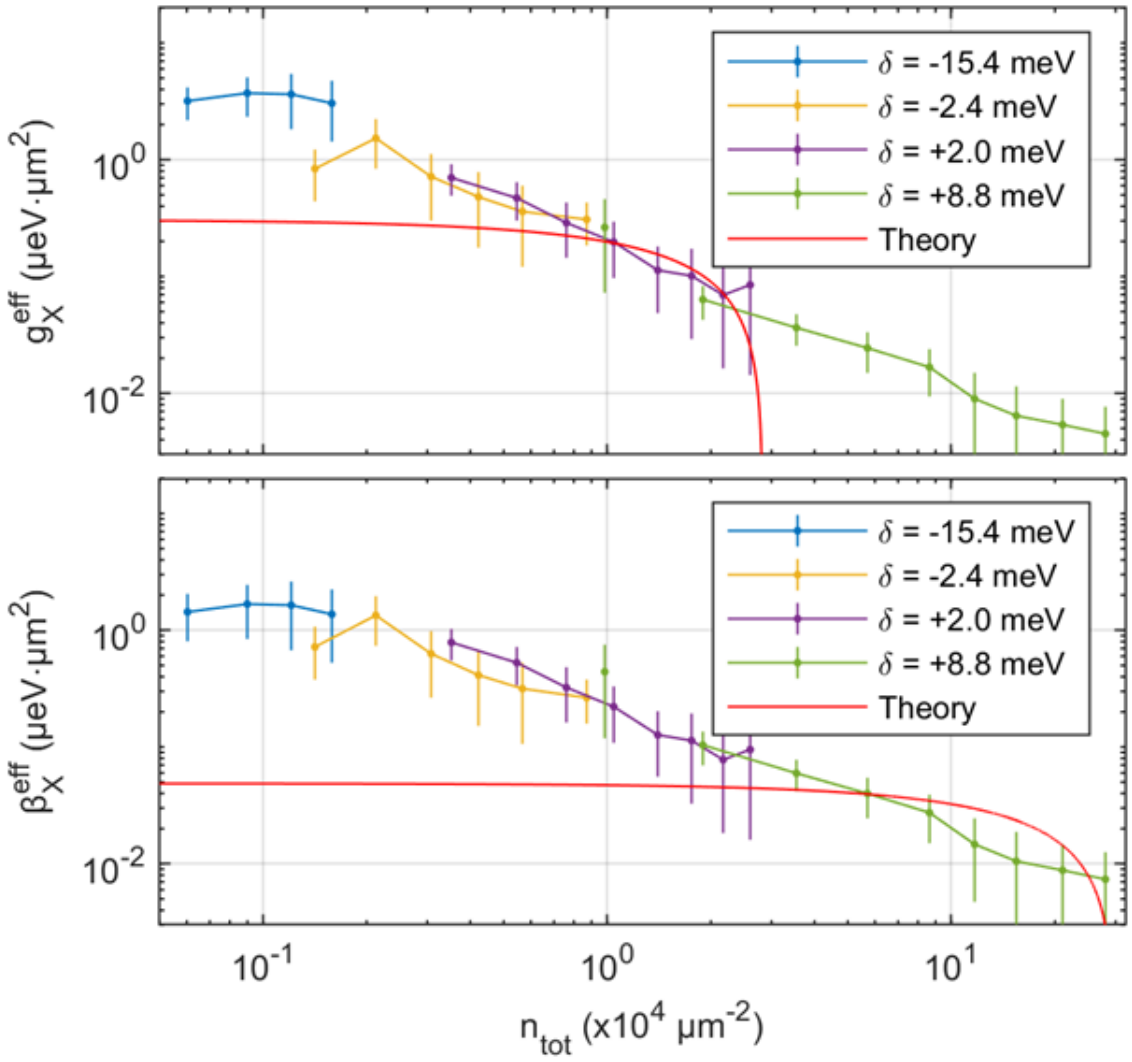

Fig. 6.12 The experimental effective interaction constants g_X^{eff} (**top panel**) and β_X^{eff} (**bottom panel**) as a function of the estimated exciton density, n_{tot}. The data correspond to four different cavity-exciton detunings (δ): $+8.8$ *meV* (olive), $+2.0$ *meV* (purple), -2.4 *meV* (orange), and -15.4 *meV* (blue). The error bars (95% CI) are deduced taking into account errors in determining the MPB peak positions at each pump power (exciton density). The red solid curve corresponds to the theoretical values.

Now, let us assume instead that the Mechanism (1) is the only dominant mechanism over the whole density range. In this case, we can observe that the theoretical β_X^{th}-factor is well below the experimental values of the upper limit of β_X^{eff} at $n_{tot} < 10^4\ \mu m^{-2}$ as shown in

Figure 6.12 (bottom panel). β_X^{th} approaches the experimental values only at higher densities $n_{tot} > 3 \cdot 10^4\ \mu m^{-2}$. Such a discrepancy between the experiment and theory indicates that our assumption is incorrect: phase-space filling for neutral exciton-polaritons [Mechanism (1)] becomes important only at very high exciton densities $n_{tot} > 3 \cdot 10^4\ \mu m^{-2}$, when the average distance between excited excitons is less than $5-6\ nm$ and becomes comparable to the exciton Bohr radius $a_B \sim 1\ nm$. By contrast, Mechanism (2) is the dominant mechanism at intermediate exciton densities $n_{tot} < 3 \cdot 10^4\ \mu m^{-2}$.

6.6 Summary

In summary, the main result shown in this chapter consists in the experimentally measured significant energy shift of trion-polaritons at low photon fluxes under on-resonant 100fs-pulsed excitation. It arises from the phase-space filling effect at the low electron density in our hBN-encapsulated $MoSe_2$ sample due to natural doping, leading to the quenching of the strong coupling. The value of the trion-polariton nonlinearity ($\beta_T^{eff} \approx 37\ \mu eV \cdot \mu m^2$) is 2 to 3 orders of magnitude higher than that related to exciton-polaritons, with the latter that is overall dominated by the exciton resonance blueshift (g_X^{eff}).
From that, it was possible to extrapolate the nonlinear refractive index n_2 per single flake in the strong coupling regime. Its value of $\sim 10^{-10}\ m^2/W$ is $10^3 - 10^5$ times bigger than that previously measured in systems weakly coupled to light [152].

Chapter 7

Nonlinear UV pulse propagation in a GaN-waveguide up to room temperature

7.1 Introduction

As stated in Section 1.1, the small Kerr-like nonlinearity in systems weakly coupled to light is a strong limitation for practical devices, since they should preferably work at low power. GaAs-waveguides in the strong coupling regime have already solved this problem [10], but they still need cryogenic cooling, not ideal for technological applications. Emerging GaN-waveguides [101] are promising to overcome this limitation, thanks to the high binding energy of its excitons. Furthermore, this material operates in the UV spectral range, where currently there is no on-chip platform. Therefore, we aim to study nonlinear properties of exciton-polaritons in GaN-based waveguides.

In this chapter, we present the first experimental measurements of nonlinear UV pulse propagation in a AlInGaN-based device. Our GaN/AlGaN QW polariton waveguide structure allows us to observe strong light-matter coupling and nonlinearity up to room temperature. From the spectral broadening arising from SPM, we deduce an effective nonlinear refractive index three orders of magnitude larger than those measured in other materials commonly used for ultrafast nonlinear optics in the UV [155] which are in the weak light-matter coupling regime. This enables nonlinear effects with three orders of magnitude lower power pulses. Our nonlinearity arises from excitonic interactions with strength comparable to those in polariton devices in other material systems such as GaAs which, however, do not operate in the UV up to room temperature.

First of all, we characterised the polariton resonance under off-resonant excitation through k-space measurements in the GaN-waveguides designed and grown by Dr. J.-F. Carlin and Dr. J. Ciers at the École Polytechnique Fédérale de Lausanne (EPFL), Switzerland. We then injected optical pulses into the waveguide through the grating couplers fabricated by Dr. Z. Zaidi, where they evolve over a length of 100 μm and become strongly modulated, leading to spectral widths at the output up to 80 meV. This spectral broadening, which cannot occur in the linear regime, is the essential signature of pulse temporal envelope modulation [156]. We find that the spectral broadening depends strongly on the detuning of the pulses from the temperature dependent exciton frequency, as expected for an interaction based on strong photon-exciton coupling.

Picosecond nonlinear dynamics are evidenced by the complex broadband spatio-temporal envelopes of the generated light, which are consistent with numerical modelling of the coupled photon-exciton field equations, performed by Dr. A. V. Yulin and reported in Appendix B, as well as FDTD simulation to quantify the coupling efficiency of our system, executed by Dr. P. M. Walker.

The results shown in this chapter and in the respective Appendix B are published in Reference [117].

7.2 Dispersion measurement and fitting

We first confirmed the presence of the strong light-matter coupling regime by studying the waveguide dispersion relation using non-resonant excitation and measuring angle-resolved PL.

For the measurements of dispersion curves the sample was excited at various points between two grating couplers set 200 μm apart (see Figure 7.1, left panel), using a CW He-Cd laser emitting at $\lambda_0 = 325$ nm, i.e. well above the bandgap. So, all polariton states are populated by hot carrier relaxation (see Section 1.2.3.1). Polaritons then propagate to the grating couplers and are scattered out at angles near normal to the sample surface (0° in Figure 7.1, middle and right panel). The incident laser spot for these non-resonant measurements had FWHM 12.5 μm.

We measured the polariton waveguide frequency (wavelength) vs. wavenumber (angle) dispersion relation along the propagation direction x. Considering that the spectrometer resolution depends on the width of its input slit, for these measurements the spectrometer

resolution was 6.7 *meV* due to the 200 μm entrance slit size used to collect more light from the sample and obtain a good signal to noise ratio, owing to the low PL intensity. Projecting the Fourier plane of the emission onto an entrance slit of this size corresponds in our case to averaging over a transverse angular range (angle in the y direction, orthogonal to the propagation direction x, as shown in Figure 3.5) of $\theta_T \sim \pm 0.4^\circ$ inside the waveguide. This is equivalent to a frequency change $\omega \sin^2 \theta_T$ of only 0.2 *meV* and so the averaging over transverse angles has a negligible effect on resolution.

The relation between CCD pixel number and emission angle was carefully calibrated by placing a commercial 300 lines/mm UV diffraction grating in the position of the sample and recording the diffraction pattern.

To make the polariton modes more visible, spectra were resolved in polarisation using a broadband UV half-waveplate and a linear polariser, presented in Section 4.3. The spectra cross-polarised with the TE-polarised polariton mode were subtracted from the co-polarised spectra to remove the exciton luminescence while retaining the polariton mode emission.

The luminescence spectra are shown for temperatures T = 4 K and 300 K in Figure 7.1 (middle and right panels, respectively). We were able to extract the wavelength of the emission peak for each angle with low uncertainty (the exact value of uncertainty depends on the emission strength at the angle in question but is typically less than $\pm$ 0.5 *meV*), much lower than the spectrometer resolution, by fitting the peaks with Gaussian functions. The lower polariton branch modes ($LPB_{1,2}$) are symmetric about zero angle, which is due to polaritons propagating in the forward and backward directions in the waveguide. Both dispersion relations show a clear anticrossing and are well fit by a coupled oscillator model (solid white lines) with Rabi splitting 91 $\pm$ 4 and 70 $\pm$ 20 meV at 4 K and 300 K respectively, demonstrating that the system is strongly coupled up to room temperature. The white dashed curves give the exciton wavelength (X) and the uncoupled waveguide photon dispersion (Γ) calculated from a transfer matrix model of the planar waveguide structure.

The fitting parameters of the coupled oscillator model were: the exciton frequency E_X, the Rabi splitting Ω (which gives the photon-exciton coupling rate), and a rigid frequency offset E_Γ of the uncoupled photon mode Γ compared to the raw uncoupled photon mode dispersion obtained from the transfer matrix code. The last parameter accounts for the fact that there are inevitably small differences between the nominal and actual layer thicknesses and/or temperature dependent refractive indexes. Including all three was essential to obtain a good quality fit, as can be seen from the good agreement between the model and the luminescence spectra in Figure 7.1. We note that including E_Γ as a fitting parameter was vital to minimise the square error of the fit r^2. Without it, we obtained smaller values for the

Rabi splitting but much worse fits, e.g. 3.5 times the r^2 error when fitting with 2 parameters rather than 3. The additional uncertainty in Rabi splitting Ω and the exciton frequency E_X due to including E_Γ as a fitting parameter is included in the quoted values. The values of E_Γ obtained from the fit are less than 15 meV or 0.5% of the photon frequency, consistent with small errors in the material parameters entering into the transfer matrix model. For this reason, we believe that our Rabi splitting values ~ 90 meV are reliable, even though they are larger than those found in [101], which were effectively fit using the raw photonic modes from FDTD simulations.

The slight blueshift of LPB_2 compared to the model in Figure 7.1 (middle panel) is due to the repulsive polariton interactions directly under the excitation laser spot. Going into detail, for these data the laser excitation spot overlapped the edge of one of the gratings. LPB_1 corresponds to the polariton mode that propagates away from the excitation onto the main body of the grating and couples out. By contrast, the emission from LPB_2 can only come from the section of grating directly under the excitation spot, since the spot is on the edge of the grating and polaritons propagating away in the LPB_2 direction simply enter the un-grated region and are never detected. LPB_2 thus presents a nonlinear frequency blueshift of up to ~ 0.7 nm compared to LPB_1 and to the modelled LPB dispersion, which arises from the relatively high exciton and polariton density generated directly under the spot. We noted that we measured the dispersion for a number of spot positions relative to the gratings and confirmed that the spectra are symmetrical when the excitation spot is not very close to one of the gratings.

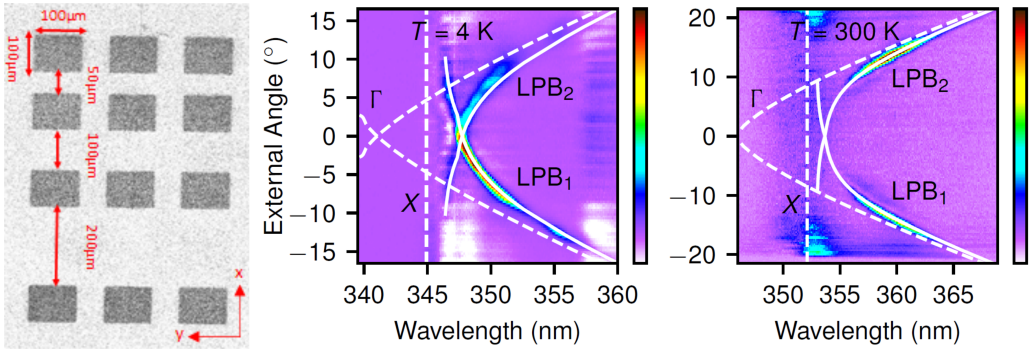

Fig. 7.1 **Left panel**: scanning electron microscope (SEM) image of the sample showing the 100 $\mu m \times 100$ μm gratings and the 50 μm, 100 μm and 200 μm waveguides, with x and y axes as reference. Angle-resolved luminescence spectra at T = 4 K (**middle panel**) and T = 300 K (**right panel**). Solid white curves denote the best fit lower polariton branch (LPB), dashed curves give the uncoupled photon (Γ) and exciton (X). The exciton emission has been subtracted to highlight the polariton modes.

7.3 Resonant excitation and detection of propagating polariton pulses

In order to study the pulse propagation through the waveguide, we excited our structure with laser pulses of the same frequency and incidence angle as the polariton mode. Contrary to the dispersion curve measurements, in this case we directly inject particles into the polaritonic guided mode and there is no need for carrier relaxation. We inject pulses with a range of central frequencies (and corresponding angles) through an input grating coupler and detect the output from a second grating placed at a distance $L = 100\ \mu m$. The incident laser spot size on the input grating was $6.5\ \mu m$.

As described in Chapter 4, the UV laser pulses were obtained from the system depicted in Figure 4.2. To match the bandwidth of the sample grating couplers, the initially $\sim 100\ fs$ pulses were spectrally filtered using a diffractive 4f pulse shaper. The beam polarisation was controlled using a Glan polariser and half-wave plate. The angle of the incident light was controlled to match the guided mode on the grating coupler by translating the incident beam through the Fourier plane of the objective. The incident laser angle, polarisation, and position relative to the input coupler edge were optimised by maximising the observed transmitted intensity at the output coupler for low incident powers. The light coming out of the waveguide was collected by the same microscope objective used for excitation and sent to the detection apparatus by means of a non-polarising beamsplitter cube. The light was imaged onto the entrance slit of an imaging spectrometer using a pair of relay lenses and recorded on a thermo-electrically cooled CCD camera (for further details, see Figure 4.8).

The laser powers used for the experiments were obtained by measurement using a commercial laser power meter. For low laser powers at the sample surface, below the sensitivity limit of the power meter, the power was measured at a position in the beam path before the laser beam was attenuated using commercial pre-calibrated UV-fused-silica reflective metallic neutral density (ND) filters (FRQ series from Newport/MKS) so as not to saturate the CCD. We confirmed that the attenuation factor of the ND filters was equal to that specified in the calibration data provided by the manufacturer. Thus we could measure the beam power at a position where it was well above the sensitivity limit of the power meter while having highly accurate knowledge of the much lower power at the sample surface. For these measurements, the slit was set to $50\ \mu m$ width and the resolution was $1.7\ meV$, well below the initial pulse spectral FWHM of $4.2\ meV$.

The color maps in Figure 7.2 show the spectrum of the pulses at the output for T = 10 K and 200 K (left and right panel, respectively), for increasing pulse energy coupled into the waveguide. The intensity is plotted vs. wavelength λ and the spatial position y transverse to the propagation direction x. At the lowest pulse energy the unmodulated transmitted spectrum can be seen in the $\sim \pm 3\ \mu m$ region near y = 0 (red), surrounded by a background of a few percent of the peak (green) extending out to large y. This background comes from scatter of the incoming UV laser beam from the optics and is not related to the light transmitted through the waveguide. As the energy of the injected laser pulses increases, the spectra broaden both in wavelength λ and along y, resulting in spectra with a complex inter-dependence of y vs. λ at the highest powers. We note that the spectral shape of the background scatter remains constant. As we confirm by comparison with simulations (see Section B.3), the broadening of the waveguided light arises due to simultaneous nonlinear modulation of the pulse temporal and spatial (y) envelope [156]. The large spectral width and non-trivial y(λ) dependence imply an optical field with features that vary rapidly, on a timescale equal to the inverse of the spectral width, which can only be produced by sub-picosecond nonlinear dynamics.

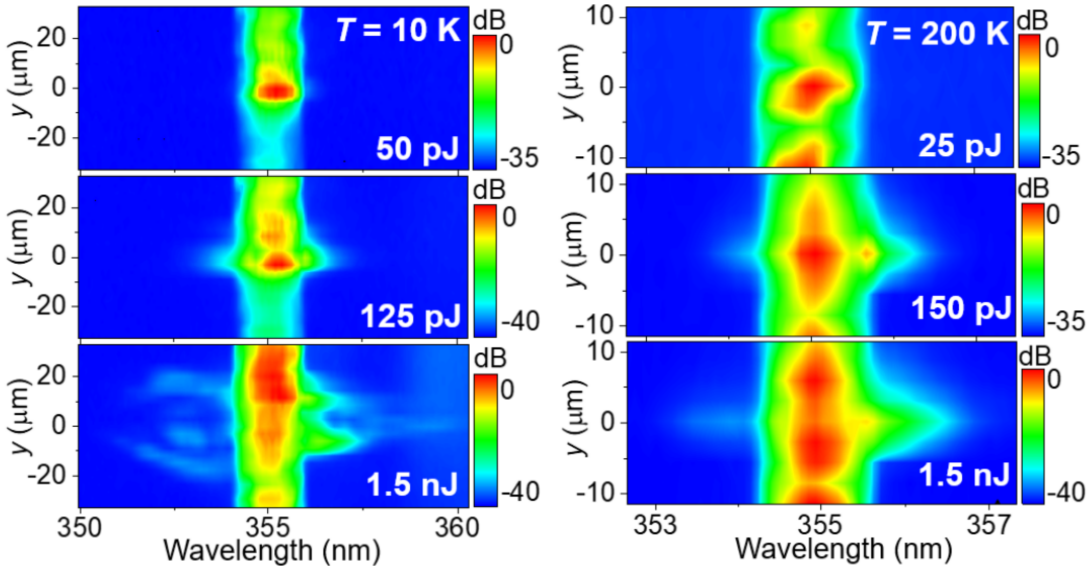

Fig. 7.2 Spectra after nonlinear pulse propagation. Colour maps of the output intensity vs. wavelength, λ, and position y transverse to the propagation direction for increasing pulse energy coupled into the waveguide and at temperatures T = 10 K (**left panel**) and at T = 200 K (**right panel**). The injected pulses had central wavelength $\lambda = 355\ nm$ and the propagation distance $L = 100\ \mu m$.

We now explore the overall broadening in λ for a range of parameters.

Figure 7.3 show the y-integrated spectra for a wide range of temperatures T = 8 - 300 K and for a constant detuning $\Delta \sim -90\ meV$ of the laser pulses from the exciton frequency. With increasing pulse energy we observe spectral broadening over the whole temperature range with spectral widths at the highest measured powers of 58 *meV* for T = 8 K, 45 *meV* for T = 250 K, and 29 *meV* for T = 300 K (Figure 7.3, left, middle and right panels, respectively). These compare to initial pulse widths of less than 16 *meV*.

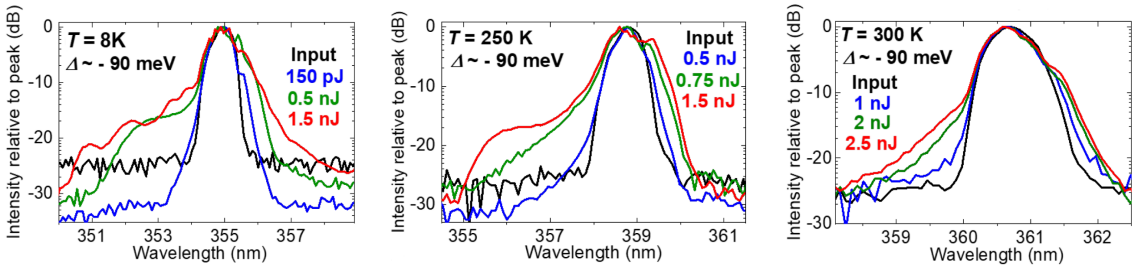

Fig. 7.3 Spectra integrated along y for a range of temperatures, T = 8 K (**left panel**), 250 K (**middle panel**), and 300 K (**right panel**) all at pulse-exciton detuning $\Delta \sim -90\ meV$.

In Figure 7.4 we show the integrated spectra at T = 200 K for three different detunings Δ. For the smallest detuning of $-60\ meV$ (Figure 7.4, left panel), the spectra are broadened asymmetrically with stronger broadening on the long λ side of the pulse peak. We attribute this asymmetry to the strong absorption of wavelengths on the short λ side which are very close to the exciton. When the detuning is increased to $\Delta = -80\ meV$ (Figure 7.4, middle panel) the spectra broaden on both sides of the peak with a slight asymmetry in the height of the spectral side-lobes on either side. Finally, at $\Delta = -100\ meV$ (Figure 7.4, right panel), the broadening is strong on the short wavelength side but weak for long wavelengths. This kind of asymmetry is known to arise from a frequency dependent nonlinearity due to the excitonic component of the polaritons [157]. Our observations show that the nonlinearity varies strongly on the scale of a few tens of meV, comparable to the Rabi splitting, which is expected for a nonlinearity arising from the strong photon-exciton coupling [119, 156]. Overall, we manage to achieve spectral broadening above 50 *meV* for different detunings at T = 200 K.

We were also able to obtain a spectral broadening of up to 80 *meV* at T = 8 K and of up to 66 *meV* at T = 100 K (see Figure 7.5).

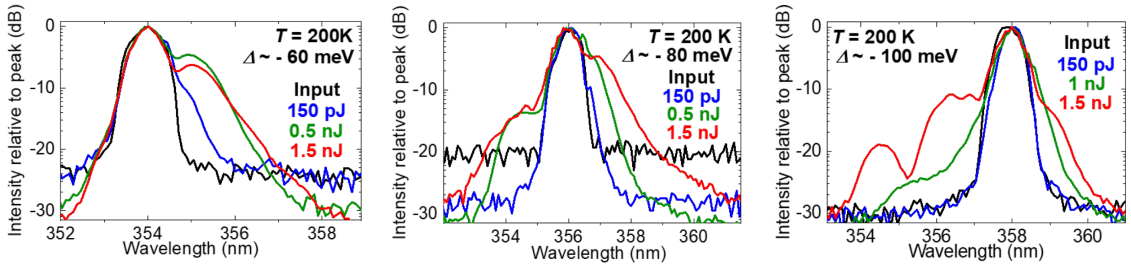

Fig. 7.4 Spectra integrated along the y-direction for a range of detunings $\Delta \sim -60\ meV$ (**left panel**), $-80\ meV$ (**middle panel**), and $-100\ meV$ (**right panel**), all at T = 200 K.

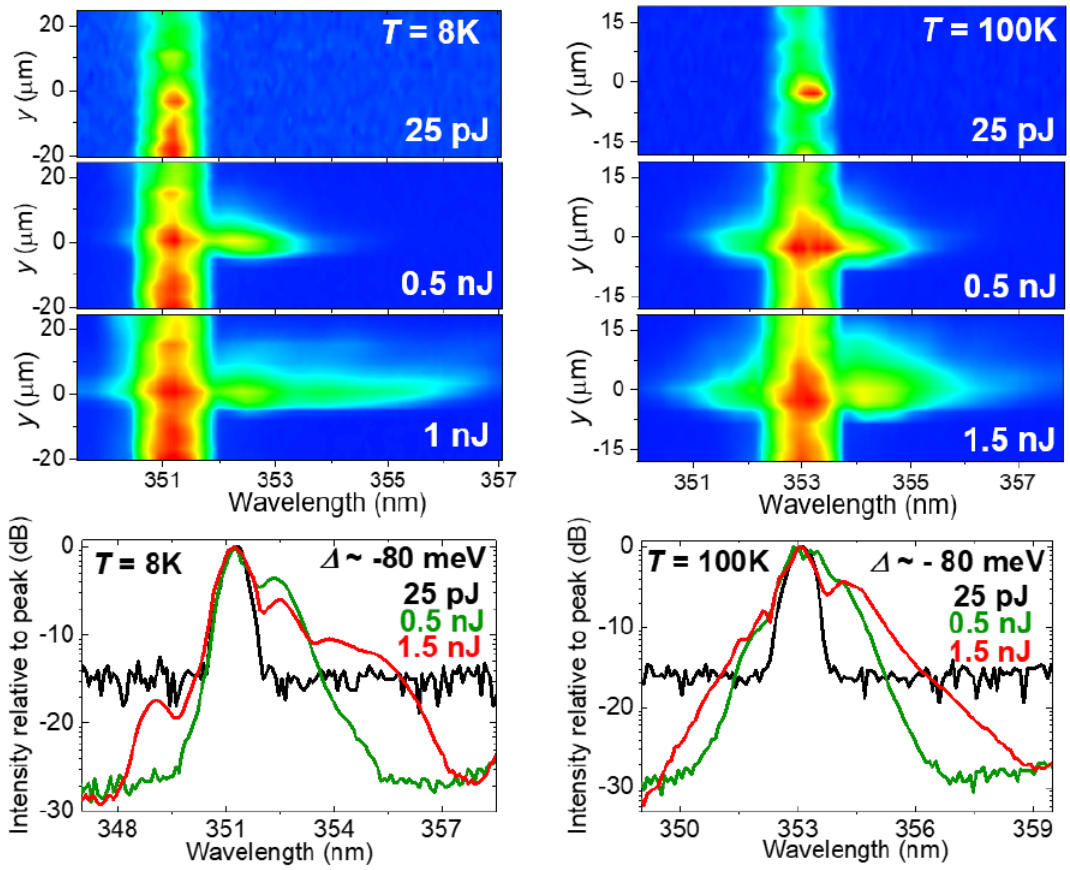

Fig. 7.5 Spectra after nonlinear pulse propagation. **Top row**: colour maps of the output intensity vs. wavelength, λ, and position y transverse to the propagation direction for increasing pulse energy coupled into the waveguide and at temperatures T = 8 K (**left panel**) and T = 100 K (**right panel**). The injected pulses had central wavelength $\lambda = 355\ nm$ and the propagation distance $L = 100\ \mu m$. **Bottom row**: spectra integrated along y for T = 8 K (**left panel**) and 100 K (**right panel**), both at pulse-exciton detuning $\Delta \sim -80\ meV$.

7.4 Self-phase modulation

Before going into detail on the analysis of the experimental results just shown, it is necessary to fully introduce the nonlinear phenomenon that characterises pulse propagation within a waveguide, called self-phase modulation (SPM), already discussed in Section 1.2.3.
Once the propagation constant

$$\beta = \frac{\omega}{c}\, n_{eff} \tag{7.1}$$

has been defined in Section 3.3, as well as the nonlinear refractive index n_2 arising from the optical Kerr effect

$$n = n_0 + n_2\, I \tag{7.2}$$

in Section 1.2.3, it is possible to show that the phase shift characterising SPM is given by [34]

$$\delta\phi = \frac{2\pi}{\lambda_{peak}}\, \delta n_{eff}\, L_{eff} \tag{7.3}$$

where λ_{peak} is the excitation wavelength, and

$$\delta n_{eff} = n_2\, I_{eff}(t) = n_2 \frac{P_{peak}}{A_{eff}} = n_2 \frac{1}{A_{eff}} \frac{E_{peak}}{\tau_{pulse}} \tag{7.4}$$

is the correction to the effective index arising from the Kerr nonlinearity, with A_{eff} the mode area, P_{peak} the laser pulse peak power, E_{peak} the laser pulse peak energy and τ_{pulse} the laser pulse duration, while

$$L_{eff} = L_{loss}\left(1 - e^{-\frac{L}{L_{loss}}}\right) \tag{7.5}$$

is the effective length including the decay length L_{loss}. Considering a phase change with time, we get a change in frequency

$$\Delta\omega = -\frac{\partial}{\partial t}\delta\phi(t) = -\frac{2\pi}{\lambda_{peak}}\, n_2\, L_{eff}\, \frac{\partial}{\partial t} I_{eff}(t) \tag{7.6}$$

Then, using a Gaussian temporal intensity distribution [124]

$$I_{eff}(t) = I_{in} e^{-\frac{t^2}{\tau_{pulse}^2}} \tag{7.7}$$

we finally obtain

$$\Delta\omega = +\frac{2\pi}{\lambda_{peak}}\, n_2\, L_{eff}\, \frac{2t}{\tau_{pulse}^2}\, I_{in} e^{-\frac{t^2}{\tau_{pulse}^2}} = \frac{2\pi}{\lambda_{peak}}\, n_2\, L_{eff}\, \frac{2t}{\tau_{pulse}^2}\, \frac{P_{peak}}{A_{eff}} \tag{7.8}$$

This equation implies that the guiding tail (for $t < 0$) of the pulse manifests a decreased frequency, while the trailing tail (for $t > 0$) of the pulse manifests an increased frequency, leading to the spectral broadening mentioned in Section 1.2.3 caused by the nonlinear Kerr effect. So, a light pulse travelling through a nonlinear medium accumulates a nonlinear phase which leads to a characteristic broadened spectrum.

In order to evaluate the role of the SPM on the spectral broadening and then obtain the values of the nonlinear refractive index n_2, it is necessary to determine the coupling efficiency and propagation losses, as clearly arises from the discussion above. To do that, we use a combination of measurements and electromagnetic modelling (finite-difference time-domain method, FDTD), performed using Luminal 3D FDTD solver, whose details are given in the Section B.2.

We deduce the strength of the nonlinearity by comparing the lowest pulse energy experimental spectra to a SPM model [158].
The time-varying phase then corresponds to new spectral components. Combining Equations 7.3 and 7.4, the accumulated nonlinear phase at the peak of the pulse can be written as

$$\delta\phi = \frac{2\pi}{\lambda_{peak}}\, n_2\, \frac{P_{peak}}{A_{eff}} L_{eff} \tag{7.9}$$

where $\lambda_{peak} = 353.4\ nm$ is the wavelength at the centre of the pulse spectrum, $A_{eff} = 1\ \mu m^2$ is the waveguide effective nonlinear cross-sectional area, obtained from $A_{eff} \approx \Delta z\, \Delta y \frac{\pi}{2\, ln(2)}$ [158] and L_{eff} is the effective distance over which the nonlinearity acts accounting for loss (see Equation 7.5). The device length is $L = 100\ \mu m$ and L_{loss} is the characteristic decay length due to loss. In calculating A_{eff}, we have used the 79 *nm* FWHM waveguide mode profile obtained from Lumerical FDTD simulations (see Section B.2) for the intensity profile in the growth direction and the 6.5 μm FWHM gaussian spot at the input as the transverse intensity profile, noting that the spot did not diffract significantly over the 100 μm device length at the low powers where we perform this fitting.

Before describing the fitting, we briefly comment on the validity of the model. But first, we need to introduce another fundamental concept related to waveguides. Because of the dependence of the refractive index $n(\omega)$ on the optical frequency ω, different spectral

components of a propagating short pulse travel at different phase velocities $v = c/n(\omega)$, leading to dispersion-induced pulse broadening. Calculating the Taylor series expansion about the central frequency ω_0 of the propagation constant $\beta(\omega) = n(\omega)\ \omega/c$, it is possible to show that the second derivative is $\beta_2 = 1/c\ (2\ dn/d\omega + \omega\ d^2n/d\omega^2)$ and it is called group-velocity dispersion (GVD) parameter, causing pulse broadening. When $\beta_2 < 0$, the system is said to have anomalous dispersion and the high-frequency components travel faster than the low-frequency components (i.e. $dn/d\omega < 0$).
From the measured polariton dispersion relation (see Section 7.2), we obtain the second order dispersion coefficient $|\beta_2| < 250\ ps^2\ m^{-1}$. Combined with the spectral FWHM $\hbar\Delta\omega < 5\ meV$, the characteristic dispersion length [158] $L_D = 4log(2)/(\beta_2\ \Delta\omega^2) > 200\ \mu m$ is much larger than the loss length and the device length, so the dispersion can be neglected. For low powers, where the pulses accumulate small nonlinear phase, only the third order term in the system nonlinear response is significant so that the waveguide can be described as an effective Kerr-like waveguide with nonlinear refractive index n_2. We remember that in the polariton system both the exciton blueshift and oscillator strength saturation effects are third order nonlinear processes (see Section 1.2.3). In this regime of low power and negligible dispersion, the model of SPM may be applied and used to find n_2. We note that at the higher pulse energies shown in Figure 7.6, the experimental spectra become slightly asymmetric, which arises due to the frequency dependent polariton nonlinearity. This effect cannot be captured by a simple SPM model, but least squares fitting averages over the spectral components on either side of the peak to give an average value of the phase. The phases obtained for these higher pulse energies lie on a straight line with those at lower pulse energy (Figures 7.6(c) and (d)), where the asymmetry is negligible, showing that this approach works well.

For each pulse energy, we deduce the nonlinear phase $\delta\phi$ at the peak of the pulse by fitting the experimental spectrum with modelled SPM-broadened spectra. The experimental spectra and fits are shown in Figures 7.6(a) and (b) on a logarithmic scale as dotted lines and points respectively for two temperatures. Good agreement is achieved over a range of pulse energies. At the lowest powers, SPM manifests as a growth of low intensity spectral side-bands which eventually become comparable to the main peak as the power is increased [158]. We therefore fit the model to the logarithm of the spectra (as shown in Figure 7.6), since this maximises the sensitivity to these low intensity side-bands. The fit was performed using experimental points down to $-20\ dB$, where the data is at least a factor of 2 above the noise floor. The initial (zero power limit) pulse used in the SPM model was the unchirped Gaussian pulse whose spectrum was the best fit for the experimental one in the linear regime, having temporal FWHM $\tau_{pulse} = 425 \pm 4\ fs$. Using an unchirped Gaussian pulse shape is

equivalent to assuming a maximum pulse peak power for a given pulse energy. If the pulse was chirped or had a different shape, then the peak power would be lower and the actual values of n_2 would be larger than those we deduce.

We plot the obtained $\delta\phi$ vs. pulse energy in Figure 7.6(c) and (d) for two temperatures along with the best fit straight lines. The points lie on a straight line within the uncertainty, as expected for an SPM spectral broadening mechanism, which confirms the validity of our approach. The linear fitting gives a slope of $50 \pm 10\ pJ \cdot rad^{-1}$ for 100 K and $32 \pm 9\ pJ \cdot rad^{-1}$ for 200 K. From this, n_2 can be obtained using

$$n_2 = \frac{\delta\phi}{\delta E_{pulse}}\ \tau_{pulse}\ \frac{\lambda_{peak}}{2\pi}\ \frac{A_{eff}}{L_{loss}[1-exp(-L/L_{loss})]} \tag{7.10}$$

given by the combination of Equations 7.5 and 7.9, where $\delta\phi/\delta E_{pulse}$ is the rate of change of nonlinear phase with pulse energy obtained from the SPM fitting. The pulse width $\tau_{pulse} < 430 \pm 40\ fs$ (independent of temperature) was obtained from the measured spectrum at low power under the assumption that the pulses are unchirped and Gaussian. The values of $\delta\phi/\delta E_{pulse}$ are obtained by fitting the experimental spectra with theoretical spectra of SPM-broadened Gaussian pulse [158].

So, from the slope, we deduce an effective nonlinear refractive index $n_2 = (1.9 \pm 0.3) \times 10^{-17}\ m^2/W$ for 100 K and $n_2 = (3.7 \pm 1.0) \times 10^{-17}\ m^2/W$ for 200 K. Here the quoted uncertainty accounts for the random errors in the fitting, coupling efficiency, waveguide losses and all other parameters entering into the model. As well as these, there may be some systematic overestimation of the pulse peak power leading to underestimation of n_2 (see Section B.2). We note that we rigorously propagated statistical uncertainties in all model parameters to the final quoted values of n_2. In principle, disorder in the fabricated grating couplers could lead to lower coupling efficiency than that obtained via FDTD, while our assumption of unchirped Gaussian pulses is equivalent to assuming the minimum possible τ_{pulse} for our measured spectrum. Thus there may be a small systematic underestimation in our values of n_2. We finally note that we quote the coupled pulse energy which is the product of the measured incident pulse energy and the coupling efficiency.

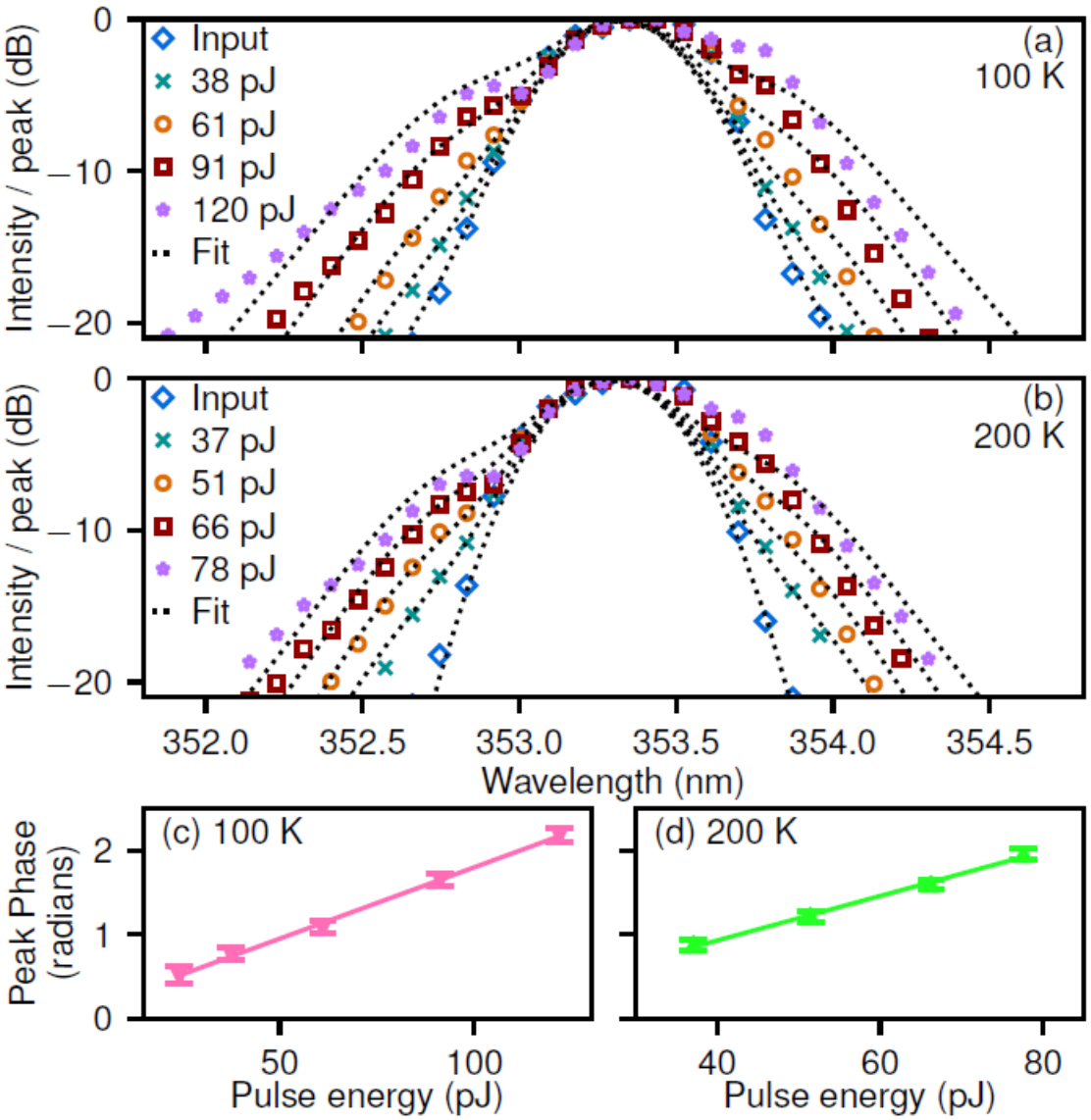

Fig. 7.6 Spectral broadening in the low power limit. **a, b**: comparison of experimental spectra (points) and best fit of SPM model (dotted lines) for two temperatures and several pulse energies. **c, d**: peak phase with corresponding error bars from the SPM fits in (a) and (b). Solid lines show the linear best fit. Error bars give the uncertainty in phase obtained from the fitting procedure. Further details on the discussion of how the coupled pulse energies were deduced can be found in Section B.2.

7.5 Estimate of nonlinear refractive index from first-principle calculations

We finally note that it is also possible to estimate n_2 in our polariton waveguide from first-principle calculations. The nonlinearity in our polariton waveguide is due to the renormalisation of the exciton frequency (exciton blueshift) ΔE_X and saturation of the exciton oscillator strength resulting in a change in Rabi splitting $\Delta(\hbar\Omega_X)$ as the exciton density n_X increases [28], as stated in Section 1.2.3. Both of these effects lead to a frequency blueshift of the lower polariton branch for a given wavenumber or, equivalently, a decrease in wavenumber for any given frequency. This nonlinear change in wavenumber vs. frequency is equivalent to a nonlinear change in refractive index. Remembering that the blueshift and change in Rabi splitting are (to first order) $\Delta E_X = g_X n_X$ and $\Delta(\hbar\Omega_X) = \beta_X n_X$, where g_X and β_X are the interaction constants already introduced in Section 1.2.3, we will first consider the size of the excitonic blueshift and oscillator strength parameters following the method given in [28] and using the GaN QW exciton Bohr radius [159]. We will then express the nonlinear response as a nonlinear refractive index.

The exciton-exciton interaction constant is given by [28]:

$$g_X = \frac{3e^2 a_B}{4\pi\varepsilon_0\varepsilon} \tag{7.11}$$

where e is the electron charge, a_B is the exciton effective Bohr radius, $\varepsilon \sim 10.28$ is the static dielectric constant [160], and ε_0 is the vacuum permittivity. The exciton effective Bohr radius can be expressed as:

$$a_B = a_B^{3D}\left(1 + \frac{d-3}{2}\right)^2 \tag{7.12}$$

where $a_B^{3D} \sim 3.2\ nm$ is the bulk exciton Bohr radius and d is the fractional dimensionality of the excitonic system [56], in turn given by

$$d = 1 + 2\sqrt{\frac{R_X}{E_B}} \tag{7.13}$$

where $R_X = 25\ meV$ is the bulk exciton Rydberg constant [161], and $E_B = 40\ meV$ is the exciton binding energy [101], which in our case yields a fractional dimensionality of $d = 2.58$. This then gives an effective Bohr radius of $a_B = 2.0\ nm$.

The interaction constant dealing with the saturation density of the system is given by [28]:

$$\beta_X = -\frac{8\pi}{7}\,\hbar\Omega_X\,a_B^2 \tag{7.14}$$

where $\hbar\Omega_X \sim 90\ meV$ is the Rabi splitting.

We finally obtain the exciton blueshift per unit density per quantum well $g_X \sim 0.85\ \mu eV \cdot \mu m^2$ and the change in Rabi splitting per unity density per quantum well is $\beta_X \sim -1.3\ \mu eV \cdot \mu m^2$. These values are comparable with those predicted and measured in GaAs ($g_X \sim \beta_X \sim 2.5\ \mu eV \cdot \mu m^2$ for linear polarisation) [28], when one accounts for the much smaller exciton Bohr radius of GaN [56]. However, in our GaN device the nonlinearity is not restricted to cryogenic temperatures. The total nonlinearity (g_X and β_X) for a single QW is comparable with that observed per inorganic layer in hybrid inorganic-organic perovskites at around 516 *nm* [61]. Here we take such strong polariton interactions into the UV in a robust material system which does not suffer from photo-bleaching.

When one considers the total system of waveguide photonic mode coupled to $N_{QW} = 22$ QWs, the theoretical value of the effective nonlinear refractive index, n_2, may be derived from the change in frequency vs. wavenumber of the polariton dispersion. It is given by:

$$|n_2| = \frac{n_g^2\,\Delta z}{c(\hbar\omega)^2}\frac{|C_X|^4}{|C_{ph}|^4}\left(\frac{g_X}{N_{QW}} - \frac{\beta_X}{N_{QW}}\frac{|C_{ph}|}{|C_X|}\right) \tag{7.15}$$

where $n_g = 4.9\ (5.4)$ is the uncoupled-photon group velocity index at 100 K (200 K) (with the frequency dependence coming from the nitride material dispersion), $\Delta z = 79\ nm$ is the guided mode width (FWHM) in the z direction obtained from FDTD calculations, c is the light speed in vacuum, $\hbar\omega = 3.51\ eV$ is the frequency of the pulse in energy units, and $|C_X|^2/|C_{ph}|^2 = 0.31 \pm 0.05\ (0.42 \pm 0.06)$ is the ratio of excitonic and photonic fractions of the polaritons at 100 K (200 K). From these, we obtain the theoretical values of $n_2 = (3.3 \pm 0.9) \times 10^{-17}\ m^2/W$ and $(6.5 \pm 1.5) \times 10^{-17}\ m^2/W$ at T = 100 K and 200 K, respectively. These are in good agreement, within a factor of 1.8, of the measured values.

7.6 Comparison of nonlinear refractive index with literature values

In our polariton waveguide, we measure $n_2 = (1.9 \pm 0.3) \times 10^{-17}\ m^2/W$ for 100 K and $n_2 = (3.7 \pm 1.0) \times 10^{-17}\ m^2/W$ for 200 K using propagating sub-picosecond pulses. These are three orders of magnitude larger than values in other materials commonly used for UV nonlinear optics [155]. Values quoted for GaN are typically in the range $1 - 7 \times 10^{-18}\ m^2/W$ for the near-infrared to visible spectral region [162, 163] but values greater than $10^{-16}\ m^2/W$ have been reported in the UV close to the bandgap [164]. This latter result, however, was measured using high repetition rate (82 MHz) laser pulses and Z-scan measurements where the nonlinearity is probed by nonlinear modulation of the refractive index in space. Under these conditions the nonlinearity is probed at the same spatial position as the system is pumped. Combined with the high repetition rate these types of experiment can be strongly influenced by thermal lensing effects or free carrier excitation. The latter was shown to make a very strong contribution to nonlinear refraction even in the green spectral range [162, 165] with the effects lasting on the order of 1 ns [165], compared to only 12 ns between excitation pulses, so that a significant population could build up during a typical 1 s (8×10^7 pulses) time-averaged measurement at 82 MHz. This would lead to a spatial nonlinear modulation detected by the Z-scan measurement, but since the relaxation time of this free-carrier type of nonlinearity is long [165], it is not clear how useful it is for applications requiring ultrafast pulse self- and cross-phase modulations (XPM).

In our work we avoid these pitfalls by using 1 kHz repetition rate and pulses which propagate 100 μm between pump and detection positions (the pump spot was 6.5 μm FWHM). Even if a free carrier background develops in our device, it would not vary with the $\sim ps$ temporal shape of the pulse and so would not lead to the characteristic SPM spectra we observe. This is the first time the UV nonlinear refractive index in a GaN-based device has been measured using such a propagating pulse modulation which directly evidences its ultrafast timescale. So, we obtain values approximately an order magnitude larger than those typically found in bulk GaN for the near-infrared to visible spectral region (excluding slow-free carrier related nonlinearity) [162, 163]. This is expected since strong photon-exciton coupling enhances nonlinearity for frequencies close to the exciton resonance compared to the Rabi splitting [156].

7.7 Summary

In conclusion, in this chapter we showed the first experimental measurements of nonlinear phase-modulation in a sub-millimeter AlInGaN-based waveguide, working in the UV spectral range and in the strong coupling regime up to room temperature. We detected a maximum spectral broadening due to SPM at the output grating of a $100\mu m$-waveguide up to 80 meV, depending on the exciton-photon detuning and the temperature. From that, we got a nonlinear refractive index $n_2 \sim 10^{-17}\ m^2/W$, which is 10^3 times larger than that measured in other materials used in the UV [155].
The same value was obtained from first-principle calculations, with nonlinearity arising from both exciton blueshift (g_X) and Rabi splitting reduction (β_X). Remarkably, this value is also comparable to that in the IR GaAs-polariton waveguide [10], but this GaN-based device is able to work up to room temperature.

Chapter 8

Conclusions and future perspectives

8.1 Summary

The main aim of this thesis is to investigate the nonlinearity of exciton-polaritons in different spectral range (from infrared to ultraviolet), adopting different active media (TMDC, specifically $MoSe_2$, and GaN, respectively) and photonic microstructures (hemispherical tunable open-access microcavity and waveguide, respectively), with the ultimate purpose of exploiting the acquired knowledge for near future devices.

Bare TMDC MLs have already demonstrated their emerging role for practical applications. Implementing them into microcavities, exciton-polaritons certainly further increase the TMDC appeal for the development of new technological platforms, thanks to the dual nature of these quasi-particles, superposition of light and matter.

Another interesting active material to be investigated for its technological importance is represented by AlInGaN compounds. Their tunability across the UV range and the stability up to room temperature of their excitons make them ideal for practical applications of nonlinear optics. The implementation in polariton waveguides can certainly further exalt these peculiar properties, paving the way towards a new generation of nonlinear devices.

In this last chapter, we first summarise the experimental results obtained in both systems and then present possible future directions of our work.

8.2 Discussion on experimental results

8.2.1 $MoSe_2$-microcavity

In Chapter 5, we presented the preliminary measurements performed to fully characterise TMDC-polaritons in a tunable open-access hemispherical microcavity within our brand new custom-built helium bath cryostat that allows transmission experiments to resonantly excite the polariton state, with the ultimate purpose of exploring nonlinear TMDC-polariton interactions.

We first compared the bare $MoSe_2$ MLs fabricated using the two techniques highlighted in Section 2.2.2. Exfoliated samples appear to have a better optical quality than CVD samples thanks to their brightness and narrower exciton linewidth, promising characteristics for a stronger coupling with cavity photons. Unfortunately, the exciton resonance of the exfoliated sample at RT was too broad to guarantee polariton formation, preventing interesting practical application in the near future. Further improvements are needed in the sample fabrication process for this purpose, that could be guaranteed by a fully encapsulation with hBN.

We then performed power dependence studies on the bare flake, noting an irreversible photoinduced damage (and lattice heating even with the implementation of a chopper) under CW excitation, while pulsed lasers seemed to be safer below a certain pump power threshold in preserving the optical integrity of the TMDC ML. Importantly, we detected redshift of the exciton resonance under CW excitation due to sample heating, while blueshift was observed under pulsed excitation (that prevents heating thanks to its duty cycle) arising from exciton-exciton interaction. As a consequence, we then decided to explore TMDC-polariton nonlinearities only under pulsed excitation.

Once the bare flakes were characterised, we moved them in the open-cavity setup to study exciton-polaritons. Changing the distance between the two mirrors under off-resonant excitation, we observed photon coupling with both exciton and trion resonances, which undergo an energy shift (so-called Stokes shift) that can be used as a qualitative indicator of the $MoSe_2$ doping level.

Finally, performing a resonant experiment under different excitation configurations (see Sections 5.3.2 and 5.3.3), we note the importance of trions over excitons in nonlinear TMDC-polariton behaviour: the closer to the former resonance, the stronger the energy shift. Moreover, the redshift (blueshift) of the ground mode when resonantly excited in MPB (LPB) anticipates the quench of the trion-photon coupling, that leads to the high nonlinearity quantitatively studied in Chapter 6.

In Chapter 6, we measured the nonlinearity due to trion-polaritons with respect to that due to neutral exciton-polaritons. We observed that, depending on the exciton-photon energy detuning, the trion-polariton nonlinearity is 10 to ~ 100 times larger than that due to neutral exciton-polaritons, where the variation of neutral exciton-polariton nonlinearity with density is attributed to higher order exciton-exciton and trion-exciton interactions. For example, the trion-polariton energy redshift of the order of 1 meV is observed at an excitation power of ~ 20 nW (see Figure 6.6, left panel) at $\delta_{C-X} \sim -15$ meV, whereas in the case of neutral exciton-polaritons the same energy shift is observed at excitation powers of ~ 400 nW and ~ 4 μW at $\delta_{C-X} \sim -15$ meV and $\delta_{C-X} \sim 2$ meV in Figures 6.8 (left panel) and 6.10, respectively. This is consistent with fact that the deduced average value of $\beta_T^{eff} \approx 37$ $\mu eV \cdot \mu m^2$ is 10 to ~ 100 times larger than the values g_X^{eff} observed in Figure 6.12 (top panel) at $n_{tot} < 10^4$ μm^{-2}.

Determination of the measured absolute values β_T^{eff} and g_X^{eff} requires careful deduction of the total polariton (exciton/trion) density excited with a single resonant pulse in the system in order to minimise possible systematic errors. The most accurate way to do this would be to use the incident energy of the excitation pulse and the coupling efficiency of the external radiation to the 0D polariton mode. In our experiment, this coupling efficiency is not known, since the excitation beam does not match well the spatial profile of the polariton mode. Instead, we deduce the total exciton/trion density using the transmitted power and the ratio of the measured polariton linewidth to that of the bare cavity mode linewidth. The latter gives an upper bound on the ratio of the polaritons absorbed into the reservoir to polaritons emitted into free space since scattering into the reservoir cannot be faster than the total loss rate of polaritons. The accuracy of this method can be judged by the fact the values of g_X^{eff} of about $1 - 0.3$ $\mu eV \cdot \mu m^2$ at exciton densities in the range $10^3 - 10^4$ μm^{-2} are consistent within a factor of 2 to 3 with $g_X^{eff} \sim 1 \pm 0.4$ $\mu eV \cdot \mu m^2$ measured in [166] for neutral exciton-polaritons realised in a slab waveguide photonic crystal in the same density range. In [166], the exciton density was derived accurately using femtosecond excitation and detection and measurement of the absolute power of the resonant excitation pulse and the coupling efficiency of the incident radiation to the polariton mode. In that case polariton absorption is not relevant. Since in the current work the trion-polariton nonlinearity is measured with respect to the neutral exciton-polariton nonlinearity, we can take g_X^{eff} as a reference point and confirm that the value $\beta_T^{eff} \simeq 37$ $\mu eV \cdot \mu m^2$ is likely to be accurate within a factor of 2 to 3 as well. Good agreement between our theory of the trion-polariton nonlinearity (which does not use fitting parameters) and the experiment (Figure 6.8, right panel) further supports this statement.

It is also useful to relate parameter β_T^{eff} to nonlinear refractive index coefficient n_2 widely used in the field of nonlinear optics to characterise Kerr-like nonlinearity of materials. We estimated the value of n_2 per single flake associated with strong trion-photon coupling to be around $\sim 10^{-10}\ m^2/W$ (see Section 6.4.1.2). This value is $3-5$ orders of magnitude greater than the nonlinear refractive coefficient of 2D TMDC materials and graphene studied in the weak light-matter coupling regime (see Section 6.4.1.2). The nonlinear refractive index n_2 due to trion-polaritons of a hybrid monolayer-cavity system is also found to be $3-4$ orders magnitude larger than the n_2 coefficient of widely used bulk optical materials (see Section 6.4.1.1).

8.2.2 GaN-waveguide

In Chapter 7, we first characterised our GaN-based waveguides under off-resonant excitation. We observed in far-field experiments that GaN excitons strongly coupled to TE waveguided mode up to room temperature, with an obvious decreasing of the Rabi splitting with temperature (from $\sim 90\ meV$ at 4 K to $\sim 70\ meV$ at 300 K), making this platform promising for practical devices.

We then explored the nonlinear behaviour of this structure under resonant excitation, coupling the pulse-shaped laser to the waveguide through suitably designed gratings. We performed these measurements by varying different parameters in order to fully characterised the nonlinear modulation, specifically temperature, pump power and exciton-photon detuning. We detected a spectral broadening that decreases with temperature (reduction of the Rabi splitting) from 58 meV at T = 8 K to 29 meV at T = 300 K for the same exciton-photon detuning. As expected from a polariton system, the nonlinearity is also affected by the exciton content of the quasi-particles. Indeed, the resulting spectra manifest asymmetry on the long (short) wavelength side for small (big) negative detuning, for strong exciton absorption and frequency dependent nonlinearity respectively.

The corresponding nonlinear refractive index n_2, that we deducted by measured SPM, has a value of $\sim 10^{-16}\ m^2/W$ at T = 200 K, which is 1000 times higher than the values already reported in UV systems [155] and comparable to that of IR GaAs-polariton devices [10], however obtained at cryogenic temperatures.

This value was further confirmed by first-principle calculations, through which we got nonlinear interaction strengths arising from both exciton blueshift (g_X) and Rabi splitting reduction (β_X) of $\sim 1\ \mu eV \cdot \mu m^2$ per unit exciton density per QW, comparable to the values characterising GaAs [28].

We experimentally demonstrated for the first time the ultrafast picosecond nonlinear SPM in the UV range up to room temperature, with an effective nonlinear refractive index three orders of magnitude higher than that measured in other UV systems [155].

8.3 Outlook

The results obtained in Chapters 5 and 6 demonstrate the potential to establish polariton blockade. Notably, the deduced trion-polariton nonlinearity is of the same order as that observed in microcavities with a single quantum dot [167, 168], where strong renormalisation of Rabi-splitting ($\sim 100\ \mu eV$) occurs at a single photon level [167]. The average value of $\beta_T^{eff} \simeq 37\ \mu eV \cdot \mu m^2$ is also $\sim 5-10$ times larger [10, 28] or comparable [169, 30] to the reported coefficients characterising neutral exciton-polariton nonlinearity in a GaAs system. So, the value of β_T^{eff} can be further verified by studying the second-order correlation function ($g^{(2)}(\tau)$) of the emission from the resonantly driven polariton mode [12, 170]. Strong interactions can lead to polariton blockade and antibunching [12]. As we elaborate theoretically in Section A.4, polariton quantum effects can potentially be realised in high-Q microcavities with embedded high quality homogeneous TMDC samples [137], where very narrow polariton resonances with a linewidth given just by the cavity mode lifetime could be achieved. Such a high-quality sample would also lead to strong coupling even at room temperature, as allowed by the high binding energy of excitons in TMDCs.

Instead of taking advantage of only the natural doping of $MoSe_2$ to observe trions, applying a gate voltage it would be possible to electrically control their amount by converting neutral excitons into charged excitons. In order to do that, a heterostructure similar to that employed in [82] can be used (see Figure 8.1). To further improve that design for a $MoSe_2$ gated structure, we could use a flat DBR terminating with a high-refractive index $\lambda/(4n)$ layer of Nb_2O_5. After the deposition of a graphene layer, used as a bottom gate to control the electron density in the ML, a low-refractive index $\lambda/(4n)$ layer of SiO_2 could be deposited by e-beam evaporation, in order to preserve the surface quality and not damage the graphene underneath. With this configuration, the $MoSe_2$ would be located at the antinode of the electric-field, while the graphene would be at the node of the cavity, avoiding degradation of the cavity Q-factor. To improve the emitter linewidth, encapsulation with hBN layers would be necessary: in this case, a great precision in hBN thickness choice, achievable with AFM, would be mandatory.

Given the dependence of conventional polariton blockade on the electron density, this configuration may lead to lower $g^{(2)}(0)$ values.

Qualitatively, the trion-polariton blockade can be understood in the following way: the effective beta-factor, which we derived, defines the energy renormalisation of the polariton resonance with adding of one excitation to the system. If the polariton linewidth is narrower than this energy renormalisation then the effect of the polariton blockade and photon anti-bunching would be possible (see Figure 8.2).
However, there is another phenomenon that allows to relax the stringent conditions on strong trion-polariton energy shift just mentioned, namely unconventional polariton blockade. It takes advantage of the existence of two possible ways to populate the two-photon state that could destructively interfere: the direct optical excitation and the trion-mediated path (see Figure 8.3).

Our work paves the way towards development of scalable active nanophotonic devices based on 2D materials (where the exciton level is the same across large areas in contrast to 0D quantum dots) utilising the polariton nonlinearity for control of light by light, potentially at quantum level.

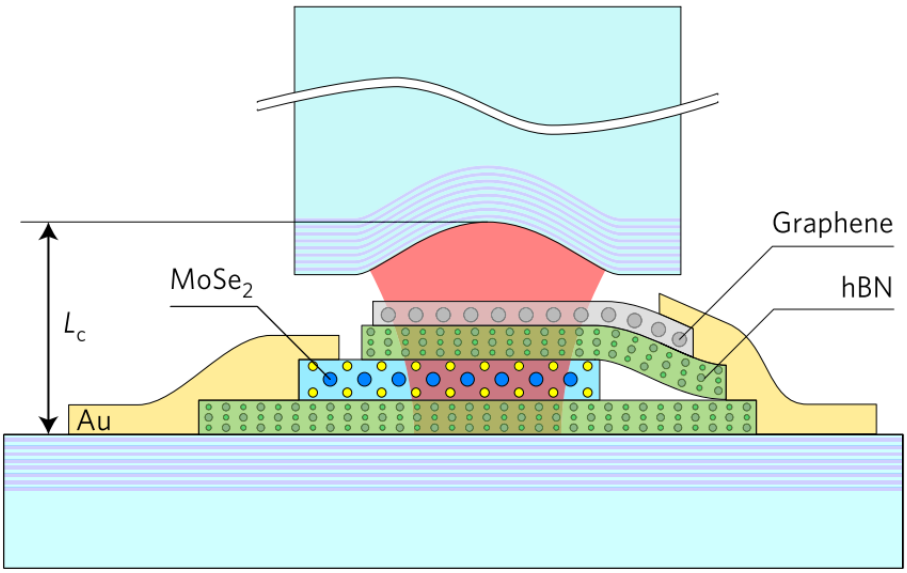

Fig. 8.1 $MoSe_2$ sample sandwiched between hBN layers. This gated structure permits to vary the electron density in the TMDC. Source: [82]

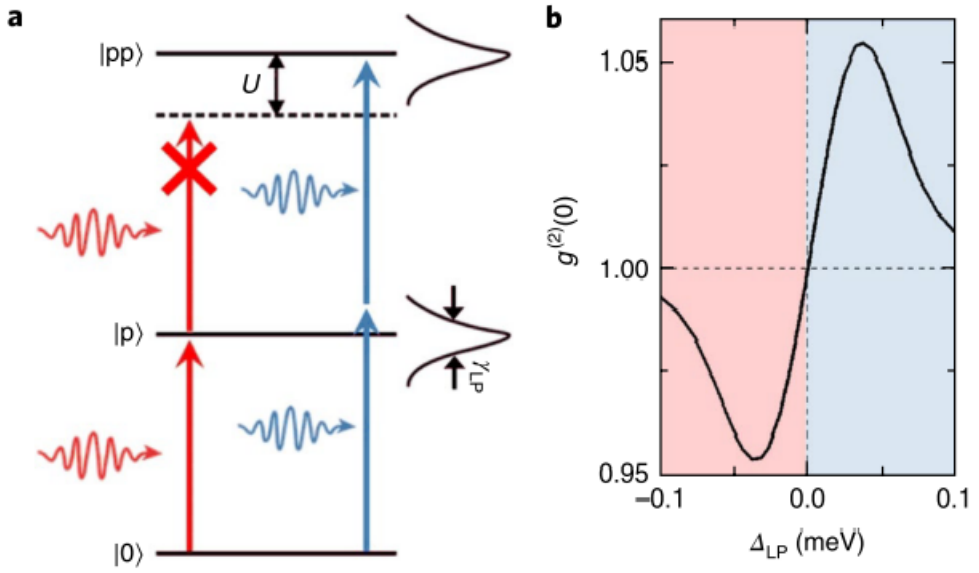

Fig. 8.2 **a**: the two-polariton state $|p,p\rangle$ is blue-shifted in energy by U = polariton–polariton interaction. If this quantity is larger than the polariton linewidth γ_{LP}, the injection of a second (slightly red-detuned) photon is inhibited, resulting in antibunching due to conventional polariton blockade. On the other hand, the presence of a second photon is enhanced for a blue-detuned pump, giving rise to bunching. **b**: consequently, we observe antibunching (bunching) for a pump which is red- (blue-)detuned compared to the polariton resonance. Source: [12]

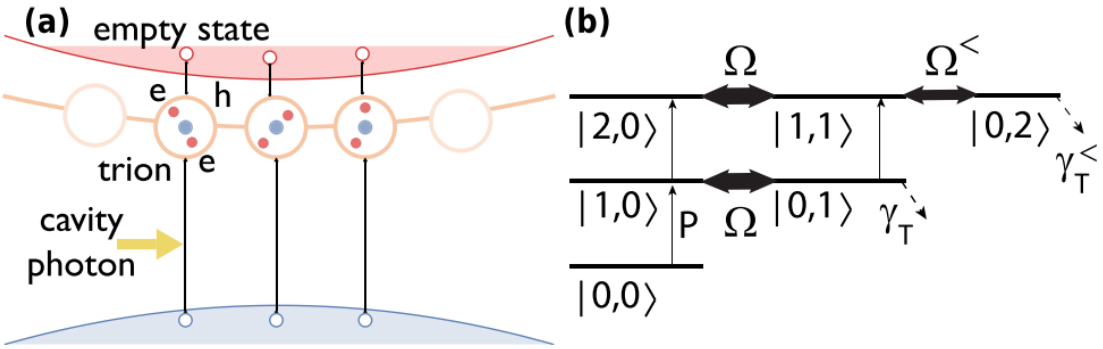

Fig. 8.3 **(a)**: schematic of trion formation, where a cavity photon produces an electron-hole pair and catches an electron. **(b)**: energy level scheme in photon-trion basis $|N_C,N_T\rangle$, where the unconventional polariton blockade arises from the destructive interference between the direct excitation path and trion-mediated path thanks to the coupling reduction in the presence of two trions. Source: [171]

Another fascinating future research might involve a little investigated mixed state called dipolar polariton (or dipolariton), shown in Figure 8.4. Apparently, they could enhance the nonlinear exciton-exciton interaction up to two orders of magnitude compared to standard exciton-polaritons. For example, they can be created by applying a static electric field orthogonally to the waveguide plane [172]. This huge increasing in the interaction strength could allow observation of nonlinear phenomena at lower powers and shorter length scales. Therefore, to do that, we can take advantage of indirect excitons. They can be formed by employing multiple QWs (MQWs) [173] or atomically thin heterostructures [60]. Indeed, since their constituent electrons and holes belong to different QWs (or MLs) [174], these long-lived indirect excitons show permanent out-of-plane electric dipole moments all aligned with each other, causing a repulsive interaction between them. The tunability of the TMDC heterostructures using different materials, changing the angle of the moiré lattice [175] and varying the composition of their alloys, offers a great flexibility which is still unexplored.

This amazing characteristic of TMDC heterostructures can also be exploited to obtain lasing at different wavelengths in a grating cavity [176]. These interlayer excitons (that maintain large oscillator strength) could be interesting for ultrafast lasing at low power threshold. As shown in Figure 8.5(b), the whole structure creates the classical three-level system necessary to reach population inversion for photon lasing, thanks to the rapid electron transfer from one CB to the other and the long lifetime of the subsequent indirect exciton. But a further use of this photonic crystal slab would be of course represented by the implementation of polaritons. Indeed, realisation of polariton lasing (linked to BEC) would avoid the need of population inversion, reducing even more the lasing power threshold. In order to do that, coupling of the active medium with optical bound states in the continuum could be exploited [177]. Properly designing the confinement structure, it is possible to open a bandgap at the exciton resonance, then creating polaritons with negative effective mass and so negative GVD, also leading to soliton formation [166].

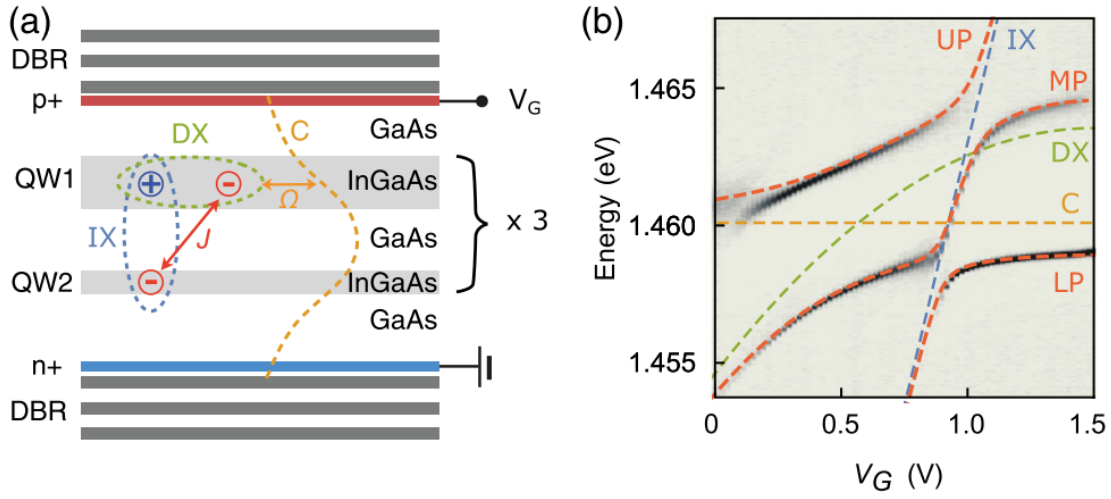

Fig. 8.4 **(a)**: schematic of a possible sample structure, with MQWs to exploit indirect excitons (IXs). **(b)**: spectrum as a function of gate voltage V_G showing changes in direct exciton (DX - green dashed line) and IX (blue dashed lines) energies, leading to variation in the energies of the polariton branches. Source: [173]

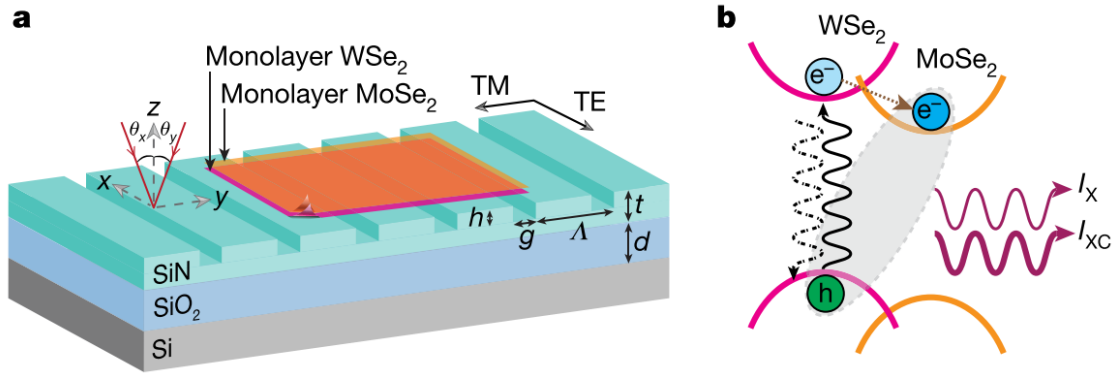

Fig. 8.5 **a**: schematic of sample structure, consisting in a grating cavity with a TMDC heterostructure on top. **b**: indirect exciton formation, with consequent population inversion for lasing. Source: [176]

Intensively studied in GaAs-based waveguides (see Figure 8.6) [10, 120], optical solitons (introduced in Section 1.2.3) could be also investigated in GaN-waveguides up to room temperature.

For polariton in the LPB of a waveguide in the strong coupling regime, the GVD parameter β_2 (introduced in Section 7.4) is negative. In this scenario, if the dispersion-induced broadening is balanced by SPM nonlinear effect, optical solitons can exist [158].

They already manifest in optical fibers, but for on-chip applications we want them to form over short length scale. To do so, the large nonlinearity provided by exciton-polaritons make them potentially interesting for ultrafast communication technologies.

A ridge waveguide, providing lateral confinement, would inhibit propagation in all directions and then increase nonlinear interactions.

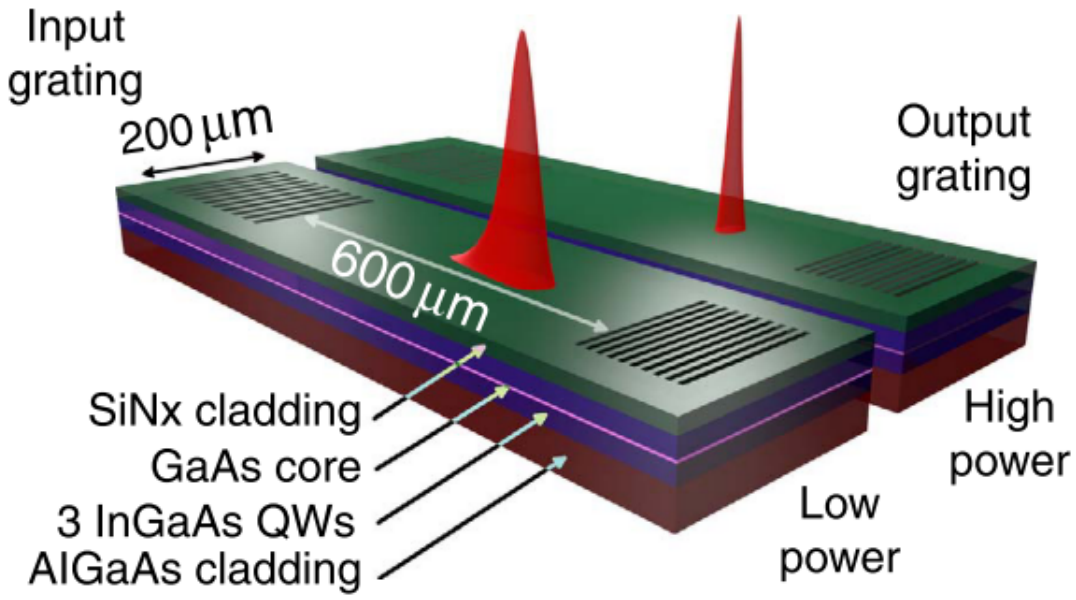

Fig. 8.6 Schematic of a waveguide under low and high pump power. Source: [10]

Another interesting emerging field, where polaritons can play an important role thanks to their increased photon-photon interactions, is that of topological photonics, where the protected edge states guarantee unidirectional propagation of light [178]. The corresponding topological polaritons (or topolaritons) mix, as usual, the characteristics of both the constituents: in this specific case, we are interested in the Zeeman splitting arising from the non-negligible magnetic moment due to the the electron-hole spins of the exciton component and the TE-TM splitting of the photon component, which acts as an effective magnetic field. The combination of both these phenomena conducts to the opening of a topological gap [179]. Two proposal have been made to make the most of it: employ an honeycomb lattice under a magnetic field [180] or manipulate the exciton-photon coupling phase in microcavities or dielectric slab waveguides [181]. However, taking advantage from the valley properties of TMDCs described in Secion 2.2.1, there would be no need for an external magnetic field [182]. The structure shown in Figure 8.7 could be used for this kind of study.

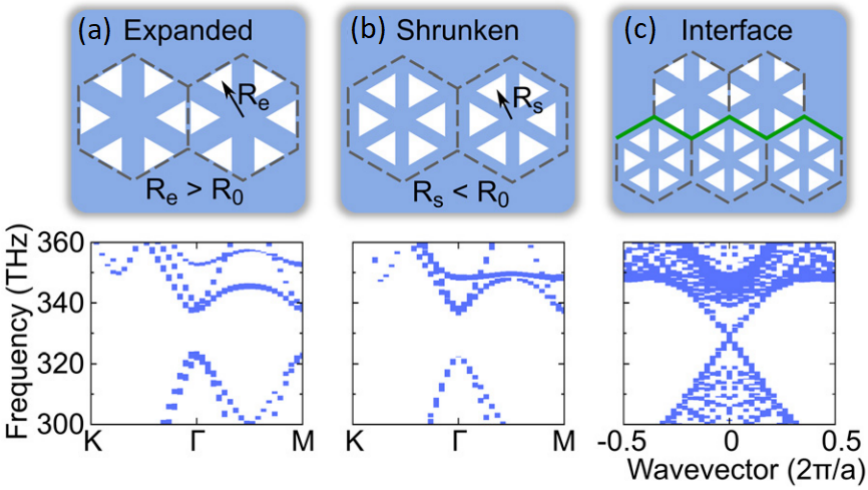

Fig. 8.7 Schematic of **(a)** expanded and **(b)** shrunken unit cells, with corresponding band diagram. Note the opening of the bandgap for this new configuration. **(c)**: the edge modes at the interface between the two different unit cells show band crossing. Source: [183]

As reported in Reference [1], an all-optical ultrafast switching device could be realised implementing the symmetric Mach-Zehnder (SMZ) interferometer depicted in Figure 8.8. In this scheme, the switching operation arises from the phase shift due to the control beam, leading to interference between the two branches of the interferometer. From this point of view, our highly nonlinear GaN-based waveguides in the strong coupling regime might play an important role.

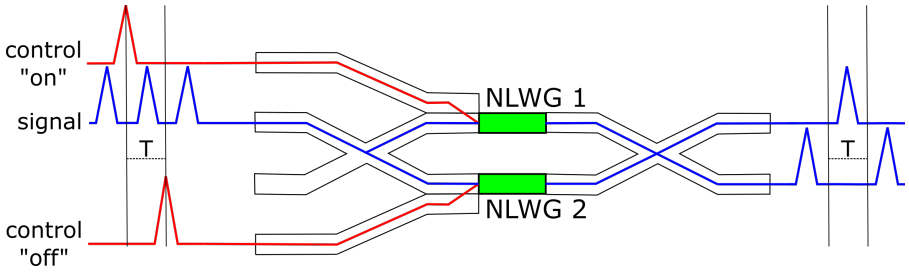

Fig. 8.8 Schematic of a switch device based on nonlinear waveguides (NLWGs) in a Mach-Zehnder interferometer. The switching process for the signal arises from the phase shift due to the change in the refractive index caused by the control pulses in the two arms, consecutively injected after a short interval T.

However, for phase shift, it would be also possible to exploit two different polarisation states instead of two waveguides. But we need to always remember that, as alluded in Sec-

tion 1.1, pure photonic approach to quantum computation is limited by the extremely weak interactions between photons. Indeed, a photon in one optical mode should ideally change the phase of a different photon in another optical mode by π, so strong interaction would be needed. Given the scalability limitation of cavity photon systems coupled to atoms and QDs (keep in mind what stated in Section 1.1), an alternative approach might be represented by XPM arising from Kerr-like nonlinearity [158]. This nonlinear phase shift is generated by another field with different wavelength and/or polarisation, where the presence of one photon in the medium changes the refractive index perceived by the other photon. In order to exploit this phenomenon, quantum effects can be enhanced by using systems with discrete optical modes, since they can reduce the quantum noise due to the reduction of available energy states for scattering [184]. Having said that, 0D micropillars (shown in Figure 8.9) and hemispherical microcavities, with reduced mode area and linewidths, could be the most effective systems thanks to their scalability and quantised optical modes. Moreover, they allow ultrafast operation due to their characteristic lifetimes ($\sim 10\ ps$). The linear polarisation of a signal photon in the excited state would rotate because of the presence of a circularly polarised control photon in the ground state, giving rise to a phase shift at single-particle level.

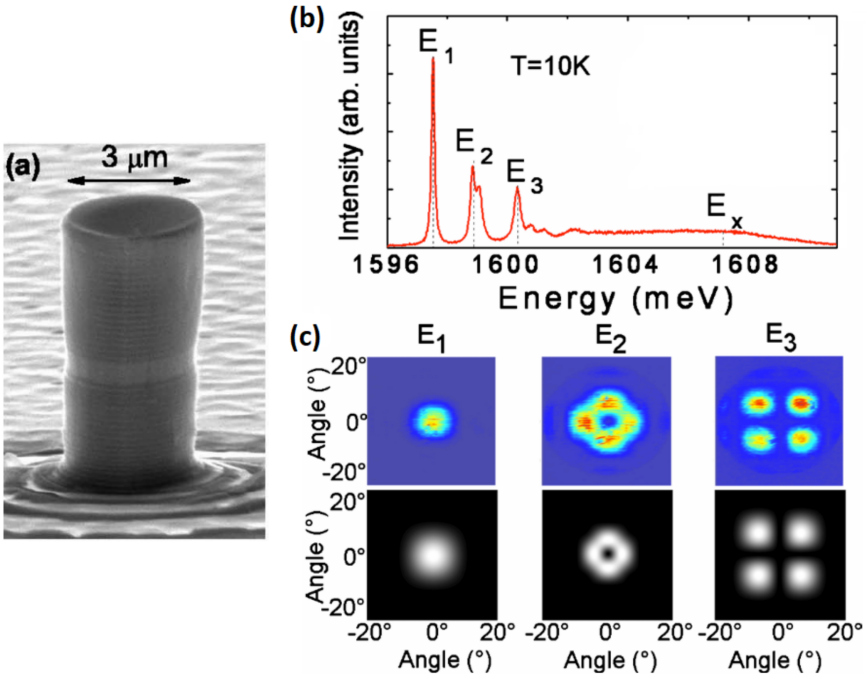

Fig. 8.9 **(a)**: scanning electron microscope (SEM) image of a micropillar. Source: [185]. **(b)**: PL emission of the first three discrete modes. **(c)**: 2D far-field patterns for the first three discrete modes. Source: [186]

Last but not least, exciton-polaritons could be used to reach high temperature superconductivity. Indeed, according to Bardeen-Cooper-Schrieffer (BCS) theory, the attractive electron-electron interaction necessary to form a Cooper pair is mediated by a phonon. Given its weak coupling, superconductivity is observed at cryogenic temperatures. Instead of this kind of boson, microcavity exciton-polaritons can be exploited. Specifically, these new quasi-particles formed by two attractively interacting electrons and a polariton, called "quatrons" (or quadrions), present the fundamental characteristic of being boson with electric charge, leading to a superfluid propagation of current, i.e. superconductivity [187]. Moreover, the critical temperature to observe this transition only depends on that of the BEC and the electron-electron interaction strength would just be affected by the polaritons density, so by the pump power. Theoretically, the critical density to achieve superfluidity was shown to be lower that the Mott density, especially for TMDCs due to their small exciton Bohr radius. A suitable structure might be the one shown in Figure 8.10. Another possible configuration could be given by n-doped QW (containing a two-dimensional degenerate electron gas - 2DEG) sandwiched between two undoped QWs (containing a BEC) [188].

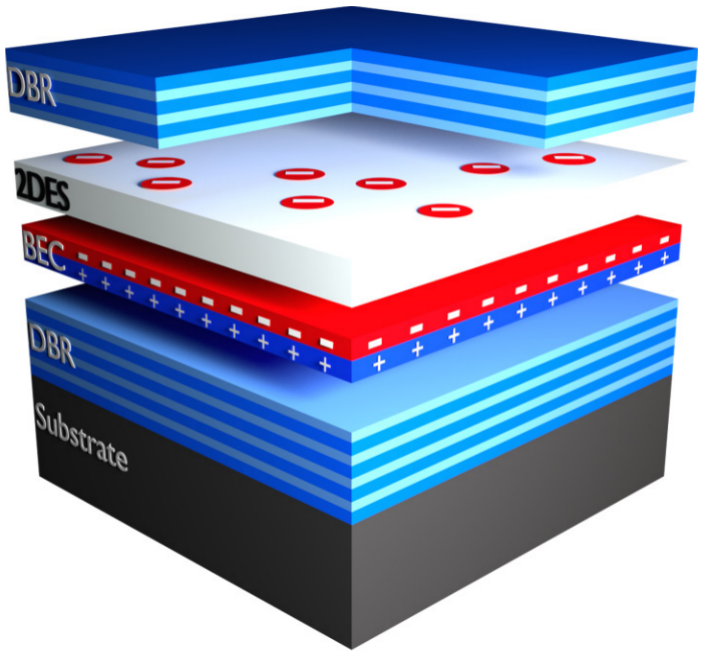

Fig. 8.10 Possible configuration to observe exciton-polariton superconductivity, where the BEC can strongly interact with the 2DEG within a microcavity in a TMDC monolayer. Source: [189]

References

[1] O. Wada. Femtosecond all-optical devices for ultrafast communication and signal processing. *New Journal of Physics*, 6:183, 2004.

[2] D. Chang et al. Quantum nonlinear optics - photon by photon. *Nature Photonics*, 8:685–694, 2014.

[3] S. Sun et al. A quantum phase switch between a single solid-state spin and a photon. *Nature Nanotechnology*, 11:539–545, 2016.

[4] Q. A. Turchette et al. Measurement of conditional phase shifts for quantum logic. *Physical Review Letters*, 75:4710–4713, 1995.

[5] D. Englund et al. Ultrafast photon-photon interaction in a strongly coupled quantum dot-cavity system. *Physical Review Letters*, 108:093604, 2012.

[6] D. Sanvitto et al. The road towards polaritonic devices. *Nature Materials*, 15:1061–1073, 2016.

[7] S. I. Pekar. Theory of electromagnetic waves in a crystal with excitons. *Journal of Physics and Chemistry of Solids*, 5:11–22, 1958.

[8] J. J. Hopfield. Theory of the contribution of excitons to the complex dielectric constant of crystals. *Physical Review*, 112:1555–1567, 1958.

[9] C. Weisbuch et al. Observation of the coupled exciton-photon mode splitting in a semiconductor quantum microcavity. *Physical Review Letters*, 69:3314–3317, 1992.

[10] P. M. Walker et al. Ultra-low-power hybrid light-matter solitons. *Nature Communications*, 6:8317, 2015.

[11] A. Cuevas et al. First observation of the quantized exciton-polariton field and effect of interactions on a single polariton. *Science Advances*, 4:eaao6814, 2018.

[12] G. Munoz-Matutano et al. Emergence of quantum correlations from interacting fibre-cavity polaritons. *Nature Materials*, 18:213–218, 2019.

[13] D. Ballarini et al. All-optical polariton transistor. *Nature Communications*, 4:1778, 2013.

[14] C. Sturm et al. All-optical phase modulation in a cavity-polariton Mach-Zehnder interferometer. *Nature Communications*, 5:3278, 2014.

[15] J. Kasprzak et al. Bose-Einstein condensation of exciton polaritons. *Nature*, 443:409–414, 2006.

[16] A. Amo et al. Superfluidity of polaritons in semiconductor microcavities. *Nature Physics*, 5:805–810, 2009.

[17] R. Stevenson et al. Continuous wave observation of massive polariton redistribution by stimulated scattering in semiconductor microcavities. *Physical Review Letters*, 85:3680–2683, 2000.

[18] M. Sich et al. Observation of bright polariton solitons in a semiconductor microcavity. *Nature Photonics*, 6:50–55, 2011.

[19] C. Kittel. *Introduction to solid state physics - 8th ed.* Wiley, 2004.

[20] C. F. Klingshirn. *Semiconductor optics - 4th ed.* Springer, 2012.

[21] H. Deng et al. Exciton-polariton Bose-Einstein condensation. *Reviews of Modern Physics*, 82:1489–1537, 2010.

[22] L. Novotny. Strong coupling, energy splitting, and level crossings: A classical perspective. *American Journal of Physics*, 78:1199–1202, 2010.

[23] A. V. Kavokin et al. *Microcavities*. Oxford University Press, 2007.

[24] C. E. Whittaker. *Pattern formation, photonic spin-orbit coupling and topological states in semiconductor microcavities and micropillar lattices*. PhD thesis, The University of Sheffield, 2018.

[25] M. Fox. *Quantum Optics - An Introduction*. Oxford University Press, 2005.

[26] P. Renucci et al. Microcavity polariton spin quantum beats without a magnetic field: A manifestation of Coulomb exchange in dense and polarized polariton systems. *Physical Review B*, 72:075317, 2005.

[27] I. Carusotto et al. Quantum fluids of light. *Reviews of Modern Physics*, 85:299–366, 2013.

[28] A. S. Brichkin et al. Effect of Coulomb interaction on exciton-polariton condensates in GaAs pillar microcavities. *Physical Review B*, 84:195301, 2011.

[29] F. Tassone et al. Exciton-exciton scattering dynamics in a semiconductor microcavity and stimulated scattering into polaritons. *Physical Review B*, 59:10830–10842, 1999.

[30] S. R. K. Rodriguez et al. Interaction-induced hopping phase in driven-dissipative coupled photonic microcavities. *Nature Communications*, 7:11887, 2016.

[31] N. Bélanger et al. Soliton-like pulses in self-defocusing AlGaAs waveguides. *Journal of the Optical Society of America B*, 14:3003, 1997.

[32] A. Blanco-Redondo et al. Observation of soliton compression in silicon photonic crystals. *Nature Communications*, 5:3160, 2014.

[33] P. Colman et al. Temporal solitons and pulse compression in photonic crystal waveguides. *Nature Photonics*, 4:862, 2010.

[34] A. Yariv et al. *Photonics: Optical Electronics in Modern Communications - 6th ed.* Oxford University Press, 2007.

[35] M. Sich. *Effects of Spin-Dependent Polariton-Polariton Interactions in Semiconductor Microcavities: Spin Rings, Bright Spatial Solitons and Soliton Patterns*. PhD thesis, The University of Sheffield, 2013.

[36] F. Tassone et al. Bottleneck effects in the relaxation and photoluminescence of microcavity polaritons. *Physical Review B*, 56:7554–7563, 1997.

[37] A. I. Tartakovskii et al. Relaxation bottleneck and its suppression in semiconductor microcavities. *Physical Review B*, 62:2283–2286, 2000.

[38] M. S. Skolnick et al. Polariton-polariton interactions and stimulated scattering in semiconductor microcavities. *Materials Science and Engineering C*, 19:407–416, 2002.

[39] K. Lagoudakis. *The Physics of Exciton-Polariton Condensates*. EPFL Press, 2013.

[40] Y. Sun et al. Bose-Einstein Condensation of long-lifetime polaritons in thermal equilibrium. *Physical Review Letters*, 118:016602, 2017.

[41] T. Byrnes et al. Exciton-polariton condensates. *Nature Physics*, 10:803–813, 2014.

[42] F. London. The λ-phenomenon of liquid helium and Bose-Einstein degeneracy. *Nature*, 141:643–644, 1938.

[43] A. Amo et al. Collective fluid dynamics of a polariton condensate in a semiconductor microcavity. *Nature*, 457:291–295, 2009.

[44] G. Nardin et al. Hydrodynamic nucleation of quantized vortex pairs in a polariton quantum fluid. *Nature Physics*, 7:635–641, 2011.

[45] K. G. Lagoudakis et al. Quantized vortices in an exciton-polariton condensate. *Nature Physics*, 4:706–710, 2008.

[46] G. Roumpos et al. Single vortex-antivortex pair in an exciton-polariton condensate. *Nature Physics*, 7:129–133, 2010.

[47] A. Amo et al. Polariton superfluids reveal quantum hydrodynamic solitons. *Science*, 332:1167–1170, 2011.

[48] S. Pigeon et al. Hydrodynamic nucleation of vortices and solitons in a resonantly excited polariton superfluid. *Physical Review B*, 83:144513, 2011.

[49] P. G. Savvidis et al. Angle-resonant stimulated polariton amplifier. *Physical Review Letters*, 84:1547–1550, 2000.

[50] A. Baas et al. Optical bistability in semiconductor microcavities. *Physical Review A*, 69:023809, 2004.

[51] A. Baas et al. Optical bistability in semiconductor microcavities in the nondegenerate parametric oscillation regime: Analogy with the optical parametric oscillator. *Physical Review B*, 70:161307, 2004.

[52] D. M. Whittaker. Effects of polariton-energy renormalization in the microcavity optical parametric oscillator. *Physical Review B*, 71:115301, 2005.

[53] D. N. Krizhanovskii et al. Self-organization of multiple polariton-polariton scattering in semiconductor microcavities. *Physical Review B*, 77:115336, 2008.

[54] R. L. Greene et al. Binding energies of Wannier excitons in GaAs-$Ga_{1-x}Al_xAs$ quantum well structures. *Solid State Communications*, 45:831–835, 1983.

[55] S. Christopoulos et al. Room-temperature polariton lasing in semiconductor microcavities. *Physical Review Letters*, 98:126405, 2007.

[56] S. Christmann et al. Room temperature polariton lasing in a GaN/AlGaN multiple quantum well microcavity. *Applied Physics Letters*, 93:051102, 2008.

[57] T. Guillet et al. Polariton lasing in a hybrid bulk ZnO microcavity. *Applied Physics Letters*, 99:161104, 2011.

[58] F. Li et al. From excitonic to photonic polariton condensate in a ZnO-based microcavity. *Physical Review Letters*, 110:196404, 2013.

[59] N. Lundt et al. Monolayered $MoSe_2$: A candidate for room temperature polaritonics. *2D Materials*, 4:015006, 2017.

[60] V. Ardizzone et al. Emerging 2D materials for room-temperature polaritonics. *Nanophotonics*, 8:1547–1558, 2019.

[61] A. Fieramosca et al. Two-dimensional hybrid perovskites sustaining strong polariton interactions at room temperature. *Science Advances*, 5:eaav9967, 2019.

[62] D. G. Lidzey et al. Strong exciton-photon coupling in an organic semiconductor microcavity. *Nature*, 395:53–55, 1998.

[63] S. Kéna-Cohen et al. Room-temperature polariton lasing in an organic single-crystal microcavity. *Nature Photonics*, 4:371–375, 2010.

[64] C. Schneider et al. Two-dimensional semiconductors in the regime of strong light-matter coupling. *Nature Communications*, 9:2695, 2018.

[65] D. Ballarini et al. Polaritonics: From microcavities to sub-wavelength confinement. *Nanophotonics*, 8:641–654, 2019.

[66] L. F. Mattheiss. Band structures of transition-metal-dichalcogenide layer compounds. *Physical Review B*, 8:3719–3740, 1973.

[67] K. S. Novoselov et al. Electric field effect in atomically thin carbon films. *Science*, 306:666–669, 2004.

[68] M. Chhowalla et al. The chemistry of two-dimensional layered transition metal dichalcogenide nanosheets. *Nature Chemistry*, 5:263–275, 2013.

[69] A. V. Kolobov et al. *Two-Dimensional Transition-Metal Dichalcogenides*. Springer, 2016.

[70] K. F. Mak et al. Photonics and optoelectronics of 2D semiconductor transition metal dichalcogenides. *Nature Photonics*, 10:216–226, 2016.

[71] J. Xiao et al. Excitons in atomically thin 2D semiconductors and their applications. *Nanophotonics*, 6:1309–1328, 2017.

[72] R. Roldán et al. Electronic properties of single-layer and multilayer transition metal dichalcogenides MX_2 (M = Mo, W and X = S, Se). *Annalen der Physik*, 526:347–357, 2014.

[73] A. Chernikov et al. Exciton binding energy and nonhydrogenic Rydberg series in monolayer WS_2. *Physical Review Letters*, 113:076802, 2014.

[74] G. Wang et al. Colloquium: Excitons in atomically thin transition metal dichalcogenides. *Reviews of Modern Physics*, 90:021001, 2018.

[75] X. Xu et al. Spin and pseudospins in layered transition metal dichalcogenides. *Nature Physics*, 10:343–350, 2014.

[76] J. R. Schaibley et al. Valleytronics in 2D materials. *Nature Reviews Materials*, 1:16055, 2016.

[77] M. Koperski et al. Optical properties of atomically thin transition metal dichalcogenides: Observations and puzzles. *Nanophotonics*, 6:1289–1308, 2017.

[78] H. Yu et al. Valley excitons in two-dimensional semiconductors. *National Science Review*, 2:57–70, 2015.

[79] K. F. Mak et al. Tightly bound trions in monolayer MoS_2. *Nature Materials*, 12:207–211, 2013.

[80] K. Hao et al. Neutral and charged inter-valley biexcitons in monolayer $MoSe_2$. *Nature Communications*, 8:15552, 2017.

[81] J. S. Ross et al. Electrical control of neutral and charged excitons in a monolayer semiconductor. *Nature Communications*, 4:1474, 2013.

[82] M. Sidler et al. Fermi polaron-polaritons in charge-tunable atomically thin semiconductors. *Nature Physics*, 13:255–261, 2017.

[83] I. Kylänpää et al. Binding energies of exciton complexes in transition metal dichalcogenide monolayers and effect of dielectric environment. *Physical Review B*, 92:205418, 2015.

[84] S. Schwarz. *Microcavity-enhanced light-matter interaction in van der Waals heterostructures*. PhD thesis, The University of Sheffield, 2015.

[85] K. S. Novoselov et al. 2D materials and van der Waals heterostructures. *Science*, 353:aac9439, 2016.

[86] J. D. Caldwell et al. Photonics with hexagonal boron nitride. *Nature Reviews Materials*, 4:552–567, 2019.

[87] Y. Zhao et al. Large-area synthesis of monolayer $MoSe_2$ films on SiO_2/Si substrates by atmospheric pressure chemical vapor deposition. *Royal Society of Chemistry Advances*, 7:27969–27973, 2017.

[88] H. Wang et al. Revealing the microscopic CVD growth mechanism of $MoSe_2$ and the role of hydrogen gas during the growth procedure. *Nanotechnology*, 29:314001, 2018.

[89] S. Nakamura. Nobel lecture: Background story of the invention of efficient blue InGaN light emitting diodes. *Reviews of Modern Physics*, 87:1139–1151, 2015.

[90] W. Bi et al. *Handbook of GaN Semiconductor Materials and Devices*. CRC Press, 2018.

[91] Y. P. Varshni. Temperature dependence of the energy gap in semiconductors. *Physica*, 34:149–154, 1967.

[92] L. Vi na et al. Temperature dependence of the dielectric function of germanium. *Physical Review B*, 30:1979–1991, 1984.

[93] D. Brunner et al. Optical constants of epitaxial AlGaN films and their temperature dependence. *Journal of Applied Physics*, 82:5090–5096, 1997.

[94] I. Vurgaftman et al. Band parameters for nitrogen-containing semiconductors. *Journal of Applied Physics*, 94:3675–3696, 2003.

[95] W. Paszkowicz et al. Rietveld-refinement for indium nitride in the 105-295 K range. *Powder Diffraction*, 18:114–121, 2004.

[96] W. Paszkowicz et al. Rietveld-refinement study of aluminium and gallium nitrides. *Journal of Alloys and Compounds*, 382:100–106, 2004.

[97] O. Ambacher et al. Pyroelectric properties of Al(In)GaN/GaN hetero- and quantum well structures. *Condensed Matter*, 14:3399–3434, 2002.

[98] A. V. Rodina et al. Free excitons in wurtzite GaN. *Physical Review B*, 64:115204, 2001.

[99] B. Monemar. Recombination of free and bound excitons in GaN. *Physica Status Solidi (b)*, 245:1723–1740, 2008.

[100] B. Gil et al. Internal structure of the neutral donor-bound exciton complex in zinc-blende and wurtzite semiconductors. *Physical Review B*, 75:085204, 2007.

[101] J. Ciers et al. Propagating polaritons in III-Nitride slab waveguides. *Physical Review Applied*, 7:034019, 2017.

[102] P. Sohi et al. Critical thickness of GaN on AlN: impact of growth temperature and dislocation density. *Semiconductor Science and Technology*, 32:075010, 2017.

[103] S. Nakamura et al. Novel metalorganic chemical vapor deposition system for GaN growth. *Applied Physics Letters*, 58:2021–2023, 1991.

[104] J. A. S. Ciers. *Light-Matter Interaction in III-Nitride Waveguides: Propagating Polaritons and Optical Gain*. PhD thesis, École Polytechnique Fédérale de Lausanne, 2018.

[105] A. Castiglia et al. Emission characteristics of GaN-based blue lasers including a lattice matched $Al_{0.83}In_{0.17}N$ optical blocking layer for improved optical beam quality. *Applied Physics Letters*, 97:111104, 2010.

[106] R. Butté et al. Current status of AlInN layers lattice-matched to GaN for photonics and electronics. *Journal of Physics D: Applied Physics*, 40:6328–6344, 2007.

[107] J. Vahala. Optical microcavities. *Nature*, 424:839–846, 2003.

[108] X. Yu et al. Strong coupling in microcavity structures: Principle, design, and practical application. *Laser and Photonics Reviews*, 13:1800219, 2018.

[109] C. Schneider et al. Exciton-polariton trapping and potential landscape engineering. *Reports on Progress in Physics*, 80:016503, 2017.

[110] C. E. Whittaker et al. Exciton polaritons in a two-dimensional Lieb lattice with spin-orbit coupling. *Physical Review Letters*, 120:097401, 2018.

[111] F. Li. *Fabrication and characterization of ZnO-based microcavities working in the strong coupling regime: polariton laser*. PhD thesis, Université Nice Sophia Antipolis, 2014.

[112] V. Savona et al. Optical properties of microcavity polaritons. *Phase Transitions*, 68:169–279, 1999.

[113] P. Dolan et al. Femtoliter tunable optical cavity arrays. *Optics Letters*, 35:3556–3558, 2010.

[114] S. Dufferwiel. *Strongly Confined Exciton-Polaritons in a Tunable Microcavity*. PhD thesis, The University of Sheffield, 2014.

[115] A. E. Siegman. *Lasers*. Science Books, 1986.

[116] A. Trichet et al. Topographic control of open-access microcavities at the nanometer scale. *Optics Express*, 23:17205–17216, 2015.

[117] D. M. Di Paola et al. Ultrafast-nonlinear ultraviolet pulse modulation in an AlInGaN polariton waveguide operating up to room temperature. *arXiv:2009.02059*, 2020.

[118] L. L. C. Tinkler. *Optical nonlinearities in semiconductor polariton waveguides*. PhD thesis, The University of Sheffield, 2015.

[119] P. M. Walker et al. Exciton polaritons in semiconductor waveguides. *Applied Physics Letters*, 102:012109, 2013.

[120] P. M. Walker et al. Dark solitons in waveguide polariton fluids shed light on interaction constants. *Physical Review Letters*, 119:097403, 2017.

[121] E. M. Alexeev et al. Imaging of interlayer coupling in van der Waals heterostructures using a bright-field optical microscope. *Nano Letters*, 17:5342–5349, 2017.

[122] O. Svelto. *Principles of Lasers - 5th ed.* Springer, 2010.

[123] D. Strickland et al. Compression of amplified chirped optical pulses. *Optics Communications*, 56:219–221, 1985.

[124] E. J. Sie. *Coherent Light-Matter Interactions in Monolayer Transition-Metal Dichalcogenides*. Springer Theses, 2018.

[125] T. G. Brown et al. *The Optics Encyclopedia*. Wiley-VCH, 2004.

[126] G. Scuri et al. Large exciton reflectivity of monolayer $MoSe_2$ encapsulated in hexagonal boron nitride. *Physical Review Letters*, 120:037402, 2018.

[127] X. Liu et al. Strong light-matter coupling in two-dimensional atomic crystals. *Nature Photonics*, 9:30–34, 2014.

[128] F. Barachati et al. Interacting polariton fluids in a monolayer of tungsten disulfide. *Nature Nanotechnology*, 13:906–909, 2018.

[129] S. Dufferwiel et al. Valley-addressable polaritons in atomically thin semiconductors. *Nature Photonics*, 11:497–501, 2017.

[130] J. C. Shaw et al. Chemical vapor deposition growth of monolayer $MoSe_2$ nanosheets. *ACS Nano*, 8:5125–5131, 2014.

[131] G. Plechinger et al. A direct comparison of CVD-grown and exfoliated MoS_2 using optical spectroscopy. *Semiconductor Science and Technology*, 29:064008, 2014.

[132] C. H. Chang et al. Orbital analysis of electronic structure and phonon dispersion in MoS_2, $MoSe_2$, WS_2, and WSe_2 monolayers under strain. *Physical Review B*, 88:195420, 2013.

[133] S. Horzum. Phonon softening and direct to indirect band gap crossover in strained single-layer $MoSe_2$. *Physical Review B*, 87:125415, 2013.

[134] G. Moody. Intrinsic homogeneous linewidth and broadening mechanisms of excitons in monolayer transition metal dichalcgenides. *Nature Communications*, 6:8315, 2015.

[135] S. Dufferwiel et al. Exciton-polaritons in van der Waals heterostructures embedded in tunable microcavities. *Nature Communications*, 6:8579, 2015.

[136] Q. Zhang et al. Recoil effect and photoemission splitting of trions in monolayer MoS_2. *ACS Nano*, 11:10808–10815, 2017.

[137] F. Cadiz et al. Excitonic linewidth approaching the homogeneous limit in MoS_2-based van der Waals heterostructures. *Physical Review X*, 7:021026, 2017.

[138] A. Chernikov et al. Population inversion and giant bandgap renormalization in atomically thin WS_2 layers. *Nature Photonics*, 9:466–470, 2015.

[139] C. Chakraborty et al. Localized emission from defects in $MoSe_2$ layers. *Optical Materials Express*, 6:2081–2087, 2016.

[140] E. J. Sie et al. Observation of exciton redshift-blueshift crossover in monolayer WS_2. *Nano Letters*, 17:4210–4216, 2017.

[141] C. Ruppert et al. The role of electronic and phononic excitation in the optical response of monolyaer WS_2 after ultrafast excitation. *Nano Letters*, 17:644–651, 2017.

[142] F. Yang et al. Origin of the Stokes shift: A geometrical model of exciton spectra in 2D semiconductors. *Physical Review Letters*, 70:323–326, 1993.

[143] K. M. McCreary et al. The effect of preparation conditions on Raman and photoluminescence of monolayer WS_2. *Scientific Reports*, 6:35154, 2016.

[144] M. Manca et al. Enabling valley selective exciton scattering in monolayer WSe_2 through upconversion. *Nature Communications*, 8:14927, 2017.

[145] L. Giriunas et al. Formation of a macroscopically occupied polariton state in a tunable open-access microcavity under resonant excitation. *Journal of Applied Physics*, 124:025703, 2018.

[146] R. P. A. Emmanuele et al. Highly nonlinear trion-polaritons in a monolayer semiconductor. *Nature Communications*, 11:3589, 2020.

[147] D. Sarkar et al. Polarization bistability and resultant spin rings in semiconductor microcavities. *Physical Review Letters*, 105:216402, 2010.

[148] D. W. Snoke et al. Spin flip of excitons in GaAs quantum wells. *Physical Review B*, 55:13789, 1997.

[149] J. O. Tollerud et al. Revealing and characterizing dark excitons through coherent multidimensional spectroscopy. *Physical Review Letters*, 117:007401, 2016.

[150] J. M. Ménard et al. Revealing the dark side of a bright exciton-polariton condensate. *Nature Communications*, 5:4648, 2014.

[151] T. Gu et al. Regenerative oscillation and four-wave mixing in graphene optoelectronics. *Nature Photonics*, 6:554, 2012.

[152] K. Wang et al. Broadband ultrafast nonlinear absorption and nonlinear refraction of layered molybdenum dichalcogenide semiconductors. *Nanoscale*, 6:10530, 2014.

[153] C. Torres-Torres et al. Third order nonlinear optical response exhibited by mono- and few-layers of WS_2. *2D Materials*, 3:021005, 2016.

[154] V. Shahnazaryan et al. Exciton-exciton interaction in transition-metal dichalcogenide monolayers. *Physical Review B*, 96:115409, 2017.

[155] Y. P. Kim et al. Intensity-induced nonlinear effects in UV window materials. *Applied Physics B*, 49:469–478, 1989.

[156] P. M. Walker et al. Spatiotemporal continuum generation in polariton waveguides. *Light: Science & Applications*, 8:6, 2019.

[157] F. Yang et al. Effects of dispersive two-photon transitions on femtosecond pulse propagation in semiconductor waveguides. *Applied Physics Letters*, 63:1304–1306, 1993.

[158] G. P. Agrawal. *Nonlinear fiber optics - 5th ed.* Academic Press, 2013.

[159] G. Rossbach et al. Impact of saturation on the polariton renormalization in III-nitride based planar microcavities. *Physical Review B*, 88:165312, 2013.

[160] F. Bernardini et al. Polarization-based calculation of the dielectric tensor of polar crystals. *Physical Review Letters*, 79:3958–3961, 1997.

[161] K. Kornitzer et al. Photoluminescence and reflectance spectroscopy of excitonic transitions in high-quality homoepitaxial GaN films. *Physical Review B*, 60:1471–1473, 1999.

[162] V. Pačebutas et al. Picosecond Z-scan measurements on bulk GaN crystals. *Applied Physics Letter*, 78:4118–4120, 2001.

[163] G. F. B. Almeida et al. Third-order nonlinear spectrum of GaN under femtosecond-pulse excitation from the visible to the near infrared. *Photonics*, 6:69, 2019.

[164] Y.-L. Huang et al. Femtosecond Z-scan measurement of GaN. *Applied Physics Letters*, 75:3524–3526, 1999.

[165] B. Taheri et al. Picosecond four-wave-mixing in GaN epilayers at 532 *nm*. *Applied Physics Letters*, 68:587–589, 1996.

[166] V. Kravtsov et al. Nonlinear polaritons in a monolayer semiconductor coupled to optical bound states in the continuum. *Light: Science Applications*, 9:56, 2020.

[167] T. Voltz et al. Ultrafast all-optical switching by single photons. *Nature Photonics*, 6:605–609, 2012.

[168] S. Sun et al. A single-photon switch and transistor enabled by a solid-state quantum memory. *Science*, 361:57–60, 2018.

[169] L. Ferrier et al. Interactions in confined polariton condensates. *Physical Review Letters*, 106:126401, 2011.

[170] A. Delteil et al. Towards polariton blockade of confined exciton-polaritons. *Nature Materials*, 18:219–222, 2019.

[171] O. Kyriienko et al. Nonlinear quantum optics with trion-polaritons in 2D monolayers: conventional and unconventional photon blockade. *Physical Review Letters*, 125:197402, 2020.

[172] I. Rosenberg et al. Strongly interacting dipolar-polaritons. *Science Advances*, 4:eaat8880, 2018.

[173] E. Togan et al. Enhanced interactions between dipolar polaritons. *Physical Review Letters*, 121:227402, 2018.

[174] J. Wilkes et al. Excitons and polaritons in planar heterostructures in external electric and magnetic fields: A multi-sub-level approach. *Superlattices and Microstructures*, 108:32–41, 2017.

[175] E. M. Alexeev et al. Resonantly hybridized excitons in moiré superlattices in van der Waals heterostructures. *Nature*, 567:81–97, 2019.

[176] E. Paik et al. Interlayer exciton laser of extended spatial coherence in atomically thin heterostructures. *Nature*, 576:80–84, 2019.

[177] C. Hsu. Bound states in the continuum. *Nature Reviews Materials*, 9:16048, 2016.

[178] M. Hasan et al. Colloquium: Topological insulators. *Reviews of Modern Physics*, 82:3045–3067, 2010.

[179] T. Ozawa et al. Topological photonics. *Reviews of Modern Physics*, 91:15006, 2019.

[180] A. Nalitov et al. Polariton Z topological insulator. *Physical Review Letters*, 114:116401, 2015.

[181] T. Karzig et al. Topological polaritons. *Physical Review X*, 5:31001, 2015.

[182] K. F. Mak et al. The valley hall effect in MoS_2 transistors. *Science*, 344:1489–1492, 2014.

[183] M. Jalali Mehrabad et al. A semiconductor topological photonic ring resonator. *Applied Physics Letters*, 116:061102, 2020.

[184] T. Boulier et al. Polariton-generated intensity squeezing in semiconductor micropillars. *Nature Communications*, 5:3260, 2014.

[185] D. Bajoni et al. Polariton parametric luminescence in a single micropillar. *Applied Physics Letters*, 90:051107, 2007.

[186] L. Ferrier et al. Polariton parametric oscillation in a single micropillar cavity. *Applied Physics Letters*, 97:031105, 2010.

[187] F. Laussy et al. Superconductivity with excitons and polaritons: review and extension. *Journal of Nanophotonics*, 6:064502, 2012.

[188] F. Laussy et al. Exciton-polariton mediated superconductivity. *Physical Review Letters*, 104:106402, 2010.

[189] O. Cotlet et al. Superconductivity and other collective phenomena in a hybrid Bose-Fermi mixture formed by a polariton condensate and an electron system in two dimensions. *Physical Review B*, 93:054510, 2016.

[190] M. Combescot et al. The many-body physics of composite bosons. *Physics Report*, 463:215320, 2008.

[191] M. Kira et al. Many-body correlations and excitonic effects in semiconductor spectroscopy. *Progress in Quantum Electronics*, 30:155296, 2006.

[192] G. Rochat et al. Excitonic bloch equations for a two-dimensional system of interacting excitons. *Physical Review B*, 61:13856, 2000.

[193] P. Cudazzo et al. Dielectric screening in two-dimensional insulators: Implications for excitonic and impurity states in graphane. *Physical Review B*, 84:085406, 2011.

[194] T. C. Berkelbach et al. Theory of neutral and charged excitons in monolayer transition metal dichalcogenides. *Physical Review B*, 88:045318, 2013.

[195] S. Larentis et al. Large effective mass and interaction-enhanced Zeeman splitting of K-valley electrons in $MoSe_2$. *Physical Review B*, 97:201407, 2018.

[196] M. Combescot. Trions in first and second quantizations. *European Physical Journal B*, 33:311320, 2003.

[197] E. Mostani et al. Diffusion quantum Monte Carlo study of excitonic complexes in two-dimensional transition-metal dichalcogenides. *Physical Review B*, 96:075431, 2017.

[198] G. Ramon et al. Theory of neutral and charged exciton scattering with electrons in semiconductor quantum wells. *Physical Review B*, 67:045323, 2003.

[199] D. W. Kidd et al. Binding energies and structures of two-dimensional excitonic complexes in transition metal dichalcogenides. *Physical Review B*, 93:125423, 2016.

[200] R. Rapaport et al. Negatively charged polaritons in a semiconductor microcavity. *Physical Review B*, 63:235310, 2001.

[201] S. Y. Shiau et al. Way to observe the implausible "trion-polariton". *Euro Physics Letters*, 117:57001, 2017.

[202] Y. C. Chang et al. Cross-over from trion-hole to exciton-polaron in n-doped semiconductor quantum wells. *Physical Review B*, 98:235203, 2018.

[203] S. Y. Shiau et al. Trion ground state, excited states, and absorption spectrum using electron-exciton basis. *Physical Review B*, 86:115210, 2012.

[204] M. Combescot et al. Trion oscillator strength. *Solid State Communications*, 128:273277, 2003.

[205] S. De Liberato et al. Stimulated scattering and lasing of intersubband cavity polaritons. *Physical Review Letters*, 102:136403, 2009.

[206] M. Combescot et al. General many-body formalism for composite quantum particles. *Physical Review Letters*, 104:206404, 2010.

[207] M. Combescot et al. Effective scatterings between electrons, excitons and trions. *European Physical Journal B*, 79:401421, 2011.

[208] R. Rapaport et al. Negatively charged quantum well polaritons in a GaAs/AlAs microcavity: An analog of atoms in a cavity. *Physical Review Letters*, 84:1607, 2000.

[209] K. Hammerer et al. Quantum interface between light and atomic ensembles. *Reviews of Modern Physics*, 82:1041, 2010.

[210] M. Combescot et al. Composite boson many-body theory for Frenkel excitons. *European Physical Journal B*, 68:161, 2009.

[211] T. Holstein et al. Field dependence of the intrinsic domain magnetization of a ferromagnet. *Physical Review*, 58:1098, 1940.

[212] C. Emary et al. Quantum chaos triggered by precursors of a quantum phase transition: The Dicke model. *Physical Review Letters*, 90:044101, 2003.

[213] C. Emary et al. Chaos and the quantum phase transition in the Dicke model. *Physical Review E*, 67:066203, 2003.

[214] S. Dufferwiel et al. Strong exciton-photon coupling in open semiconductor microcavities. *Applied Physics Letters*, 104:192107, 2014.

[215] S. Dufferwiel et al. Tunable polaritonic molecules in an open microcavity system. *Applied Physics Letters*, 107:201106, 2015.

[216] B. Besga et al. Polariton boxes in a tunable fiber cavity. *Physical Review Applied*, 3:014008, 2015.

[217] E. W. Martin et al. Encapsulation narrows excitonic homogeneous linewidth of exfoliated $MoSe_2$ monolayer. *arXiv:1810.09834*, 2018.

[218] T. C. H. Liew et al. Single photons from coupled quantum modes. *Physical Review Letters*, 104:183601, 2010.

[219] M. Bamba et al. Origin of strong photon antibunching in weakly nonlinear photonic molecules. *Physical Review A*, 83:021802, 2011.

[220] A. Verger. Polariton quantum blockade in a photonic dot. *Physical Review B*, 73:193306, 2006.

Appendix A

Theory on TMDC-polaritons in microcavities

A.1 Introduction

In this appendix, we describe the microscopic theory for exciton-polaritons (Section A.2) and trion-polaritons (Section A.3) which were used for the theoretical modelling employed in Chapter 6. In Section A.4, we discuss possible quantum effect with trion-polaritons in transition metal dichalcogenides materials.

To describe the observed polariton nonlinearity, we begin with the conceptually more simple case of a neutral exciton-polariton, where the trion fraction is negligible.

Gaining the knowledge from the exciton case, we consider the trion-dominated regime. The excitation process then corresponds to the creation of a trion from a free electron. We account for phase space filling effects, which become important at increasing excited trion density. This leads to the quenching of the collective trion oscillator strength. Taking into account the deviation of statistics for trions from that of ideal fermions, we calculate the influence of phase-space filling on the trion Rabi frequency.

The whole theoretical model was provided by Dr. O. Kyriienko, Dr. V. Shahnazaryan and Prof. I. A. Shelykh.

The theory provided in this appendix refers to Chapter 6 and it is published in Reference [146].

A.2 Nonlinear neutral exciton-polaritons

In the first section we describe the exciton-photon coupled system, accounting for the composite electron-hole (e-h) nature of the neutral exciton. The case of a trion mode coupled to the optical mode is considered in the next section.

A.2.1 Exciton-polariton Rabi splitting

To start, we consider an optical cavity described by the bosonic annihilation and creation operators $\hat{c}$ and $\hat{c}^\dagger$, such that their commutation relations are $[\hat{c},\hat{c}^\dagger]=1$, $[\hat{c}^\dagger,\hat{c}^\dagger]=[\hat{c},\hat{c}]=0$. Coupled to a semiconducting medium, an optical photon creates an exciton, corresponding to the bound electron-hole pair. The creation of an electron with the momentum $\mathbf{q}$ is described by the fermionic operator $\hat{a}^\dagger_{\mathbf{q}}$, and hole creation is described by the operator $\hat{b}^\dagger_{\mathbf{q}}$. Their corresponding anti-commutation relations read $\{\hat{a}_{\mathbf{q}},\hat{a}^\dagger_{\mathbf{q}'}\}=\hat{a}_{\mathbf{q}}\hat{a}^\dagger_{\mathbf{q}'}+\hat{a}^\dagger_{\mathbf{q}'}\hat{a}_{\mathbf{q}}=\delta_{\mathbf{q},\mathbf{q}'}$, $\{\hat{a}_{\mathbf{q}},\hat{a}_{\mathbf{q}'}\}=\{\hat{a}^\dagger_{\mathbf{q}},\hat{a}^\dagger_{\mathbf{q}'}\}=0$, where $\delta_{\mathbf{q},\mathbf{q}'}$ is Kronecker delta function (and the same holds for $\hat{b}_{\mathbf{q}}$). Accounting for the attractive Coulomb interaction between an electron and a hole, the excitonic operator can be written as a composite boson $\hat{X}_\nu$, where ν is a general index which denotes the center-of-mass (CM) and internal degrees of freedom. The transition between electron-hole and composite exciton picture follows as $\hat{X}^\dagger_\nu=\sum_{\mathbf{k}_\alpha,\mathbf{k}_\beta}\langle\mathbf{k}_\beta,\mathbf{k}_\alpha|\nu\rangle\hat{a}^\dagger_{\mathbf{k}_\alpha}\hat{b}^\dagger_{\mathbf{k}_\beta}$. Here, $\mathbf{k}_{\alpha,\beta}$ correspond to electron and hole momenta, and $\langle\mathbf{k}_\beta,\mathbf{k}_\alpha|\nu\rangle$ is an exciton wave function written in the momentum space. The reversed transformation for describing an electron-hole pair in bosonic language can be written as $\hat{a}^\dagger_{\mathbf{k}_\alpha}\hat{b}^\dagger_{\mathbf{k}_\beta}=\sum_\nu\langle\nu|\mathbf{k}_\beta,\mathbf{k}_\alpha\rangle\hat{X}^\dagger_\nu$, where summation goes over possible states of composite excitons ν in the appropriate orthonormal basis, such that $\sum_\nu|\nu\rangle\langle\nu|=\mathbf{1}$.

In the following we are interested in the system with strong light-matter coupling, where a composite exciton of certain CM momentum is coupled to the cavity mode. The Hamiltonian for the considered system reads

$$\hat{\mathscr{H}}=\hat{H}_{\text{cav}}+\hat{H}_X+\hat{H}_{\text{coupl}} \tag{A.1}$$

where the first and second terms describe the free energy for the cavity photon mode, $\hat{H}_{\text{cav}}=\sum_{\mathbf{q}}\omega_{\text{cav},\mathbf{q}}\hat{c}^\dagger_{\mathbf{q}}\hat{c}_{\mathbf{q}}$ ($\hbar=1$ hereafter), and composite exciton $\hat{H}_X$ (i.e. coupled electron-hole) Hamiltonians. $\omega_{\text{cav},\mathbf{q}}$ denotes the two-dimensional dispersion for the planar cavity mode, with typically ultralow mass, such that only small q's are considered. The third term describes the coupling between light and matter excitations. It can be written as a creation of

an electron-hole pair by the cavity field with a coupling constant g,

$$\hat{H}_{\text{coupl}} = \sum_{\mathbf{k}_\alpha,\mathbf{k}_\beta,\mathbf{q}} (g\hat{a}^\dagger_{\mathbf{k}_\alpha+\mathbf{q}}\hat{b}^\dagger_{\mathbf{k}_\beta}\hat{c}_{\mathbf{q}} + h.c.) = \sum_{\mathbf{k}_\alpha,\mathbf{k}_\beta,\mathbf{q}}\sum_i (g\langle i|\mathbf{k}_\beta,\mathbf{k}_\alpha\rangle \hat{X}_i^\dagger \hat{c} + h.c.) \tag{A.2}$$

where in the second equality we have exploited excitonic form for the electron-hole pair, and considered a dipolar transition with negligible transferred cavity momentum, $\hat{c}_{\mathbf{q}\to 0} \equiv \hat{c}$, being a usual assumption for description of strong coupling. Here, $g = \frac{ep_{cv}}{m}\sqrt{\frac{\hbar^2}{2\varepsilon\varepsilon_0\omega_{\text{cav}}L_{\text{cav}}A}}$, where p_{cv} is a matrix element for a valence-to-conduction band transition, m is a free electron mass, L_{cav} is a cavity length, A is an area of the system. We consider an exciton mode at the fixed center-of-mass momentum, which for brevity is set to zero, $\hat{X}_0$, and derive the corresponding Heisenberg equations of motion. It reads

$$i\frac{d\hat{X}_0}{dt} = [\hat{X}_0,\hat{H}_X] + [\hat{X}_0,\hat{H}_{\text{coupl}}] = [\hat{X}_0,\hat{H}_X] + g\sum_{\mathbf{k}_\alpha,\mathbf{k}_\beta}\sum_i \langle i|\mathbf{k}_\beta,\mathbf{k}_\alpha\rangle \left[\hat{X}_0,\hat{X}_i^\dagger\right]\hat{c} \tag{A.3}$$

The first term generally describes the energy ω_X at which the excitonic mode oscillates. The second, being proportional to $\hat{c}$ operator, provides the coupling to photonic mode, which we generally denote as $G = g\sum_{\mathbf{k}_\alpha,\mathbf{k}_\beta}\sum_i\langle i|\mathbf{k}_\beta,\mathbf{k}_\alpha\rangle\left[\hat{X}_0,\hat{X}_i^\dagger\right]$. If the exciton corresponds to an ideal boson, i.e. $[\hat{X},\hat{X}^\dagger] = 1$, the coupling term reduces to $G = g\sum_{\mathbf{k}_\alpha,\mathbf{k}_\beta}\langle i|\mathbf{k}_\beta,\mathbf{k}_\alpha\rangle \equiv g\sum_{\mathbf{k}}\phi^*_{\mathbf{k}} = \Omega_X^{(0)}/2$, where we introduced the relative electron-hole momentum $\mathbf{k}$ and the Fourier transform of the exciton wave function $\phi_{\mathbf{k}}$. This energy corresponds directly to the Rabi energy for the light-matter coupled system. Performing the diagonalization of the system at zero detuning ($\omega_{\text{cav}} = \omega_X$), the Rabi-splitting between normal modes of the system is equal to $\Omega_X^{(0)}$.

We proceed by considering the composite structure of an exciton, which is formed by two fermions. This comes from the fact that creation of a (correlated) electron-hole pair is not equivalent to a boson creation, as long as number of created pairs grows. It originates from the Pauli exclusion principle, which does not allow certain pair configurations in the full fermionic treatment, while disregarded in the purely bosonic picture [190, 191]. The details for the difference between two cases were worked out by Monique Combescot and co-workers, and summarized in the so-called *coboson approach* to excitonic systems [190]. In the following, we apply the coboson formalism to find corrections to Rabi and exciton energy appearing due to effects of non-bosonicity.

The main consequence of the composite nature of an exciton is its peculiar statistics, which resembles bosonic one for small e-h pair concentration $n \equiv N/A$, but changes once it becomes comparable to the inverse of the effective exciton area. The generic commutation

relations between composite bosons can be formulated as (see [190], Equation [4.16])

$$[\hat{X}_m, \hat{X}_i^\dagger] \equiv \delta_{m,i} - \hat{D}_{mi} \tag{A.4}$$

where an operator $\hat{D}_{mi}$ describes the deviation from bosonicity for excitons due to its composite nature.

In particular, this can be observed when one writes the commutator in Equation (A.4) using the expression for composite exciton with zero CM momentum and relative momentum $\mathbf{k}$, which is described by $\hat{X}_0^\dagger = \sum_{\mathbf{k}} \langle \mathbf{k}|0\rangle \hat{a}_{\mathbf{k}} \hat{b}_{-\mathbf{k}} \equiv \sum_{\mathbf{k}} \phi_{\mathbf{k}} \hat{a}_{\mathbf{k}} \hat{b}_{-\mathbf{k}}$. The commutator reads

$$[\hat{X}_0, \hat{X}_0^\dagger] = \sum_{\mathbf{k}_1} \sum_{\mathbf{k}_2} (\phi_{\mathbf{k}_1} \phi^*_{\mathbf{k}_2} \hat{a}_{\mathbf{k}_1} \hat{b}_{-\mathbf{k}_1} \hat{b}^\dagger_{-\mathbf{k}_2} \hat{a}^\dagger_{\mathbf{k}_2} - \phi^*_{\mathbf{k}_2} \phi_{\mathbf{k}_1} \hat{b}^\dagger_{-\mathbf{k}_2} \hat{a}^\dagger_{\mathbf{k}_2} \hat{a}_{\mathbf{k}_1} \hat{b}_{-\mathbf{k}_1}) = \sum_{\mathbf{k}_1} \sum_{\mathbf{k}_2} \phi_{\mathbf{k}_1} \phi^*_{\mathbf{k}_2} \times$$

$$\times (\delta_{\mathbf{k}_1,\mathbf{k}_2} - \hat{a}^\dagger_{\mathbf{k}_1} \hat{a}_{\mathbf{k}_2} \delta_{\mathbf{k}_1,\mathbf{k}_2} - \hat{b}^\dagger_{-\mathbf{k}_1} \hat{b}_{-\mathbf{k}_2} \delta_{\mathbf{k}_1,\mathbf{k}_2}) = 1 - \sum_{\mathbf{k}} |\phi_{\mathbf{k}}|^2 (\hat{a}^\dagger_{\mathbf{k}} \hat{a}_{\mathbf{k}} + \hat{b}^\dagger_{\mathbf{k}} \hat{b}_{\mathbf{k}}) \tag{A.5}$$

The explicit form for the deviation operator is $\hat{D}_{00} = \sum_{\mathbf{k}} |\phi_{\mathbf{k}}|^2 (\hat{a}^\dagger_{\mathbf{k}} \hat{a}_{\mathbf{k}} + \hat{b}^\dagger_{\mathbf{k}} \hat{b}_{\mathbf{k}})$. Its structure thus hints that the deviation depends on the electron (or exciton) number N.

To calculate the influence of the non-bosonicity on Rabi energy renormalization we need to estimate the expectation value of the last term in Eq. (A.3) considering the (unnormalized) many-coboson state $|N\rangle = (\hat{X}_0^\dagger)^N |\emptyset\rangle$, and singling out the prefactor in front of the cavity photon operator $\hat{c}$. Here, $|\emptyset\rangle$ denotes coboson vacuum state, and corresponding norm reads $\sqrt{\langle N|N\rangle} = \langle \emptyset | \hat{X}_0^N (\hat{X}_0^\dagger)^N |\emptyset\rangle^{1/2}$. Note that in the case of composite bosons it was shown to differ exponentially from an ideal boson normalization for large N,[190] though for physical observables the difference appears as higher order terms in the small N expansion.

The expectation value for the commutator can be written as

$$G(N) = \frac{\langle N | g \sum_{\mathbf{k}_\alpha, \mathbf{k}_\beta} \sum_i \langle i | \mathbf{k}_\beta, \mathbf{k}_\alpha \rangle \left[\hat{X}_0, \hat{X}_i^\dagger \right] | N \rangle}{\langle N|N\rangle} =$$

$$= g \frac{\langle N | \sum_{\mathbf{k}} \phi^*_{\mathbf{k}} | N \rangle}{\langle N|N\rangle} - g \frac{\langle N | \sum_{\mathbf{k}_\alpha, \mathbf{k}_\beta} \sum_i \langle i | \mathbf{k}_\beta, \mathbf{k}_\alpha \rangle \hat{D}_{0i} | N \rangle}{\langle N|N\rangle} \tag{A.6}$$

The first term in Eq. (A.6) yields $g \sum_{\mathbf{k}} \phi^*_{\mathbf{k}}$ and is simply a Rabi frequency in the dilute system limit. The second term, however, involves the non-bosonicity operator. Accounting

for the many-coboson state explicitly, it can be rewritten as

$$g\frac{\langle\emptyset|\hat{X}_0^N\sum_{\mathbf{k}_{\alpha,\beta}}\sum_i\langle i|\mathbf{k}_\beta,\mathbf{k}_\alpha\rangle\hat{D}_{0i}(\hat{X}_0^\dagger)^N|\emptyset\rangle}{\langle N|N\rangle}=g\frac{\langle\emptyset|\sum_{\mathbf{k}_{\alpha,\beta}}\sum_i\langle i|\mathbf{k}_\beta,\mathbf{k}_\alpha\rangle\hat{X}_0^N\left[\hat{D}_{0i},(\hat{X}_0^\dagger)^N\right]|\emptyset\rangle}{\langle N|N\rangle} \tag{A.7}$$

where we have accounted for the fact that the action of the deviation operator on the ground state gives 0, i.e. $\hat{D}_{0i}|\emptyset\rangle=0\cdot|\emptyset\rangle$. Thus, its estimation relies on the commutator of the deviation operator with an exciton creation operator to the power N. For the first power, this can be derived as[190]

$$\left[\hat{D}_{mi},\hat{X}_j^\dagger\right]=\sum_n\left[\lambda\begin{pmatrix}n&j\\m&i\end{pmatrix}+\lambda\begin{pmatrix}m&j\\n&i\end{pmatrix}\right]\hat{X}_n^\dagger \tag{A.8}$$

where λ denotes the Pauli scattering element for input indices (i,j) and output (n,m). It reads explicitly

$$\lambda\begin{pmatrix}n&j\\m&i\end{pmatrix}=\int d\mathbf{r}_{\alpha_1}d\mathbf{r}_{\alpha_2}d\mathbf{r}_{\beta_1}d\mathbf{r}_{\beta_2}\phi_m^*(\mathbf{r}_{\alpha_1},\mathbf{r}_{\beta_2})\phi_n^*(\mathbf{r}_{\alpha_2},\mathbf{r}_{\beta_1})\phi_i(\mathbf{r}_{\alpha_1},\mathbf{r}_{\beta_1})\phi_j(\mathbf{r}_{\alpha_2},\mathbf{r}_{\beta_2}) \tag{A.9}$$

where $\phi_i(\mathbf{r}_{\alpha_1},\mathbf{r}_{\beta_1})$ is a generic coboson wavefunction written in the real space representation. It can be rewritten as a product of CM and relative motion component, $\phi_i(\mathbf{r}_\alpha,\mathbf{r}_\beta)=(e^{i\mathbf{Q}_i\cdot\mathbf{R}_{\alpha\beta}}/\sqrt{A})\langle\mathbf{r}_{\alpha\beta}|i\rangle$, where $\mathbf{R}_{\alpha\beta}$ and $\mathbf{r}_{\alpha\beta}$ are CM and relative coordinates for e-h pair, which correspond to coboson with CM momentum $\mathbf{Q}_i$ and relative motion quantum number i. The relative motion wavefunction can be also rewritten in the momentum space as $\langle\mathbf{r}|i\rangle=\sum_{\mathbf{k}}\langle\mathbf{r}|\mathbf{k}\rangle\langle\mathbf{k}|i\rangle=\sum_{\mathbf{k}}(e^{i\mathbf{k}\cdot\mathbf{r}}/\sqrt{A})\langle\mathbf{k}|i\rangle$, which we will use in future.

Proceeding with the estimation for the influence of the deviation in the many-coboson state, the commutator with N-exciton creation operator reads

$$\left[\hat{D}_{0i},(\hat{X}_j^\dagger)^N\right]=N(\hat{X}_0^\dagger)^{N-1}\sum_n\left[\lambda\begin{pmatrix}n&i\\0&0\end{pmatrix}+\lambda\begin{pmatrix}0&i\\n&0\end{pmatrix}\right]\hat{X}_n^\dagger \tag{A.10}$$

Using this, Equation (A.6) can be rewritten as

$$G(N)=g\sum_{\mathbf{k}}\phi_{\mathbf{k}}^*-gN\sum_{\mathbf{k}_{\alpha,\beta}}\sum_{i,n}\langle i|\mathbf{k}_\beta,\mathbf{k}_\alpha\rangle\left\{\lambda\begin{pmatrix}n&i\\0&0\end{pmatrix}+\lambda\begin{pmatrix}0&i\\n&0\end{pmatrix}\right\}\frac{\langle\emptyset|\hat{X}_0^N\hat{X}_n^\dagger(\hat{X}_0^\dagger)^{N-1}|\emptyset\rangle}{\langle N|N\rangle} \tag{A.11}$$

One can immediately see in the second term on the RHS that the Rabi frequency depends on the exciton concentration N, times the prefactors coming from Pauli scattering elements.

First, let us consider the intuitively easy case where the internal coboson index i coincides with the mode of interest, labeled as 0. Later, we show that this corresponds to the lower-order-in-N correction. In this case the expectation value $\langle \emptyset | \hat{X}_0^N \hat{X}_n^\dagger (\hat{X}_0^\dagger)^{N-1} | \emptyset \rangle / \langle N|N\rangle|_{n=0} = 1$. Considering the first Pauli scattering term $\lambda(0,\, i;\, 0,\, 0)$, the summation over internal coboson index is performed as

$$\sum_{\mathbf{k}} \sum_i \lambda \begin{pmatrix} 0 & i \\ 0 & 0 \end{pmatrix} \langle i|\mathbf{k}\rangle = \frac{1}{A^2} \sum_{\mathbf{k}} \int d\mathbf{r}_{\alpha_1} d\mathbf{r}_{\alpha_2} d\mathbf{r}_{\beta_1} d\mathbf{r}_{\beta_2} \langle 0|\mathbf{r}_{\alpha_1} - \mathbf{r}_{\beta_2}\rangle \langle 0|\mathbf{r}_{\alpha_2} - \mathbf{r}_{\beta_1}\rangle \langle \mathbf{r}_{\alpha_1} - \mathbf{r}_{\beta_1}|0\rangle \times$$

$$\times \sum_i \langle \mathbf{r}_{\alpha_2} - \mathbf{r}_{\beta_2}|i\rangle \langle i|\mathbf{k}\rangle = \sum_{\mathbf{k},\mathbf{k}_1,\mathbf{k}_2,\mathbf{k}_3} \frac{1}{A^4} \int d\mathbf{r}_{\alpha_1} d\mathbf{r}_{\alpha_2} d\mathbf{r}_{\beta_1} d\mathbf{r}_{\beta_2} e^{-i\mathbf{k}_1\cdot(\mathbf{r}_{\alpha_1} - \mathbf{r}_{\beta_2})} e^{-i\mathbf{k}_2\cdot(\mathbf{r}_{\alpha_2} - \mathbf{r}_{\beta_1})} \times$$

$$\times e^{i\mathbf{k}_3\cdot(\mathbf{r}_{\alpha_1} - \mathbf{r}_{\beta_1})} e^{i\mathbf{k}\cdot(\mathbf{r}_{\alpha_2} - \mathbf{r}_{\beta_2})} \langle 0|\mathbf{k}_1\rangle \langle 0|\mathbf{k}_2\rangle \langle \mathbf{k}_3|0\rangle = \sum_{\mathbf{k}} |\phi_{\mathbf{k}}|^2 \phi_{\mathbf{k}} \tag{A.12}$$

Here, for passing through the first equation sign we used that: 1) coboson states form a full orthonormal basis, $\sum_i |i\rangle\langle i| = \mathbf{1}$; 2) transition element between between real and momentum space reads $\langle \mathbf{r}_{\alpha_2} - \mathbf{r}_{\beta_2}|\mathbf{k}\rangle = e^{i\mathbf{k}\cdot(\mathbf{r}_{\alpha_2} - \mathbf{r}_{\beta_2})}/\sqrt{A}$. For the second equality we exploited Dirac delta function definition in 2D, being $\int d\mathbf{r} e^{i\mathbf{k}\cdot\mathbf{r}} = A\delta_{\mathbf{k},\mathbf{0}}$, which reduces summation to a single index, and recall our definition $\langle \mathbf{k}|0\rangle \equiv \phi_{\mathbf{k}}$. The second Pauli scattering term gives the same contribution.

In the case of 1s neutral exciton in a two-dimensional material the relative motion part of wavefunction in real space can be written as $\phi(\mathbf{r}) = \sqrt{2/\pi a_B^2}\, e^{-r/a_B}$, with $\mathbf{r}$ being the relative (e-h) coordinate. The momentum space version then reads

$$\phi_{\mathbf{k}} = \sqrt{\frac{8\pi a_B^2}{A}} (1 + a_B^2 k^2)^{-3/2} \tag{A.13}$$

where a_B corresponds to the 2D variational parameter.

Collecting everything together and performing summation as $\sum_{\mathbf{k}} \to \frac{A}{(2\pi)^2} \int d\mathbf{k}$, the renormalized Rabi frequency as a function of concentration (in lowest order of na_B^2) reads

$$G(n) = G(0) \left(1 - 2N \frac{\sum_{\mathbf{k}} |\phi_{\mathbf{k}}|^2 \phi_{\mathbf{k}}}{\sum_{\mathbf{k}'} \phi_{\mathbf{k}'}^*} + O[N^2] \right) = G(0) \left(1 - \frac{16\pi n a_B^2}{7} + O[n^2 a_B^4] \right) \tag{A.14}$$

where $G(0) = g\sqrt{2A/\pi a_B^2} = \frac{e p_{cv}}{m a_B} \sqrt{\frac{\hbar^2}{\pi \varepsilon \varepsilon_0 \omega_{\text{cav}} L_{\text{cav}}}}$. Finally, we need to account for the fact that $G(n)$ is a derived term in the equations of motion, which includes $\propto n$ correction. Thus it

originates from the effective nonlinear Hamiltonian $\hat{H}_{\text{coupl}}^{(\text{nonlin})}$ which contains three excitonic operators and a photonic one, and on the contrary to the linear case provides extra factor of 2 in the equations of motion. The modified Hamiltonian with exciton density-dependent Rabi frequency then reads (at fixed momentum)

$$\hat{H}_{\text{coupl}} = \frac{\Omega_X(n_X)}{2}(\hat{X}^\dagger \hat{c} + \hat{c}^\dagger \hat{X}) \tag{A.15}$$

where the renormalized Rabi frequency is

$$\frac{\Omega_X(n_X)}{2} = \frac{\Omega_X^{(0)}}{2}\left(1 - \frac{8\pi n_X a_B^2}{7} + O[n_X^2 a_B^4]\right) \tag{A.16}$$

where we denoted the exciton concentration as n_X. The result above coincides with the estimates by Tassone and Yamamoto,[29] and Rochat et al.,[192] although derived in a different way, without involving Usui transformation.

We can proceed to calculate the terms being higher order in (na_B^2). This relies on the exact calculation of the average as [190]

$$\langle \emptyset | \hat{X}_0^N \hat{X}_j^\dagger (\hat{X}_0^\dagger)^{N-1} | \emptyset \rangle / \langle N|N\rangle = \delta_{0,j}\frac{F_{N-1}}{F_N} - (N-1)\lambda \begin{pmatrix} 0 & 0 \\ 0 & j \end{pmatrix} \frac{F_{N-2}}{F_N} + O[n^3 a_B^6] \tag{A.17}$$

where F_N is a coefficient which defines the deviation of statistics through $\langle N|N\rangle \equiv N! F_N$, with F_N being 1 for purely bosonic states. Exploiting coboson theory, the ratio reads

$$\frac{F_{N-1}}{F_N} = 1 + N\sum_{\mathbf{k}} |\phi_{\mathbf{k}}|^4 \tag{A.18}$$

and $F_{N-2}/F_N \approx (F_{N-1}/F_N)^2$. The first term in Equation (A.18) corresponds to the previously obtained case with $\sim na_B^2$ scaling. Performing the same procedure as before, we extend the results to include $n^2 a_B^4$ contribution. After some algebra, we obtain

$$G(n) = G(0)\left(1 - 2N\frac{\sum_{\mathbf{k}} |\phi_{\mathbf{k}}|^2 \phi_{\mathbf{k}}}{\sum_{\mathbf{k}'} \phi_{\mathbf{k}'}^*} - 2N^2 \frac{(\sum_{\mathbf{k}} |\phi_{\mathbf{k}}|^4)(\sum_{\mathbf{k}''} |\phi_{\mathbf{k}''}|^2 \phi_{\mathbf{k}''})}{\sum_{\mathbf{k}'} \phi_{\mathbf{k}'}^*} + 2N^2 \frac{(\sum_{\mathbf{k}} |\phi_{\mathbf{k}}|^4 \phi_{\mathbf{k}})}{\sum_{\mathbf{k}'} \phi_{\mathbf{k}'}^*} + \right.$$

$$\left. + O[N^3]\right) = G(0)\left(1 - \frac{16\pi n a_B^2}{7} + \frac{1152\pi^2 n^2 a_B^4}{455} + O[n^3 a_B^6]\right) \tag{A.19}$$

where the derivation was performed up to $\sim n^3 a_B^6$ terms. The corresponding modified Rabi frequency then reads

$$\frac{\Omega_X(n_X)}{2} = \frac{\Omega_X^{(0)}}{2}\left(1 - \frac{8\pi n_X a_B^2}{7} + \frac{384\pi^2 n_X^2 a_B^4}{455} + O[n_X^3 a_B^6]\right) \tag{A.20}$$

Interestingly, we observe that the light-matter coupling strength is a monotonically decreasing function of density, and its expansion has a sign-changing pattern. It is thus tempting to suggest that it has the exponential dependence. Namely, we can express it as $G(n) = G(0)\, e^{-(16\pi/7)na_B^2} \approx G(0)\Big\{1 - (16\pi/7)na_B^2 + (128\pi^2/49)n^2 a_B^4 + O[n^3 a_B^6]\Big\}$, and observe that the expansion of the exponent gives nearly the same quadratic term, with their ratio being $1.03175 \approx 1$. This gives us confidence in the conjectured dependence.

A.2.2 Nonlinear exciton energy shift

In the previous section, we have considered the renormalization of the light-matter coupling term, which gains n-dependence. Now, let us consider similar effects which provide nonlinear energy term for composite excitons. To do so, we write the exciton Hamiltonian in terms of basic constituents, being electrons and holes. This is given by

$$\hat{H}_X = \hat{H}_e^{(0)} + \hat{H}_h^{(0)} + \hat{H}_{e-h} + \hat{H}_{e-e} + \hat{H}_{h-h} \tag{A.21}$$

where the first two terms correspond to energies of the electrons and holes, and read $\hat{H}_e^{(0)} = \sum_{\mathbf{k}_\alpha} \varepsilon_{\mathbf{k}_\alpha}^{(e)} \hat{a}_{\mathbf{k}_\alpha}^\dagger \hat{a}_{\mathbf{k}_\alpha}$ and $\hat{H}_h^{(0)} = \sum_{\mathbf{k}_\beta} \varepsilon_{\mathbf{k}_\beta}^{(h)} \hat{b}_{\mathbf{k}_\beta}^\dagger \hat{b}_{\mathbf{k}_\beta}$. The dispersions can be written in the quadratic form, being $\varepsilon_{\mathbf{k}_\alpha}^{(e)} = E_c + k_\alpha^2/2m_e$ and $\varepsilon_{\mathbf{k}_\beta}^{(h)} = E_v + k_\beta^2/2m_h$. $(E_c - E_v) = E_g$ corresponds to the bandgap energy, and $m_{e,h}$ are effective electron and hole masses, respectively, measured in units of free electron mass. The third term in Equation (A.21) corresponds to electron-hole Coulomb interaction, which ultimately leads to the formation of the bound state. It reads $\hat{H}_{e-h} = -\sum_{\mathbf{p},\mathbf{p}',\mathbf{q}} V_q \hat{a}_{\mathbf{p}+\mathbf{q}}^\dagger \hat{b}_{\mathbf{p}'-\mathbf{q}}^\dagger \hat{b}_{\mathbf{p}'} \hat{a}_{\mathbf{p}}$, where $V_q = 2\pi e^2/(AqS_q)$ is the standard Fourier transform for Coulomb interaction in 2D, S_q denotes the screening function (so far unspecified), and we accounted explicitly for attraction between an electron and a hole. Finally, the terms $\hat{H}_{e-e}$ and $\hat{H}_{h-h}$ correspond to Coulomb interaction with only electrons and only holes. When accounting for the excitonic structure of e-h complexes, these lead to Kerr-type exciton-exciton interaction.

To account for the non-bosonicity and exchange-based Coulomb scattering between the cobosons on the equal footing, we can derive the total energy of the system, $E_X = \langle \hat{H}_X \rangle$, where

expectation value is taken over N-exciton state. Following [190], the nonlinear (quadratic and higher) contribution to the energy of N excitons reads

$$\langle \hat{H}_X \rangle_N = N \Bigg[E_X^{(0)} + \frac{N}{2}\frac{F_{N-2}}{F_N} \left\{ \xi \begin{pmatrix} 0 & 0 \\ 0 & 0 \end{pmatrix} - \xi^{\text{in}} \begin{pmatrix} 0 & 0 \\ 0 & 0 \end{pmatrix} \right\} + \frac{N^2}{4}\frac{F_{N-3}}{F_N} \times$$

$$\times \left\{ -2\sum_n \lambda \begin{pmatrix} 0 & n \\ 0 & 0 \end{pmatrix} \xi \begin{pmatrix} n & 0 \\ 0 & 0 \end{pmatrix} + \sum_{mn} \lambda \begin{pmatrix} 0 & 0 \\ 0 & n \\ 0 & m \end{pmatrix} \xi \begin{pmatrix} n & 0 \\ m & 0 \end{pmatrix} \right\} \Bigg] \tag{A.22}$$

where $E_X^{(0)} = E_g - E_b$ is a density independent exciton energy, and nonbosonicity factor reads $F_{N-3}/F_N \approx (F_{N-1}/F_N)^3$. Here,

$$\xi \begin{pmatrix} n & j \\ m & i \end{pmatrix} = \int d\mathbf{r}_{\alpha_1} d\mathbf{r}_{\alpha_2} d\mathbf{r}_{\beta_1} d\mathbf{r}_{\beta_2} \phi_m^*(\mathbf{r}_{\alpha_1}, \mathbf{r}_{\beta_1}) \phi_n^*(\mathbf{r}_{\alpha_2}, \mathbf{r}_{\beta_2}) \phi_i(\mathbf{r}_{\alpha_1}, \mathbf{r}_{\beta_1}) \phi_j(\mathbf{r}_{\alpha_2}, \mathbf{r}_{\beta_2}) \times$$

$$\times \left[\mathscr{V}_{\alpha\alpha}(\mathbf{r}_{\alpha_1}, \mathbf{r}_{\alpha_2}) + \mathscr{V}_{\beta\beta}(\mathbf{r}_{\beta_1}, \mathbf{r}_{\beta_2}) + \mathscr{V}_{\alpha\beta}(\mathbf{r}_{\alpha_1}, \mathbf{r}_{\beta_2}) + \mathscr{V}_{\alpha\beta}(\mathbf{r}_{\alpha_2}, \mathbf{r}_{\beta_1}) \right] \tag{A.23}$$

is a direct Coulomb scattering term between excitons [see Equation (A.9) for comparison], and $\mathscr{V}_{ff'}(\mathbf{r}_{f_1}, \mathbf{r}_{f_2'})$ corresponds to the real space Coulomb potential between carriers f, f'. The ξ^{in} term denotes exchange Coulomb scatterings, where either electron or hole is swapped between two composite excitons,

$$\xi^{\text{in}} \begin{pmatrix} n & j \\ m & i \end{pmatrix} = \int d\mathbf{r}_{\alpha_1} d\mathbf{r}_{\alpha_2} d\mathbf{r}_{\beta_1} d\mathbf{r}_{\beta_2} \phi_m^*(\mathbf{r}_{\alpha_1}, \mathbf{r}_{\beta_2}) \phi_n^*(\mathbf{r}_{\alpha_2}, \mathbf{r}_{\beta_1}) \phi_i(\mathbf{r}_{\alpha_1}, \mathbf{r}_{\beta_1}) \phi_j(\mathbf{r}_{\alpha_2}, \mathbf{r}_{\beta_2}) \times$$

$$\times \left[\mathscr{V}_{\alpha\alpha}(\mathbf{r}_{\alpha_1}, \mathbf{r}_{\alpha_2}) + \mathscr{V}_{\beta\beta}(\mathbf{r}_{\beta_1}, \mathbf{r}_{\beta_2}) + \mathscr{V}_{\alpha\beta}(\mathbf{r}_{\alpha_1}, \mathbf{r}_{\beta_2}) + \mathscr{V}_{\alpha\beta}(\mathbf{r}_{\alpha_2}, \mathbf{r}_{\beta_1}) \right] \tag{A.24}$$

which combines Pauli scattering and Coulomb interaction. Finally, the exchange term between three composite excitons (where carriers are swapped but no Coulomb vertex is included) yields

$$\lambda \begin{pmatrix} p & k \\ n & j \\ m & i \end{pmatrix} = \int d\mathbf{r}_{\alpha_1} d\mathbf{r}_{\alpha_2} d\mathbf{r}_{\alpha_3} d\mathbf{r}_{\beta_1} d\mathbf{r}_{\beta_2} d\mathbf{r}_{\beta_3} \times$$

$$\times \phi_m^*(\mathbf{r}_{\alpha_1}, \mathbf{r}_{\beta_2}) \phi_n^*(\mathbf{r}_{\alpha_3}, \mathbf{r}_{\beta_1}) \phi_p^*(\mathbf{r}_{\alpha_2}, \mathbf{r}_{\beta_3}) \phi_i(\mathbf{r}_{\alpha_1}, \mathbf{r}_{\beta_1}) \phi_j(\mathbf{r}_{\alpha_2}, \mathbf{r}_{\beta_2}) \phi_k(\mathbf{r}_{\alpha_3}, \mathbf{r}_{\beta_3}) \tag{A.25}$$

For composite excitons with $\mathscr{V}_{\alpha\beta}(r) = -\mathscr{V}_{\alpha\alpha}(r)$, which is true for the electron-hole potential, the direct term vanishes, $\xi(0,\ 0;\ 0,\ 0) = 0$. This can be seen as well-known absence of direct contribution at zero exchanged momentum, valid both for III-V semiconductors and TMDs.

Similarly, $\sum_n \lambda(0,\,0;\,0,\,0)\xi(0,\,0;\,0,\,0) = 0$, and only exchange terms shall be accounted. They can be calculated as

$$\xi^{\text{in}} \begin{pmatrix} n & j \\ m & i \end{pmatrix} = 2\sum_{\mathbf{k},\mathbf{k}'} V_{\mathbf{k}-\mathbf{k}'} \Big\{ |\phi_{\mathbf{k}}|^2 |\phi_{\mathbf{k}'}|^2 - |\phi_{\mathbf{k}}|^2 \phi^*_{\mathbf{k}} \phi_{\mathbf{k}'} \Big\} \tag{A.26}$$

and

$$\sum_{mn} \lambda \begin{pmatrix} 0 & 0 \\ 0 & n \\ 0 & m \end{pmatrix} \xi \begin{pmatrix} n & 0 \\ m & 0 \end{pmatrix} = 2\sum_{\mathbf{k},\mathbf{k}'} V_{\mathbf{k}-\mathbf{k}'} |\phi_{\mathbf{k}}|^4 \Big\{ |\phi_{\mathbf{k}'}|^2 - \phi^*_{\mathbf{k}} \phi_{\mathbf{k}'} \Big\}. \tag{A.27}$$

The sums (A.26) and (A.27) can be converted into intergrals, and evaluated numerically for the exciton wavefunction in the form (A.13). As an important consequence of the monolayer structure of the TMDC, the potential is chosen to be screened,[193, 194, 73] and has the form

$$V_{\mathbf{q}} = \frac{2\pi e^2}{(4\pi\varepsilon_0)\kappa q(1 + r_0 q/\kappa)}, \tag{A.28}$$

where e is an electron charge, ε_0 is a vacuum permittivity (note that SI units are used), r_0 is a screening length, and $\kappa = (\varepsilon_{s1} + \varepsilon_{s2})/2$ is an average dielectric permittivity for substrates from two sides.[73] This directly follows from the well-known Keldysh potential of the form

$$\mathscr{V}_{ee}(\mathbf{r}) = \frac{e^2}{(4\pi\varepsilon_0) r_0} \frac{\pi}{2} \left[H_0\left(\frac{\kappa r}{r_0}\right) - Y_0\left(\frac{\kappa r}{r_0}\right) \right], \tag{A.29}$$

defined with the help of Struve and Bessel functions of the second kind, and shown for the case of two electrons.

Finally, collecting the terms up to N^2 order, the nonlinear energy of the excitonic mode (as appearing in the Hamiltonian) can be written as

$$E_X(n_X) = E_0 + \frac{8}{\pi} \frac{e^2}{4\pi\varepsilon_0 \kappa a_B} \mathscr{I}_4(r_0) n_X a_B^2 - \frac{128}{5} \frac{e^2}{4\pi\varepsilon_0 \kappa a_B} \Big[5\mathscr{I}_6(r_0) - 2\mathscr{I}_4(r_0) \Big] n_X^2 a_B^4, \tag{A.30}$$

where exchange integrals for dimensionless length ($x = r/a_B$) depend on the screening length r_0 and read

$$\mathscr{I}_4(r_0) = \int_0^\infty \int_0^{2\pi} \frac{dx dx' d\theta 2\pi x x'}{\sqrt{x^2 + x'^2 - 2xx'\cos\theta}\,(1 + \frac{r_0}{\kappa a_B}\sqrt{x^2 + x'^2 - 2xx'\cos\theta})} \times$$

$$\times \frac{(-1)}{(1+x^2)^3}\left(\frac{1}{(1+x'^2)^3}-\frac{1}{(1+x^2)^{3/2}}\frac{1}{(1+x'^2)^{3/2}}\right) \tag{A.31}$$

$$\mathscr{I}_4(r_0)=\int_0^\infty\int_0^{2\pi}\frac{dxdx'd\theta 2\pi xx'}{\sqrt{x^2+x'^2-2xx'\cos\theta}(1+\frac{r_0}{\kappa a_B}\sqrt{x^2+x'^2-2xx'\cos\theta})}\times$$

$$\times \frac{(-1)}{(1+x^2)^6}\left(\frac{1}{(1+x'^2)^3}-\frac{1}{(1+x^2)^{3/2}}\frac{1}{(1+x'^2)^{3/2}}\right) \tag{A.32}$$

where in the case of TMDC materials the dimensionless parameter $r_0/(\kappa a_B)$ enters the integrals. We perform the calculations considering $MoSe_2$ on hBN, where $r_0 = 4\ nm$ [194], $\kappa = (\varepsilon_{s1}+\varepsilon_{s2})/2 = 4$ for hBN substrates, and leaving a_B as a tuning parameter.

A.2.3 Exciton-polaritons at increasing density

Taking our previously derived results for the renormalization of coupling and exciton properties, let us translate it to the case of polaritons.[28] In the cases where trion mode can be excluded out considerations (it is weakly coupled and/or largely detuning), we use the two coupled modes Hamiltonian, concentrating on the exciton-photon coupling. This is justified by the experimental data at large detuning, where the trion fraction at X-C anti-crossing is estimated to be small ($< 2\%$). The normal modes of neutral exciton-polariton system read

$$E_\pm(n_X)=\frac{E_C+E_X(n_X)}{2}\pm\frac{1}{2}\sqrt{\Omega_X(n_X)^2+[E_C-E_X(n_X)]^2} \tag{A.33}$$

where $E_-(n_X)\equiv E_{\mathrm{MPB}}(n_X)$ corresponds to the middle polariton mode we are interested in.

We proceed with applying the presented theory to explain the nonlinear blueshift of the middle polariton branch as function of an exciton concentration, for the case where trion resonance is largely detuned. Using the coefficients derived above, and corresponding density dependences for the coupling $\Omega_X(n_X)$ and exciton energy $E_X(n)$ terms, we plot the nonlinear energy shift as function of concentration. The theoretical results are shown in Figure 6.10 by red solid curves. Taking the exciton Bohr radius as the only fitting parameter, we set it to be $a_B = 0.85\ nm$, which allows to qualitatively the behavior of the system. Furthermore, we verify the obtained value performing the variational procedure to obtain exciton properties in $MoSe_2$ covered with hBN. This can be done using the standard procedure with screened Keldysh potential with $r_0 = 4\ nm$, $\kappa = 4$, and the effective electron mass $m_e = 0.8\ m_0$, [195] which was measured to be rather large in $MoSe_2$ and similar to the effective mass of the hole, taken $m_h = 0.84\ m_0$. This leads to the reduced mass $\mu = 0.41\ m_0$. Performing minimization,

we get $a_B^{(\mathrm{calc})} = 0.93\ nm$ and binding energy $E_b^{(\mathrm{calc})} = 259\ meV$. These values lie close to the fitted value and experimentally measured energy, respectively. (As a bonus, in the next section devoted to trions we explicitly show how the same result can be easily obtained in the momentum space.)

We note that the ability to reproduce measured energy shift of E_{MPB} is only possible once both Rabi frequency reduction and nonlinear interactions are considered, while otherwise failing to provide required scaling. Namely, the inclusion of Coulomb-based exchange can only explain the observed behavior (2 meV shift within at order of magnitude change for the density) for either largely increased exciton Bohr radius in TMDC, which is unlikely, or much higher concentration going into $\sim 10^{13}\ cm^{-2}$ range. At the same time, if only Rabi renormalization is accounted, the saturation of nonlinear shift cannot be reproduced.

A.3 Nonlinear trion-polaritons

A.3.1 Trion-polariton Rabi splitting

We consider the system with an initial doping, and study the effects of light-matter coupling with a multiparticle bound state. In the $MoSe_2$ TMDC this corresponds to a negatively charged exciton (trion) which is spectroscopically located 30 meV below the excitonic resonance. We aim to estimate of the Rabi-splitting change for the case of a trion. In the similar fashion, the deviation from ideal statistics changes the value of trion-photon coupling. However, we note that the strong light-matter coupling regime for trion is much less studied, and its treatment requires extra care.

We begin with the interaction between the cavity and the trion mode. The latter can be generally described by a composite creation operator which creates two electrons and a hole from the vacuum state, $\hat{a}^\dagger_{\mathbf{k}_e,s_e}\hat{a}^\dagger_{\mathbf{k}_{e'},s_{e'}}\hat{b}^\dagger_{\mathbf{k}_h,s_h}|\emptyset\rangle$. Here, $\mathbf{k}_{e,e',h}$ are the momenta of the respective individual constituents (so-called carrier coordinates [196]), and $s_{e,e',h}$ are the spin indices. We note that the most favorable trion configuration in $MoSe_2$ monolayer is the singlet state with two electrons having anti-parallel spin.[197] The operator corresponding to the creation of a singlet state can be written as[198]

$$\hat{T}^\dagger_{\mathbf{K},\uparrow} = \sum_{\mathbf{k}_1,\mathbf{k}_2} \phi^T_{\beta_e\mathbf{K}-\mathbf{k}_1,\beta_e\mathbf{K}-\mathbf{k}_2} \frac{(\hat{a}^\dagger_{\mathbf{k}_1,\uparrow}\hat{a}^\dagger_{\mathbf{k}_2,\downarrow} - \hat{a}^\dagger_{\mathbf{k}_2,\downarrow}\hat{a}^\dagger_{\mathbf{k}_1,\uparrow})}{\sqrt{2}} \hat{b}^\dagger_{\mathbf{K}-\mathbf{k}_1-\mathbf{k}_2,\uparrow} \tag{A.34}$$

with wavefunction being separated into a trivial center-of-mass part with momentum $\mathbf{K}$, $\beta_e = 1-\beta_X = m_e/(2m_e+m_h)$, and the relative motion part described by trial wavefunction

for the relative motion $\phi^T_{\mathbf{k}_1,\mathbf{k}_2}$ (we consider zero CM momentum case). The wavefunction is written for the relative electron-hole coordinates $\mathbf{r}_1$ and $\mathbf{r}_2$, being radius-vectors between the first electron and the hole, and the second electron and the hole, respectively. In the real space it corresponds to the two exponentially decaying functions

$$\phi^T(\mathbf{r}_1,\mathbf{r}_2) = \frac{1}{\sqrt{2}}\frac{1}{\sqrt{1+\chi^2}}\left\{\sqrt{\frac{2}{\pi\lambda_1^2}}e^{-r_1/\lambda_1}\sqrt{\frac{2}{\pi\lambda_2^2}}e^{-r_2/\lambda_2}+\sqrt{\frac{2}{\pi\lambda_2^2}}e^{-r_1/\lambda_2}\sqrt{\frac{2}{\pi\lambda_1^2}}e^{-r_2/\lambda_1}\right\} \tag{A.35}$$

where λ_1 and λ_2 are the variational parameters corresponding to the distances between electrons and a hole. Note, that $\phi^T(\mathbf{r}_1,\mathbf{r}_2)$ is symmetrized and is normalized to unity, with $\chi = 4\lambda_1\lambda_2/(\lambda_1+\lambda_2)^2$. The momentum space version then reads

$$\phi^T_{\mathbf{k}_1,\mathbf{k}_2} = \frac{1}{\sqrt{2}}\frac{1}{\sqrt{1+\chi^2}}\left\{\sqrt{\frac{8\pi\lambda_1^2}{A}}(1+\lambda_1^2k_1^2)^{-3/2}\sqrt{\frac{8\pi\lambda_2^2}{A}}(1+\lambda_2^2k_2^2)^{-3/2}+\right.$$

$$\left.+\sqrt{\frac{8\pi\lambda_2^2}{A}}(1+\lambda_2^2k_1^2)^{-3/2}\sqrt{\frac{8\pi\lambda_1^2}{A}}(1+\lambda_1^2k_2^2)^{-3/2}\right\} \equiv \mathscr{N}\left\{\phi^{(1)}_{\mathbf{k}_1}\phi^{(2)}_{\mathbf{k}_2}+\phi^{(2)}_{\mathbf{k}_1}\phi^{(1)}_{\mathbf{k}_2}\right\} \tag{A.36}$$

where we defined $\mathscr{N} = [2(1+\chi^2)]^{-1/2}$ and $\phi^{(j)}_{\mathbf{k}} = \sqrt{8\pi\lambda_j^2/A}\ (1+\lambda_j^2k^2)^{-3/2}$. Finally, reordering the electron operators in Equation (A.34), and considering CM momentum much smaller then typical relative momenta, we can write trion creation operator as

$$\hat{T}^\dagger_{\mathbf{K},\uparrow} = \sum_{\mathbf{k}_1,\mathbf{k}_2}\mathscr{N}\left\{\phi^{(1)}_{\mathbf{k}_1}\phi^{(2)}_{\mathbf{k}_2}+\phi^{(2)}_{\mathbf{k}_1}\phi^{(1)}_{\mathbf{k}_2}\right\}\hat{a}^\dagger_{\mathbf{k}_1,\uparrow}\hat{a}^\dagger_{\mathbf{k}_2,\downarrow}\hat{b}^\dagger_{\mathbf{K}-\mathbf{k}_1-\mathbf{k}_2,\uparrow} \tag{A.37}$$

The choice of the wavefunction (A.36) is of course far from optimal, as to describe quantitatively the shape of trion solution, more complicated ansatzes with hundreds of orbitals shall be used.[199] However, in order to get any sensible result for Rabi frequency renormalization, this is the form we shall adopt.

Once there is a non-zero number of free electrons, the absorption of a circularly polarized photon can then allow a creation of a trion. The Hamiltonian of the system can be written as the sum $\hat{\mathscr{H}}^T = \hat{\mathscr{H}}^T_0 + \hat{\mathscr{H}}^T_{\text{coupl}}$ of non-interaction cavity/electron/trion Hamiltonian $\hat{\mathscr{H}}^T_0$

$$\hat{\mathscr{H}}^T_0 = \sum_{\mathbf{q}}\omega_{\text{cav},\mathbf{q}}\hat{c}^\dagger_{\mathbf{q}}\hat{c}_{\mathbf{q}}+\sum_{\mathbf{K}}\omega^T_{\mathbf{K}}\hat{T}^\dagger_{\mathbf{K}}\hat{T}_{\mathbf{K}}+\sum_{\mathbf{k}}\varepsilon_{\mathbf{k}}\hat{a}^\dagger_{\mathbf{k}}\hat{a}_{\mathbf{k}} \tag{A.38}$$

and the coupling Hamiltonian for light and matter,

$$\hat{\mathscr{H}}^{T}_{\text{coupl}} = \sum_{\mathbf{k},\mathbf{q},\mathbf{k}_1,\mathbf{k}_2} g\phi^{T}_{\mathbf{k}_1,\mathbf{k}_2} \hat{T}^{\dagger}_{\mathbf{k}+\mathbf{q},\uparrow} \hat{a}_{\mathbf{k},\downarrow} \hat{c}_{\mathbf{q},\Uparrow} + h.c. \tag{A.39}$$

with g being conduction-to-valence band transition matrix element, previously defined in the exciton case. $\varepsilon_{\mathbf{k}}$ is an electron dispersion, $\omega^{T}_{\mathbf{K}}$ is a trion dispersion, and in Equation (A.38) the summation over spin is assumed. In Equation (A.39), similarly to the exciton case, the wavefunction of the relative motion appears due to the fact that out of free electron-hole complex the bound trion state appears. The process in Equation (A.39) in simple terms can be seen as a creation of electron-hole pair attached to the electron in a Fermi sea, while the electron state is (slightly) changed. This can be conveniently described by the quasi-bosonic excitation, defined by the operator $\hat{B}_j$, which reads

$$\hat{B}^{\dagger}_{\mathbf{K}}|\text{FS}\rangle = \frac{1}{\sqrt{N_e}} \sum_{\mathbf{k}} \hat{T}^{\dagger}_{\mathbf{K}+\mathbf{k}} \hat{a}_{\mathbf{k}}|\text{FS}\rangle \tag{A.40}$$

It creates an excitation out of Fermi sea state $|\text{FS}\rangle$, and N_e is a number of free electrons available for trion creation, which can correspond to the selected spin configuration, meaning that the total number of electrons in the system reads as $N^{\text{tot}}_e = 2N_e$. The combinatorial prefactor $1/\sqrt{N_e}$ comes from the number of different ways the excitation can be created,[200] and we note that Equation (A.40) holds for low temperatures where electron gas is degenerate. As the excitation operator $\hat{B}^{\dagger}_{\mathbf{K}}$ represents a composite boson, similarly to excitons described in the previous section B, it is prone to the phase space filling effects. At the same time, it is not a bound state, and thus exhibits different statistics deviation behaviour. We will describe this point in details later, when trion-based saturation effects are considered.

We note that previously the light-matter coupling in $MoSe_2$ TMDC material was also considered for the case of exciton-polarons.[82] This corresponds to similar creation operator $\hat{B}^{\dagger}_j$, but different ansatz for the wave function, which accounts for dressing of photo-created exciton with electrons in the Fermi sea. We stress that both trion-dominated or polaron-dominated regimes can be possible, as considered in [201]. Recent predictions for the GaAs samples estimate the cross-over into exciton-polaron regime to happen for Fermi wave vector to be comparable with inverse Bohr radius for the system, $k_{cr} \sim 0.8\, a_B^{-1}$.[202] As we show later, the experiment is conducted in the $k_F \ll a_B^{-1}$ limit of small concentration, which corresponds to the trion-dominated regime.

Next, we proceed with the estimation of trion Rabi-splitting, or conversely the free electron density. It is given by the bare coupling constant g multiplied by the square root of electron density and the wave function part responsible for absorption renormalization due to

the confinement. First, we account for the fact that photon momentum has typically small values q, being much less than other relevant wavevectors. This also translates into nearly zero center-of-mass momentum of the generated exciton, where an electron and a hole are located close to each other. Here, we follow the approach introduced in [203, 204], where the so-called electron-exciton coordinates are used. These correspond to the electron-hole relative coordinate (seen as an exciton) and the relative coordinate of the CM for "exciton" to the second electron. They are generally described by length parameters λ and λ'. Due to complex symmetrization requirements, they do not allow to choose wavefunction in the simple form, thus preventing the analytical calculation. However, in the limit of large $\lambda_2 \gg \lambda_1$ the e-h and e-X coordinates become nearly equivalent, and we can set $\lambda \approx \lambda_1$ and $\lambda' \approx \lambda_2$.

Taking the trion wavefunction to be Fourier transformed with respect to an exciton internal motion,

$$\phi^T_{\mathbf{k}_1,\mathbf{k}_2} = \int d\mathbf{r}_1 \frac{e^{i\mathbf{k}_1\cdot\mathbf{r}_1}}{\sqrt{A}} \mathscr{N}\left\{ \sqrt{\frac{2}{\pi\lambda_1^2}} \exp(-r_1/\lambda_1) \sqrt{\frac{8\pi\lambda_2^2}{A}} (1+\lambda_2^2 k_2^2)^{-3/2} + \right.$$

$$\left. + \sqrt{\frac{2}{\pi\lambda_2^2}} \exp(-r_1/\lambda_2) \sqrt{\frac{8\pi\lambda_1^2}{A}} (1+\lambda_1^2 k_2^2)^{-3/2} \right\} \tag{A.41}$$

the coupling then can be estimated setting $r_1 = 0$ (i.e. for the closely located photocreated e-h pair). Simultaneously, we shall account that Fermi wavevector $k_F \ll \lambda_1^{-1}, \lambda_2^{-1}$, and thus the wavefunction in Eq. (A.39) can be considered as a constant at k_2 $\lambda_{2,1} = 0$, going in front of the sum. Altogether, the coupling Hamiltonian can be rewritten as

$$\hat{\mathscr{H}}^T_{\text{coupl}} = \frac{\Omega_T}{2} \sum_{\mathbf{q}} (\hat{B}^\dagger_{\mathbf{q}} \hat{c}_{\mathbf{q}} + h.c.) \tag{A.42}$$

where the trion Rabi frequency reads

$$\frac{\Omega_T}{2} = g\sqrt{N_e} 4\mathscr{N} \left(\frac{\lambda_2}{\lambda_1} + \frac{\lambda_1}{\lambda_2} \right) = \frac{\Omega_X}{2} \sqrt{8\pi a_B^2} \mathscr{N} \left(\frac{\lambda_2}{\lambda_1} + \frac{\lambda_1}{\lambda_2} \right) \sqrt{n_e} \tag{A.43}$$

where we used the Rabi frequency definition for the neutral exciton case, $\Omega_X/2 = g\sqrt{2A/\pi a_B^2}$, and $n_e = N_e/A$ is a concentration of free electrons which can form trions. Equation (A.43) then allows to estimate n_e using

$$n_e = \left(\frac{\Omega_T}{\Omega_X} \right)^2 \frac{1}{4\pi a_B^2} \frac{[1 + 16\lambda_1^2\lambda_2^2/(\lambda_1+\lambda_2)^4]}{(\lambda_2/\lambda_1 + \lambda_1/\lambda_2)^2} \tag{A.44}$$

once the variational parameters are known.

A.3.2 Trion binding energy and variation

Next, we proceed to define λ_1 and λ_2 for trions in TMDC. We follow the approach outlined in [198], using the wavefunction from Equation (A.37). The expectation value for the trion Hamiltonian (includes kinetic terms for relative motion and Coulomb interaction) then can be written as

$$E^{(T)} = \frac{\mathscr{I}_1 + 2\chi\mathscr{I}_2 + \mathscr{J}_1 + \mathscr{J}_2}{1+\chi^2} \tag{A.45}$$

where we define auxiliary quantities:

$$\mathscr{I}_1 = \left(\frac{1}{\lambda_1^2} + \frac{1}{\lambda_2^2}\right)(1+\gamma) - \frac{4}{\lambda_1}\int_0^\infty \frac{dx}{(1+\frac{2r_0}{\kappa\lambda_1}x)}\frac{1}{[1+x^2]^{3/2}} - \frac{4}{\lambda_2}\int_0^\infty \frac{dx}{(1+\frac{2r_0}{\kappa\lambda_2}x)}\frac{1}{[1+x^2]^{3/2}} \tag{A.46}$$

$$\mathscr{I}_2 = \frac{4(1+\gamma)}{(\lambda_1+\lambda_2)^2} - \frac{(\lambda_1+\lambda_2)\chi^2}{2\tilde{\lambda}^2}\int_0^\infty dx \frac{1}{(1+\frac{r_0}{\kappa\tilde{\lambda}}x)}\frac{1}{[1+x^2]^{3/2}} \tag{A.47}$$

$$\mathscr{J}_1 = \frac{4}{\lambda_1}\int_0^\infty dx \frac{1}{(1+\frac{2r_0}{\kappa\lambda_1}x)}\frac{1}{[1+x^2]^{3/2}}\frac{1}{[1+(\lambda_2/\lambda_1)^2x^2]^{3/2}} \tag{A.48}$$

$$\mathscr{J}_2 = \frac{2\chi^2}{\tilde{\lambda}}\int_0^\infty dx \frac{1}{(1+\frac{r_0}{\kappa\tilde{\lambda}}x)}\frac{1}{[1+x^2]^3} \tag{A.49}$$

where $\gamma = m_e/m_h$, $\tilde{\lambda} = \lambda_1\lambda_2/(\lambda_1+\lambda_2)$, and we remind that r_0 is screening parameter, κ is average dielectric permittivity of the substrate. Here, all length parameters are measured in the units of

$$a_0 = \frac{\hbar^2\varepsilon_0 4\pi\kappa}{e^2 m_e} \tag{A.50}$$

and energies are measured in units of

$$E_0 = \frac{\hbar^2}{2m_e a_0^2} \tag{A.51}$$

To obtain the binding energy for the trion complex, we minimize $E^{(T)}[\lambda_1,\lambda_2]$ with respect to variational parameters, and subtract the exciton binding energy contribution E_b^X. The latter is

obtained from minimization of

$$E^{(X)}[\lambda_0] = \frac{(1+\gamma)}{\lambda_0^2} - \frac{4}{\lambda_0}\int_0^\infty dx \frac{1}{(1+\frac{2r_0}{\kappa\lambda_0}x)}\frac{1}{[1+x^2]^{3/2}} \tag{A.52}$$

which for previously defined parameters of $m_e = 0.8\ m_0$, $m_h = 0.84\ m_0$, $r_0 = 4\ nm$, $\kappa = 4$, gives $\lambda_0 = 0.93\ nm$ and binding energy of $E_b^X = -\min\{E^{(X)}[\lambda_0]\} = 259\ meV$. The variational procedure for the trion then gives the binding energy of $E_b^T = -\min\{E^{(T)}[\lambda_1,\lambda_2]\} - E_b^X = 26\ meV$ for $\lambda_1 = 0.87\ nm$ and $\lambda_2 = 2.54\ nm$. These are the parameters which will be used in the following. Although we remind that considered variation with two parameters is oversimplistic, it provides energy estimate to be very close experimentally measured trion binding energy of 30 meV.

Finally, substituting obtained radii $\lambda_{1,2}$, $a_B = 0.93\ nm$, and experimentally measured Rabi-splittings $\Omega_T = 5.8\ meV$, $\Omega_X = 17.2\ meV$, using Equation (A.44) we estimate the electron concentration available for trion creation to be $n_e = 4.05\times10^{10}\ cm^{-2}$, with the full concentration corresponding to $n_e^{\text{tot}} = 8.1\times10^{10}\ cm^{-2}$. Note that so far only variation and parameters obtained from the exciton-polariton case were used, with no fitting involved.

A.3.3 Trion Rabi splitting quench

We continue with the calculation of the modified trion Rabi frequency due to the deviation of statistics. For this, similarly to excitonic case [Equation (A.3)], we derive the equations of motion for the excitation mode $\hat{B}_j$ using Hamiltonian (A.42). The nontrivial dynamics part comes from the light-matter coupling term

$$i\frac{d\hat{B}_{\mathbf{q}'}}{dt}\Big|_{\text{coupl}} = [\hat{B}_{\mathbf{q}'}, \hat{\mathscr{H}}^T_{\text{coupl}}] = \frac{\Omega_T}{2}\sum_{\mathbf{q}}\hat{c}_{\mathbf{q}}[\hat{B}_{\mathbf{q}'}, \hat{B}^\dagger_{\mathbf{q}}] \tag{A.53}$$

and relies on the calculation of commutator $[\hat{B}_{\mathbf{q}'}, \hat{B}^\dagger_{\mathbf{q}}]$. To do so, it is instructive to rewrite the excitation operator in terms of trion and electron, yielding

$$\left[\hat{B}_{\mathbf{q}'}, \hat{B}^\dagger_{\mathbf{q}}\right] = \frac{1}{N_e}\left[\sum_{\mathbf{k}'}\hat{a}^\dagger_{\mathbf{k}'}\hat{T}_{\mathbf{q}'+\mathbf{k}'}, \sum_{\mathbf{k}}\hat{T}^\dagger_{\mathbf{q}+\mathbf{k}}\hat{a}_{\mathbf{k}}\right] =$$

$$= \frac{1}{N_e}\sum_{\mathbf{k},\mathbf{k}'}\left(\hat{a}^\dagger_{\mathbf{k}'}\left\{\hat{T}_{\mathbf{q}'+\mathbf{k}'}, \hat{T}^\dagger_{\mathbf{q}+\mathbf{k}}\right\}\hat{a}_{\mathbf{k}} - \hat{T}^\dagger_{\mathbf{q}+\mathbf{k}}\hat{T}_{\mathbf{q}'+\mathbf{k}'}\delta_{\mathbf{k},\mathbf{k}'}\right) \tag{A.54}$$

In the case of low pumping intensity, the trion anti-commutation relations resemble that of ideal fermions, $\{\hat{T}_i, \hat{T}_j^\dagger\} = \delta_{i,j}$, and the number of trions goes to zero. Then, the commutator for $\mathbf{q} = \mathbf{q}'$ reduces to integral over distribution function $f_\mathbf{k}$ and gives unity,

$$\left[\hat{B}_\mathbf{q}, \hat{B}_\mathbf{q}^\dagger\right] = \frac{1}{N_e}\sum_\mathbf{k} f_\mathbf{k} = 1 \tag{A.55}$$

as it should be for an ideal bosonic mode. However, for the increase of pumping we observe two contributions which change the commutation relation. First contribution comes from deviation of fermionicity for composite trion operator, such that $\{\hat{T}_{\mathbf{q}'+\mathbf{k}'}, \hat{T}_{\mathbf{q}+\mathbf{k}}^\dagger\}$ is not a simple delta function anymore. For equal momenta this starts at the value of unity, and decreases with powers of $n_T\lambda^2$.

The second contribution comes from the composite nature of the quasi-bosonic operator $\hat{B}_\mathbf{q}$, which ultimately depends on the ratio between number of trions and available free electrons for their creation. To demonstrate this point, let us rewrite Equation (A.54) as

$$\left[\hat{B}_{\mathbf{q}'}, \hat{B}_\mathbf{q}^\dagger\right] = \delta_{\mathbf{q},\mathbf{q}'} - \hat{D}_{\mathbf{q},\mathbf{q}'} \tag{A.56}$$

where the deviation operator is formally introduced as

$$\hat{D}_{\mathbf{q},\mathbf{q}'} = \delta_{\mathbf{q},\mathbf{q}'} - \frac{1}{N_e}\sum_{k<k_\mathrm{F}}\left(\hat{a}_{\mathbf{k}+\mathbf{q}-\mathbf{q}'}^\dagger\hat{a}_\mathbf{k} - \hat{T}_{\mathbf{q}+\mathbf{k}}^\dagger\hat{T}_{\mathbf{q}'+\mathbf{k}}\right) \tag{A.57}$$

where we have considered the limit of $n_T\lambda^2 \ll 1$, such that trions can be approximately treated as ideal fermions. We observe that while conceptually the deviation operator resembles the one used for excitons in the previous section, the fact that trion-electron excitation is not bound leads to different closure relations and statistics. In this case, it is reminiscent to intersubband excitations [205] with trion being an excitation over the Fermi sea. We proceed by deriving the commutation relations for the devation operator and excitation operator, which reads

$$\left[\hat{D}_{\mathbf{q},\mathbf{q}'}, \hat{B}_{\mathbf{q}''}^\dagger\right] = \frac{2}{N_e}\hat{B}_{\mathbf{q}''+\mathbf{q}-\mathbf{q}'}^\dagger \tag{A.58}$$

and it can be recursively generalized to the case of N_T particles as

$$\left[\hat{D}_{\mathbf{q},\mathbf{q}'}, (\hat{B}_{\mathbf{q}''}^\dagger)^{N_T}\right] = \frac{2N_T}{N_e}(\hat{B}_{\mathbf{q}''}^\dagger)^{N_T-1}\hat{B}_{\mathbf{q}''+\mathbf{q}-\mathbf{q}'}^\dagger \tag{A.59}$$

The derived commutation relations, which are dependent on N_T/N_e ratio, will be later shown to ultimately lead to the quench of trion Rabi frequency, where the commutator $\langle \left[\hat{B}_{\mathbf{q}'}, \hat{B}^{\dagger}_{\mathbf{q}}\right] \rangle$ averaged over highly-excited many-body state vanishes.

In the following, we proceed with considering the two aforementioned contributions one-by-one.

A.3.4 Deviation from fermionicity for the composite trion anti-commutator

To account for the deviation of statistics, we use the generalized many-body formalism for composite n-particles [206]. This allows to calculate anti-commutator for the composite fermion (trion in our case), which consists of three particles of different flavor (opposite spin electrons an a hole). In the general form, it reads

$$\left\{\hat{T}_m, \hat{T}_i^{\dagger}\right\} = \delta_{m,i} - \hat{\Xi}_{mi} \tag{A.60}$$

where deviation from fermionicity operator $\hat{\Xi}_{mi}$ is defined as

$$\left[\hat{\Xi}_{mi}, \hat{T}_j^{\dagger}\right] = \sum_n \hat{T}_n^{\dagger} \sum_{\rho} \left(\lambda_{\rho} \begin{pmatrix} n & j \\ m & i \end{pmatrix} - \lambda_{\rho} \begin{pmatrix} n & i \\ m & j \end{pmatrix} \right) + \hat{\Xi}^{\dagger}_{mij} \tag{A.61}$$

and the operator $\hat{\Xi}^{\dagger}_{mij}$ is defined through the anticommutator

$$\left\{\hat{\Xi}^{\dagger}_{mij}, \hat{T}_k^{\dagger}\right\} = \sum_{p,n} \hat{T}_p^{\dagger} \hat{T}_n^{\dagger} \Lambda_{p,k,n,j,m,i} \tag{A.62}$$

Here single exchange integrals $\lambda_{\rho}(j,i,n,m)$ are as in Equation (A.9) (though with three particle wavefunction), and ρ denotes the carrier to be exchanged. In total, it provides six contributions, which in the case of zero exchanged momentum we expect to be the same. The last term in Equation (A.61) corresponds to three-particle exchanges $\Lambda_{p,k,n,j,m,i}$ with all permutations. As it typically corresponds to $\sim \lambda^4$ scaling, which shall be accompanied by the quadratic density contribution, we refrain from considering it, and concentrate on lower order terms only. However, we note that the missing term might still effect the quench of a trion Rabi, as at increasing concentration the terms in all orders become important.

The trion exchange is calculated using the trial wavefunction

$$\Phi^T_{\mathbf{p},\mathbf{k}} = \sqrt{\frac{8\pi\lambda^2}{A}}(1+\lambda^2 p^2)^{-3/2}\sqrt{\frac{8\pi\lambda'^2}{A}}(1+\lambda'^2 k^2)^{-3/2} \tag{A.63}$$

in the electron-exciton basis without symmetrization, which is accounted at latter stage, and we take hole exchange as an example. In analogy to the case of trion interaction [207] it reads

$$\lambda_h \begin{pmatrix} 0 & 0 \\ 0 & 0 \end{pmatrix} = \sum_{\mathbf{k},\mathbf{p},\mathbf{p}'} |\Phi^T_{\mathbf{p},\mathbf{k}}|^2 |\Phi^T_{\mathbf{p}',\mathbf{k}+\alpha_h(\mathbf{p}-\mathbf{p}')}|^2 = \lambda_T \tag{A.64}$$

To evaluate Equation (A.64), we use new coordinates $\mathbf{p}-\mathbf{p}' = \delta\mathbf{p}, (\mathbf{p}+\mathbf{p}')/2 = \mathbf{P}$, make momenta dimensionless multiplying it by λ, and define $\xi = \lambda'/\lambda$. Finally, following the same procedure as for composite excitons, the anti-commutator $\langle N_T|\{\hat{T}_{\mathbf{q}'}, \hat{T}^\dagger_{\mathbf{q}}\}|N_T\rangle$ is averaged over a state of N_T composite particles (now *fermions*), such that N_T contributions is obtained. This leads to the estimate for the deviation

$$\langle \left[\hat{B}_{\mathbf{q}}, \hat{B}^\dagger_{\mathbf{q}}\right]_{nF} \rangle \equiv \frac{1}{N_e}\langle \sum_{\mathbf{k},\mathbf{k}'} \hat{a}^\dagger_{\mathbf{k}'}\hat{\Xi}_{\mathbf{q}'+\mathbf{k}',\mathbf{q}+\mathbf{k}}\hat{a}_{\mathbf{k}}\rangle = -\left\{6\frac{128}{\pi}\left(\frac{\lambda'^4}{\lambda^2}\right)\frac{N_T}{A}\mathscr{I}_T + (\lambda \leftrightarrow \lambda')\right\} = -\Delta_{nF} \tag{A.65}$$

where the dimensionless exchange integral reads

$$\mathscr{I}_T = \int_0^\infty \int_0^{2\pi} dx dx' dy d\theta_1 d\theta_2 x x' y \frac{1}{(1+x^2+x'^2/4+xx'\cos\theta_1)^3} \times$$
$$\times \frac{1}{(1+\xi^2 y^2)^3}\frac{1}{(1+x^2+x'^2/4-xx'\cos\theta_1)^3}\frac{1}{(1+\xi^2[y^2+x'^2/4-yx'\cos\theta_2])^3} \tag{A.66}$$

and we account for symmetrization between λ and λ' parameter as a separate term. As in the case of excitons, we observe that first order correction in $n_T\tilde{\lambda}^2$ reduces the coupling as a function of composite particle density ($\tilde{\lambda}$ is an effective parameter of length dimensionality).

A.3.5 Effects of medium saturation

Next, we find that the increased number of trions as a consequence of increasing pump intensity provides another contribution for the trion Rabi frequency reduction. To derive the trion-density dependence for Ω_T, we employ the same strategy as previously used for composite excitons in Section A.2.1. For this, we consider the ground state of the system as

a Fermi sea of free electrons $|\mathrm{FS}\rangle$ available for the trion creation. The relevant excited states then correspond to multi-trion states $|N_T\rangle \equiv (\hat{B}^{\dagger}_{\mathbf{q}''})^{N_T}|\mathrm{FS}\rangle$. The nonlinear contribution to the trion Rabi frequency associated to the composite nature of $\hat{B}_{\mathbf{q}''}$ comes from the average

$$\langle N_T|\left[\hat{B}_{\mathbf{q}'},\hat{B}^{\dagger}_{\mathbf{q}}\right]|N_T\rangle = \langle N_T|N_T\rangle - \langle \mathrm{FS}|\hat{B}^{N_T}_{\mathbf{q}''}\left[\hat{D}_{\mathbf{q},\mathbf{q}'},\hat{B}^{\dagger N_T}_{\mathbf{q}''}\right]|\mathrm{FS}\rangle \approx 1-2N_TN_e+O[(N_T/N_e)^2] \tag{A.67}$$

where we used Equation (A.59) and the fact that q,q',q'' are small. The analysis of Equation (A.67) shows that modified commutation relations can ultimately leads to the quench of the strong coupling once the number of trions becomes comparable to half the number of free electrons $N_T = N_e/2$. However, this only corresponds to the lowest order corrections, and higher terms shall be accounted for increasing N_T/N_e ratio to get the full treatment. In this case, smooth reduction of Ω_T is expected up to $N_T = N_e$.

Finally, collecting all contributions together (including the one described in Section A.3.4), we can write the effective commutator at growing trion density $n_T = N_T/A$ as a function

$$\langle\left[\hat{B}_{\mathbf{q}},\hat{B}^{\dagger}_{\mathbf{q}}\right]\rangle = 1-\frac{2n_T}{n_e}-\Delta_{nF}+\Delta^2_{nF}/2+O[n_T\tilde{\lambda}^2] := f_T(n_T,n_e,\lambda,\lambda') \tag{A.68}$$

where similarly to exciton case we conjectured the appearance of the quadratic term $\Delta^2_{nF}/2$, which appears in the expansion of the exponent. The function $f_T(N_T,N_e,\lambda,\lambda')$ is decreasing from 1 to 0, and we consider it zero after the quench. The important parameter then is the half of available electron density $n_e/2$, which defines the excitation density at which quench is observed. The resulting density dependent trion Rabi frequency, defined as in Equation (A.53), then reads

$$\frac{\Omega_T(n_T)}{2} = \frac{\Omega_T(0)}{2}\left(1-\frac{2n_T}{n_e}-\Delta_{nF}+\Delta^2_{nF}/2\right) \tag{A.69}$$

and is used later to calculate the density dependence for the polariton modes.

Intuitive explanation. To explain the leading trend of linearly decreased coupling for the number of trion equal to half the number of free electrons, we note that the coupling of the trion mode to the cavity bares analogy to the atom-photon coupling[200, 208] (contrary to the neutral exciton case). This is readily seen in the $\propto \sqrt{n_e}$ dependence for the coupling constant, similarly to the common square root enhancement for the N two-level emitters.[209] Given this correspondence, we show how the coupling between trion and photon changes for high

excitation power. For the trion case, the state $|g\rangle$ corresponds to a free electron, while excited state $|e\rangle$ corresponds to the created trion. The total number of available excitations is thus equal to the number of free electrons $n_e \equiv N$. Using the analogy, we write the Hamiltonian of the system as

$$\hat{H} = \omega_c \hat{a}^\dagger \hat{a} + \sum_j^N \left\{ \Delta |e\rangle_j \langle e| + g(|e\rangle_j \langle g| \hat{a} + h.c.) \right\} \tag{A.70}$$

where $\hat{a}^\dagger$ ($\hat{a}$) is a creation (annihilation) operator for a cavity mode, and j corresponds to the considered two level system. The coupling term $\propto g$ thus describes polaritonic physics. For simplicity, we can take $\Delta = 0$ and measure cavity mode energy ω_c from this value.

The usual way to treat light-matter coupling in Equation (A.70) is to assume weak excitation conditions and perform effective bosonization [209] (i.e. make Holstein-Primakoff transformation). For this, the excitation creation operator reads

$$\hat{b}^\dagger = \frac{1}{\sqrt{N}} \sum_j |e\rangle_j \langle g| \tag{A.71}$$

where $1/\sqrt{N}$ corresponds to the normalization condition, and $\hat{b}$ can be written similarly. The overall meaning of $\hat{b}^\dagger$ is the creation of excitation out available two-level emitters (free electrons) as a superposition. With the new operators Hamiltonian (A.70) can be recast in the familiar form

$$\hat{H} = \omega_c \hat{a}^\dagger \hat{a} + g\sqrt{N}(\hat{b}^\dagger \hat{a} + h.c.) \tag{A.72}$$

where the last term corresponds to the usual polaritonic coupling with the superradiant enhancement, as for coupling to an ensemble of emitters. To see the influence of the light-matter coupling on the energy of the system (polaritonic shift), we take the many-body wave function in the form

$$|\Psi_G\rangle = \{|n_{ph}, n_{exc}\rangle, |n_{ph}, n_{exc} - 1\rangle, |n_{ph} - 1, n_{exc}\rangle, |n_{ph} - 1, n_{exc} - 1\rangle, ...\} \tag{A.73}$$

where n_{ph} corresponds to the number of photons and n_{exc} to the number of excitations (i.e. number of $|1\rangle_j$ atomic states). Only certain states will be coupled by the off-diagonal light-matter interaction term. The expectation value for the Hamiltonian (A.72) yields

$$\langle \hat{H} \rangle = \omega_c n_{ph} + \langle n_{ph} - 1, n_{exc} | g\sqrt{N} \hat{b}^\dagger \hat{a} | n_{ph}, n_{exc} - 1 \rangle =$$

$$= \omega_c n_{ph} + g\sqrt{N}\langle n_{ph}-1, n_{exc}|\sqrt{n_{ph}}\sqrt{n_{exc}}|n_{ph}-1, n_{exc}\rangle = n_{ph}(\omega_c + g\sqrt{N})$$

where we considered number of excitations to be equal to number of photons. One observes that the expectation value contains the same value of coupling $g\sqrt{N}$ as before, which is equal to Rabi frequency.

The situation is however different when weak excitation conditions are not met. In this case effective bosonic picture (and Holstein-Primakoff transform) is not longer valid. To compare the two cases, the full basis in Equation (A.70) must be considered. Choosing the wave function with $N-m$ states to excited, and m states be in ground state $\{0_i^m\}$, we can write it as

$$|\Psi_E\rangle = \{|n_{ph}\rangle \otimes |1_1, 1_2, .., 0_{i_1}, ..0_{i_2}, .., 1_N\rangle, ...\} \tag{A.74}$$

We note that Equation (A.74) is of course an approximation, and the full state may contain components with different number of excited stated. However, as the coherent state distribution is expected, their influence is suppressed.

Taking the expectation value for Equation (A.70), for Equation (A.74) one gets

$$\langle \hat{H}\rangle = \omega_c n_{ph} + \langle \Psi_E| \sum_j^N g|e\rangle_j\langle g|\hat{a}|\Psi_E\rangle = \omega_c n_{ph} + g\sqrt{n_{ph}}\sqrt{m} = n_{ph}(\omega_c + g\sqrt{m/n_{ph}}) \tag{A.75}$$

where the coupling reduced by the factor $\sqrt{m/N}$. For growing number of excitations n_{exc} (and increasing number of atom in ground state), this prefactor can be expanded into series, leading to $\propto \sqrt{m/N} \approx 1 - 2n_{exc}/N + O[n_{exc}/N]^2$ dependence. Finally, it is easy to see that for all states being excited ($m = 0$) the coupling goes to zero, as there are no states to couple. This leads to the conclusion that for the inverted medium (maximal number of trions), the cavity becomes decoupled from the matter. Of course, in reality other effects coming from non-fermionicity play the role, and linear quech to zero is expected to change into a smooth function.

A.3.6 Trion-polaritons at increasing density

Finally, we describe the process of trion Rabi quench, evidenced by the behavior of the middle polariton branch. To describe Figure 6.8 (left panel), we perform the diagonalization

of the full photon-trion-exciton system, which can be written as

$$\mathbf{H}_{\mathrm{T-pol}} = \begin{pmatrix} E_C & \frac{1}{2}\Omega_X(n_X) & \frac{1}{2}\Omega_T(n_T) \\ \frac{1}{2}\Omega_X(n_X) & E_X(n_X) & 0 \\ \frac{1}{2}\Omega_T(n_T) & 0 & E_T \end{pmatrix} \tag{A.76}$$

Here we consider the nonlinear contributions to both trion and exciton modes, taking experimentally measured values $E_T^{(0)} = 1621.02\ meV$, $E_C = 1630.32\ meV$, $E_X^{(0)} = 1645.72\ meV$, $\Omega_T = 5.8\ meV$, $\Omega_X = 17.2\ meV$, obtained exciton Bohr radius $a_B = 0.85\ nm$, variation parameters $\lambda_1 \approx \lambda = 0.87\ nm$, $\lambda_2 \approx \lambda' = 2.54\ nm$, and using the estimated electron concentration $n_e = 4.05 \times 10^{10}\ cm^{-2}$. The result is shown in Figure 6.8 (left panel) by the red solid curve, and allows to reproduce the initial red shift of E_{MPB} due to quenched trion Rabi-splitting, followed by the weak blue shift caused by exciton-exciton interactions.

Finally, we notice that in experiment the energy blue shift of the MPB at small exciton concentrations (see Figures 6.8, left panel and6.12, top panel) is about one order of magnitude larger than that predicted by the theory. The missing blueshift contribution, which manifests as a plateau due to competition with Ω_T quench and subsequent linear growth, is identified as a trion-exciton interaction. Indeed, the full trion Rabi quench appears when high order terms are neglected, with function $f_T(n_T)$ reaching zero non-smoothly. However, their account shall provide non-zero Ω_T even for $n_T \approx n_e/2$, leading to residual coupling and small trion admixture. This for instance can lead to several percent fraction of the trion in MPB branch, and contribute as trion-exciton exchange. The interaction can substantially increase the energy of MPB state even for the trion being weakly coupled to light. As a result, at exciton densities $5-10$ times above the maximum density of the excited trions, the MPB can exhibit substantial blueshift well above that predicted by the theory, which considers only neutral exciton-exciton interactions.

The full calculation of trion-exciton interaction energy is formidable and is typically limited due to its large dependence on the trion wavefunction ansatz [207]. Nevertheless, the overall strength of trion-exciton interaction is estimated to be one-to-two orders of magnitude stronger than that of exciton-exciton exchange. This is because of the following reasons: 1) Firstly, the number of electron and hole exchange processes is increased compared to the X-X exchange case; 2) the outer shell of the trion, described by λ_2, defines the scattering cross-section, which is larger than for exciton; 3) the direct Coulomb term is expected to play a role, unlike for the neutral exciton-exciton interaction case.

A.4 Quantum trion-polaritons

We now present a theoretical estimate of how a system analogous to the one considered in the current paper can be used to observe strong nonlinear response at the quantum level of a few photons. The experimental signature of such behavior is a pronounced antibunching of the photon emission, which can be monitored by measuring the second order coherence function. To calculate the latter, we consider a system described by the trion-photon Hamiltonian, where the coupling is between a single photonic mode of the cavity, described by the bosonic operators $\hat{c}, \hat{c}^\dagger$, and a trion mode with zero in-plane momentum $\mathbf{K} = 0$, characterized by the operators $\hat{B}_0, \hat{B}_0^\dagger$ [see definition in Equation (A.40)]. The Hamiltonian can be written in the rotating frame as

$$\hat{H} = \omega_c \hat{c}^\dagger \hat{c} + \omega_T \hat{B_0}^\dagger \hat{B}_0 + \frac{\Omega_T}{2}(\hat{B}_0^\dagger \hat{c} + \hat{B}_0 \hat{c}^\dagger) + P(\hat{c}e^{i\omega_p t} + \hat{c}^\dagger e^{-i\omega_p t}) \tag{A.77}$$

where P denotes the pump strength for a cw coherent optical drive of frequency ω_p. In Equation (A.77) the first two terms correspond to free cavity photons and trions and the third term describes the photon-trion coupling. The Rabi splitting Ω_T is given by Equation (A.43). The effective polariton energies in the weak excitation limit read $\omega_{L,U} = (\omega_c + \omega_T)/2 \mp \sqrt{\Omega_T^2 + (\omega_c - \omega_T)^2}/2$. Finally, it is convenient to go to the rotating frame with respect to the last term in Equation (A.77), such that the system is described by the detuning from the pump frequency.

The non-bosonic operator $\hat{B}_0^\dagger$ is characterized by its matrix elements in the Hilbert space spanned by the Fock states for trions, $|N_T\rangle$. The matrix elements read

$$\langle N_T - 1|\hat{B}_0|N_T\rangle = \frac{\langle \emptyset|\hat{B}_0^{N_T-1}\hat{B}_{\mathbf{q}\to 0}(\hat{B}_0^\dagger)^{N_T}|\emptyset\rangle}{\sqrt{(N_T-1)!F_{N_T-1}}\sqrt{N_T!F_{N_T}}} \tag{A.78}$$

where $F_{N_T} \equiv \langle \emptyset|\hat{B}_0^{N_T}\hat{B}_0^{\dagger N_T}|\emptyset\rangle/N_T!$ corresponds to the correction factor accounting for the composite nature of the trion excitation (in the case of bosonic excitations $F_{N_T} = 1$). Its explicit form can be derived using the recursive relation

$$F_{N_T-n} = \frac{(N_e - N_T)!N_e^n}{(N_e - N_T + n)!}F_{N_T} \tag{A.79}$$

which is similar to those reported earlier for Frenkel excitons [210] and intersubband excitations [205].

As for the numerator, it can be evaluated using the commutation relation

$$[\hat{B}_{\mathbf{q}}, \hat{B}^{\dagger N}_{\mathbf{q}'}] = N(\hat{B}^{\dagger}_{\mathbf{q}'})^{N-1}(\delta_{\mathbf{q},\mathbf{q}'} - \hat{D}_{\mathbf{q},\mathbf{q}'}) - \frac{N(N-1)}{N_e}\hat{B}^{\dagger}_{2\mathbf{q}'-\mathbf{q}}(\hat{B}^{\dagger}_{\mathbf{q}'})^{N-2} \tag{A.80}$$

derived iteratively from Equation (A.54). A careful treatment of recursion in arbitrary order gives a closed expression for the matrix elements

$$\langle N_T - 1|\hat{B}_0|N_T\rangle = \sqrt{N_T\left(1 - \frac{N_T}{N_e+1}\right)}\sqrt{\frac{N_e}{N_e+1}}\left[1 - (-1)^{N_T}\frac{(N_e - N_T)!N_T!}{N_e!}\right] \tag{A.81}$$

and a similar expression can be derived for its complex conjugate. Importantly, Equation (A.81) works for the relevant case of few trion excitations $N_T \leq N_e$ (contrary to the Holstein-Primakoff approach [211, 212, 213] which fails in the limit where $N_T = 1$). This will be important for obtaining correct quantum statistical properties for the cavity emission.

The dynamics is studied by numerically solving the master equation for the full density matrix of the system in the truncated trion-photon Hilbert space. It reads

$$\frac{\partial\hat{\rho}}{\partial t} = i[\hat{\rho}, \hat{H}] + \gamma_c\left[\hat{c}\hat{\rho}\hat{c}^{\dagger} - \frac{1}{2}\left(\hat{c}^{\dagger}\hat{c}\hat{\rho} + \hat{\rho}\hat{c}^{\dagger}\hat{c}\right)\right] + \gamma_T\left[\hat{B}_0\hat{\rho}\hat{B}^{\dagger}_0 - \frac{1}{2}\left(\hat{B}^{\dagger}_0\hat{B}_0\hat{\rho} + \hat{\rho}\hat{B}^{\dagger}_0\hat{B}_0\right)\right] \tag{A.82}$$

where the first term on the right hand side corresponds to the coherent part of the evolution, the second term describes photonic dissipation (characterized by the finite broadening of the cavity mode related to the finite lifetime of the cavity photons), $\gamma_c = \tau_c^{-1}$, and the third term describes trion dissipation characterized by non-radiative broadening $\gamma_T = \tau_T^{-1}$.

To characterize the statistics of the cavity output we evaluated the second order coherence function at zero delay for the cavity photons, defined as

$$g^{(2)}(0) = \frac{\mathrm{Tr}\left[\hat{c}^{\dagger}\hat{c}^{\dagger}\hat{c}\hat{c}\hat{\rho}_s\right]}{\mathrm{Tr}\left[\hat{c}^{\dagger}\hat{c}\hat{\rho}_s\right]^2} \tag{A.83}$$

where $\hat{\rho}_s$ denotes the steady state density matrix for the continuously driven dissipative system.

In the current experiment we measured a Rabi frequency $\Omega_T = 5.8\ meV$ and estimated the free electron density $n_e = 4 \times 10^{10}\ cm^{-2}$, with the corresponding number of electrons being ~ 1200 in the cavity of area $A = 3\ \mu m^2$. These experimental values already imply the expected trion-photon coupling strength for the case of a single electron in the cavity area, $g_c = \Omega_T/\sqrt{N_e} = 0.17\ meV$. In improved devices the photonic mode area can potentially be reduced to $A = 1\ \mu m^2$ using a curved top mirror with smaller radius of curvature [214, 215] so

that the coupling strength is enhanced by a factor of $\sqrt{3}$, giving $g_c = 0.29\ meV$. Meanwhile, the photon decay rates for an open cavity routinely reach $\sim 0.1\ meV$ values, and can be as low as $\gamma_c = 10\ \mu eV$ ($\sim 65\ ps$ lifetime) in the state-of-the-art samples [216, 215]. Furthermore, electron concentrations down to $n_e = 10^{10}\ cm^{-2}$ can be realised in gated samples. In this case the expected Rabi splitting will be $\sim 3\ meV$ for an average cavity occupation of 100 electrons, making phase-space filling effects even more pronounced and going far beyond the electronic confinement regime. Finally, in TMDC samples of high purity, which are encapsulated between thick hBN-layers, the trion inhomogeneous broadening as well as non-radiative recombination may become negligible such that the trion nonradiative linewidth γ_T will be determined by pure dephasing due to scattering with phonons[217]. This may result in nonradiative trion linewidths as small as $\gamma_T \sim 10\ \mu eV$ at a temperature T of $1\ K$ [217].

While studying the second-order coherence in the system, we note two possible mechanisms which can reduce the multi-photon component and facilitate single photon emission. The first mechanism corresponds to the conventional blockade-type antibunching, where two-photon occupation is suppressed by strong trion-photon coupling at the single particle level, $g_c/\gamma_{c,T} \gg 1$. In the following we show that this shall be possible in future high-quality samples. The second mechanism can be identified as an unconventional-type single photon blockade [218, 219] due to phase space filling effects, which does not require strong coupling and works at optimal parameters of $g_c \sim \gamma_T$ and $\omega_p \approx \omega_c$ (see [171] for the full analysis). It relies on destructive interference between the direct coherent optical excitation two photons and the trion-mediated excitation path [219], thus relaxing the requirement for strong energy shift. At the same time, it causes oscillations of the second-order coherence as a function of delay, and generally has smaller emission probability. Below, we consider the two regimes as long-term and near-term goals for nonlinear trion-polaritonics with TMDC materials.

The results of the second-order coherence calculations are shown in Figure A.1. First, in Figure A.1 (panel a) we plot $g^{(2)}(0)$ for a range of pump frequencies close to the cavity transition. For this, we consider cavity linewidth $\gamma_c = 0.05\ meV$, $\omega_c = \omega_T$, and $g_c = 0.29\ meV$ with 100 electrons. Studying the dependence for different values of the non-radiative trion decay rate γ_T we observe the appearance of an antibunching window when $g_c \approx \gamma_T$. At the same time, for narrow linewidths $\gamma_T \ll g_c$ the antibunching behaviour disappears from the $\omega_p \approx \omega_c$ region, signifying the resonant interference-based nature of the effect and the modest coupling requirement. At the same time, we note the limited efficiency of the single photon emission in this window, as cavity occupation is typically in $\langle \hat{c}^\dagger \hat{c} \rangle \sim 10^{-3} - 10^{-4}$.

We envisage that in practise the optimal parameters would be tuned using sample positioning in an open cavity as a tool.

In Figure A.1 (panel b), we consider a different range of pump detunings, where the coherent drive is nearly resonant with the lower trion-polariton, $\omega_p \approx \omega_L$, which corresponds to non-zero $\omega_c - \omega_p$ detuning. In the calculations we assume a high-quality cavity with $\gamma_c = 10\ \mu eV$ and improved values of the trion linewidth limited by thermal effects. The plot for $g^{(2)}(0)$ shows an antibunching for pump frequencies slightly below the transition, with single photon purity gradually improving as the coupling ratio $g_c/\gamma_{c,T}$ increases. The Fano-shape profile of the $g^{(2)}(0)$ dependence draws the connection to conventional Kerr-based polariton blockade [220], which can be accessed in structures of larger lateral size and favours the strong binding energy limit for excitons.

Finally, Figure A.1 (panel c) shows the minimal value of $g^{(2)}(0)$, minimized over a wide range of pump detunings spanning both regimes, as a function of the trion nonradiative linewidth γ_T. For trion decay rate comparable to the light-matter coupling constant g_c the unconventional antibunching can be observed ($\gamma_T > 0.1$ meV). For long-lived trions with small non-radiative decay (0.01 meV) we also observe pronounced antibunching due to conventional blockade, which is limited by the cavity quality factor. This shows that single photon emission with trion-polaritons in $MoSe_2$ is possible in high quality samples.

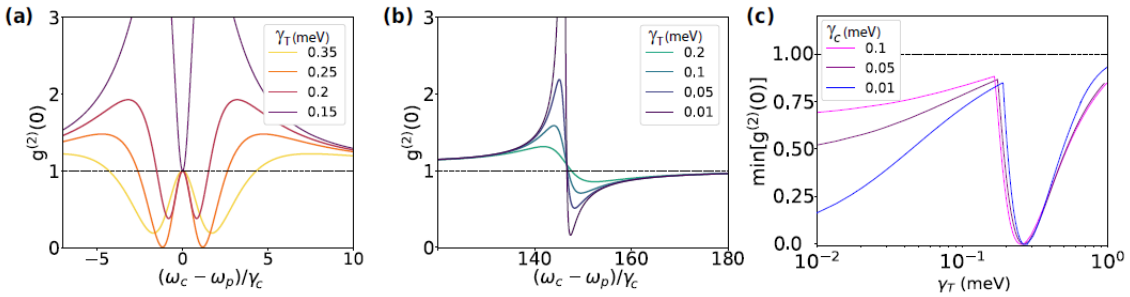

Fig. A.1 Second order coherence at zero delay for the $MoSe_2$ trion-polariton system. **(a)** $g^{(2)}(0)$ as a function of pump detuning plotted in the vicinity of the cavity resonance (we consider $\omega_c = \omega_T$), for several values of the nonradiative decay rate γ_T of the trion mode ($N_e = 100$). The destructive interference leads to the appearance of antibunching as $\gamma_T \sim g_c = \Omega_T/\sqrt{N_e}$, corresponding to unconventional photon blockade. **(b)** $g^{(2)}(0)$ for pump frequencies close to the lower polariton frequency, $\omega_p \sim \omega_L$. Conventional photon blockade leads to the appearance of antibunching at small $\gamma_{T,c}$. **(c)** The minimal $g^{(2)}(0)$, minimized over pump detuning, and shown as a function of trion decay γ_T for several cavity quality factors. Qualitatively different behaviour is visible for $\gamma_T \ll g_c = 0.29\ meV$ and $\gamma_T \sim g_c$.

Appendix B

Theory on GaN-based polariton waveguides

B.1 Introduction

In this Appendix, we describe both the FDTD and numerical simulations performed by Dr. P. M. Walker and Dr. A. V. Yariv, respectively. They are separately presented in Section B.2 and in Section B.3. The former technique was used to quantify the coupling efficiency of the investigated GaN-waveguides, while the latter was employed to deepen the experimentally observed spectral broadening.

The theory provided in this appendix refers to Chapter 7 and it is published in Reference [117].

B.2 Coupling efficiency and losses

Deduction of n_2 requires accurate deduction of the pulse energy E_{pulse} inside the waveguide, which is proportional to the measured incident pulse energy and the coupling effciency of the input grating coupler. We determine the coupling efficiency and propagation losses by complementing the finite-difference time-domain (FDTD) calculations with direct measurements of the output power from the waveguide vs. incident power. In this way, we minimised the uncertainty in our values of n_2, which strongly constrain the values of the product of E_{pulse} and $L_{loss}[1-exp(-L/L_{loss})]$ appearing in Equation 7.9, and so reduce the dependence on n_2 on the coupling efficiency. Here we explain our method by way of an example using the data

presented in Figure 7.6.

We first measured the ratio of power coming out from the output coupler vs. that incident on the input coupler. The incident power was measured directly using a power meter. The power coming out the output coupler was below the sensitivity of the power meter and so it was measured using the count rate on the CCD camera (as already described in Section 7.3). The CCD count rate vs. laser power at the sample surface was calibrated by sending the excitation laser at a know power to the CCD along exactly the same path used for detection. We obtained the ratio output power divided by input power $\eta = (4.3 \pm 0.4) \times 10^{-5}$ and $(1.8 \pm 0.2) \times 10^{-5}$ for temperatures 100 K and 200 K respectively.

The output vs. incident power ratio η arises from the input and output coupling efficiency and the propagation losses and can be expressed as $\eta = (\kappa_{up}/\kappa)^2 \cdot F \cdot exp(-L/L_{loss})$. The lengths L and L_{loss} are, respectively, device length and the characteristic propagation loss length. The rate κ_{up} is the coupling rate of the guided mode to the free space propagating mode above the sample used for excitation/detection, while κ gives the coupling of the guided mode to all channels including to the excitation/detection mode and into the substrate. It also includes ohmic losses in the metallic coupler. The ratio κ_{up}/κ is squared since, by reciprocity, this factor is the same for the input and output couplers. The factor F accounts for the imperfect mode matching of the Gaussian excitation beam to the exponentially decaying guided mode at the input coupler. The optimal value of F is 0.8, which occurs when the Gaussian spot size is matched to the decay length of the mode on the grating and the spot is positioned optimally with respect to the grating edge. In our experiment, the spot size and decay length were comparable at 6.5 μm and $3.5 \pm 0.4 \mu m$ respectively, and in each experiment we carefully optimised the spot position and incidence angle (as already mentioned in Section 7.3). We therefore assume optimal coupling, $F = 0.8$ and note that if the real value is smaller then less power would be coupled into the waveguide than we assume so that the value of n_2 would be larger than we deduce.

To evaluate κ_{up}/κ, we performed FDTD simulations of the waveguide and grating structure using the commercial Lumerical FDTD package. We used the full 3D solver but, since our structure is homogeneous in the y direction (transverse to the propagation) we assumed plane-wave behaviour in the y direction to allow achievable simulation run times. This is well justified for the non-diffracting spot sizes we have in the experiment in the low power regime where we calibrate the coupling efficiencies. The guided mode of the (simulated) waveguide was excited away from the output coupler and the fraction of power in the guided mode which is coupled into the free space above the output grating

was recorded. The nitride material refractive indexes were taken from [101]. The exact values of complex permittivity chosen for the nickel grating coupler were found to make some difference to the results so we performed the simulation using a range of experimental values from the literature and took an average. We obtain $\kappa_{up}/\kappa = (5 \pm 1)\%$ and $(6 \pm 1)\%$ for 100 K and 200 K temperature, respectively, where the uncertainties include the spread due to variation in material parameters between sources. The corresponding input coupling efficiencies are $F \cdot (\kappa_{up}/\kappa) = (4.2 \pm 0.9)\%$ and $(5 \pm 1)\%$ for 100 K and 200 K, respectively. The uncertainties come from variations in material parameters obtained from different sources in the literature. To check for consistency, the simulated decay length on the grating was $4.6 \pm 0.2 (4.9 \pm 0.2)$ μm for 100 K (200 K) which agrees well with the experimental value suggesting that the effect of the grating is accurately modelled. The simulated emission angle of the out-coupled light also agrees well with the experimentally measured values.

Taking these values of F, κ_{up}/κ and the experimentally measured values of η we are then able to deduce the losses in the waveguide. We obtain characteristic loss lengths $L_{loss} = 25 \pm 3$ μm for 100 K and 21 ± 2 μm for 200 K. These are slightly smaller than the values $\sim 50 \pm 15$ μm reported for similar exciton fractions in [101] which were, however, measured between 4 K and 30 K. This difference could arise from the increased homogeneous exciton linewidth at elevated temperatures. These can even exceed the inhomogeneous broadening and begin to dominate below-bandgap absorption. The increase in propagation losses between 100 K and 200 K may be due to a reduction in internal quantum efficiency of the MQWs, which was previously observed in photoluminescence measurements on the near-identical sample of [101]. It originates due to increased scattering of excitons away from the radiatively coupled states at higher temperatures [104].

We finally note that the uncertainties in all the parameters we discuss in this section are robustly incorporated into the uncertainty we give for the nonlinear parameter n_2.

B.3 Numerical simulations

The experimental spectra are in agreement with numerical simulations of propagating polaritons, shown in Figure B.1(a) for parameters corresponding to T = 100 K, $\Delta = -92$ meV and incident pulse energies 200 pJ (black lines) and 750 pJ (blue). We found good agreement between the widths of the numerical and experimental spectra for pulse energies up to 225 pJ (see Figures B.2, B.3 and B.4 for further details). The spatio-temporal distributions of the field intensity corresponding to the spectra in Figure B.1(a) are shown in Figures B.1(b-c).

As the pulse energy is increased from Figure B.1(b) to B.1(c), we observe an increasing modulation of the field intensity coinciding with increasing spectral broadening, confirming that the spectral broadening arises from the sub-picosecond nonlinear modulation. At pulse energies higher than 225 pJ the simulations continue to show this qualitative trend although the spectral broadening no longer agrees quantitatively with the experiment. This may be due to failure of the slowly varying amplitude approximation for large broadening.

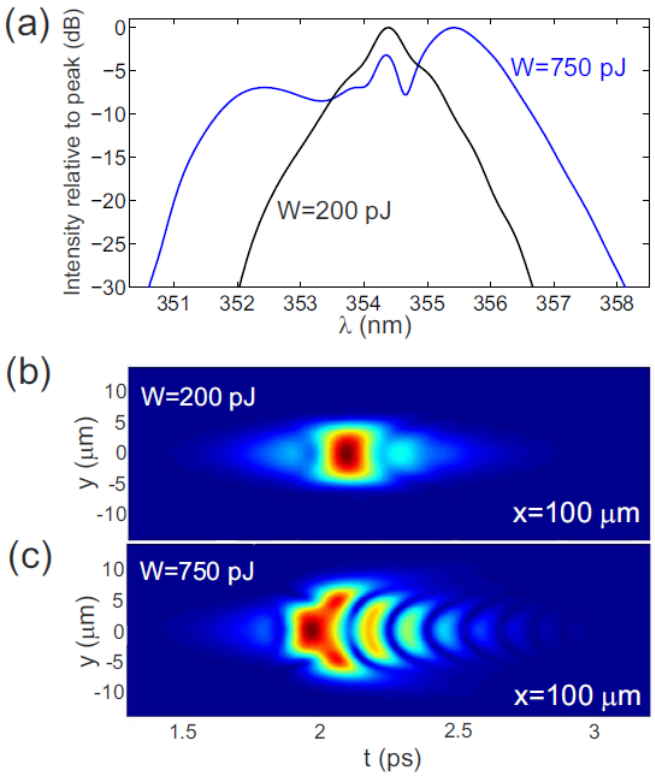

Fig. B.1 Simulated nonlinear pulse propagation. (a) Numerically calculated normalized spectra of the output field corresponding to T = 100 K, $\Delta = -92$ meV and pulse energies of 200 pJ (black lines) and 750 pJ (blue). (b,c) The numerically calculated spatio-temporal distributions of the intensity of the field after 100 μm propagation in the planar waveguide for incident pulse energies 200 pJ (b) and 750 pJ (c).

The manifestation of strong nonlinear effects, in particular spectral broadening, is also observed in direct numerical simulations. The dynamics of the photons and the excitons is described by a simple model of coupled equations for the slow varying amplitude of the photonic mode U and the excitonic mode ψ (see [10]), where this approach is used to describe the propagation of nonlinear pulses in GaAs-waveguides. In this work we use a very similar

model but take into account the dispersion of the photon mode and the dependence of the photon-exciton interaction strength (Rabi splitting) on the density of the excitons. We assume that the vertical structure (along the z coordinate) of the mode is fixed and the dispersion of the guided modes is known from the experiment. Let us mention that in spatially uniform systems the frequency of a plane wave depends only on the absolute value of the wavevector and thus the dispersion $\omega(k_x,k_y)$ reduces to $\omega(k)$ with $k=\sqrt{k_x^2+k_y^2}$. In what follows we consider wave envelopes of finite duration and aperture propagating along the x coordinate. Assuming that the duration and the aperture are large (so that in the spectral domain the pulse is narrow) we can look for a solution in the form $E=U(t,x,y)\exp(i\omega_0-ik_0x)$ for the electric field and $\Psi=\psi(t,x,y)\exp(i\omega_0-ik_0x)$ for the exciton field. The frequency ω_0 is the frequency of the exciton resonance and k_0 is the wavevector of the uncoupled photon mode at which it crosses ω_0, such that $\omega_0=\omega(k_0)$. Then for the slow varying amplitudes $U(t,x,y)$ and $\psi(t,x,y)$ we can write the system of coupled equations

$$\partial_t U=\hat{\omega}U-\gamma_p U+i\frac{\Omega}{1+\beta|\psi|^2}\psi+p(t,x,y) \tag{B.1}$$

$$\partial_t \psi=i\alpha|\psi|^2\psi-\gamma_x\psi+i\frac{\Omega}{1+\beta|\psi|^2}U \tag{B.2}$$

where $\hat{\omega}$ is the operator accounting for the photon subsystem dispersion and diffraction in the slow varying amplitudes representation, γ_p and γ_x account for the losses in the photon and in the exciton subsystems respectively, and Ω is the Rabi splitting in the linear regime. We assume that both the exciton frequency and the Rabi splitting depend on the exciton density $|\psi|^2$. This is accounted for by the Kerr like term in (B.2) and by the dependence of the photon-exciton interaction strength $\frac{\Omega}{1+\beta|\psi|^2}$ on the exciton density, where the parameter β controls the closing of the gap at high exciton densities. In the Fourier representation the operator $\hat{\omega}$ can be approximated by a Taylor expansion in the vicinity of the point $k_x=k_0$, $k_y=0$. Then the polynomial approximation of the operator can be written as $\omega(k_x,k_y)=\sum_n\sum_m\frac{1}{n!m!}\partial_{k_x}^m\partial_{k_y}^n\omega|_{k_x=k_0,k_y=0}q_x^m k_y^n$, where $q_x=k_x-k_0$. The approximation of the dependency $\omega(k)$ is known from the experiment and this allows us to calculate the coefficients in the expansion. In coordinate representation the operator $\hat{\omega}$ has the form $\hat{\omega}=\sum_n\sum_m\frac{1}{n!m!}\partial_{k_x}^m\partial_{k_y}^n\omega|_{k_x=k_0,k_y=0}(i\partial_x)^m(i\partial_y)^n$. Let us mention that if the dispersion of the photon mode is neglected and so $\omega=v_g k$ then, accounting only for the terms up to second order, we obtain $\hat{\omega}=v_g(\partial_x+\frac{1}{2k_0}\partial_y^2)$. In this simple case the model coincides exactly with the model used in [10]. In this work we take into account the real photon dispersion and we use the time as an evolution coordinate. If the problem is posed in this way then the initial condition is the spatial distribution of the field. It is also possible to account for the excitation

pulse by a source p in Figure B.2. Then we can set the zero initial condition and excite the field by the source to reproduce the effect of the incident pulse in the experiment. The pulse duration and the frequency detuning of the pulse from the linear exciton resonance is taken into account by the temporal dependency of the source p. The spatial dependency of the source p accounts for the spatial distribution of the incident pulse and the structure of the coupler. For the numerical simulations the parameters were tuned to fit the experiment at temperature $T = 100\ K$ and pump wavelength $\lambda = 354\ nm$.

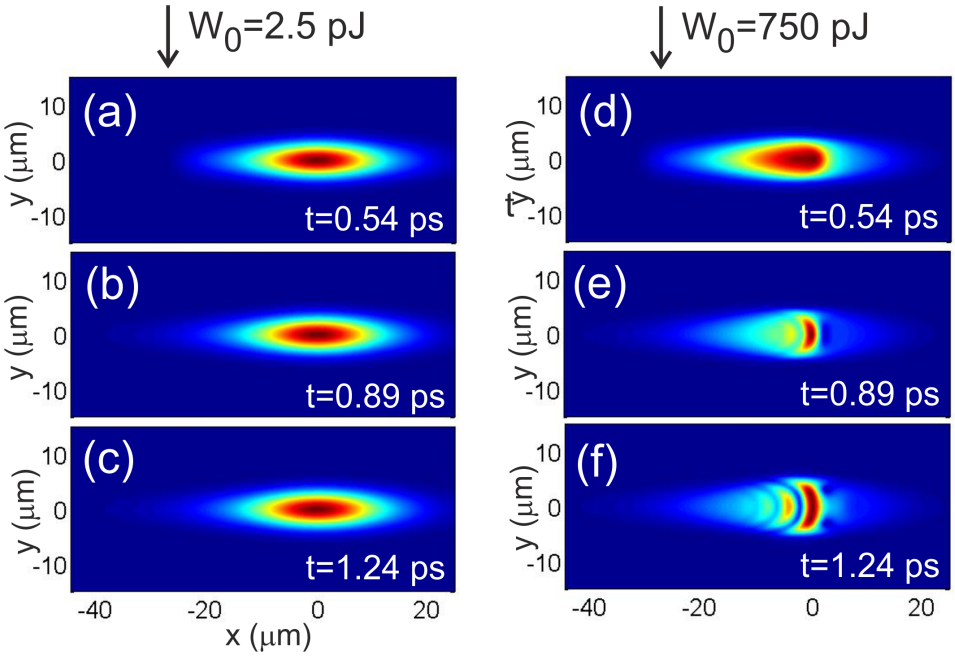

Fig. B.2 Calculated spatio-temporal distributions of the intensity of the field propagating in the planar waveguide for pulse parameters corresponding to the experiment and central wavelength $\lambda = 354\ nm$. The left column (panels (a)-(c)) shows the nonlinear propagation with pulse energy $W_0 = 200$ pJ while the right column (panels (d)-(f)) shows the same for $W_0 = 750\ pJ$. No significant change in pulse was observed in the linear propagation regime ($W_0 = 2.5\ pJ$). Time $t = 0$ corresponds to the intensity peak of the incident pulse.

The evolution of the pulse as it propagates is shown in Figure B.2 for two different pulse energies. For GaN systems it is expected that the prevailing nonlinearity is caused by the dependence of the coupling strength (Rabi splitting) on the exciton concentration (see Section 7.5) so the simulations presented here are done for the case $\alpha = 0$. We later show that both types of nonlinearity give qualitatively the same behaviour. It is seen that during propagation in the nonlinear regime the pulse becomes slightly broader in the y direction but gets significantly compressed in the x direction because of the interplay of the

normal dispersion, diffraction and effective defocusing nonlinearity. Figures B.2 (b) and (e) correspond to the experimental device length of 100. Even at pulse energy $W_0 = 200$ pJ the pulse has compressed and become modulated by then end of the device. At $W_0 = 750$ pJ the pulse is strongly modulated even by 50 propagation (see Figure B.2(d)). After the initial compression and modulation the pulse begins to spread out due to dispersion and diffraction as can be seen by comparing the intensity envelopes for 150 (Figures B.2 (c) and (f)) with those at 100 (Figures B.2 (b) and (e)). This is because system losses reduce the total intensity so that, at longer propagation distances, the nonlinearity cannot compensate the dispersion.

We assume that light is rapidly coupled out by the output coupler over a length scale small compared to the coupler size. In this case the size of the output coupler is not important. This is justified by the experimental measurment of 3.5 decay length on the coupler, compared to 100 size. To reproduce the experimental conditions the output coupler in numerical simulations is situated on the axis of the radiation propagation ($y_0 = 0$) at the distance of x_0 from the excitation spot. The calculated time-dependencies of the normalized field intensity $|U|^2$ at $x = x_0$, $y = 0$ are shown in Figure B.3(a) for different energies of the initial pulse. It is seen that for higher pulse energies the compression of the pulse takes place. It is worth mentioning here that the exciton frequency blueshift can lead to a similar effect. The field intensity distributions calculated for the case of pure nonlinear exciton blueshift are shown in Figure B.3(b). It is seen that the compression of the pulse is very much similar to the one observed in the case where Rabi splitting depends on the density of excitons.

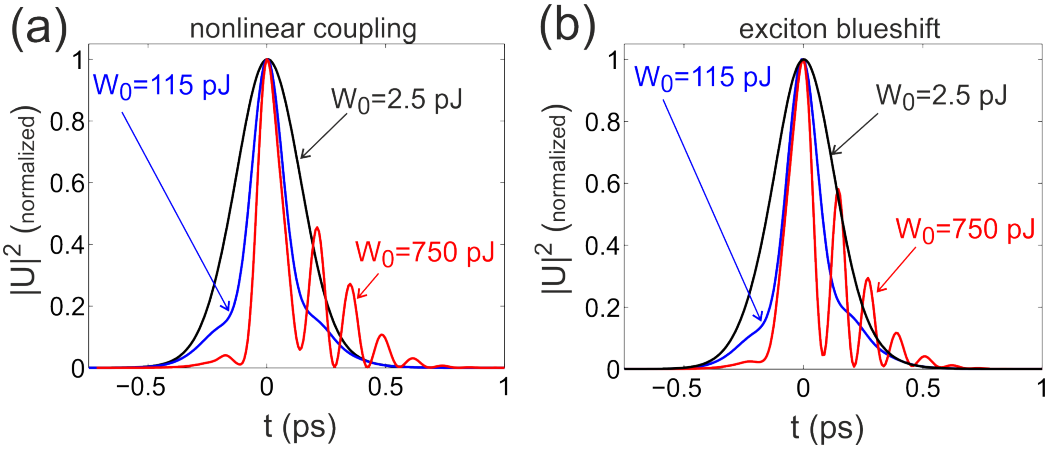

Fig. B.3 The calculated temporal intensity profiles at the transverse centre of the output coupler ($y = 0, x = x_0 = 100$) for different pulse energies. (a) The case where the nonlinearity is caused by the density dependent photon-exciton coupling (Rabi splitting). (b) The case where the nonlinearity is caused by density dependent exciton frequency. Time $t = 0$ corresponds to the arrival of the pulse at the input coupler. Simulations are done pulse central wavelength $\lambda = 354$ μm.

Now let us discuss the spectra of the output field. We define the temporal spectrum of the field measured at point x as $S(\omega) = \int |\int U(x = x_0, y, t) \exp(-i\omega t) dt|^2 dy$. This quantity is equivalent to the experimental value obtained by the integration of the spectra measured at all points across the coupler. The spectra calculated for the incident pulse energies $W_0 = 115\ pJ$ and $W_0 = 750\ pJ$ are shown in Figures B.4(a),(b) for the case where the exciton-photon coupling depends on the exciton density.

For relatively low intensities the calculated dependencies of the pulse spectral width match the experimental one well. At the same time the comparison shows that for higher intensities the model no longer has quantitative agreement with the experiment. One of the reasons explaining this fact is that the GaN samples have complex nonlinearity and the assumption that the main contribution comes from the dependency of the effective Rabi splitting on the exciton density does not apply for high energy pulses. Another reason of the discrepancy between the theoretical and the experimental results is that at higher powers the broadening of the spectrum becomes significant (in both the frequencies and the wave vectors) and therefore the slow varying amplitude approach fails to account for the dispersion of the generated frequencies.

It is instructive to show the dependencies of the pulse spectral width on the energy in the incident pulse. We define the spectral width as $\Delta S = \lambda_1 - \lambda_2$, where $\lambda_2 = \frac{2\pi c}{\omega_2 + \omega_0}$, $\lambda_1 = \frac{2\pi c}{\omega_1 + \omega_0}$ and $\omega_{1,2}$ are found from the condition $\int_{-\infty}^{\omega_1} S(\omega) d\omega = \frac{1}{4} W$, $\int_{\omega_2}^{\infty} S(\omega) d\omega = \frac{1}{4} W$, $W = \int_{-\infty}^{\infty} S(\omega) d\omega$. Physically it means that a quarter of pulse energy is in the frequencies higher than ω_2 and a quarter of the pulse energy is in the frequencies lower then ω_1.

The theoretical and experimental dependencies of the spectrum width are shown in Figure B.4(c). It is seen that for relatively low pulse energies the numerical dependency matches the experimental one well, however at higher energy levels the deviation increases. This can be seen in more detail in Figure B.4(d) which shows the experimental and theoretical dependencies over a large range of pulse energies.

As already mentioned above, the effective defocusing nonlinearity has two contributions - from the dependency of the exciton resonance frequency on the exciton density and from the dependency of the Rabi splitting on the exciton density. We have modelled the spectral broadening for both types of nonlinearity. We find that the nonlinearity arising from the exciton frequency blueshift does not lead to any qualitative differences in the spectral broadening of the pulse compared to that arising from Rabi splitting reduction. This can be seen in Figure B.4(d) where the dependencies of the spectral width on the pulse energy are presented for the pure nonlinear Rabi splitting, pure exciton blueshift and for the case where the nonlinearities contribute equally to the spectrum broadening. It is seen that the curves are

very much similar. However, it is good to note that the nonlinear Rabi splitting gives slightly better fit to the experimental dependency, which can be seen as an indication that this is the dominating source of the nonlinearity.

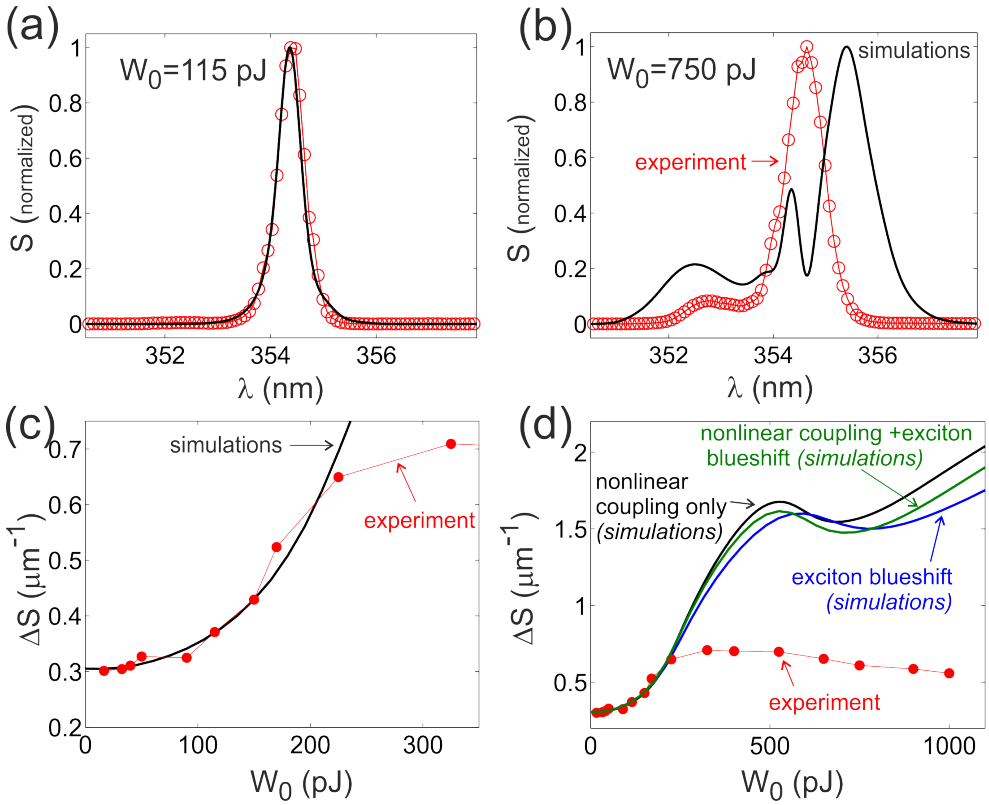

Fig. B.4 Comparison of numerically calculated and experimental spectra at the output. (a) and (b) compare numerical (black lines) and experimental (open red circles) spectra for incident pulse energies $W = 115$ pJ and $W = 750$ pJ respectively. (c) and (d) compare numerical and experimental dependence of the spectral width on pulse energy for small and large ranges of pulse energy respectively. The simulations for (a)-(c) are done for the case when the nonlinearity is caused solely by the dependence of the Rabi splitting on the exciton density. (d) compares nonlinearities caused by the density dependent Rabi splitting (black curve), density dependent exciton frequency (blue curve), and an equal contribution of both (green curve).